



HAL
open science

Study and modeling of a Fe-Cr-Co magnet based Variable Flux Memory Machine for its supply and mechanical sensorless control at high speed

Flávia Domingues de Sousa

► **To cite this version:**

Flávia Domingues de Sousa. Study and modeling of a Fe-Cr-Co magnet based Variable Flux Memory Machine for its supply and mechanical sensorless control at high speed. Electric power. Université de Lorraine, 2023. English. NNT : 2023LORR0105 . tel-04217492

HAL Id: tel-04217492

<https://theses.hal.science/tel-04217492v1>

Submitted on 25 Sep 2023

HAL is a multi-disciplinary open access archive for the deposit and dissemination of scientific research documents, whether they are published or not. The documents may come from teaching and research institutions in France or abroad, or from public or private research centers.

L'archive ouverte pluridisciplinaire **HAL**, est destinée au dépôt et à la diffusion de documents scientifiques de niveau recherche, publiés ou non, émanant des établissements d'enseignement et de recherche français ou étrangers, des laboratoires publics ou privés.



**UNIVERSITÉ
DE LORRAINE**

**BIBLIOTHÈQUES
UNIVERSITAIRES**

AVERTISSEMENT

Ce document est le fruit d'un long travail approuvé par le jury de soutenance et mis à disposition de l'ensemble de la communauté universitaire élargie.

Il est soumis à la propriété intellectuelle de l'auteur. Ceci implique une obligation de citation et de référencement lors de l'utilisation de ce document.

D'autre part, toute contrefaçon, plagiat, reproduction illicite encourt une poursuite pénale.

Contact bibliothèque : ddoc-theses-contact@univ-lorraine.fr
(Cette adresse ne permet pas de contacter les auteurs)

LIENS

Code de la Propriété Intellectuelle. articles L 122. 4

Code de la Propriété Intellectuelle. articles L 335.2- L 335.10

http://www.cfcopies.com/V2/leg/leg_droi.php

<http://www.culture.gouv.fr/culture/infos-pratiques/droits/protection.htm>

THÈSE

Présentée à

l'Université de Lorraine

En vue de l'obtention du grade de

Docteur de l'Université de Lorraine

Specialité: Énergie et Mécanique

Soutenue par **Flávia DOMINGUES DE SOUSA**

*Study and modeling of a Fe-Cr-Co magnet based Variable Flux
Memory Machine for its supply and mechanical sensorless
control at high speed*

Soutenue publiquement le 05 juin 2023 devant le jury composé de :

Président :	Prof. Corinne ALONSO	Université de Toulouse, LAAS
Rapporteurs :	MCF HDR Hamid BEN AHMED	ENS Rennes, SATIE
	MCF HDR Christophe SAUDEMONT	Université de Lille, L2EP
Membres invités :	Dr. Najla HAJE OBEID	IFP Énergies nouvelles
	M. Misa MILOSAVLJEVIC	IFP Énergies nouvelles
Examineurs :	Dr. Alexandre BATTISTON (Co-encadrant)	IFP Énergies nouvelles
	Prof. Farid MEIBODY-TABAR (Codirecteur)	Université de Lorraine, LEMTA
	Prof. Serge PIERFEDERICI (Directeur)	Université de Lorraine, LEMTA

Thèse préparée au Laboratoire Énergies & Mécanique Théorique et Appliquée (UMR 7563) en partenariat avec l'IFP Énergies nouvelles (Rueil-Malmaison)

Remerciements

Je remercie Alexandre Battiston pour la confiance que vous avez placée en moi au cours de toutes ces années. Votre soutien constant, vos conseils avisés et votre expertise m'ont été d'une aide inestimable tout au long de ma thèse (et de mon stage). J'espère être à la hauteur de votre exemple, et poursuivre mon parcours professionnel avec autant de détermination et d'engagement. Je suis profondément reconnaissante de t'avoir eu comme tuteur.

Je tiens à remercier très sincèrement Farid Meibody-Tabar et Serge Pierfedericci, mes encadrants de thèse, très complémentaires, qui ont partagé avec moi leurs connaissances et leurs expériences. Vous avez toujours été un modèle de rigueur, de passion pour la recherche et d'excellence académique. Merci également à Babak Nahid-Mobarakeh et Nouredine Takorabet pour avoir accepté de faire partie de mon comité de suivi de thèse et pour les multiples conseils et encouragements qui m'ont été partagés.

J'adresse mes remerciements aux membres du jury, Corinne Alonso, Hamid Benahmed et Christophe Saudemont pour avoir accepté d'évaluer mes travaux de thèse.

Tous mes remerciements à L'IFP Énergies nouvelles d'avoir financé ce projet ambitieux et de me fournir les outils nécessaires pour me permettre d'arriver aux résultats attendus. J'exprime ma profonde gratitude à Fabrice Le Berr et Christian Angelberger pour m'avoir accueillie au sein du département R10 et permis de réaliser ce travail dans les meilleures conditions. Je remercie chaleureusement l'ensemble des membres de l'équipe R10 pour avoir contribué à créer un environnement de travail agréable. Merci à tous pour votre enthousiasme constant à apporter votre aide en cas de besoin. Je remercie particulièrement Denis Grosjean, Julien Thiriot et Misa Milosavljevic pour avoir participé directement à la réalisation de ce projet de thèse. Je tiens à adresser une pensée toute particulière à Najla Haje Obeid, qui m'a apporté un soutien inestimable lors des moments difficiles.

Merci à mes collègues doctorantes, pour tous ces moments du quotidien partagés et merci de m'avoir apporté cette force et cette énergie à travers votre solidarité et votre bienveillance. Votre enthousiasme constant à l'idée de partager des discussions scientifiques et à apporter votre aide en cas de besoin ont été essentiels.

Je tiens à remercier mes amis de Paris (ma petite famille brésilienne en France) ainsi que mes amis du Brésil. Votre présence, votre soutien et votre regard extérieur m'ont été extrêmement précieux et enrichissants tout au long de cette aventure. Vos sourires, vos rires et votre amitié ont été une source constante de bonheur et de réconfort.

Je tiens à exprimer toute ma gratitude envers ma famille pour leur soutien inconditionnel dans toutes les épreuves de la vie. Votre croyance en moi et votre bienveillance ont été une source constante de force et de motivation. Rien de tout cela n'aurait été possible sans vous. Merci infiniment à toute ma famille pour tout ce que vous avez fait pour moi.

Un remerciement spécial à toi, Moisés, pour ton énorme soutien, ton écoute active, tes conseils avisés, ta patience et ton amour inconditionnel. Nous sommes une véritable équipe, et grâce à toi, j'ai pu relever tous les défis avec plus de confiance et de détermination. Je suis extrêmement reconnaissante de t'avoir dans ma vie.

Flávia Domingues de Sousa

Abstract

Study and modeling of a Fe-Cr-Co magnet based Variable Flux Memory Machine for its supply and mechanical sensorless control at high speed

Permanent Magnet Synchronous Machines (PMSMs) have been widely used for electrification transportation applications. Producing their magnet flux from rare-earth magnets (e.g., Nd-Fe-B magnets), these machines have had their long-term use increasingly questioned due to the risks of supply, price variability, and environmental challenges related to the extraction and recycling of these mentioned materials. To this scenario, can also be added the limitations of PMSMs for being used in large torque-speed ranges, usually requiring the implementation of flux-weakening strategies based on supplying the machine with an increasingly negative direct stator current component as the rotor speed also increases. In the case of non-salient pole machines, the Joule losses can be enhanced and the efficiency consequently reduced.

Capable of operating in a wide torque-speed range, Variable Flux Memory Machines (VFMMs) have emerged as an option characterized by controllable magnetic flux density from short-time current pulses supplying the armature windings. All this is thanks to the highly non-linear hysteresis loop characterizing the low coercive force magnets used as a source of flux. Al-Ni-Co alloys have been the choice of many researchers for these applications. However, similar magnetic materials as Fe-Cr-Co are still little explored, despite their advantageous characteristics, such as their lower content of Cobalt and mechanical properties. Within this framework, this thesis proposes the study of a single-type AC-magnetized single-pole pair VFMM composed of a Fe-Cr-Co-based rotor. The machine geometry is designed from a PMSM, in which the rotor of Nd-Fe-B is directly replaced by a solid cylinder of FeCrCo36/5.

First, a focus on the study of the magnetic behavior of the magnet when inserted in the machine environment. Because of the anisotropy differentiating the hysteresis loop of the FeCrCo36/5 in the easy or hard magnetization directions, two different methodologies are proposed for describing the partial magnetization profile via experimental tests at standstill and Finite Element Analysis simulations. The achieved results are compared with the reference obtained from ideal measuring equipment (HysteresisGraph). The effects of stator saturation and geometry, as well as the anisotropy shape, are explored to justify the differences observed. A following study focused on the magnetization under operation and the torque control is developed considering an adapted sensorless algorithm. In this context, the present research proposes the use of a Proportional Integral Phase Locked-Loop for estimating the rotor position and speed. Attention is also given to the offset angle compensation required for adjusting the mentioned position according to the acquisition system (active filters) and the characteristics of the estimation method used. A parametric sensitivity study allows the identification of the dq-axis inductances as the most critical parameters for an accurate correction angle estimation. For this reason, this research thesis is also interested in proposing a methodology to describe the d- and q-axis inductances from FEA simulations performed by considering the anisotropy effects of the magnet and also the saturation of the stator material. A variable reluctance is identified in the machine, and its effect on the correction angle is studied.

***Index Terms:* Variable Flux Memory Machines, Fe-Cr-Co Magnets, Standstill Magnetization, Running Magnetization, Sensorless control.**

Résumé

*Étude et modélisation d'une Machine à Mémoire de Flux Variable
à base des aimants Fe-Cr-Co pour son alimentation et sa commande sans capteur
mécanique à haute vitesse*

Les Machines Synchrones à Aimants Permanents (MSAPs) sont largement utilisées pour les applications d'électrification des transports. En produisant son flux magnétique à partir des aimants à base des terres rares (par exemple, Nd-Fe-B), ces machines ont été remise en question ces dernières années en raison des risques d'approvisionnement, de la variabilité des prix et des défis environnementaux liés à ces matériaux magnétiques mentionnés. À ce scénario, s'ajoutent également les limitations d'usage des MSAPs dans de grandes plages de couple-vitesse, nécessitant généralement des stratégies de défluxage, mises en œuvre en imposant une valeur de plus en plus négative à la composant direct du courant statorique à mesure que la machine accélère. Dans le cas de machines à pôles lises, en conséquence du défluxage, les pertes par effet Joule augmentent et le rendement réduit.

Capables de fonctionner dans une large plage couple-vitesse, les Machines à Mémoire de Flux Variable (MMFVs) ont émergé comme une option caractérisée par une densité de flux magnétique réglable à partir des impulsions de courant de courte durée alimentant les enroulements de l'armature. Tout cela grâce à la boucle d'hystérésis fortement non linéaire qui caractérise les aimants à faible force coercitive utilisés comme source de flux. Les alliages Al-Ni-Co sont le choix de nombreuses recherches pour ces applications. Des matériaux magnétiques similaires comme le Fe-Cr-Co sont encore peu explorés, malgré leurs avantages comme sa faible teneur en Cobalt et ses propriétés mécaniques. Dans ce cadre, cette thèse propose l'étude d'une MMFV du type simple, avec une paire de pôles et sans enroulement dédié à la magnétisation. La géométrie de la machine est conçue à partir d'une MSAP, pour laquelle un rotor à base des aimants Nd-Fe-B est remplacé par un cylindre massif à base de FeCrCo36/5.

Tout d'abord, nous nous concentrons sur l'étude du comportement magnétique de l'aimant lorsqu'il est inséré dans l'environnement de la machine. En raison de l'anisotropie différenciant la boucle d'hystérésis du Fe-Cr-Co dans les directions facile ou difficile d'aimantation, deux méthodologies sont proposées pour décrire le profil d'aimantation partielle via des tests expérimentaux à l'arrêt et des simulations par éléments finis. Les résultats obtenus sont comparés à la référence définie par des mesures à partir d'un équipement idéal (HysteresisGraph). Les effets dû à la géométrie et saturation du stator, et encore, à l'anisotropie de forme, justifient les différences observées. Les études qui suivent sont focalisés sur la magnétisation et le contrôle du couple en dynamique à partir de l'utilisation d'un algorithme de commande sans capteur de position au rotor. Dans ce contexte, cette recherche propose l'implémentation d'une Boucle à Verrouillage de phase du type Proportionnel Intégral pour estimer la position et la vitesse du rotor à partir de la mesure des tensions statoriques. Une attention est portée sur la compensation de l'angle de décalage nécessaire pour ajuster la position mentionnée en fonction du système d'acquisition (filtres actifs) et des caractéristiques de la méthode d'estimation utilisée. Une étude de sensibilité paramétrique identifie les inductances d'axes d et q comme des paramètres critiques pour l'estimation de l'angle de correction. Ainsi, cette thèse s'intéresse également à proposer une méthodologie pour décrire ces inductances à partir simulations par éléments finis. Les effets d'anisotropie de l'aimant et aussi la saturation statorique sont prises en compte. Une réluctance variable est identifiée dans la machine et son impact sur l'angle de correction étudié.

Mots clés : Machines à Mémoire de Flux Variable, Aimants Fe-Cr-Co, Aimantation à l'Arrêt, Aimantation en Dynamique, Commande sans Saptteur Mécanique.

Contents

General Introduction

1 Variable Flux Memory Machines: a literature review	1
1.1 Overview on Magnetic Properties	1
1.1.1 Historical context	1
1.1.2 Fundamentals of the magnetization	2
1.1.3 Types of magnetic materials	4
1.1.4 The Hysteresis loop	5
1.1.4.1 The major and minor hysteresis loops	5
1.1.4.2 The hysteresis loop modeling	8
1.2 The characterization of the magnets used for generating the magnetic flux in electrical machines	10
1.2.1 Rare-earth magnets	10
1.2.2 Substitution of rare-earth magnets in transportation electrification applications	16
1.2.2.1 The magnet selection for Variable Flux Memory Machines: first insights	17
1.2.2.2 Aluminum-Nickel-Cobalt magnets	18
1.2.2.3 Iron-Chrome-Cobalt magnets	19
1.2.2.4 Ferrite magnets	20
1.3 Variable Flux Memory Machines	22
1.3.1 Introduction	22
1.3.2 The positioning of Variable Flux Memory Machines in the electrical machine scenario	25
1.3.3 The mathematical modeling of Variable Flux Memory Machines in the dq-reference frame	27
1.3.3.1 Electrical equations	27
1.3.3.2 Mechanical equations	29
1.3.4 The magnetic behavior of a Variable Flux Memory Machine	30
1.3.4.1 Description of the operating principle	30
1.3.5 Characteristics of the magnetization process	34
1.3.5.1 Strategies of magnetization of Variable Flux Memory Machines	34
1.3.5.2 The magnetization current pulses	34
1.3.6 First challenge on the use of Variable Flux Memory Machines: the armature reaction	35
1.3.7 The classification of the Variable Flux Memory Machines	36
1.3.7.1 DC-magnetized Variable Flux Memory Machines	36
1.3.7.2 AC-magnetized Variable Flux Memory Machines	37
1.4 Conclusion of Chapter I	40

2 Standstill Magnetization Strategy of a Fe-Cr-Co-based Variable Flux Memory	
Machine	41
2.1 Introduction	41
2.2 Presentation of the system analyzed	42
2.2.1 The power electronics system	43
2.3 Initial study concerning the magnetic behavior of the Fe-Cr-Co magnet: analysis of the hard magnetization direction	45
2.3.1 Analytical calculation of the magnet working point	48
2.3.2 Study of the magnetic behavior of the FeCrCo36/5 in the hard magnetization direction via simulations	51
2.3.3 Investigations concerning the armature reaction in the machine studied	52
2.4 Proposal of replacement of the magnet composing the rotor	56
2.4.0.1 Validation of the magnet behavior of the FeCrCo36/5 in the easy magnetization direction via simulations	56
2.5 Proposal of experimental methodology and experimental tests at standstill	57
2.5.1 Presentation of the setup and description of the procedure used	58
2.5.2 Results obtained via experimental tests	60
2.5.2.1 Experimental results considering the machine manufactured to ensure a magnet flux through the rotor in the hard magnetization direction	61
2.5.2.2 Experimental results considering the machine manufactured to ensure a magnet flux through the rotor in the easy magnetization direction	66
2.6 Analysis of the magnetic behavior of the internal hysteresis loops via HysteresisGraph	69
2.7 Evaluation of the magnetic behavior of the FeCrCo36/5 considering a standstill magnetization	70
2.7.1 First estimation of the magnetic behavior of the magnet when magnetized in the easy magnetization direction	70
2.7.2 Proposition of an adapted model for describing the behavior of the recoil lines	73
2.7.2.1 Description of the methodology proposed	73
2.7.2.2 Evaluation of the results obtained from the methodology proposed	76
2.7.2.3 Studies for analyzing the differences observed between the results achieved by the methodologies discussed	78
2.7.3 Evaluation of the demagnetization results	84
2.8 Conclusions of Chapter 2	87
3 Running Magnetization Strategy of a Fe-Cr-Co-based Variable Flux Memory	
Machine	90
3.1 Introduction of sensorless strategies	90
3.2 The use of sensorless strategies in VFMM applications: proposition a sensorless PLL-based strategy for the Fe-Cr-Co-based VFMM	91
3.2.1 The global angle compensation	93
3.2.2 The description of the PLL angle (θ_{PLL})	94
3.2.3 The description of the filtering angle (θ_{filter})	95
3.2.4 The description of the calculus angle (θ_{cal})	96
3.2.5 Parametric sensitivity: first insights	97
3.3 Presentation of the control strategy	100

3.4	Presentation of the final system	101
3.5	Validation of the control system via simulations	101
3.5.1	Validation of the PLL-based sensorless strategy	102
3.5.2	Parametric sensitivity analysis	104
3.6	Investigation of the correction angle via experimental tests: description of results obtained by manually adjusting the angle $\Delta\theta_c$	104
3.6.1	Studies of the running magnetization control	104
3.6.1.1	Study of the variation of the magnetization current amplitude	104
3.6.1.2	Study of the variation of the current loop regulation parameters	108
3.6.1.3	Study of errors on the global correction angle $\Delta\theta_c$	109
3.6.1.4	Conclusions obtained from these magnetization control tests	109
3.6.2	Studies of the torque control	111
3.6.2.1	Studies for defining the global correction angle $\Delta\theta_c$	111
3.6.2.2	Studies causing an unintentional control loss	113
3.7	Analyses of errors observed in the errors in the global correction angle	115
3.8	The the dq-axis inductances modeling	116
3.8.1	Estimation of the dq-axis inductances according to the FeCrCo36/5 hysteresis curve	116
3.8.2	Evaluation of the inductances estimated from the methodology described	118
3.9	Study of the global correction angle ($\Delta\theta_c$) considering the reluctance effects	119
3.9.1	Analysis via simulation considering a defined amplitude of current: a case study at $I_{ref} = 70A$	120
3.9.2	Definition of the equation calculating the global offset angle for a reluctance machine	121
3.9.3	Evaluation of the global correction angle considering the reluctance machine	122
3.10	Proposition of improvements in the dq-axis inductance modeling	123
3.10.1	Analysis of the impact of the stator material in the dq-axis inductance modeling proposed	123
3.10.2	Evaluation of the global offset angle considering the improved model of reluctance machine	125
3.10.3	Evaluation in different operating points (regime and current) of the results achieved via the improved reluctance model assumption	130
3.10.4	Impact of the reluctance model in the global correction angle measured during the adjustment of the magnetization state	131
3.11	Conclusion of the Chapter 3	132
	General Conclusions	134
	Bibliography	138
	Appendix	149
	A State of the Art	150
A.1	Soft and hard magnetic materials	150
A.2	The anisotropy of magnetic materials	150
A.3	Rare-earth magnets: insights about the reuse of these magnetic materials	151
A.4	Hysteresis loop of commercial available magnets	152
A.4.1	Neodymium Iron Bor magnets	152
A.4.2	Aluminium Nickel Cobalt magnets	153
A.4.3	Iron Chrome Cobalt magnets	154

A.4.4 Ferrites	155
A.5 Critical Minerals for the United States and Europe	155
A.6 Power electronics architectures for generating the current pulses: first insights	156
B Chapter 1	158
B.1 Specifications of the HysteresisGraph	158
B.2 Magnetic characterization of the FeCrCo36/5 studied in the three magnetization directions	158
B.3 Magnetic characterization of the FeCrCo12/4 studied in the three directions	160
B.4 Simulations of magnet behavior - analysis of the magnet flux crossing the rotor	160
B.5 Modeling of working points in the hysteresis loop of the Fe-Cr-Co magnetized in the hard magnetization direction (via simulations by FEA)	162
B.6 Modeling of working points in the hysteresis loop of the Fe-Cr-Co magnetized in the easy magnetization direction (via simulations by FEA)	162
B.7 Evaluation of the magnetic behavior of the FeCrCo36/5 considering a standstill magnetization - Hard magnetization direction	164
B.7.1 Description of the methodology proposed	164
B.7.2 Evaluation of the results obtained from methodology proposed	166
B.7.2.1 Analysis of the differences observed	167
C Chapter 2	175
C.1 Machine Parameters	175
C.2 Parametric sensitivity according to the angle between the voltage and current vectors	176
C.3 Validation of the PLL-based sensorless strategy	176
C.4 Parametric sensitivity	178
C.5 Study of the Global Offset angle considering the reluctance effects	179
List of publications	182
Extended abstract (French version)	183

List of Figures

1.1	Illustration of the ideal $B=f(H)$ and $J=f(H)$ loops (left) and typical $B=f(H)$ and $J=f(H)$ loops (right) - Adapted from [1] and [2].	6
1.2	Illustration of the characteristics describing a typical hysteresis loop - Adapted from [2][1] - Point (1) defines the positive saturation, (2) the remanence, (3) the coercivity, (4) the $(BH)_{max}$ and (5) a minor hysteresis loop.	7
1.3	Magnetic properties of various magnetic materials [2].	8
1.4	Linear model of the hysteresis loop - Adapted from [1][3][4].	9
1.5	The relative abundance in earth's crust of some chemical elements [5].	10
1.6	Temperature dependency of the most commercial magnets [6].	11
1.7	Production of rare-earths by country - 2020 [7].	12
1.8	Price of Neodymium and Dysprosium from 2005 to 2014 [8].	13
1.9	Demand/supply ratio for Neodymium, Praseodymium, Dysprosium, and Terbium (all sectors) - Adapted from [7].	14
1.10	Energy and water associated with oversupplied rare-earth elements until 2050 [9].	14
1.11	Effect environmental of the life cycle of materials commonly used in electrical machines- Adapted from [10] - Analysis per unit mass.	15
1.12	Flowchart of rare-earth magnets recycling [11], where WEEEs - waste electrical and electronic equipment.	15
1.13	Illustration of the theoretical behavior of (a) the torque-speed envelope and (b) the currents operating in a large speed range - Adapted from [12][13].	17
1.14	Harmonic components of the air gap flux densities obtained by simulation before and after demagnetization, considering the (a) Al-Ni-Co-based, (b) Ferrite-based and (c) SmCo-based series variable flux memory machine [14].	21
1.15	Demagnetization curve (2^{nd} quadrant of the hysteresis loop) of typical commercially available magnets - Adapted from [15].	22
1.16	Illustration of theoretical control of the magnet flux in Variable Flux Memory Machines, considering a flux-enhancing strategy for high torque operations on the left and flux-weakening strategies for high-speed operations on the right.	23
1.17	Illustration of theoretical voltage regulation in Permanent Magnet Synchronous Machines (left) and Variable Flux Memory Machines (right) - Adapted from [16].	24
1.18	Torque envelope(left) and efficiency (right) of an Al-Ni-Co-based VFMM in different regimes for a $V=450V$ considering (1)torque production without the use of flux-weakening strategies, (2)torque production with continuous injection of negative d-axis current and (3)torque production considering a flux regulation by negative d-axis current pulses [17].	24

1.19 For a flux-weakening strategy via pulses of negative d-axis current: (a) Torque x speed, (b) Magnet Flux and Q-axis current x Speed, and (c) Efficiency - Power factor x Speed. For a flux-weakening strategy via both continuous and pulses of negative d-axis current: (d) Torque x speed, (e) Magnet Flux x Speed, and (f) Efficiency - Power factor x Speed [18].	25
1.20 Analysis of a single-type magnetic circuit.	30
1.21 Variation of the Permanence Coefficient according to the magnet geometry, considering variations on the magnet dimensions.	31
1.22 Variation in the load line placement according to the magnetization current supplying the armature windings.	32
1.23 On the left, theoretical working points are placed in the hysteresis loop of a LCF material according to the magnetization current supplying the machine. On the right, the behavior of the magnetization state/magnet flux for these different operating conditions.	33
1.24 Illustration of the armature reaction - Excitation field generated by (a) d-axis currents and (b) q-axis currents and (c) interaction between excitation and armature field that creates (d) regions of field-weakening and field-enhancing in the magnet.	35
1.25 Categories of Variable Flux Memory Machines - Adapted from [19].	36
1.26 Partitioned stator switched flux hybrid magnet memory machine - Adapted from [20].	37
1.27 Flux-switching memory machine design (left) and Reluctance memory machines (right) [21].	37
1.28 Cross-sectional view of an eight-pole magnetized(left) and six-pole magnetized(right) pole-changing memory motor [22].	38
1.29 First Variable Flux Machine presented in the literature - Cross-sectional view in a full magnetized condition [23].	38
1.30 Single-type Al-Ni-Co-based Variable Flux Machine - Adapted from [24].	39
2.1 E-turbo system prototype including Variable Flux Memory Machine.	42
2.2 Design of the Variable Flux Memory Machine.	42
2.3 Magnetic characteristic of the electric steel COGENT NO20 composing the stator.	43
2.4 Presentation of the power electronics architecture proposed for supplying the armature windings during the experimental tests.	44
2.5 Resultant flux crossing the machine according to different three-phase current patterns.	45
2.6 Hystograph HG 200 - Test bench for magnet characterization at IFP Energies nouvelles.	46
2.7 Magnet specimen used for characterizing the material in the Hystograph HG 200.	47
2.8 External hysteresis loop of the FeCrCo36/5 magnetized in the hard magnetization direction obtained using the HysteresisGraph HG 200.	47
2.9 Identification of parameters for calculating the magnetic flux density characterizing each working point (rotor shaft not represented).	49
2.10 Illustration of the path traced by the flux lines through the rotor.	50
2.11 Analysis of the working points of the Fe-Cr-Co in its hard magnetization direction for different magnetization current amplitudes obtained via FEA simulations.	52
2.12 Hysteresis profile of the low (FeCrCo36/5) and the high (hypothetical PM) coercive force used for studying the effects of the armature reaction via FEA simulations.	53

2.13 Vector diagram, being θ the rotor position.	53
2.14 Magnetic flux density distribution via FEA simulations considering the supply of the LCF-based machine (a) $I_{ref} = 0A$ for $\delta = 0^\circ$ and (c) $I_{ref} = 200A$ for $\delta = 4^\circ$ and of the HCF-based machine (b) $I_{ref} = 0A$ for $\delta = 0^\circ$ and (d) $I_{ref} = 200A$ for $\delta = 0^\circ$ for a HCF-based machine (Magnetization axis in the Cartesian y-axis).	54
2.15 Normal component of the magnetic flux density ($B \cdot n$) measured in the air gap via simulations according to the rotor surface (θ_s).	55
2.16 External hysteresis loop of the FeCrCo36/5 magnetized in the easy magnetization direction obtained using the Hystograph HG 200.	56
2.17 Analysis of the working points of the FeCrCo36/5 in its easy magnetization direction for different magnetization current amplitudes obtained via simulations.	57
2.18 Experimental setup.	58
2.19 Standstill magnetization method proposed.	60
2.20 Current pulses of several amplitudes generated by the inverter in DC/DC mode for promoting the variation of the magnetization state of the Fe-Cr-Co-based rotor.	61
2.21 Back-EMF measured for a regime around $\Omega = 45krpm$ considering a magnetization procedure via injection of positive current pulses of different amplitudes in the armature windings at standstill.	62
2.22 Back-EMF measured at $\Omega = 45krpm$ considering a magnetization procedure via injection of different quantity of positive current pulses in the armature windings at standstill.	63
2.23 Back-EMF measured considering a demagnetization procedure via injection of negative current pulses in the armature windings at standstill.	64
2.24 Back-EMF measured considering a demagnetization procedure via injection of positive current amplitudes in the armature windings while $\Omega \neq 0$.	65
2.25 Magnetization behavior for a VFMM considering the flux crossing the hard magnetization direction of the magnet - Experimental tests at $\Omega = 45krpm$.	66
2.26 Back-EMF measured at $\Omega = 18krpm$ ((a) and (b)) and $\Omega = 45krpm$ ((c) and (d)) considering a magnetization procedure via injection of positive current pulses of several amplitudes in the armature windings at standstill.	68
2.27 Magnetization behavior for a VFMM considering the flux crossing the easy magnetization direction of the magnet - Experimental tests at $\Omega = 45krpm$.	69
2.28 Internal hysteresis loops via HysteresisGraph.	70
2.29 Recoil lines estimated via simulations considering a parallel behavior to the major hysteresis loop ($\mu_r = 1.25$) - FeCrCo36/5 magnetized in the easy magnetization direction.	71
2.30 Validation via simulations of the estimated recoil lines.	73
2.31 Overview of the methodology proposed for validating of the working point placement of the Fe-Cr-Co magnetized in the easy magnetization direction.	74
2.32 Methodology proposed - Definition of the working point placement at the load line $I_{mag} = 0A$ via FEA.	74
2.33 Recoil lines estimated via FEA for characterizing the FeCrCo36/5 magnetized in the easy magnetization direction ($B_r = 1.36T$, $H_c = -49.6kA/m$).	75
2.34 Validation of the sinusoidal profile of the back-EMF via simulations considering the estimated recoil lines.	76
2.35 Recoil lines obtained via multiple strategies.	77
2.36 Recoil lines estimated by simulations after magnetization via $I_{mag} = 250A$ and $I_{mag} = 350A$, using as methodology the parallelism to the external loop and the experimental tests results.	78

2.37 Machine geometry considering opened slot wedges.	79
2.38 FEA simulations results regarding effects of stator material saturation.	80
2.39 Short-circuit of the magnet flux lines at no-load observed from simulations by the vector plot for the magnet manufactured for being magnetized in the easy magnetization direction (zoom in the rotor).	81
2.40 Examples of recoil lines obtained by simulations for magnetization via $I_{mag} = 350A$, where the hysteresis model is corrected considering (1) the effects of saturation and closed slot wedges during the initial magnetization and (2) the flux leakage during back-EMF induction.	83
2.41 Recoil lines obtained correcting the methodology proposed for approximating the magnetic behavior of the machine to the one of the HysteresisGraph.	84
2.42 Studies of the magnetic behavior of the VFMM during demagnetization procedures.	86
2.43 Illustration of the path traced by the working point considering the linear and nonlinear recoil lines.	86
2.44 Studies of the magnetic behavior of the VFMM during demagnetization procedures.	87
3.1 Block diagram of the PLL-based algorithm.	93
3.2 Vector diagram for defining the global offset angle $\Delta\theta_c$	94
3.3 Block diagram of the PLL-based sensorless algorithm and the global offset angle to be compensated.	94
3.4 Vector diagram for defining angle θ_{PLL} established between the estimated and the rotating referential frames.	95
3.5 Schema presenting the reference of voltages measured - Definition of filtering angle.	96
3.6 Schema for presenting the control algorithm interruption sequences - Definition of calculus angle - Adapted from [25].	97
3.7 Study by simulation of parametric sensitivity of $\Delta\theta_c$ for different system parameters considering: (a) and (c) different flux linkage conditions and (b) and (d) different regime - Case (1) torque control and Case (2) magnetization control.	98
3.8 Study by simulation of sensitivity of the angle $\Delta\theta_c$ for different system parameters considering errors in the system parameters (φ_s, Ω). The case (1) represents the $I_{mag} = 0A$ and $I_q = 50A$ and (2) $I_{mag} = 50A$ and $I_q = 0A$	99
3.9 Overview on the flatness control for a PMSM.	101
3.10 Block diagram of the control system proposed.	102
3.11 Validation of the sensorless strategy - q-axis current variation considering the rotor position and speed estimated via PLL - Study at $I_q = 50A, I_q = 100A$ and $I_q = 70A$	103
3.12 Investigation of the parametric sensitivity via simulation - Study considering a variation of the machine parameters $L_q = 5\mu H, L_q = 2.5\mu H$ and $L_q = 10\mu H$, for control dq-axis inductances $L_d = L_q = 5\mu H$	105
3.13 Variation of the MS via magnetization current pulse $I_{mag} = 400A$	106
3.14 Variation of the via magnetization current pulse $I_{mag} = 300A$	107
3.15 Variation of the via magnetization current pulse $I_{mag} = 500A$	107
3.16 Variation of the MS via $I_{mag} = 200A$ for a current loop bandwidth $BW=6\text{krad/s}$	108
3.17 Variation of the MS via $I_{mag} = 200A$ for a current loop bandwidth $BW=4\text{krad/s}$	109
3.18 Variation of the MS via $I_{mag} = 300A$ for a $\Delta\theta_c$ badly estimated.	110
3.19 Variation of the MS via $I_{mag} = 300A$ for an optimal $\Delta\theta_c$	110
3.20 Torque control (multiple q-axis current amplitudes).	112
3.21 Displacement of the load line for $I_{mag} = 10A$	113
3.22 Torque control (multiple q-axis current amplitudes) - Analysis of control loss at $I_q = 80A$, for $I_d = 0A$	114

3.23 Torque control (multiple q-axis current amplitudes) - Analysis of control loss at $I_q = 90A$, for $I_d = 10A$.	114
3.24 Comparison between correction angles obtained via equations ($\Delta\theta_{calc}$) and experimental tests ($\Delta\theta_{exp}$) considering non-salient machine ($L_d = L_q = 5\mu H$ and $R_s = 5m\Omega$) at $\Omega = 45krpm$.	115
3.25 Magnet characterization for estimating the dq-axis inductances via FEA simulations - Identification of δ , the torque angle.	117
3.26 Flux estimated via FEA according to the dq-axis currents considering the anisotropic magnetic profile of the FeCrCo36/5.	118
3.27 Static inductances estimated via FEA according to the dq-axis currents considering the anisotropic magnetic profile of the FeCrCo36/5.	118
3.28 Torque measured for several amplitudes of current vector I_{ref} considering different torque angles δ ($\Gamma_e = f(\delta)$).	119
3.29 Effect of the variation of the correction angle ($\Delta\theta_c$) considering the hypothesis of a salient machine ($L_d = 6\mu H$ and $L_q = 8\mu H$) - Study for $I_{ref} = 70A$.	121
3.30 Comparison between correction angles for maximizing the torque and both DC and AC power via equations and experimental tests for multiple I_{ref} and $\delta = 0^\circ$.	123
3.31 Magnetic profile of hypothetical material composing the stator during simulations.	123
3.32 Flux estimated via FEA considering the anisotropic magnetic profile of the FeCrCo36/5 and a hypothetical ferromagnet material composing the stator.	124
3.33 Static inductances estimated via FEA considering the anisotropic magnetic profile of the FeCrCo36/5 and a hypothetical ferromagnet material composing the stator.	124
3.34 Comparison between correction angles for maximizing the torque and both DC and AC power via equations and experimental tests for multiple I_{ref} and $\delta = 0^\circ$.	125
3.35 Estimated (control) dq-voltages (V_d, V_q) for $\delta = 18^\circ$ ($I_{ref} = 70A$).	126
3.36 Torque control for $I_{ref} = 70A$ and $\delta = 18^\circ$.	126
3.37 Torque control for $I_{ref} = 70A$ and $\delta = 0^\circ$.	127
3.38 Torque control for $I_{ref} = 90A$ and $\delta = 21^\circ$.	128
3.39 Torque control for $I_{ref} = 100A$ and $\delta = 21^\circ$.	128
3.40 Estimated (control) dq-voltages (V_d, V_q) for $\delta = 21^\circ$.	129
3.41 Study of the global offset angle considering the rotor reluctance for (1) $I_{ref} = 90A$ and (2) $I_{ref} = 100A$ - Study considering $\delta = 21^\circ$ according to the torque profile in the Figure 3.28. Theoretical correction angle from analytical formulation $\Delta\theta_c = \theta_{PLL} - \theta_{filter} = -67.9^\circ$ for $t=0.10s$ to $t=0.20s$ and (2) $\Delta\theta_c = \theta_{PLL} - \theta_{filter} = -70.9^\circ$ for $t=0.35s$ to $t=0.40s$.	129
3.42 Comparison between the simulations and experimental results of the correction angles and AC power, for multiple I_{ref} and estimated $\delta = \delta_{max}$ - Study for experimental tests at $\Omega = 45krpm$.	130
3.43 Comparison between the simulations and experimental results of the correction angles and AC power, for multiple I_{ref} and estimated $\delta = \delta_{max}$ - multiple regimes.	131
3.44 Comparison between correction angles for magnetizing the VFMM via simulation and experimental tests for multiple I_{mag} .	132
A.1 Typical hysteresis loops of soft (left) and hard(right) hysteresis loops, being $H_{csoft} \gg H_{chard}$.	150
A.2 Demagnetization curves of commercially available Nd-Fe-B magnets[8].	152
A.3 Magnetic proprieties of commercially available Al-Ni-Co magnets[11].	153
A.4 Demagnetization curves of commercially available Fe-Cr-Co magnets - Provided by the supplier XFmagnets.	154
A.5 Demagnetization curves of commercially available Ferrite magnets[26].	155

A.6	Circuit topologies proposed for generating the current pulses.	156
B.1	Characterization of the magnet FeCrCo36/5 - HysteresisGraph.	159
B.2	Magnetic characterization of the magnet FeCrCo12/4.	160
B.3	Cross-section view of the machine for investigating via simulations the flux lines through the rotor for a current pattern $I_A = 0$, $I_B = I_{mag}$ and $I_C = -I_{mag}$	161
B.4	Cross-section view of the machine for investigating via simulations the magnetic flux density uniformity in the rotor for a current pattern $I_A = 0$, $I_B = I_{mag}$ and $I_C = -I_{mag}$	161
B.5	Definition of the working points characterizing the load lines for several magnetization current amplitude - FeCrCo36/5 magnetized in the hard magnetization direction ($B_r = 0.45T$, $H_c = -24.4kA/m$) - N/A = Not applicable.	163
B.6	Definition of the working points characterizing the load lines for several magnetization current amplitude - FeCrCo36/5 magnetized in the easy magnetization direction ($B_r = 1.36T$, $H_c = -49.6kA/m$)- N/A = Not applicable.	163
B.7	Overview of the methodology proposed for validating the working point placement of the Fe-Cr-Co magnetized in the hard magnetization direction.	164
B.8	Validation via simulations of the estimated recoil lines.	167
B.9	Recoil lines obtained via HysteresisGraph and simulations using the proposed methodology.	168
B.10	Remanence in terms of the excitation field in the Fe-Cr-Co magnet ($B_r = f(H_{exc})$).	169
B.11	Studies for achieving equivalence between the results obtained via experimental tests and the methodology proposed.	171
B.12	Remanence in terms of the excitation field in the Fe-Cr-Co magnet ($B_r = f(H_{exc})$) considering the corrections proposed for the model, being (1) compensation due to the closed slot wedges in the stator geometry, (2) compensation of the saturation effects in the stator and (3) compensation of the short-circuit effects observed during the back-EMF induction.	172
B.13	Recoil lines obtained by correcting the methodology proposed for approximating the magnetic behavior of the machine to the one of the HysteresisGraph.	172
B.14	Magnetic characteristic of the materials composing of the stator during simulations.	173
B.15	Remanence in terms of the excitation field ($B_r = f(H_{exc})$) of the magnet FeCrCo36/5 via HysteresisGraph and simulations, considering the stator composed of COGENT NO20 and two different hypothetical materials presented in the Figure B.14.	174
C.1	Study by simulation of sensitivity of the angle θ_{PLL} for different system parameters considering: (a) and (c) different flux linkage conditions and (b) and (d) different regimes. Case (1) represents the $I_{mag} = 0A$ and $I_q = 50A$ and (2) $I_{mag} = 50A$ and $I_q = 0A$	176
C.2	Validation of the sensorless strategy - Study at $I_d = 300A$, $I_d = 500A$ and $I_q = 200A$	177
C.3	Validation of the sensorless strategy - Study at $\Omega = 45krpm$, $\Omega = 30krpm$ and $\Omega = 20krpm$	178
C.4	Investigation of the parametric sensitivity via simulation - Study considering the variation of the machine parameter $R_s = 5m\Omega$, $R_s = 10m\Omega$ and $R_s = 2.5m\Omega$, for a control stator resistance $R_s = 5m\Omega$	179
C.5	Investigation of the parametric sensitivity via simulation - Study considering the variation of the machine parameter $L_d = 5\mu H$, $L_d = 2.5\mu H$ and $L_d = 10\mu H$, for control dq-axis inductances $L_d = L_q = 5\mu H$	180

C.6 Effect of the variation of the compensation angle ($\Delta\theta_c$) considering the hypothesis of a salient machine ($L_d = 6\mu H$ and $L_q = 8\mu H$) - Study for $I_{ref} = 50A$.	181
C.7 Catégories de machines à mémoire à flux variable - Adapté à partir de [19].	186
C.8 Banc d'essais.	186
C.9 Schéma fonctionnel de l'algorithme à Boucle de Verrouillage de Phase.	187
C.10 Courbes de démagnétisation des aimants typiquement utilisés pour produire le flux magnétique dans des machines électriques - Adapté à partir de [15].	189
C.11 Boucle d'hystérésis externe du FeCrCo36/5 obtenue à l'aide du HysteresisGraph.	189
C.12 Synthèse de la méthodologie proposée pour la validation du placement du point de travail du Fe-Cr-Co magnétisé dans la direction de la magnétisation difficile.	190
C.13 Synthèse de la méthodologie proposée pour la validation du placement du point de travail du Fe-Cr-Co magnétisé dans la direction de la magnétisation facile.	191
C.14 Schéma fonctionnel de l'algorithme sans capteur basé sur PLL et de l'angle de décalage global à compenser.	191
C.15 Comparaison entre les angles de correction et la puissance AC maximale obtenue via la simulation et les tests expérimentaux pour de multiples amplitudes de courant I_{ref} .	192
C.16 Géométrie de la Machine à Mémoire à Flux Variable étudiée.	192
C.17 Présentation de l'architecture d'électronique de puissance proposée pour l'alimentation des enroulements de l'induit lors des essais expérimentaux.	193

General Introduction

Permanent magnet synchronous machines (PMSMs) have been used in many industrial fields, being particularly attractive for traction drives used in electrical vehicles (EVs) [12, 27, 28]. Under normal operating conditions, these machines are designed to maintain a constant magnetization due to the rare-earth magnets (REMs) used as source of magnetic field. Nevertheless, the risks of supply, price variability, and environmental challenges related to the extraction and recycling of these materials have been presented in the current literature ([10, 7, 8, 29]) as major concerns for the long-term use of these machines. In addition, for extending the torque-speed range characterizing these machines beyond the base speed, flux-weakening (FW) strategies from the injection in armature windings of a negative current for generating a field in the magnetization axis (d-axis) are usually proposed to counter the increase of the back-electromotive force (EMF) [12, 27, 30]. However, additional copper losses for non-salient pole machines [17, 28] and risks of permanent demagnetization of the rare-earth magnet used [31, 32] are associated with the use of these FW strategies, which also limit the PMSMs in terms of torque production as part of the stator currents capacity is compromised [33].

Inserted in the current scenario of researches dedicated to the energy transition for more sustainable electromotive systems, this thesis research is focused on the study of Variable Flux Memory Machines (VFMMs) [23], that recently emerged as an interesting option for the transportation electrification field. Based on the use of low coercive force (LCF) magnets characterized by a highly non-linear hysteresis loop, these machines present as a major feature the possibility of having their magnetic flux density regulated by an external magnetization field created by the injection of short-time d-axis currents in the stator windings. When these d-axis currents are removed, part of the initial magnetization state of the LCF magnet is retained, which represents the "memory" of these magnets. Many authors have been using Al-Ni-Co (Aluminum-Nickel-Cobalt) alloys as LCF magnets in the VFMM ([27, 14, 34]). However, similar magnetic materials as Fe-Cr-Co (Iron-Chromium-Cobalt) are still little explored, despite presenting advantageous characteristics such as a lower content of Cobalt and good mechanical proprieties ([6, 35, 36]).

According to the excitation method used [19, 37], VFMMs can be classified as DC-magnetized, for which specific coils are arranged in the stator for injecting the magnetization currents, or as AC-magnetized, if these currents are directly injected in the existing armature windings. This last mentioned category can be divided into single-type topologies ([23, 34]), in which only LCF magnets are used to produce the magnetic flux, or into hybrid-type topologies ([33, 38]), that use high coercive force (HCF) magnets for producing a flux linked in series or in parallel with the one generated by the LCF magnet. The majority of the machine geometries studied in the current literature are hybrid-type, but this present thesis is focused on a single-type AC-magnetized Variable Flux Memory Machine having a single pole pair. This machine is designed from a PMSM geometry by replacing the Nd-Fe-B-based (neodymium-iron-boron) rotor with a solid Fe-Cr-Co-based rotor. The stator geometry is conserved, and a cylindrical shape is defined for the rotor aiming an easy adaptation to multiple stator geometries and a reduction of fragility

in high-speed operations.

The variation of the magnetization level of the magnet is proposed via two strategies: the standstill magnetization [31, 39], which considers the injection of currents in the stator windings at zero rotor speed ($\Omega = 0rpm$) and is used for initializing the magnetization state in the case of a completely demagnetized machine, and the running magnetization [40, 41], characterized by an adjustment of this magnetization state under operation ($\Omega \neq 0rpm$). For operations at $\Omega \neq 0rpm$, the use of a Field Oriented Control aiming the torque and flux control decoupling requires the identification of the direct (for magnetization control) and quadrature axis (for torque control). Errors in the rotor position can have consequences such as poor magnetization or involuntary demagnetization of the magnetic rotor. Furthermore, the mentioned torque should be theoretically controlled without modifying the magnetization state of the machine. Depending on the machine geometry and the magnet properties (low coercive force), however, an interaction between this externally created q-axis field and the magnetization one can result in the establishment of regions of flux-enhancing and flux-weakening in the magnet. Depending on the amplitude of current used for creating this mentioned q-axis field, this effect known as armature reaction ([27, 31]) can lead to demagnetization of the magnet.

Usually, the aforementioned rotor position is obtained through the use of incremental or absolute encoders or resolvers. Nevertheless, some inconveniences such as additional costs, maintenance requirements, sensitivity increase and speed limits are related to these sensors [42, 43]. Specially due to the application of the Fe-Cr-Co-based machine proposed by this research for high speed operations, for which the least unbalance on the rotor shaft is very harmful, the use of sensorless strategies is required [25, 44, 45]. Although largely explored for PMSMs, the application of sensorless strategies for VFMMs was only very recently presented in [46], which proposes a saliency-based sensorless control for a dual-layer AC-magnetized hybrid VFMM. Because for the studied Fe-Cr-Co-based VFMM a pre-defined regime is driven by an external axial airflow (no operations at zero speed), a model-based algorithm is proposed for estimating the rotor position and speed. Given this background, the studies proposed by this thesis research are divided into three chapters, detailed below:

- **Chapter 1** presents the literature review for contextualizing the use of Variable Flux Memory Machines. The basic concepts of magnetic theory are introduced, with a focus on the parameters defining the hysteresis loop that characterizes magnetic materials. The use of rare-earth magnets (REMs) for generating the flux in PMSMs is discussed as also the economic and environmental challenges related to their long-term use. Options of low coercive force magnetic materials for replacing the REMs are presented. Among them, the properties of the Fe-Cr-Co are described and compared to those of the Al-Ni-Co alloys, commonly used in VFMMs. The grade FeCrCo36/5 is presented as the one to be used for composing the cylindrical rotor of the machine studied in this research. Following, the theory behind the magnetic behavior of Variable Flux Memory machines is introduced, as also the placement of these machines in the electrical machine scenario and their classification. The mathematical modeling describing the basic operating principles of these machines is also discussed.
- **Chapter 2** is dedicated to the development and evaluation of a standstill magnetization strategy for the Fe-Cr-Co-based VFMM. The machine design considered in this research work is introduced as also the power electronics architecture composed of a two-level voltage source inverter used for generating the current pulses required for adjusting the machine magnetization state. Because of the anisotropic profile exhibited by the FeCrCo36/5, two studies are distinguished in this chapter: an introductory one, considering the first manufactured rotor crossed by the magnetic flux in the hard magnetization direction, and

a second one, considering a new rotor proposed for ensuring the flux passing through the easy magnetization direction. Experimental tests as well as simulations via Finite Element Analysis (FEA) are proposed for characterizing the magnetic behavior of these two mentioned magnetic rotors in partial magnetization states. These results are then compared to the intrinsic ones achieved via ideal equipment of measurement, a HysteresisGraph. The observed differences are evaluated, and strategies for compensating them are proposed.

- **Chapter 3** introduces a sensorless strategy from a Proportional-Integral Phase-Locked Loop (PLL) based on the measurement of the output phase-voltage for estimating the rotor position and speed. Attention is given to the compensation of the phase delays included in this initially estimated position due to the filtering chain, the estimation method (PLL) and the calculus time. Equations describing these mentioned angles are defined and their estimated values calculated considering a well-known machine model are compared to the ones obtained experimentally. The differences observed between these results are discussed on the basis of a parametric sensitivity study. Delineating the impact on the calculated angles of errors in the machine (dq-axis inductances and stator resistance) and system (regime and flux linkage) parameters, this mentioned study is used for justifying the dependence of the global compensation angle to the mentioned dq-axis inductances. In this context, an in-depth investigation for modeling these machine parameters is proposed considering the anisotropic hysteresis profile of the Fe-Cr-Co composing the rotor and also the stator material saturation.

This thesis project presents the following major objectives:

- To propose and study a single pole pair Fe-Cr-Co-based Variable Flux Memory machine designed from a PMSM geometry in which the initially used rare-earth magnet (Nd-Fe-B) will be replaced by a low coercive force magnet (Fe-Cr-Co);
- To experimentally validate the magnetization of a Variable Flux Memory Machines using a proof-of-concept;
- To evaluate the magnetic behavior of the proposed Fe-Cr-Co-based Variable Flux Memory machine from the development of strategies for evaluating the standstill and under operation magnetization control;
- To propose and develop via experimental tests and simulations a robust torque control strategy based on a sensorless algorithm adapted to high speed applications;
- To evaluate the phase delays impacting the rotor position estimation via the sensorless algorithm used and propose a strategy adapted to the machine studied for compensating them.

Chapter 1

Variable Flux Memory Machines: a literature review

1.1 Overview on Magnetic Properties

The basis of the study proposed for this research is the understanding and characterization of the magnetic properties of the magnets used for imposing the magnet flux through the stator windings in electrical machines such as Permanent Magnet Synchronous Machines and Variable Flux Memory Machines. For this reason, this section is dedicated to presenting these mentioned properties. Later, these concepts will be used for introducing the general concepts related to the magnetic behavior of Variable Flux Memory Machines.

1.1.1 Historical context

The use of magnetic materials was first reported in ancient Greece, by the discovery of the Loadstone, a piece of naturally magnetized mineral whose characteristics were discovered by Greek philosophers in 200 B.C. to 400 B.C. [47]. The first scientific work about the Loadstone was published by William Gilbert, in his book "De Magnete", where the author described the properties of attraction and repulsion of magnets [48] and also how Loadstone magnetic properties could be improved by the addition of soft iron [47]. Later, historical landmarks such as the advent of the scientific method and the definition of the theory of Electricity (Coulomb, 1750) and of Electrodynamics (Oersted, 1820) made possible contributions from authors such as Biot and Savart (defining the Biot-Savart Law, in 1820), Ampère's (demonstrating effects of magnetism from electric currents, in 1820) and Faraday (discovering the electromagnetic induction, in 1821, and demonstrating the principle of the electric motor with a steel magnet). Maxwell, in describing mathematically Faraday's Laws (1864), unified the theory of electricity, magnetism, and light, defining the basis of electrodynamics from the equations below. Other important discoveries related to the magnetic theory can be analyzed in [47, 49, 50, 48].

$$\begin{aligned}\nabla \cdot \vec{B} &= 0 && \text{Gauss's law for magnetostatics} \\ \nabla \cdot \vec{D} &= \rho && \text{Gauss's law for electrostatics} \\ \nabla \times \vec{E} &= -\frac{\partial \vec{B}}{\partial t} && \text{Faraday's law} \\ \nabla \times \vec{H} &= j_t + \frac{\partial \vec{D}}{\partial t} && \text{Ampère's law}\end{aligned}\tag{1.1}$$

where the vector fields \vec{E} (in $[V/m]$) and \vec{B} (in $[T]$) are respectively, the the electric and magnetic fields defined according to the position (\vec{r}) and time (t) such as $\vec{E}=\vec{E}(\vec{r},t)$ and $\vec{B}=\vec{B}(\vec{r},t)$. The vector \vec{D} represents the electric displacement field (in $[C/m^2]$), or electric induction. The scalar fields $\rho=\rho(\vec{r},t)$ (in $[C/m^3]$) and vector field $\vec{j}_t=\vec{j}_t(\vec{r},t)$ (in $[A/m^2]$) are, respectively, the volume charge and true current densities (being \vec{j}_t related to the free charges). The magnetic field intensity (or magnetic field strength, in $[A/m]$ or $[At/m]$) is given by \vec{H} , a variable susceptible to be controlled by the external currents[51].

The analysis of Gauss's law for magnetostatics can be rewritten in the integral form for presenting the conservative character of a magnetic flux φ crossing a closed surface:

$$\oiint_S \vec{B} \cdot d\vec{S} = 0 \quad (1.2)$$

where $d\vec{s}$ is the element defined at a point in the closed surface s in the direction of the outward normal. The flux (φ , in $[Wb]$) contribution for each element of the surface can be defined by the equation:

$$\iint_S \vec{B} \cdot d\vec{S} = \varphi \quad (1.3)$$

For analyzing Faraday's and Ampère's law, two constitutive relations are defined to describe the relation between \vec{E} and \vec{D} and \vec{B} and \vec{H} . In the free space, as presented by [52], the constitutive relations are given by:

$$\vec{D} = \epsilon_0 \vec{E} \quad (1.4)$$

$$\vec{B} = \mu_0 \vec{H} \quad (1.5)$$

The constant μ_0 ($\mu_0 = 4\pi 10^{-7}$, in $[H/m]$) defines the permeability of free space. This property characterizes the medium through which the magnetic field intensity field passes and in which the measurement of the magnetic flux density is made[53]. The permittivity of free space is given by ϵ_0 ($\epsilon_0 = 8.85 \times 10^{-12}$, in $[F/m]$). Also known as dielectric constant, this parameter is a measure of the electric polarizability of a dielectric, representing the dielectric displacement per unit electric field[54]. For a homogeneous medium (in which the constants of proportionality are invariant with space), the equations [1.4] and [1.5] above described are, respectively, calculated by $\vec{D} = \epsilon \vec{E}$ and $B = \mu \vec{H}$, in which ϵ is calculated by $\epsilon = \epsilon_0 \epsilon_r$ (in $[F/m]$) and $\mu = \mu_0 \mu_r$ (in $[H/m]$). The ϵ_r ([unitless]) and μ_r ([unitless]) are respectively the relative permittivity and permeability of the material analyzed.

1.1.2 Fundamentals of the magnetization

Some fundamental concepts regarding the magnetization of materials are exposed in this section aiming to define a theoretical basis for understanding magnetic materials. Magnetic fields originate from small regions of space called magnetic poles[55]. A north-south pole pair defines a dipole, whose magnitude is expressed by the elementary quantity in solid-state magnetism \vec{m} [48]. The amplitude of this magnetic moment (\vec{m}) is calculated by the product between the pole strength and the distance between poles. The magnetization \vec{M} (in $[A/m]$ or $[At/m]$), given by the total magnetic moment per unit volume, is defined according to the equation [55]:

$$\vec{M} = \frac{1}{V} \left(\sum_i \vec{m}_i \right) \quad (1.6)$$

The interaction between magnetic moments defines in magnetic materials the existence of spontaneous magnetization and hysteresis [51], as going to be discussed in later chapters. In the presence of external electric and magnetic fields, the material gets polarized and magnetized respectively, and the equations [1.4] and [1.5] can be rewritten by:

$$\vec{D} = \epsilon_0 \vec{E} + \vec{P} \quad (1.7)$$

$$\frac{1}{\mu_0} \vec{B} = \vec{H} + \vec{M} \quad (1.8)$$

where \vec{P} is the polarization density (in $[C/m]$), representing the density of the permanent and induced electric dipole moments in a dielectric material. The contributions of variation of polarization and magnetization with time to the total current density j formerly presented in the equation [1.9] are, respectively, described by the polarization current density $\vec{j}_p = \frac{\partial \vec{P}}{\partial t}$ and the magnetization current density $\vec{j}_M = \nabla \times \vec{M}$, which combined define the total current density as $\vec{j} = \vec{j}_t + \vec{j}_M + \vec{j}_p$, being \vec{j}_t the true current density representing the convection of free charges in the medium. The equation [1.8] as $\vec{B} = \mu_0 \vec{H} + \mu_0 \vec{M}$, which defines, in the absence of a media ($\mu_0 \vec{M}$), the constitutive relation $\vec{B} = \mu_0 \vec{H}$ formerly presented in the equation [1.5]. When $\vec{M} = 0$, the contribution of this field to \vec{B} is defined as the magnetic polarization \vec{J} .

Rewriting the equations [1.1] by using [1.7] and [1.8]:

$$\begin{aligned} \nabla \cdot \vec{B} &= 0 && \text{Gauss's law for magnetostatics} \\ \epsilon_0 \nabla \cdot \vec{E} &= \rho && \text{Gauss's law for electrostatics} \\ \nabla \times \vec{E} &= -\frac{\partial B}{\partial t} && \text{Faraday's law} \\ \left(\frac{1}{\mu_0}\right) \nabla \times B &= j + \epsilon_0 \frac{\partial \vec{E}}{\partial t} && \text{Ampère's law} \end{aligned} \quad (1.9)$$

Because Gauss's law defines $\nabla \cdot B = 0$, the equation [1.8] can be rewritten as $\nabla \cdot \vec{H} = -\nabla \cdot \vec{M}$. This field \vec{H} is present due to discontinuities in the sample magnetization, which is observed, for example, in the surface of open samples (strip, rod, sphere, etc.) and is defined as a demagnetizing field, as it is opposite to \vec{M} [51]. This field, named \vec{H}_d (in $[A/m]$) reduces the effective field (H_{eff} , in $[A/m]$) on a magnet body when it is exposed to an external magnetization field (H_{ext} , in $[A/m]$). For uniformly magnetized bodies (as the ones composed of ellipsoidal shapes¹), \vec{H}_d is calculated by [48, 57, 58]:

$$\begin{aligned} H_{eff} &= H_{ext} - H_d \\ &= H_{ext} - N_d \vec{M} \end{aligned}$$

where the N_d represents the demagnetizing factor, which has a value between 0 and 1 depending on the magnet shape [57] and on the direction of magnetization in the magnetic sample. An exhaustive study regarding concepts related to the self-demagnetizing effects in ellipsoidal bodies can be found in [56].

Regions having a uniform magnetization in a magnetic material can be defined as domains [55]. Domains, firstly postulated by Weiss in 1970, are established in order to minimize the total energy

¹According to [56], Maxwell (1873) defined that ellipsoids are the only finite bodies that can be uniformly magnetized in the presence of a uniform inducing magnetic field. Only for these bodies, an analytical computation of the self-demagnetization effect can be obtained.

of the material, representing magnetically saturated areas where all the magnetic moments lie parallel to one another [59]. Neighboring domains have different orientations and are interfaced by the domain walls [55, 59], which can be moved when energy is added to or removed from the magnetic system. This phenomenon can be described as an alignment of part of the moments composing the wall with moments in a neighboring domain orientated according to the direction of the applied field.

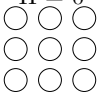
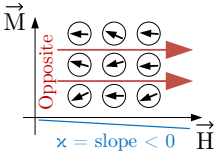
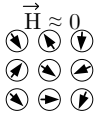
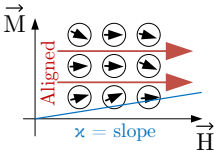
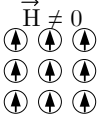
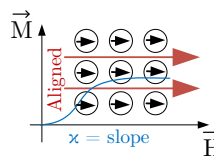
The total magnetization of a system prefers to align itself along a preferential axis costing the least energy (or low \vec{H} for achieving the same \vec{B} or \vec{M}). This orientation establishes an easy magnetization direction of magnetization. The directions in which this spontaneous orientation of the magnetization does not occur are named hard magnetization directions. This directional dependence of a magnetic material's properties is defined as its anisotropy. This propriety largely affects the internal energy of a magnetic material and consequently, the rotation of magnetic domains over an external field direction [53, 59, 60]. An overview of the magnetic anisotropy can be found in [60], [61] and [48]. Appendix A.2 describes the major factors mentioned in the literature as sources of this anisotropy. Even if this topic is not the focus of the present thesis research, this phenomenon is mentioned because some grades of the magnetic materials used for generating the magnetic flux in Variable Flux Memory Machines are anisotropic. The next sections are going to present some of these materials and explore the effects of the anisotropy on the working point achieved during the normal operating conditions of a Variable Flux Memory Machine.

1.1.3 Types of magnetic materials

Materials can be classified according to their magnetic behavior into the three main categories defined below [1, 2, 55, 59, 62]. Table 1.1 summarizes some of the distinctions between these materials.

- Diamagnetic materials are the ones characterized by having no net magnetic moments and identified as responding to an external magnetic field with an opposite internal field. The susceptibility (χ) of these materials, defined as the response of the magnetic domains when exposed to an external magnetization field, is thus negative. The diamagnetic effect, introduced by Langevin (1905), is present in all materials (but it is commonly masked by a larger paramagnetic or ferromagnetic component).
- Paramagnetic materials are the ones characterized by a small and positive susceptibility, that varies according to $1/T$ (Curie's law), where T is the temperature. These materials present a net magnetic moment and the external magnetic field tries to align all elementary dipoles to the direction of this field. The paramagnetism is usually found in transition metals, but can also be found in some metals (as in Aluminum, e.g.).
- Ferromagnetic materials are the ones characterized for presenting strongly coupled atomic dipole moments that tend to be aligned parallel to each other, which defines a high positive susceptibility. Some of these materials, even in the absence of an external magnetic field, can show a spontaneous magnetization resulting from a spontaneous ordering of their atomic magnetic moments. Others, do not show this net magnetization due to the randomized arrangement of the dipoles. For these both categories, the atomic interactions are canceled when the Curie Temperature (T_C) is achieved. At this point, the material suffers irreversible metallurgical changes due to the high thermal agitation, becoming paramagnetic.

Table 1.1: Magnetic Behavior of different types of materials - Adapted from [2].

Classification of magnetic materials				
Type of magnetism	Susceptibility (χ)	Atomic Behavior	Magnetic Behavior $M(H)$	Material/ Susceptibility (χ)
Diamagnetism	Small and negative $\chi < 0$ defining a linear function $\vec{M} = \chi\vec{H}$. No temperature dependence is observed for these materials.	Atoms have no magnetic moment $\vec{H} = 0$ 	 Slope $\chi < 0$	Bi= -166×10^{-6} Au= -34.7×10^{-6} Cu= -9.63×10^{-6} H ₂ O= -9.2×10^{-6} SiO ₂ = -6.2×10^{-6} CaCO ₃ = -4.8×10^{-6}
Paramagnetism	Small and positive $1 \gg \chi > 0$ and $M = \chi H$. A linear temperature dependence (weak) defined by $1/\chi(T)$.	Atoms have randomly oriented magnetic moments $\vec{H} \approx 0$ 	 Slope $\chi > 0$	Al= 21.1×10^{-6} $\beta - Sn = 22.7 \times 10^{-6}$ Pt= 257×10^{-6} Mn= 904×10^{-6} Air= 0.36×10^{-6} O ₂ = 2.1×10^{-6}
Ferromagnetism	Large and positive, function of the applied field, micro-structure dependent $\chi > 0$, $ \chi \gg 0$.	Atoms have parallel aligned magnetic moments $\vec{H} \neq 0$ 	 Slope $\chi > 0$	Ni Co $\approx 80 \times 10^3$ Fe

1.1.4 The Hysteresis loop

The classical electromagnetic theory defines the hysteresis loop (or BH loop), according to the concepts introduced in 1881 by James Ewing, as the description of the magnetic response of a material when submitted to an external field. The analysis of the hysteresis loop and its respective main characteristics is crucial for understanding the behavior of Variable Flux Memory Machines. As later chapters are going to present, the controllable variation of the magnetization state (MS, or magnetization level) of the magnet requires knowledge of the major and minor BH loops.

1.1.4.1 The major and minor hysteresis loops

The path traced by a hysteresis loop describes the formerly mentioned relation between the magnetization (or the induction) achieved in a material and the external field in which this material is inserted. It can be divided into four different regions, achieved from different steps. First, from a non-magnetized state, the external field is largely increased until the material is fully saturated (positive saturation, on the 2nd quadrant). From the saturation, the same external field is reduced until a large negative value, sufficient to fully demagnetize (negative saturation, on the 3rd one) the magnet. Finally, the positive saturation is achieved again by increasing the external field to reach the positive saturation. The 1st and 3rd quadrants are identical and represent the magnetization regions of the hysteresis loop. The 2nd and 4th quadrants refer to demagnetization regions[2]. Special attention is given to the 1st quadrant, in which the initial magnetization curve of the material is described as also the level of induction required for saturation, and to the 2nd quadrant, in which the behavior of the magnetic material until the complete demagnetization can be studied.

The hysteresis curve describing the magnetic behavior of materials is presented as the relation $\vec{B} = f(\vec{H})$ (known as Normal Curve) and $\vec{J} = f(\vec{H})$ (called Intrinsic Curve). The vector \vec{J} is the magnetic polarization, parameter that quantifies the Magnetization \vec{M} but scaled by the free-space permeability ($\vec{J} = \mu_0 \vec{M}$, in [T]). For hard magnetic materials, $\vec{B} = f(\vec{H})$ is significantly different than $\vec{J} = f(\vec{H})$, and this second one is often chosen as a more reliable description of

the magnetic behavior. This difference is not observed for low coercive force magnetic (LCF) materials, only for large values of \vec{H} [1]. An ideal and a typical hysteresis loop are illustrated in Figure 1.1

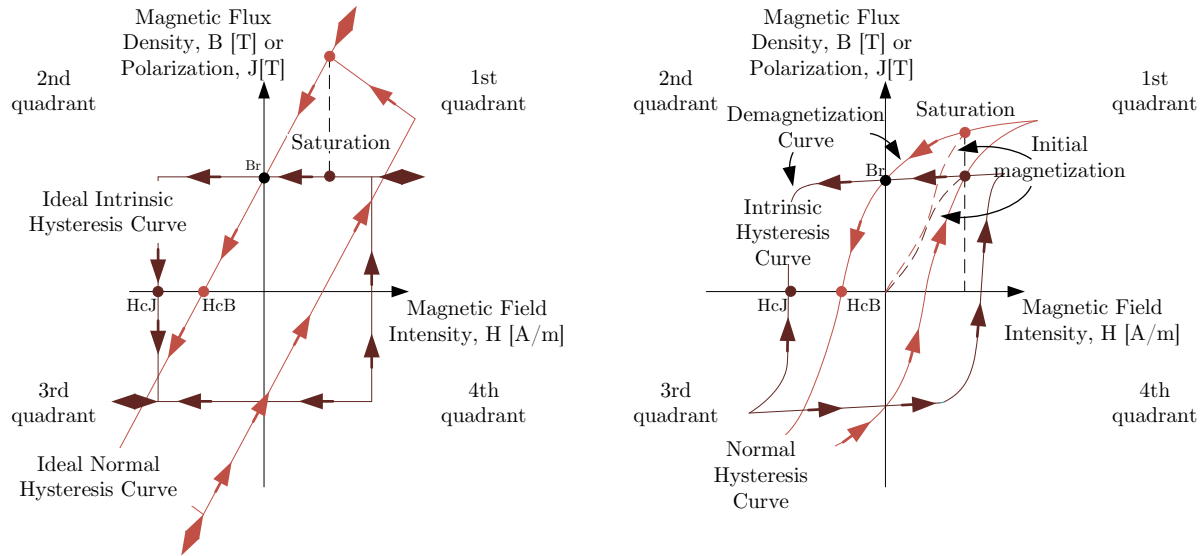


Figure 1.1: Illustration of the ideal $B=f(H)$ and $J=f(H)$ loops (left) and typical $B=f(H)$ and $J=f(H)$ loops (right) - Adapted from [1] and [2].

The main characteristics of a magnetic material identified in the hysteresis loop are [2, 51, 55, 60, 63]:

- Saturation: A saturation state is reached when the external field \vec{H} is sufficiently strong to ensure a uniform magnetization of the material. This point is identified in the first (fully positive magnetization) and in the third (fully negative magnetization) quadrants.
- Remanence or residual induction (B_r , in [T] or [gauss]): The presence of hysteresis in ferromagnetic materials implies a remanence, parameter that specifies the residual magnetization in the absence of an external field (or $\vec{H} = 0A/m$), by a material that was previously magnetized to saturation. This parameter is usually a reference to the magnetic strength of the material, as it is related to the amount of magnetic flux that can be generated by a magnet. In the hysteresis loop, it is placed at the intersection between the hysteresis loop and the \vec{B} - or \vec{J} -axis (the remanence is the same for the Normal and Intrinsic curves, as illustrated in the Figure 1.1).
- Coercivity (H_c , in [A/m] or [Oersteds]): Consists of the magnetic field required for reducing the magnet flux density of the material (or its magnetization) to saturation down to zero. This parameter indicates the inherent stability and the capability of a magnetic material to withstand demagnetization. It defines the width of the hysteresis cycle, being used to classify magnetic materials as soft, when the coercivity is low, or hard when it is high. In Appendix A.1, the difference between the hysteresis cycle obtained for these two types of magnetic materials is illustrated as an example. Two types of coercivity are identified in a hysteresis cycle, as Figure 1.1 demonstrates. The intrinsic coercivity (H_{cJ}), which

represents the field for which $\vec{J} = 0T$, is higher than the normal one (H_{cB}), which designate the field for $\vec{B} = 0T$.

- Maximum energy product ($(BH)_{max}$ or $(B_d H_d)_{max}$, in $[KJ/m^3]$ or $[MGOe]$): Determines the point on the Normal curve that presents a product between \vec{B} and \vec{H} maximized. In the hysteresis loop, this point of maximum energy is placed on the demagnetization curve (2nd quadrant). The performance of a magnet is usually qualified by this parameter, as it defines the minimal volume required by a magnet to produce the maximum product BH .

Figure 1.2 focuses on illustrating these characteristics in a typical normal hysteresis loop, characterizing a hypothetical ferromagnetic material. The most important parameters to be observed are highlighted by points (1)-(5), representing respectively: (1) the positive saturation, (2) the remanence, (3) the coercivity, (4) the $(BH)_{max}$ and (5) a minor hysteresis loop. The process of alignment of the magnetic domains (represented by the arrows) according to the level of the external field in which a material initially demagnetized is inserted is also illustrated by the three points in the initial magnetization curve. As can be seen, when the material reaches saturation, all the domains are expected to be aligned in the same direction as the external field.

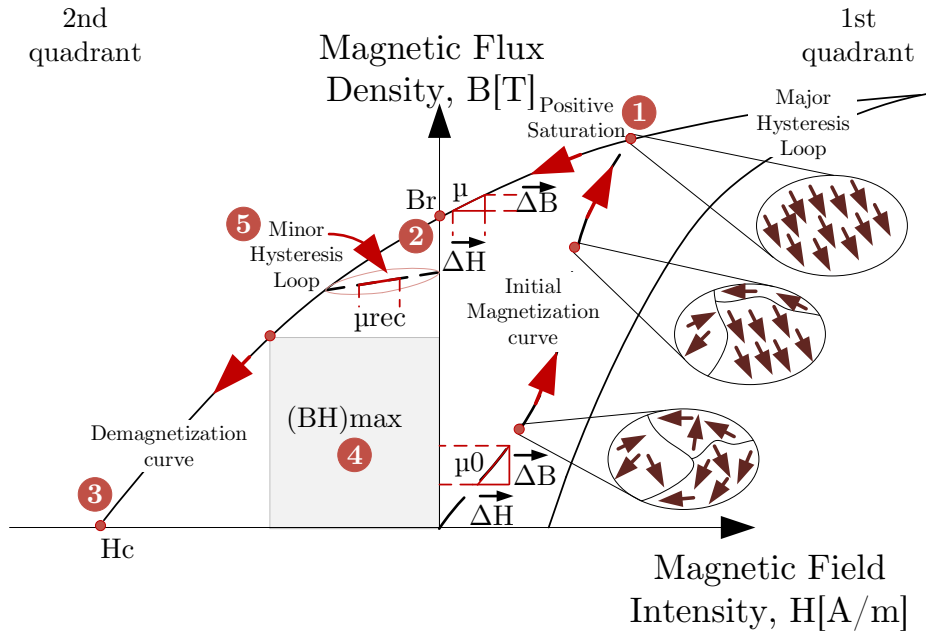


Figure 1.2: Illustration of the characteristics describing a typical hysteresis loop - Adapted from [2][1] - Point (1) defines the positive saturation, (2) the remanence, (3) the coercivity, (4) the $(BH)_{max}$ and (5) a minor hysteresis loop.

When the external field applied is insufficient to fully saturate the magnetic material and at some arbitrary point, this mentioned magnetizing field is reversed, minor hysteresis loops (or inner loops) are defined [55]. The slope of all internal hysteresis loops is similar and defined by the recoil permeability (μ_{rec} , unitless), measured on the Normal Curve. For the intrinsic curve ($\mu_{intrinsicrec}$, unitless), this parameter is equal to the one of the Normal curve minus one, or $\mu_{intrinsicrec} = \mu_{rec} - 1$ [2, 63]. Point 5 in Figure 1.2 illustrates an example of a minor hysteresis loop. The line whose slope is defined by μ_{rec} is called the recoil line, as represents the path taken in case of a remagnetization. When the curve generated by the function $\vec{B} = f(\vec{H})$ has a

linear behavior in the demagnetization region, such as is usually observed for HCF materials, the recoil lines traced from different conditions of magnetization will superpose it, and the magnet will not demagnetize in normal operating conditions [3, 12]. For a nonlinear demagnetization curve, as observed in magnets having low coercivities, each condition of magnetization will define a different recoil line, that will never superpose it [12, 3, 18]. This characteristic is particularly important for VFMMs, as going to be later explored.

The magnetic proprieties describing the hysteresis loop of typical magnets commercially available can be overviewed below:

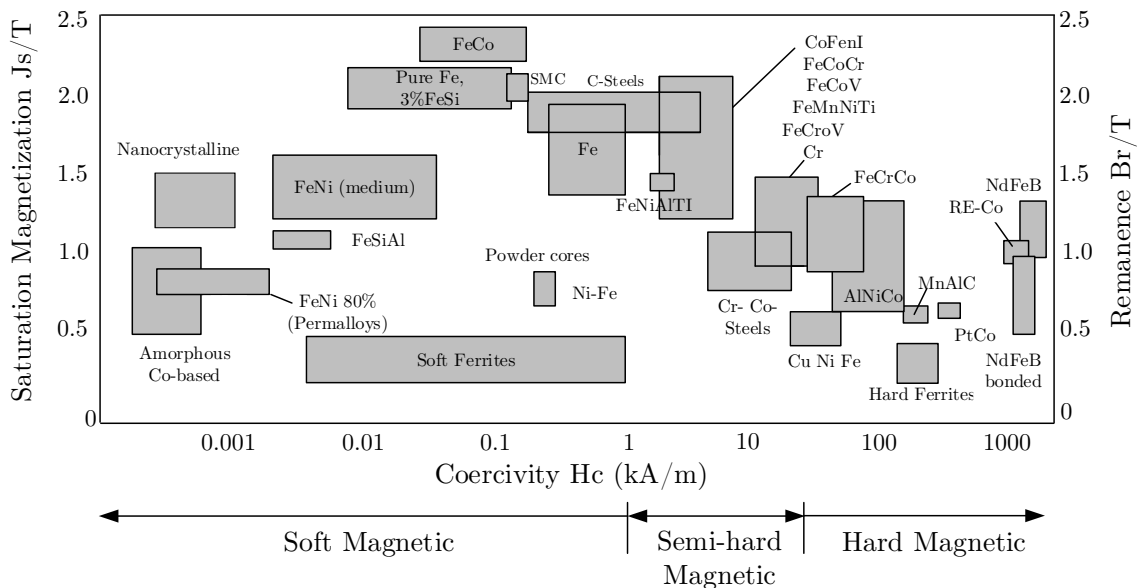


Figure 1.3: Magnetic proprieties of various magnetic materials[2].

1.1.4.2 The hysteresis loop modeling

Several methodologies have been proposed over the years for modeling the hysteresis loop of magnetic materials. Between them, the classical approaches such as Jiles-Atherton (J-A) model[64] and Preisach model[65] are the most known, being considered as the most robust and reliable models that can be applied on hard or soft magnets for identifying their parameters[66]. The focus of this research is not the development of methodologies for modeling mathematically the hysteresis loop. Nevertheless, an overview of these mentioned strategies is presented to support the definition in the next sections of a simplified model describing the magnetic behavior of low coercive force magnets used for generating the magnetic flux in VFMMs.

The first mentioned J-A approach is largely used due to low computational effort requirements as it uses differential equations and relatively small parameters for defining the hysteresis loop[67, 68]. The magnetic field strength \vec{H} and the \vec{M} are, respectively, the input and the output variables used by this method, both specified according to the current state of the material (local memory)[69, 68]. This methodology can be used for describing the major hysteresis loop characterizing a material, but also inner loops and other complex characteristics of the magnetization processes[69]. Nevertheless, this model may present a non-physical behavior in some magnetization levels which leads the algorithm to a convergence problem. This phenomenon

is particularly observed in the definition of inner BH loops, which can be inconvenient for their application in the characterization of VFMMs, as also it is the complexity of calculation.

Preisach model, published in 1935, describes the hysteresis of ferromagnetic materials as an infinite set of magnetic dipoles composed of rectangular hysteresis loops [70]. This method describes the macroscopic hysteresis phenomena by superposing a continuum of elementary asymmetric rectangular hysteresis loops, distributed in the plane classed Preisach triangle [1, 55]. Integrating the contribution of all these rectangular loops, the classical Preisach model provides the magnetic flux density [71]. As mentioned by [55], the Preisach model is criticized by some authors for generating unsatisfactory physical interpretations. This limitation motivated the use of a mathematical model proposed by Krasnosel'sii and Pokrovskii in 1983, which connects better the physical definitions of the hysteresis phenomena and the model proposed. Many other authors had also proposed contributions to the Preisach model, such as Everett and Whitton (1952), Everett and Smith (1954), Woodward and Della Torre (1960) and Del Vecchio (1980) [1].

The use of both classical Preisach and J-A models for analyzing the variation of the magnetization level observed in VFMMs can be challenging according to some authors. The main reason is exposed as the software used for analyzing the magnetic behavior of machines is based on the time-stepping finite element method (TS-FEM), which was developed for conventional PM machines, with therefore a constant level of magnetization. The association of the TS-FEM with Preisach was discussed in [70] [3] and with J-A models in [67] and [72], but exceeds the main objectives of this research.

For simplifying the model of the hysteresis loops, a normal practice in the literature studying VFMMs is to consider linear the behavior of the external demagnetization curve, and the internal recoil lines as being also linear and parallel to this external one, as illustrated in Figure 1.4. Other examples of the linear model can be observed in [12], [73], [33] and [74].

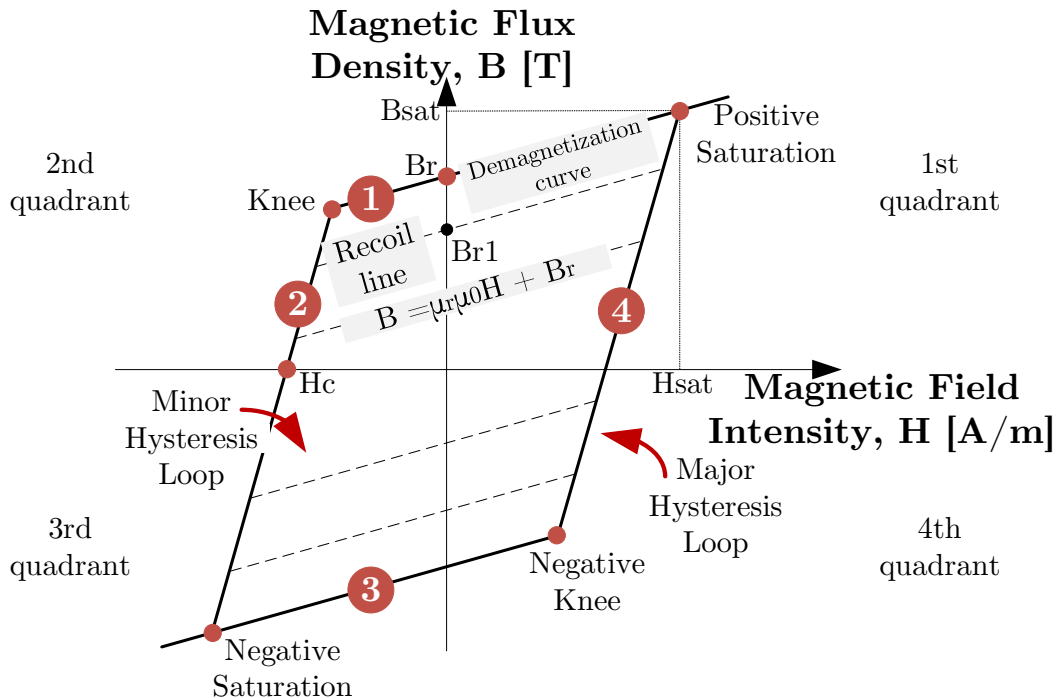


Figure 1.4: Linear model of the hysteresis loop - Adapted from [1] [3] [4].

By this linear representation, the description of $\vec{B} = f(\vec{H})$ considers the major external loop defined by four linear segments: the 1st connecting the positive saturation (in the 1st quadrant)

and the knee (in the 2nd quadrant), the 2nd connecting the knee and the negative saturation (in the 3rd quadrant), the 3rd connecting the negative saturation and the negative knee (in the 4th quadrant) and the 4th, connecting the negative knee and the positive saturation. All the recoil lines are linear and parallel to the demagnetization curve (1) [12, 27]. This parallelism indicates that the recoil permeability is equal to the relative permeability of the major demagnetization curve. A simple mathematical description of the magnetic behavior is the most important advantage of using the linear method [1] and is going to be largely explored for studying VFMMs. By this model, the equation characterizing the recoil lines can be defined by:

$$\vec{B} = \mu_0 \mu_r \vec{H} + B_r \quad (1.10)$$

where B_r represents the remanence characterizing each possible recoil line.

1.2 The characterization of the magnets used for generating the magnetic flux in electrical machines

This section aims to discuss the use of rare-earth magnets in electrical machines and also present the major concerns regarding these materials. Alternatives for substituting the permanent magnets in transportation electrification applications are discussed. Additionally, the first insights regarding the magnetic selection for Variable Flux Memory Machines are introduced.

1.2.1 Rare-earth magnets

Chemical elements with similar properties, the rare-earth elements (REEs) are called "rare" because of the difficulty of finding them in concentrations high enough for reasonably affordable extraction [75], as shown in Figure 1.5.

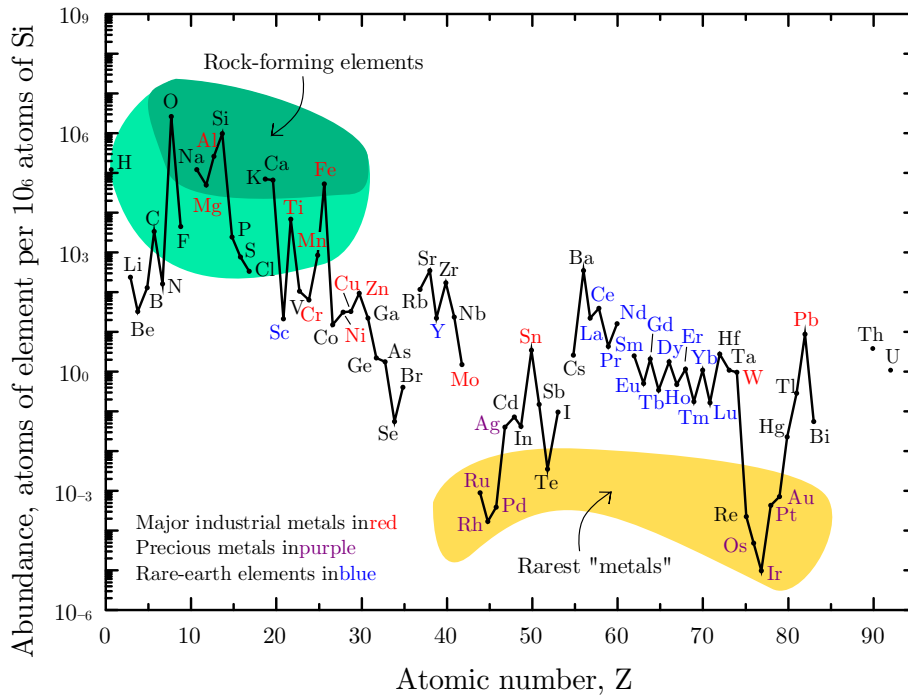


Figure 1.5: The relative abundance in earth's crust of some chemical elements [5].

Magnets composed of these rare elements were first discovered in the 1960s by Karl Strnat by the development of Samarium-Cobalt (Sm-Co) alloys. These magnets predominantly exist in two grades, SmCo5 and SmCo17 and are characterized by a high flux density magnet, a high coercive force (H_c), and a BH_{max} up to 30MGOe. Additionally, they present also good thermal stability and a small sensibility to the temperature, besides their high operating temperature (200°C - 550°C) [76, 77]. As exposed by [8], the interest in the Sm-Co magnets started to reduce in mid-1979, when a civil war in Zaire (Democratic Republic of Congo), which was responsible for about 90% of the world's cobalt supply in the world. This scenario led to an abrupt increase in the price of this material (by a factor of six), motivating researchers to develop new alloys with a reduced content of Cobalt. In this context, Masato Sagawa and John Croat discovered, in 1982, the neodymium-iron-boron (Nd-Fe-B). Because of their superior magnetic characteristics, such as the high flux density and high coercivity, this metal has been considered highly interesting for small and high electrical machines and their use has been largely disseminated.

The most used REM magnets, also known as high coercive force (or HCF magnets), contain normally four different rare-earth elements [6]: Neodymium(Nd), Praseodymium(Pr), Terbium(Tb), and Dysprosium(Dy). Neodymium and Praseodymium have as objective increasing the magnetic strength, while Dysprosium and Terbium are used to enhance the resistance to demagnetization. Thermal stabilization is achieved by using Dysprosium and Praseodymium [6]. Specially for permanent magnet synchronous machines (PMSMs), the most commonly used electrical machine for traction field as going to be later discussed, Neodymium-Iron-Boron (Nd-Fe-B) alloys are often considered. These magnets are known to be energetically strong (high BH_{max} and high B_r), with a large coercivity that avoids unintentional demagnetization under normal operating conditions. The intrinsic magnetization is therefore retained, allowing the machine to provide a high air gap flux density and, consequently, a high torque density. The thermal proprieties of the Nd-Fe-B magnets represent a limitation of their use. Figure 1.6 exhibits the dependence of the most commercial permanent magnets (PMs) to the temperature. It can be observed that the magnetic proprieties of the Nd-Fe-B are highly degraded with the increasing of the temperature. Also, it can be confirmed that the use of portions of Dy in the Nd-Fe-B alloy can stabilize the magnet behavior when the temperature varies.

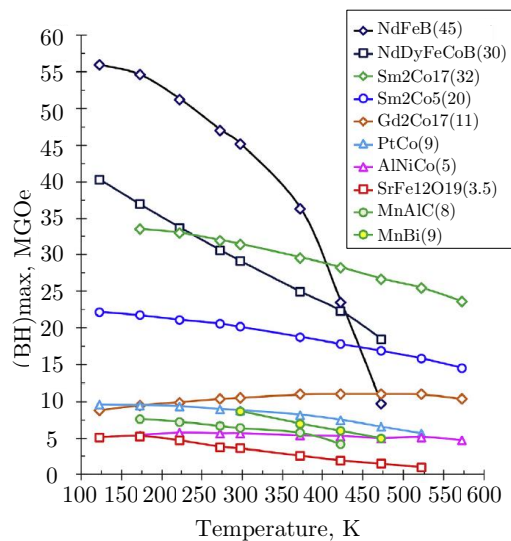


Figure 1.6: Temperature dependency of the most commercial magnets [6].

The magnetic proprieties of some grades of Nd-Fe-B can be analyzed below, in Table [1.2](#). The demagnetization characteristic of grades N40 and N30H can be analyzed in the Appendix [A.4](#).

Table 1.2: Magnetic Proprieties of Neodymium-Iron-Boron magnets [\[78\]](#).

Nd-Fe-B magnets									
Grade	Remanence		Coercivity		Intrinsic		Max. Energy		Temperature Coefficient of induction/coercivity
	(B_r)		(H_{cB})		Coercivity (H_{cJ})		Product (BH)max		
	[mT]	[G]	[kA/m]	[Oe]	[kA/m]	[Oe]	[kJ/m ³]	[MGOe]	[°C]
N40	1270	12700	923	11600	955	12000	318	40	-0.12/-0.618
N30H	1105	11050	796	10000	1353	17000	235	30	-0.12/-0.572
N42SH	1310	13100	955	12000	1592	20000	330	41	-0.12-0.549
N35UH	1210	12100	860	10800	1990	25000	283	35	-0.12/-0.510

Two major challenges are related to the constant use of rare-earth magnets: from an economic perspective, the risks of supply and the consequent price variability derived from the geopolitical scenario imposed by producer countries (especially China) [\[10\]](#); from an environmental point of view, the damages caused by the extraction, refinement, and recycling of these materials [\[12\]](#).

This geopolitical context is the most commonly presented by authors for justifying the interest in Variable Flux Memory Machines (VFMMs), as exposed by authors as [\[12\]](#), [\[73\]](#) and [\[74\]](#). Figure [1.7](#) shows the production share of rare-earth magnets by country, using data from the United States Geological Survey (USGC). According to them, more than 40% of the resources for producing REMs are located in China, which owns therefore the largest market share and consequently, controls the price of these materials.

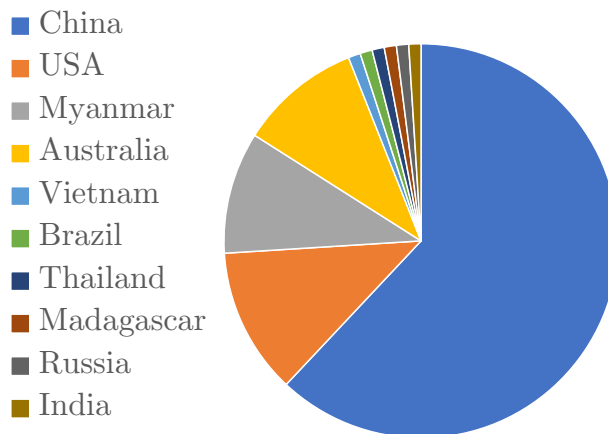


Figure 1.7: Production of rare-earths by country - 2020 [\[7\]](#).

The problem around this dependency was observed in 2010 when export quotas imposed by China exposed the world to a sharp increase in rare-earth element prices [\[7, 8\]](#). Figure [1.8](#) presents

the peak in prices of neodymium and dysprosium from 2010 to 2013. This crisis, besides exposing this mentioned market control established by China, compromised the credibility of the future supply of these metals. Even when prices fell in mid-2014, China kept control of the production and export of rare-earth materials [7].

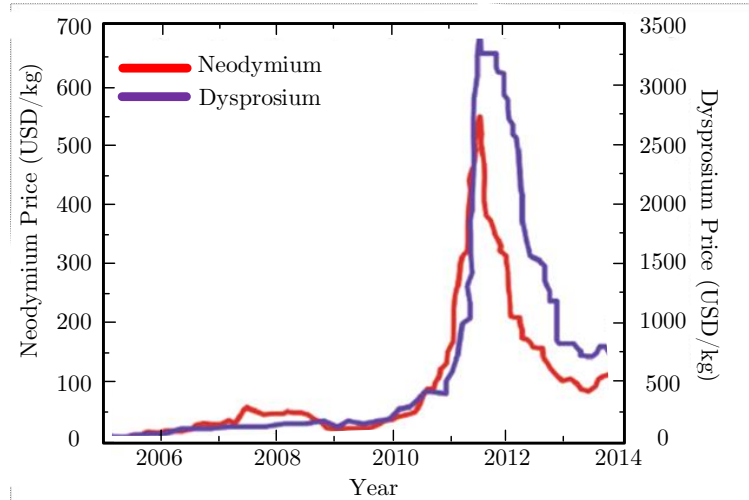


Figure 1.8: Price of Neodymium and Dysprosium from 2005 to 2014 [8].

These mentioned risks of supply have been also aggravated by the increasing demand for rare-earth magnets in multiple sectors of the economy. As discussed in [7], the use of Neodymium, Praseodymium, Terbium, and Dysprosium is expected to increase, especially in sectors such as wind turbines and e-mobility. Table 1.3 presents an estimation of the rare-earth magnets used in some common applications. Figure 1.9 exhibits the low- and high-demand scenario for the ratio demand/supply for these mentioned metals.

The current strategies proposed to face this scenario include a reduction of the demand by developing new rare-earth free technologies for the most different economic sectors and also the diversification of supply, reducing the dependency on China. The potential of other producer countries such as Canada and Australia have been discussed in [6] and [7]. Concerning the

Table 1.3: Estimated rare-earth use application (%) [79].

Application	La	Ce	Pr	Nd	Sm	Eu	Gd	Tb	Dy	Y	Other
Magnet			23.4	69.4			2	0.2	5		
Battery alloys	50	33.4	3.3	10	3.3						
Metallurgy	26	52	5.5	16.5							
Auto Catalysis	5	90	2	3							
Glass additives	24	66	1	3						2	4
Phosphors	8.5	11				4.9	1.8	4.6		69.2	
Ceramics	17	12	6	12						53	
Others	19	39	4	15	2		1			19	

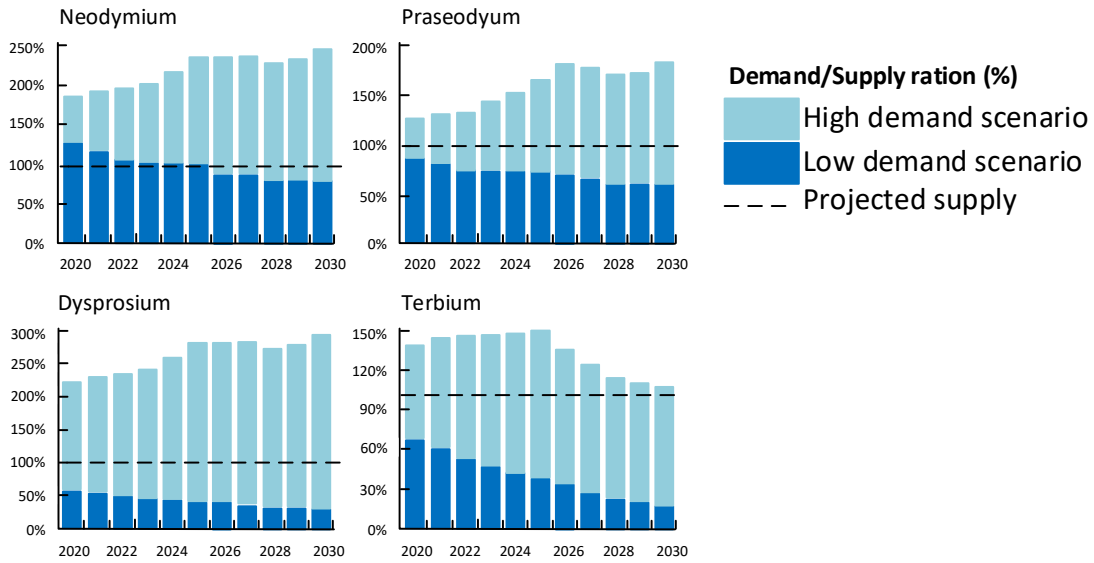


Figure 1.9: Demand/supply ratio for Neodymium, Praseodymium, Dysprosium, and Terbium (all sectors) - Adapted from [7].

demand for rare-earth magnets in Europe, further geological exploration is necessary to ensure internal market attendance. In addition, even if the potential of new mining activities exists, the most desired rare-earth elements as Dysprosium are still low in supply [6], which reinforces the necessity of reducing demand.

From an environmental perspective, the use of rare-earth magnets has also been exposed as a challenge in terms of extraction, refinement, and recycling [12]. A high level of CO_2 emissions, the permanent loss of ecosystems, soil erosion, and air pollution are some of the environmental effects related to the production of REMs [9]. Figure 1.10 exhibits as an example a future projection of the energy and water requirements related to a high-demand scenario of Dysprosium. Additionally, the authors mention the radioactivity of some ores and management strategies for dealing with radioactive waste materials as important supplementary effects of REMs production.

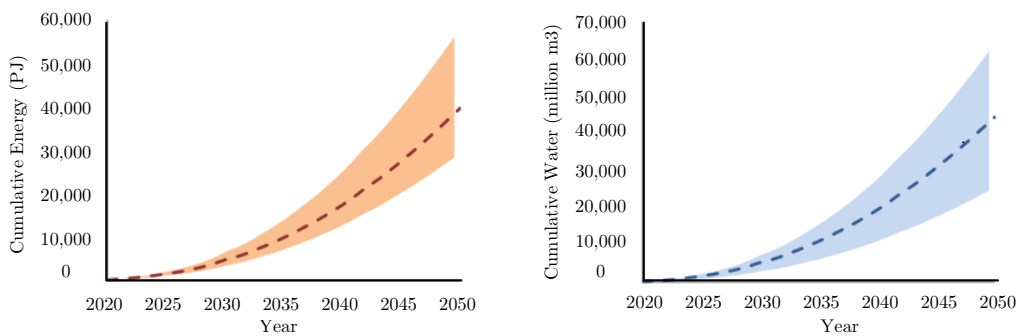


Figure 1.10: Energy and water associated with oversupplied rare-earth elements until 2050 [9].

A complementary study is presented in [10]. In this research, the author suggests that the life cycle of PMs as Nd-Fe-B is more harmful to the environment than other materials commonly used in electrical machines, such as copper and aluminum used in the windings. The "global warming potential" and "photo-chemical ozone creation potential" are shown in Figure 1.11 as some of the critical environmental effects related to the production of REMs. Authors in [7] and [29] expose that the potential of recycling PMs exists and is increasing, but is still insufficient to respond the consumer needs. The major reason is the small amount of these materials used in each final product (for example, in a smartphone) and the complexity involved in associating the collection, extraction, and recovery of these materials.

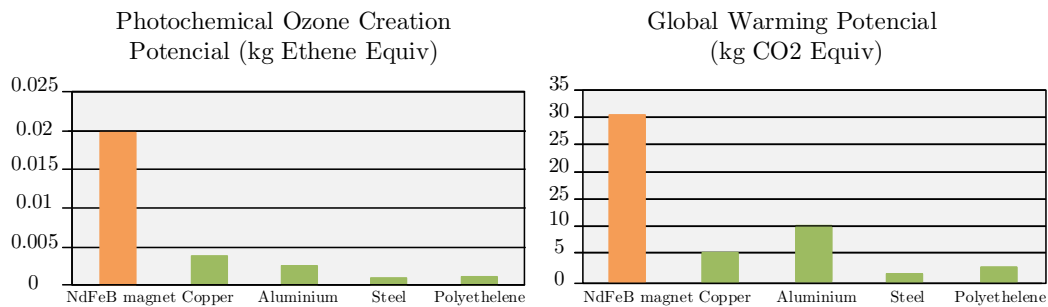


Figure 1.11: Effect environmental of the life cycle of materials commonly used in electrical machines- Adapted from [10] - Analysis per unit mass.

A simplified overview of the approaches used in the recycling of rare-earth elements is presented in Figure 1.12.

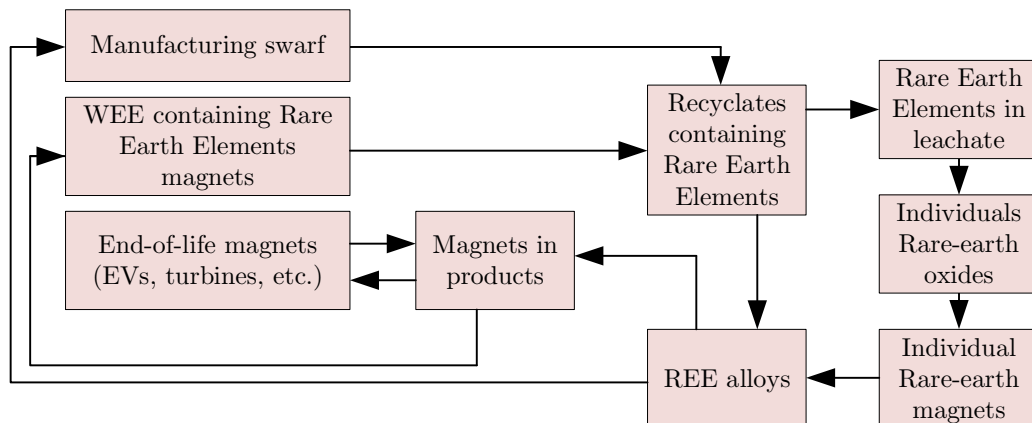


Figure 1.12: Flowchart of rare-earth magnets recycling [11], where WEEEs - waste electrical and electronic equipment.

Three possible flows are presented: the first one considers swarf originating from magnet manufacturing, the second one, corresponds to small magnets in consumer products (called WEEE or Waste Electrical and Electrical Equipment), and the last one, the large magnets in hybrid/electric vehicles and wind turbines. Due to the trade-off between costs and complexity and the amount of magnet recovered, direct reuse and recycling are only interesting for the large

magnets. Also, products containing REEs take 5-20 years until their end-of-life, the disponibility of these products for recycling/reuse is not proportional to the increase in the demand for these materials. Studies as [80] present the direct reuse of these magnets (Nd-Fe-B) from electrical vehicles, in which Surface Mounted Permanent Magnet Synchronous Machine (SPMSM) and Interior Permanent Magnet Synchronous Machine (IPMSM) are used. More insights about the reusing methods for these machines are discussed in the Appendix A.3. Some challenges involved in these processes are highlighted by the authors:

1. Difficulties of changing the shape of a magnet reused to fit in a new rotor design, especially for sintered Nd-Fe-B, because they are commonly coated.
2. Difficulties to protect Nd-Fe-B from damages during its removal from the rotor, because this magnet is brittle, requiring control of the pull-out forces, due to the thermal process required to remove the glue used to fix the magnet in some rotor designs and also and also because of risks of permanent demagnetization.
3. The reuse of the magnet can be problematic due to aide materials such as the glue mentioned above and plastic, as contamination or leaching from these aide materials can be harmful to health.

The description of some methods for recycling REMs for the extraction of REEs can be in [81], [82], and [83]. In [9], authors mention some initiatives of automotive companies such as Toyota, Honda, and Mitsubishi for recycling these materials.

Within this context, due to the challenges involved in the reuse of REMs, their substitution for electrical machines is justified. One of the available options is the Variable Flux Memory Machine, which emerged as reduced (or free) rare-earth technology as going to be explored in the next chapters.

1.2.2 Substitution of rare-earth magnets in transportation electrification applications

It is well-known that the combination of high torque per volume ratio, high efficiency, and low heat production in the rotor made the conventional PMSMs very attractive for traction drives used in electrical vehicles (EVs) [12, 27, 74, 28]. As already exposed, these machines are designed for conserving a constant and high air gap flux density under normal operating conditions thanks to the REMs used as a source of magnetic field. The section 1.2.1 related environmental and economic challenges involving the perpetuity of using the currently required amounts of rare-earth magnets in electrification transportation systems. Some machines have been proposed in the last years by big companies in the automotive sector for replacing REM-based machines in traction applications. As exposed by [10], Tesla Motor Corporation has opted for using induction machines in place of PMSMs in their electrical vehicles. The company reported the use of copper rotor cage induction machines as well as Toyota. Very recently, Renault Group, Valeo, and Valeo Siemens eAutomotive have announced a partnership for the design, co-develop, and mass manufacture of a 200kW new-generation automotive electric motor, without using rare-earths [84]. Also in 2022, BWM announced similar efforts for reducing the use of these magnets at CES (Consumer Technology Association 2022). The company proposed the use of a three-phase AC synchronous motor using brushes and a commutator for the BMW iX M60, as can be seen in [85] and [86]. In Europe, projects have been also developed in the last few years to support the reduction of the REMs amount content in electrical machines. These efforts culminate in projects as the "ReFreeDrive" one, presented in [87] in which IFP Énergie nouvelles is one of the 13 partners. These studies, focused on the development of industrially feasible power

traction systems for electrical vehicles with reduced content of rare-earth magnets, proposed an investigation about the use of two induction machines (IM), one with fabricated and the other with a die-cast rotor, and two synchronous reluctance (SynRel) machine as options for replacing PMSMs. The final results of these studies can be analyzed in [13].

Besides the mentioned reduction of REMs content, an additional improvement opportunity for PMSMs in the transportation electrification field is centered on the minimization of losses generated during high-speed operations. For regimes below the base speed, in the constant torque region presented in Figure 1.13, the internal counter electromotive force (back-EMF) increases proportionally to the motor speed. This represents a desirable behavior for the volts-per-hertz control usually applied in this mode of operation [88]. The output voltage of the inverter defines the limit of speed achievable with a constant torque. Beyond this regime, flux-weakening (FW) strategies are often used to counter the increasing back-EMF. For achieving this, the most commonly used method is based on a current vector control for continuously injecting a negative magnetization current (or direct axis current component) in the armature windings of the machine [12, 27, 30]. Nevertheless, additional copper losses are related to the use of this FW strategy in non-salient pole machines [28, 33, 89] as also risks of a permanent demagnetization of the rare-earth magnet used for the flux generation [12, 31]. Additionally, the use of FW represents an inconvenience from the torque production point of view, as part of the stator currents capacity is compromised [33, 74]. In addition, reference [12] exposes the potential divergence between the high-efficiency region of PMSMs and the highest operation duty region of EVs as the major challenge of using these machines for traction drives.

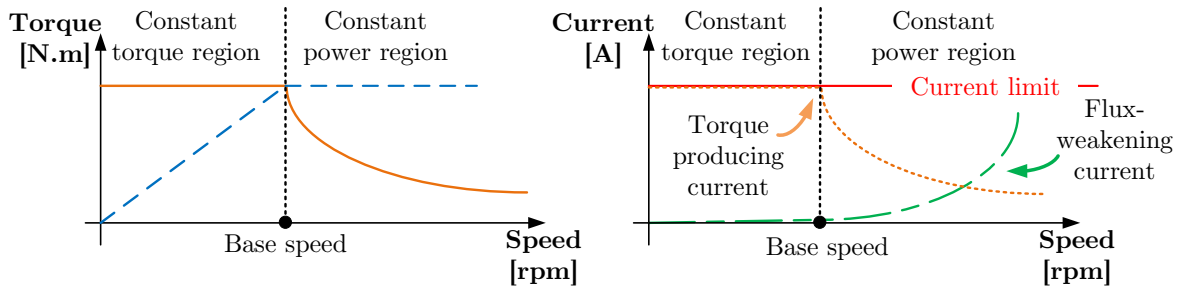


Figure 1.13: Illustration of the theoretical behavior of (a) the torque-speed envelope and (b) the currents operating in a large speed range - Adapted from [12] [13].

Variable Flux Memory Machines (VFMMs) represent in this context an option for replacing the PMSMs that responds to the two major concerns already presented in this section:

1. The reduction of the REMs content in machines providing a high torque;
2. The extension of the torque-speed envelope with reduced losses.

1.2.2.1 The magnet selection for Variable Flux Memory Machines: first insights

For reducing the REMs content in electrical machines used in traction applications, the VFMMs are proposed in designs where these materials are totally or partially replaced by magnets characterized by a lower coercive force. This section gives an overview of the magnetic materials used in VFMMs. In the next sections, the geometries and magnetic behavior of these machines are going to be further explored.

1.2.2.2 Aluminum-Nickel-Cobalt magnets

Aluminum-nickel-cobalt (Al-Ni-Co) magnets alloys were developed in the early 1930s for military electronic applications during the Second World War [90] and continuously improved since then. These alloys can be divided into two subgroups [91]: isotropic magnets, which have similar magnetic proprieties in all directions, containing 0–20 wt% (wt% is percentage by weight, in chemistry) of Cobalt (Al-Ni-Co of grades 1–4) and anisotropic alloys, which have magnetic proprieties that are dependent of the magnetization direction, with 22–24 wt% of Cobalt and a Titanium content of 5–8 wt% (Al-Ni-Co of grades 5–9). Attention is required for manufacturing anisotropic magnets because their easy and hard magnetization directions are well distinct. The magnetic proprieties of some Al-Ni-Co alloys can be summarized below in Table 1.4.

The composition of different grades of Al-Ni-Co can be observed below as also their demagnetization curves are presented in the Appendix A.4.

Table 1.4: Magnetic Proprieties of Aluminum-Nickel-Cobalt magnets [92].

Al-Ni-Co magnets								
Grade	Max. Energy		Remanence		Coercivity		Recoil	
	Product (BH) _{max}		(B_r)		(H_c)		Permeability (μ_r)	
	[MGOe]	[KJ/m^3]	[G]	[mT]	[Oe]	[KA/m]	[G/Oe]	[$10^{-3}Tm/K$]
AlNiCo2	1.60	12.7	7200	720	560	45	6.2	7.8
AlNiCo4	1.35	10.7	5500	550	720	57	4.1	5.2
AlNiCo5	5.50	43.8	12500	1250	640	51	3.7	4.6
AlNiCo9	10.50	83.6	11200	1120	1375	109	1.3	1.6

Several researches explore the use of Al-Ni-Co (especially in grades 5 and 9) for generating the magnetic flux in VFMMs [12, 23, 27, 31]. Their use is advantageous for these applications because of their high magnet flux density, equivalent to one of Nd-Fe-B alloys used in PMSMs, and their low coercive force, which is the most important characteristic explored in this machine technology [12, 23]. An additional advantage is the good thermal stability [3], with a temperature coefficient for the remanence of -0.02% [23] and a Curie and working temperatures of respectively 800°C and 500°C [90, 91]. As inconvenient, Al-Ni-Co magnets are brittleness and high hardness, requiring machining after casting [36]. Another limiting factor for extending the use of these low coercive force magnets is their price, majorly influenced by the price of Cobalt. The studies realized in [6] provide the table 1.5, which exposes the comparison of multiple magnet prices in 2016 and 2022 (projected values). The values are presented in \$/kg/kG/kOe, representing the cost proprieties ratio (magnet cost (\$/kg) divided by remanent magnetization (kG) and by coercivity (kOe)). As can be observed, the price of Nd-Fe-B had been expected to double in the mentioned period of time considered, but it would continue to be one of the less expensive magnetic materials, being in 2022 only expected to be more expensive than Ferrite. In which concerns the price of the Al-Ni-Co magnets, it is noticed that they had been expected to decrease, but not sufficiently to become this alloy competitive in the market. Reduce the Cobalt content in the Al-Ni-Co alloys could be an option for achieving these lower prices, as Cobalt has been considered a critical raw material for US [93] and for European Union [94] since 2017. Appendix A.5 summarizes both lists presenting these critical raw materials. However, the impacts of changing this Cobalt content in Al-Ni-Co would require optimizations on the fabrication process and compositions are required [6]. This represents an inconvenience for large-scale use of these magnets, and consequently, a limitation for expanding the use of the most of Variable Flux Memory Machines technologies presented nowadays in the literature.

Table 1.5: Motor magnet prices and proprieties[6].

Material	$(BH)_{max}$ [MGOe]		H_{ci} [kOe]		B_r [kG]		Price [\$/kg]		[\$/kg/kG/kOe]	
	2016	2022	2016	2022	2016	2022	2016	2022	2016	2022
NdFeBDy (NH42SH)	41	42	20	20	12.7	13	\$60	\$120	\$0.23	\$0.46
SmCo (SC-3215)	31	34	15	15	11.6	12	\$128	\$210	\$0.78	\$1.42
AlNiCo9	9	11	1.4	2	10.5	10.5	\$71	\$80	\$4.83	\$3.81
Ferrite	3.8	3.8	3	3	4	4	\$4	\$4	\$0.33	\$0.33

1.2.2.3 Iron-Chrome-Cobalt magnets

Iron-chrome-cobalt (Fe-Cr-Co) has been known since Kaneko, Homma, and Nakamura announced the production of a Fe-Cr-Co grade equivalent to the AlNiCo5 in mid-1970. The interest in using Fe-Cr-Co alloys in electrical machines was reported years later in [95], in which authors present the improvements achieved using Fe-Cr-Co alloys instead of Al-Ni-Co ones in a hysteresis motor. Their use in VFMMs is, however, still little explored. When compared to Al-Ni-Co, Fe-Cr-Co can be advantageous, as discussed in [35, 36, 96, 97, 98, 99]. This magnetic material presents better mechanical/corrosion resistance, being ductile and presetting low-cost shaping possibilities. Additionally, a lower content of Cobalt in these low coercive force magnets has a positive impact on their price, because of the supply challenges formerly described about the use of this component. Authors in [100] and producers in [101] mention a Cobalt content around 50% lower in Fe-Cr-Co in comparison with Al-Ni-Co alloy of same remanence (e.g. about 10% in Fe-Cr-Co against 22% in similar Al-Ni-Co for a $B_r \approx 1.3T$). Another important advantage can be concluded by the analysis of the resistivity of these two mentioned LCF magnets. Data obtained from [102] demonstrate that the resistivity of Al-Ni-Co magnets is around $50 \times 10^{-6}\Omega \cdot \text{cm}$ whereas for Fe-Cr-Co $70 \times 10^{-6}\Omega \cdot \text{cm}$ at a similar temperature. As regards the thermal proprieties, the Fe-Cr-Co presents a Curie and working temperature respectively of 680°C and 400°C , with a temperature coefficient for the remanence of -0.0128% [103], which indicate a good thermal stability. The presented characteristics indicate that Fe-Cr-Co magnets can be a cheaper option with equivalent magnetic proprieties to the Al-Ni-Co. These advantages for their use in VFMMs justify the interest of this present research in the study of a VFMM composed of a solid cylindrical Fe-Cr-Co-based rotor. What was, however, observed, is a lack of information in the literature about these alloys and also some difficulties regarding their commercial availability, which can represent a limiting factor for their large-scale use.

Some magnetic proprieties of Fe-Cr-Co are summarized in the Table 1.6. In the Appendix A.4, the hysteresis loop characterizing the magnet FeCrCo36/5 is exhibited.

Table 1.6: Magnetic Proprieties of Iron-Chrome-Cobalt magnets[104].

Grade	Fe-Cr-Co magnets								
	Remanence		Coercivity		Intrinsic		Max. Energy		Temperature Coefficient
	(B_r)		(H_{cB})		Coercivity (H_{cJ})		Product (BH)max		of induction/coercivity
	[T]	[KGs]	[kA/m]	[kOe]	[kA/m]	[kOe]	[KJ/m ³]	[MGOe]	[°C]
FeCrCo12/4	0.80	8.0	40	0.50	42	0.530	12	-0.05	-0.03/-0.04
FeCrCo28/5	1.00	10.0	45	0.57	46	0.580	28	3.50	-0.03/-0.04
FeCrCo36/5	1.20	12.0	52	0.66	54	0.680	36	4.50	-0.03/-0.04
FeCrCo52/5	1.35	13.5	48	0.60	49	0.620	52	6.50	-0.03/-0.04

1.2.2.4 Ferrite magnets

Another option of magnet that is considered for VFMMs is Ferrites, one of the most used magnetic materials in the world [105]. These ceramic materials were first presented in 1952 by Van Oosterhout and co-workers at the Philips Research Laboratories [106]. Ferrites are mostly used because of their magnetic proprieties, exhibited in Table 1.7. These magnets are characterized as being robust against demagnetization due to their large hysteresis loop, which makes them interesting for PMSM applications [14, 107]. The coercivity of these magnets is, however, about one-fifth to one-third of the one of Nd-Fe-B magnets [10], although still high when compared to LCF magnets as the Al-Ni-Co and Fe-Cr-Co ones. In which concerns the mechanical characteristics, Ferrite magnets require a careful design because of their low tensile and flexural strength [102]. Additionally, Ferrites are advantageous because of their easy recycling [106] and present generally lower prices than other magnets used in electrical machines, as previously shown by Table 1.5. As can be seen, the price of Ferrite in 2022 had been expected to be 40% lower than the one of Nd-Fe-B and more than 300% lower than the one of Al-Ni-Co magnets. According to producer Eclipse Magnets [105], there are 27 grades of Ferrite magnets commercially available for being produced in many shapes and sizes. The proprieties of some of them are presented below in Table 1.7. Grades C5 (also known as Feroba2, Fer2, Y30 and HF26/18) and C8 (also known as Feroba3, Fer3 and Y30H-1) are the mostly used. The temperature coefficient for the remanence of these magnetic materials is -0.2% and the Curie and working temperatures of respectively 450°C and 300°C. This low thermal performance and the low remanence are the major disadvantages of using Ferrite magnets [12]. In the Appendix A.4, the demagnetization curves of some Ferrite grades are exhibited.

Table 1.7: Magnetic Proprieties of Ferrite magnets [105].

Grade	Ferrite magnets							
	Remanence		Coercivity		Intrinsic Coercivity		Max. Energy	
	(B_r)		(H_{cB})		(H_{cJ})		Product (BH) _{max}	
	[mT]	[KG]	[kA/m]	[KOe]	[kA/m]	[KOe]	[KJ/m ³]	[MGOe]
FerriteY20	320-380	3.2-3.8	135-190	1.70-2.39	140-195	1.76-2.45	18.0-22.0	2.3-2.8
FerriteY30	370-400	3.7-4.0	175-210	2.20-2.64	180-220	2.26-2.76	26.0-30.0	3.3-3.8
FerriteY30H-1	380-400	3.8-4.0	230-275	2.89-3.46	235-290	2.95-3.64	27.0-32.0	3.4-4.0
FerriteY40	440-460	4.4-4.6	330-354	4.15-4.45	340-360	4.27-4.52	37.5-41.8	4.7-5.3

The use of Ferrite for generating the magnetic flux in VFMMs is possible but, such as in the case of Fe-Cr-Co magnets, this application is little explored when compared to Al-Ni-Co-based machines, although the very first prototype of VFMM proposed in the literature [23] was a Ferrite-based machine. As will be later exhibited in Figure 1.15, Ferrite has a larger hysteresis loop than Al-Ni-Co magnets and a wider work region (a linear region on the BH loop presented). As a consequence, more ampere-turns are required for the demagnetization of these magnets. Furthermore, as a result of the proximity of the knee observed in the hysteresis loop and the H-axis, the regulation of the magnetization state of Ferrite magnets can be challenging. This characteristic represents an important drawback for using these magnets in VFMMs, as the range of flux variability in the machine is reduced. Additionally, the considerably lower level of remanence of these materials with respect to the one of Nd-Fe-B or Al-Ni-Co magnets can be also considered a disadvantage.

Studies in [14] propose a comparison between using Al-Ni-Co, Sm-Co, and Ferrite in VFMMs for traction applications. For this, three VFMMs are evaluated. Each one is designed from

the series combination of a Nd-Fe-B-based magnet and one of the magnets mentioned (Al-Ni-Co, Sm-Co, or Ferrite) in a V-type arrangement in each rotor pole. A fourth machine is also presented, considering magnets composed of Nd-Fe-B. It is observed by the research mentioned, that air gap flux density is around 0.7T for Al-Ni-Co- and Sm-Co-based machines, while the Ferrite-based one only reaches 0.37T. The average torque produced considering the rated load current is, consequently, almost the same for Al-Ni-Co- and Sm-Co-based machines. Pure Nd-Fe-B machine exhibits in both conditions the highest peak torque, as the machine composed of Ferrite presents the lowest. An analysis of the demagnetization characteristics exhibits the possibility of gradually reducing the air gap flux density in Al-Ni-Co-based machines, meanwhile, the same current levels (2 p.u. and 4 p.u.) sharply demagnetize Ferrite-based machines. For Sm-Co-based ones, almost no demagnetization is observed. Figure 1.14 shows these results, which confirms the better controllability of the magnetization state regulation process obtained in Al-Ni-Co-based machines. Also, the study observed that the power produced for Al-Ni-Co-based and the Sm-Co-based machines are similar when both are supplied with 1 p.u. load current, and lower to the one obtained by the Nd-Fe-B-based machine, as expected, due to the higher remanence of this last-mentioned magnet. When the load currents are increased, the torque production is considerably reduced in the machine composed of Al-Ni-Co, because of involuntary demagnetization effects affecting the working point of this low coercive force magnet. The same behavior is not observed in both high coercive force magnets used in the two other machines.

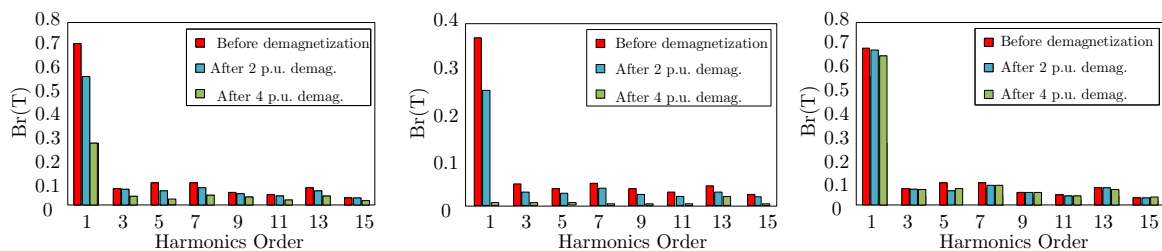


Figure 1.14: Harmonic components of the air gap flux densities obtained by simulation before and after demagnetization, considering the (a) Al-Ni-Co-based, (b) Ferrite-based and (c) SmCo-based series variable flux memory machine [14].

Finally, Figure 1.15 proposes a comparison between the demagnetization curves (2nd quadrant of the hysteresis loop) of the low and high coercive force magnets formerly introduced. The results presented by this mentioned Figure 1.15 as also by the magnetic properties of various magnetic materials exhibited in the Figure 1.3 demonstrate that, indeed, Al-Ni-Co and Fe-Cr-Co magnets present a narrow hysteresis loop when compared to the one of Nd-Fe-B and Ferrites, characterized by high coercivities. The remanence levels are observed to be equivalent for the FeCrCo36/5, AlNiCo5, and NdFeB/N45. This high remanence associated with the high coercivity is historically the major reason for using the Nd-Fe-B in PMSMs since these rare-earth magnets provide a constant magnetic flux density for a larger range of ampere-turns (working points on the right of the knee). This same behavior is observed for the FerriteY30, for which the normal and intrinsic curves are presented. It can be noticed that the remanence characterizing this magnet is around three times lower than the one observed for the Nd-Fe-B. This low B_r reduces the magnetization variation margin for a VFMM in which flux is created using these magnetic materials. As going to be later investigated, for these VFMMs, the possibility to demagnetize the magnet by injecting short-duration current pulses justifies the choice for using low coercive alloys such as Al-Ni-Co and Fe-Cr-Co ones.

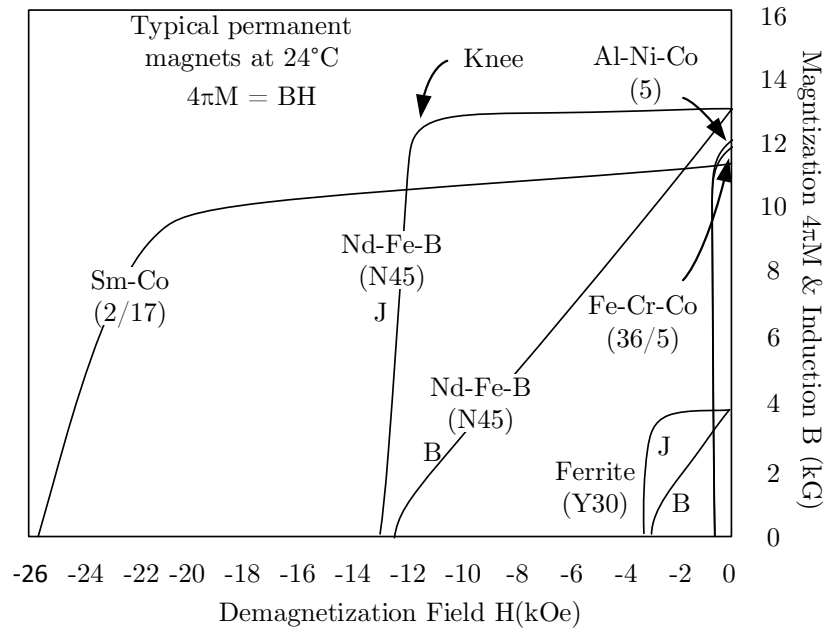


Figure 1.15: Demagnetization curve (2^{nd} quadrant of the hysteresis loop) of typical commercially available magnets - Adapted from [15].

1.3 Variable Flux Memory Machines

This section presents the Variable Flux Memory Machines. The general context about their use, their working principle, major characteristics, and designs are discussed.

1.3.1 Introduction

Variable Flux Memory Machines (or Memory Machines) were recently introduced in [23] by Vlado Ostovic as a reduced rare-earth option of machine that presents an adjustable flux produced by low coercive force (LCF) magnets. The highly nonlinear hysteresis loop of the LCF magnets, considered inconvenient for classical PMSMs due to the risk of demagnetization during normal operating conditions, makes possible the flux controllability observed in VFMMs. In the section [1.2.2] an overview concerning the magnetic materials often used in VFMMs was presented, as well as the advantages and inconveniences related to the use of each one of these materials.

The most important feature of this class of machines is the possibility of modifying the placement of the working point on the hysteresis loop of these magnets (or the air gap flux) via short-duration current pulses which supply the machine for producing a field in the magnetization axis (conventionally, the d -axis). When the currents are removed, part of the magnetization is conserved in the magnet, and so memorized [33], which justifies the name used for this machine. For some hybrid designs, as going to be the following presented, the variable magnetic flux can be combined with a constant one produced by sources such as high coercive force (HCF) magnets or currents crossing supplementary windings.

In VFMMs, the magnetization state (MS), or the percentage of the total flux production capacity used by the magnet, can be defined according to different working load requirements [39].

This feature represents an additional degree of freedom for the control of these machines in a wider torque-speed envelope. For low-speed operations, this same level can be adjusted to obtain the maximal torque from a full MS via the injection of positive short-time magnetization currents in the armature windings. Then, as the speed increases, this magnetization can be reduced via negative direct-axis (d-axis) current pulses, enlarging the torque-speed envelope. The requirement for flux-weakening (FW) currents is thus reduced in these machines, as well as extra copper losses observed in PMSMs [12, 27], which represents an advantage under dynamically changing load conditions [12], as well as electrical vehicles (EVs). The efficiency of the machine is therefore improved, being reported as higher than same-size convectional PMSMs or squirrel cage induction motors [23]. In [31] further studies regarding the torque characterization of variable flux machines are discussed, as well as the required energy to modify the magnetization state of the LCF magnets. Figure 1.16 illustrates a torque-speed envelope for representing the theoretical behavior of a magnet inserted in a VFMM. It can be observed that the flux in the machine is regulated according to three states: (1) high, (2) medium, and (3) low magnetization states.

- ① Low magnetization state ② Medium magnetization state ③ High magnetization state

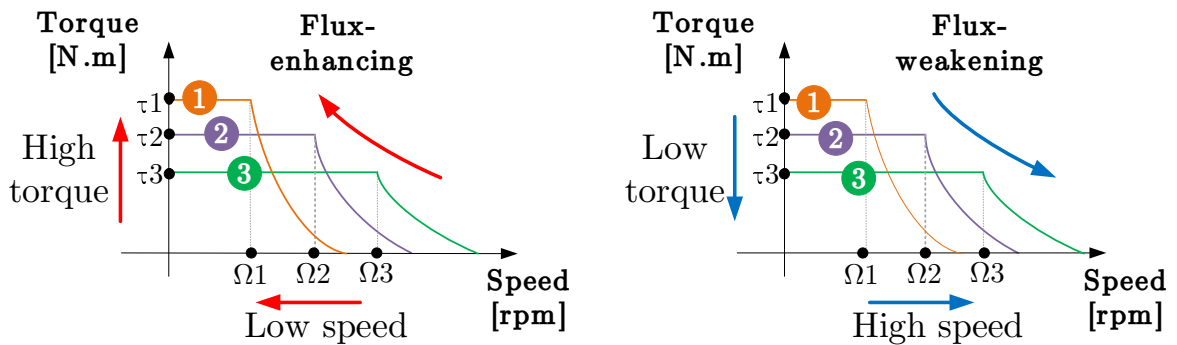


Figure 1.16: Illustration of theoretical control of the magnet flux in Variable Flux Memory Machines, considering a flux-enhancing strategy for high torque operations on the left and flux-weakening strategies for high-speed operations on the right.

A comparison between the voltage regulation method used for PMSMs, formerly described in the section 1.2.2, and the one proposed for VFMMs can be analyzed in the illustration proposed in the Figure 1.17. As shown, for the PMSM, the magnetic force of the permanent magnet is expected to be kept constant in normal operating conditions. Flux-weakening strategies are required for externally countering the increase of the induced back-EMF above the base speed, limiting it to the maximum DC voltage provided by the power supply. For VFMMs, the magnetization level of the magnets can be controlled step-by-step via pulses of negative d-axis currents according to the requirements for extending the torque-speed range. As no continuous d-axis current is required to supply the VFMM for this strategy as it is usually required by the ones applied in PMSMs, Joule losses are reduced.

In [17], the author proposes a comparison between three possible approaches for FW applied in a non-salient pole Al-Ni-Co-based VFMM: a first scenario, considering an operation without any flux-weakening strategy applied for regimes over the base speed; a second, imposing to the stator current a negative direct component of 50% of the rated current; and a third, in which the magnet flux regulation is achieved by supplying the machine with negative current pulses at standstill. For all of them, the Al-Ni-Co magnet present in the rotor is initially fully magnetized by the injection of positive d-axis current pulses in the armature windings at standstill. The

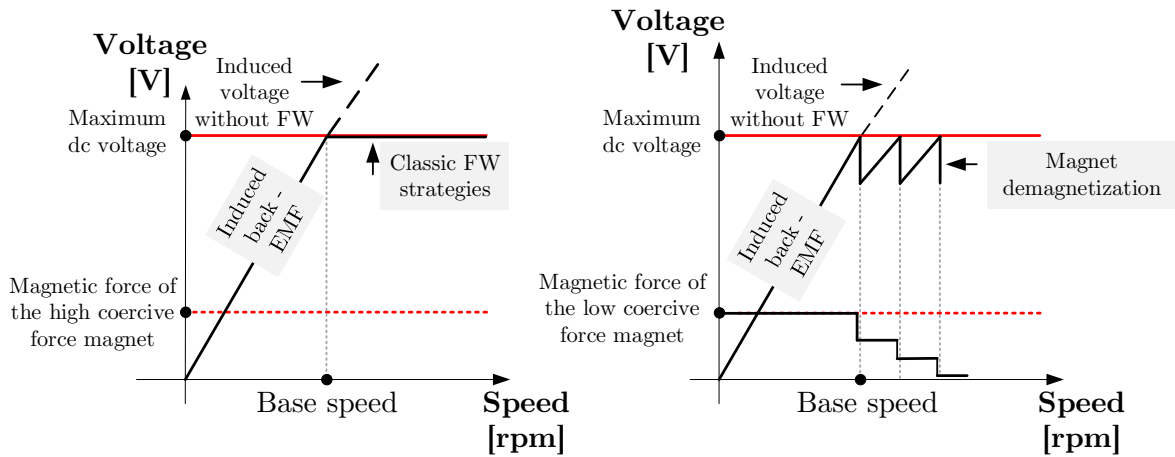


Figure 1.17: Illustration of theoretical voltage regulation in Permanent Magnet Synchronous Machines (left) and Variable Flux Memory Machines (right) - Adapted from [16].

Figure 1.18 exhibits the achieved results. The torque-speed envelope obtained demonstrates that demagnetizing the Al-Ni-Co magnets by negative magnetization current pulses (case 3 in this last-mentioned Figure 1.18) allows the machine to achieve higher speeds (wider torque-speed envelope) and higher efficiencies.

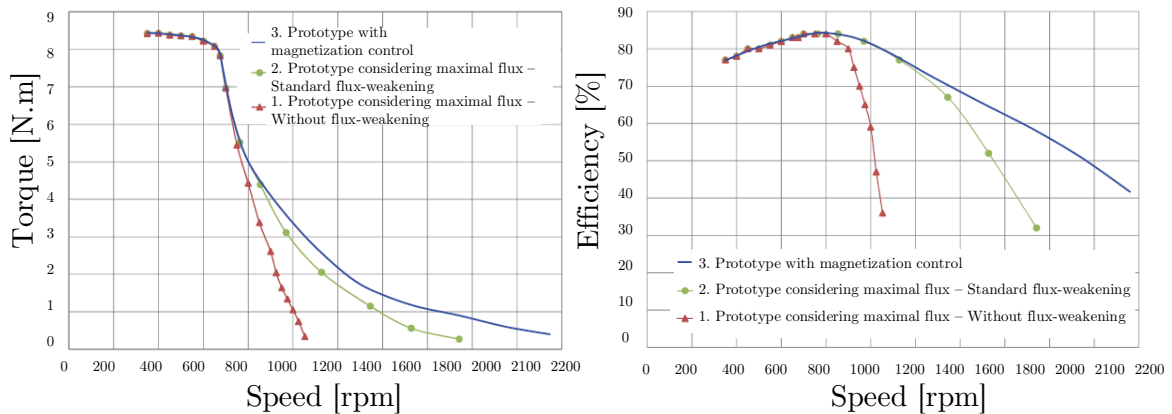


Figure 1.18: Torque envelope(left) and efficiency (right) of an Al-Ni-Co-based VFMM in different regimes for a $V=450V$ considering (1)torque production without the use of flux-weakening strategies, (2)torque production with continuous injection of negative d-axis current and (3)torque production considering a flux regulation by negative d-axis current pulses [17].

In [18], is also presented a study to validate the use of negative current pulses of magnetizing current as an efficient strategy to decrease in operation of the flux through the stator windings of an Al-Ni-Co-based VFMM. It introduces a study aiming to improve the efficiency of VFMM based on the association of classical FW strategies with the control of the magnetization state of the low coercive force alloy. To overcome the base speed, a demagnetization via pulses of negative

current amplitude is first used, reducing as a consequence, the magnetization state of the Al-Ni-Co magnet composing the machine. Then, a continuous negative current up to the amplitude of the pre-applied demagnetization pulses can be used to supply the machine without changing the magnetization state of the magnet. Because the total current is limited, the use of this strategy reduces the total current available for torque production. The major achievements are related to the increase of the output power, efficiency, and power factor, besides the enlargement of the torque-speed envelope. Some of these results are exhibited in Figure 1.19. Figures (a), (b), and (c) the performance of the VFMM when submitted to negative d-axis current pulses when operating over the base speed, as it is usually proposed for VFMMs. In Figures (d), (e), and (f), it can be analyzed the same results when the new methodology is applied by combining the classical FW strategy with the negative d-axis current pulses.

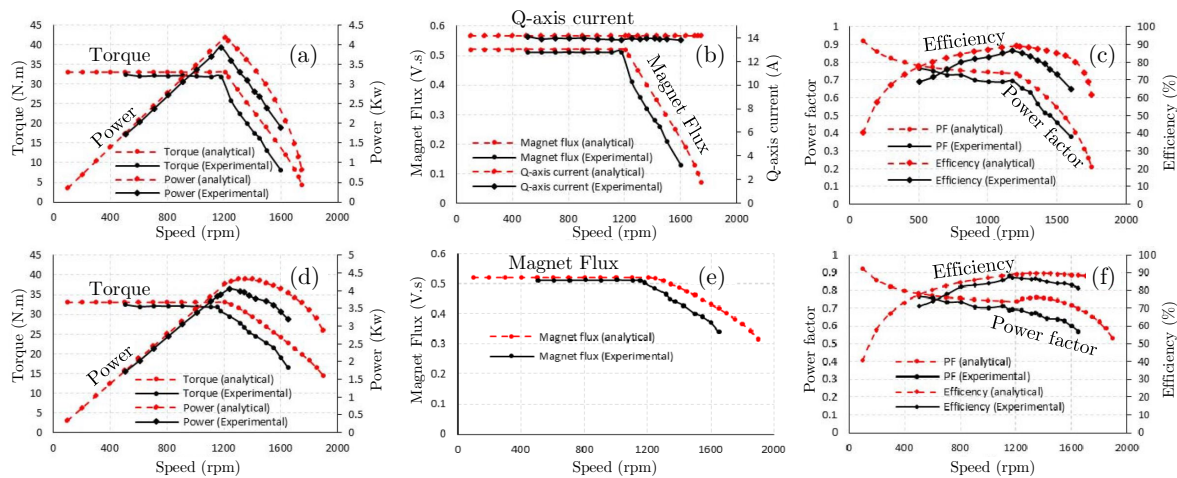


Figure 1.19: For a flux-weakening strategy via pulses of negative d-axis current: (a) Torque x speed, (b) Magnet Flux and Q-axis current x Speed, and (c) Efficiency - Power factor x Speed. For a flux-weakening strategy via both continuous and pulses of negative d-axis current: (d) Torque x speed, (e) Magnet Flux x Speed, and (f) Efficiency - Power factor x Speed [18].

1.3.2 The positioning of Variable Flux Memory Machines in the electrical machine scenario

To justify the interest of VFMMs against the other well-known synchronous machines, [23] proposes a comparison whose conclusions are presented in Table 1.8. The green parameters represent the most desirable in terms of performance and the red the less ones. As classic wound-rotor synchronous machines, VFMMs can have their back-EMF controlled, but via short-time magnetization current pulses, which considerably reduces the copper losses and avoids the necessity of using continuous negative currents as it is in flux-weakening strategy. The mechanical speed limit of VFMMs can be enlarged by exploring this characteristic of flux regulation as already mentioned. In [17], by a reduction of the magnet flux over the base speed, an extension of 300% on the torque-speed envelope is achieved when compared to the case without considering any field-weakening strategy applied. In [12], authors mention that depending on the strategy used for controlling the current vector at high speeds, the torque-speed envelope can be extended up to 202%.

With regard to torque production, [23] introduces that VFMMs should be theoretically designed to ensure that only magnetization (d-axis) currents are capable of modifying the

magnetization level of the LCF magnet used in the machine. Nevertheless, if the machine geometry is not adapted, risks of unintentional demagnetization by the load currents are present. For addressing this phenomenon known as armature reaction, the use of non-magnetic material is usually proposed. These materials work as q-axis flux barriers, deviating the path of the load flux lines. However, multiple challenges are involved in the adaptation of machines to avoid the armature reaction. As a consequence, most Variable Flux Machine geometries are susceptible to being exposed to the described effects of unintentional demagnetization. For this reason, a modification is proposed in the original Table 1.8 introduced by [23], in which the risks of demagnetization by load currents in VFMMs were considered null. Later sections are going to further investigate this topic and its impact on the geometry proposed in this present thesis.

Table 1.8: Comparison between Variable Flux Memory Machines and Conventional Synchronous Machines - Adapted from [23].

Performance Indicator	Wound Rotor	Internal PM	Surface-Mounted PM	Reluctance	Variable Flux Memory Motor
Controllability of back-EMF	Full	Limited	Extremely Limited	None	Full
Losses due to control of back-EMF (flux-weakening)	Rotor I^2R	Stator I^2R	Stator I^2R	Not applicable	Almost Zero
Mechanical speed limit	Low	High	Moderate	High	High
Risk of demagnetization by the load current	Not applicable	High	High	Not applicable	Depends on the geometry

Until in [23], a performance comparison is proposed between a VFMM, a conventional PM, and a squirrel cage machine as presented in Table 1.9. For these two first mentioned, multiples insights were already introduced in the previous section 1.1, as an example the benefits of using LCF magnets as the Fe-Cr-Co against the HCF magnets as the Nd-Fe-B ones in terms of the thermal characteristics (as also discussed in [17] and [12]). The magnet price was also investigated, as presented in Table 1.5, which identified that LCF magnets are currently more expensive than PMs, although the disponibility of rare-earth elements tends to reduce over the years (which will probably cause an increase on prices). Due to this conclusion, a modification is suggested in Table 1.9 originally presented in [23]: prices of the PM magnets of conventional PMSM can be considered as low, but increasing.

The low sensitivity of LCF magnets to corrosion and the possibility of mounting the rotor with these magnets in a non-magnetized state can be also considered important advantages of VFMMs mentioned by [23]. Besides this, following the studies introduced in the previous section, the differences in the FW strategies for operating the machine over the base speed are also highlighted as an advantage of VFMMs against PMSMs. For squirrel cage machines, the FW is easily achieved by well-known direct vector control, but as in PMSMs, the efficiency of this machine is reduced due to the rotor losses. These same losses are responsible for demanding a better cooling system in the induction machines, which increases their size.

Additionally, the injection of magnetization currents for varying the magnetization state of VFMMs as well as of the ones used for producing torque depends on a good knowledge of the rotor position as is also the case of PMSMs, but not of induction machines. Sensors are often used for obtaining this rotor position information, but they significantly increase the maintenance, complexity, and cost of the system, affecting its robustness and reliability. The development of sensorless techniques emerged as an option to improve these systems, which is especially

challenging for VFMMs as a later chapter is going to explore. Until the publication of [23], no sensorless had been proposed for VFMMs. However, these methodologies have been developed in the last few years. This justifies another modification proposed in Table 1.9 in comparison to the one in the [23], where the position sensor is indicated as a requirement for magnet-based machines.

Table 1.9: Comparison between Variable Flux Memory Machines and Conventional PM and Induction machines [23].

Performance Indicator	Squirrel Cage	Conventional PM	Variable Flux Memory Motor
Efficiency	Medium	Medium	High
Flux-weakening strategy	Simple and direct	Lossy	Low losses
Inverter size	Medium	Small	Small
Dependence on rotor position information	No	Yes	Yes
Machine size	Medium	Small	Small
Air gap width	Small	Large	Small
Thermal proprieties	Not applicable	Poor	Good
Magnet price	Not applicable	Low, but increasing	Acceptable
Magnet corrosion and handling	Not applicable	Strong and complex, respectively	Low and simple, respectively

1.3.3 The mathematical modeling of Variable Flux Memory Machines in the dq-reference frame

1.3.3.1 Electrical equations

For defining the electrical equations describing the machine, some hypotheses are raised:

- The distribution of magnetomotive forces is sinusoidal.
- The eddy currents are neglected.
- The damping effect at the rotor is neglected.

In these conditions, the electrical modeling of the machine considering a three-phase reference frame (abc) is defined by:

$$\begin{bmatrix} v_a \\ v_b \\ v_c \end{bmatrix} = R_s \begin{bmatrix} i_a \\ i_b \\ i_c \end{bmatrix} + \frac{d}{dt} \begin{bmatrix} \varphi_a \\ \varphi_b \\ \varphi_c \end{bmatrix} \quad (1.11)$$

where R_s defines the resistance of the stator windings, $[v_a \ v_b \ v_c]^t$, $[i_a \ i_b \ i_c]^t$ and $[\varphi_a \ \varphi_b \ \varphi_c]^t$ are respectively the vectors of the phase voltages, phase currents and the total magnetic flux through the stator windings. Using Clarke Transformation (C_{23} , considering a balanced electrical system), these equations can be rewritten considering the translation of the three-phase reference frame to the two-axis orthogonal stationary reference frame (defining the $\alpha\beta$ -axis, related to the stator) by:

$$\begin{bmatrix} v_\alpha \\ v_\beta \end{bmatrix} = R_s \begin{bmatrix} i_\alpha \\ i_\beta \end{bmatrix} + \frac{d}{dt} \begin{bmatrix} \varphi_\alpha \\ \varphi_\beta \end{bmatrix} \quad (1.12)$$

where

$$\begin{bmatrix} x_\alpha \\ x_\beta \end{bmatrix} = C_{23} \begin{bmatrix} x_a \\ x_b \\ x_c \end{bmatrix}, \text{ where } C_{23} = \frac{2}{3} \begin{bmatrix} 1 & -\frac{1}{2} & -\frac{1}{2} \\ 0 & \frac{\sqrt{3}}{2} & -\frac{\sqrt{3}}{2} \end{bmatrix} \quad (1.13)$$

being x in the Equation [1.13](#) a machine quantity, as the voltage (v), current (i) or the flux (φ). Applying the Park Transform-based ($P(\theta)$) for expressing the same equations in the orthogonal rotating reference frame (defining the dq-axis, related to the rotor, which position is given by θ , in [rad]) it can be defined:

$$\begin{bmatrix} v_d \\ v_q \end{bmatrix} = R_s \begin{bmatrix} i_d \\ i_q \end{bmatrix} + \frac{d}{dt} \begin{bmatrix} \varphi_d \\ \varphi_q \end{bmatrix} + \omega P\left(\frac{\pi}{2}\right) \begin{bmatrix} \varphi_d \\ \varphi_q \end{bmatrix} \quad (1.14)$$

where

$$\begin{bmatrix} x_d \\ x_q \end{bmatrix} = P(-\theta) \begin{bmatrix} x_\alpha \\ x_\beta \end{bmatrix}, \text{ where } P(\theta) = \begin{bmatrix} \cos \theta & -\sin \theta \\ \sin \theta & \cos \theta \end{bmatrix} \quad (1.15)$$

where $[v_d \ v_q]^t$, $[i_d \ i_q]^t$ and $[\varphi_d \ \varphi_q]^t$ are respectively the direct (d) and quadrature (q) components of the voltage, current and the total flux (or flux linkage) through the stator windings. Considering the cross-coupling effects, one proposes to model the relation between flux and current in the dq-referential by:

$$\begin{cases} \varphi_d(i_d, i_q) = L_d(i_d, i_q)i_d + (MS)\varphi_{s_{max}}(i_d, i_q) = L_d(i_d, i_q)i_d + \varphi_s \\ \varphi_q(i_d, i_q) = L_q(i_d, i_q)i_q \end{cases} \quad (1.16)$$

where $\varphi_{s_{max}}$ (in [Wb]) is the maximal flux linkage through the stator windings. The magnetization state (MS), defined in the equation [1.20](#), allows the adjustment of the flux through the stator windings, defined by φ_s (in [Wb]). It is assumed, in the domain variation of the dq-axis currents for the machine considered, that $\varphi_{s_{max}}$ and consequently φ_s are little affected by the saturation effects and can be considered constant for a given magnetization state (MS). The terms $L_d(i_d, i_q)$ and $L_q(i_d, i_q)$ are, respectively, the static dq-axis inductances. Applying the equation [1.16](#) in the equation [1.14](#), it can be defined:

$$\begin{bmatrix} v_d \\ v_q \end{bmatrix} = R_s \begin{bmatrix} i_d \\ i_q \end{bmatrix} + \begin{bmatrix} \hat{L}_d & \hat{M}_{dq} \\ \hat{M}_{qd} & \hat{L}_q \end{bmatrix} \frac{d}{dt} \begin{bmatrix} i_d \\ i_q \end{bmatrix} + \omega P\left(\frac{\pi}{2}\right) \begin{bmatrix} L_d & 0 \\ 0 & L_q \end{bmatrix} \begin{bmatrix} i_d \\ i_q \end{bmatrix} + \begin{bmatrix} \varphi_s \\ 0 \end{bmatrix} \quad (1.17)$$

where are identified the static self-inductances (L_d and L_q), given by:

$$\begin{cases} L_d = \frac{\varphi_d(i_d, i_q) - \varphi_s}{i_d} & L_q = \frac{\varphi_q(i_d, i_q)}{i_q} \end{cases} \quad (1.18)$$

And the dynamic self-inductances (\hat{L}_d and \hat{L}_q) and cross-coupling (\hat{M}_{dq} and \hat{M}_{qd}) inductances are given by:

$$\begin{cases} \hat{L}_d = \frac{\partial \varphi_d(i_d, i_q)}{\partial i_d} \\ \hat{L}_q = \frac{\partial \varphi_q(i_d, i_q)}{\partial i_q} \\ \hat{M}_{dq} = \hat{M}_{qd} = \frac{\partial \varphi_d(i_d, i_q)}{\partial i_q} = \frac{\partial \varphi_q(i_d, i_q)}{\partial i_d} \end{cases} \quad (1.19)$$

The dynamic cross-coupling inductances are supposed to be enough small and therefore considered negligible. In the case of a non-saturated machine, the dynamic dq-axis inductances are equal to the static ones ($\hat{L}_d = L_d$ and $\hat{L}_q = L_q$).

The adjustment of the flux linkage through the stator windings in the machine is quantified by the magnetization state, calculated by [31]:

$$MS[\%] = \frac{\varphi_s}{\varphi_{smax}} \times 100 \quad (1.20)$$

While for PMSMs the magnetization state is constant and conserved during a normal machine operating ($MS = 100\%$), for VFMMs, this same parameter is quantified by values in the range $-100\% \leq MS \leq 100\%$. In this case, "-100%" and "100%" represent the full magnetization in negative and positive directions (or saturation observed in the third and first quadrant, respectively). When " $MS = 0$ ", the magnet is considered in a complete demagnetization state. Values in the middle of this interval represent a partial magnetization state.

Authors in [12] propose the calculation of the magnetization state directly by the hysteresis curve, using the ratio between the remanence characterizing the recoil line and the external one. This method, however, is not practical in real applications as the remanence of the internal loops cannot be directly measured. Experimentally, this magnetization state can be estimated after each variation of the magnetization state by the amplitude of the phase back-EMF induced in the stator windings (e, in [V]). This strategy, commonly used by authors studying VFMMs [17, 12, 31], will be the one explored in this present research in the next chapters. The equation [14] for non-saturated machines can be rewritten as:

$$\begin{bmatrix} v_d \\ v_q \end{bmatrix} = R_s \begin{bmatrix} i_d \\ i_q \end{bmatrix} + \begin{bmatrix} L_d & 0 \\ 0 & L_q \end{bmatrix} \frac{d}{dt} \begin{bmatrix} i_d \\ i_q \end{bmatrix} + \omega P \left(\frac{\pi}{2} \right) \begin{bmatrix} L_d & 0 \\ 0 & L_q \end{bmatrix} \begin{bmatrix} i_d \\ i_q \end{bmatrix} + \begin{bmatrix} e_d \\ e_q \end{bmatrix} \quad (1.21)$$

where e_d and e_q are the direct and quadrature component of the back-EMF. For machines having a sinusoidal, $e_d = 0$ and $e_q = \omega \varphi_s$. For a non-salient pole machine as the one analyzed in this present research, the equation [21] can be simplified considering equal the dq-axis inductances ($L_d = L_q$).

1.3.3.2 Mechanical equations

The mechanical equation of synchronous machines can be defined by [103]:

$$J \frac{d\Omega}{dt} = \Gamma_e - \Gamma_{load} - f\Omega \quad (1.22)$$

where J is the moment of inertia, Γ_e is the electromagnetic torque (in [N.m]), Γ_{load} is the load torque (in [N.m]), f is the friction coefficient (damping) and Ω the mechanical speed (in [rad/s]).

$$\Gamma_e = (3/2)p(\varphi_d I_q - \varphi_q I_d) = (3/2)p[\varphi_s I_q + (L_d - L_q)I_d I_q] \quad (1.23)$$

Two components are identified in the equation [1.23](#). The first one $((3/2)p\varphi_s i_q)$ is related to the magnet excitation torque, while the second one $((3/2)p(L_d - L_q)I_d I_q)$, corresponds to the reluctance torque. For non-salient pole machines:

$$\Gamma_e = (3/2)p\varphi_s I_q \quad (1.24)$$

1.3.4 The magnetic behavior of a Variable Flux Memory Machine

This section is focused on explaining the behavior of the magnet working point in the hysteresis curve due to the variation of the magnetization state in VFMMs. These concepts are directly applied to the understanding of the theoretical control of the magnetization state in a machine for which the flux is produced directly from the LCF magnet (single-type VFMM). This study represents a generalization, but some modifications to the development presented can be required according to the machine geometry.

1.3.4.1 Description of the operating principle

From a magnetic point of view, the working point of a VFMM is placed at the intersection of the hysteresis loop of the magnet, an intrinsic propriety of the magnetic material, and a load line, defined according to the magnet circuit in which the magnet is inserted (in this case, the machine). Figure [1.20](#) illustrates a single-type magnetic circuit, in which the air gap flux is produced by a hypothetical LCF magnet. A core of high relative permeability is considered ($\mu_r \rightarrow \infty$). Effects of flux leakage and fringing are neglected. Therefore, the same magnetic amount of magnetic flux (φ_m) crosses the core, the air gap, and the magnet, all these regions are supposed to have the same cross-sectional area (respectively given by A_c , A_g and A_m , in $[m^2]$). The length (l , in $[m]$) of each of the magnetic paths in these mentioned regions is defined by l_c , l_g , and l_m , respectively.

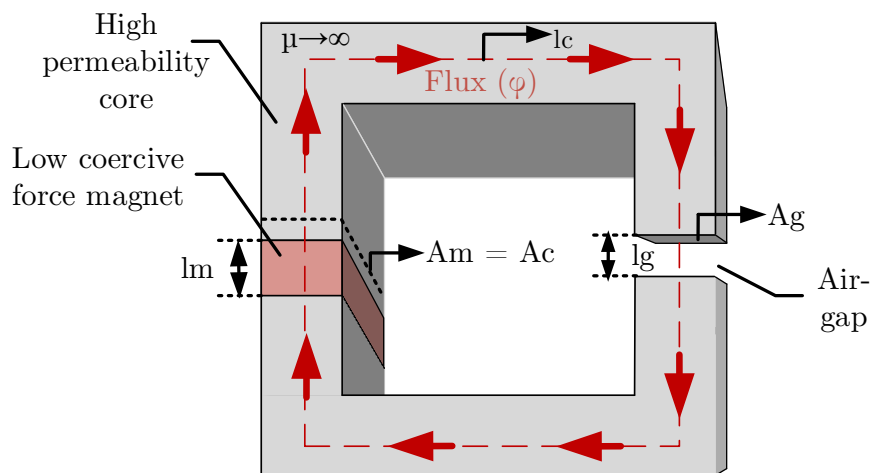


Figure 1.20: Analysis of a single-type magnetic circuit.

Applying the Ampère's law previously presented in the equation [1.1](#) to magnetic circuits, the total magnetomotive force (MMF) can be calculated as:

$$\oint \vec{H} \cdot d\vec{l} = \vec{I}$$

$$H_g l_g + H_m l_m + H_c l_c = NI \quad (1.25)$$

where N ([unitless]) is the number of spires of the source of MMF that are crossed by a current. For the VFMM, because this mentioned flux is created by the magnet, $NI = 0$. By the equation [1.5](#) defining the function $\vec{B}/\vec{H} = \mu$, it can be concluded that, for a circuit composed of a high permeability core ($\mu_r \rightarrow \infty$), the magnetic field intensity tends to zero. Thus, the term $H_c l_c$ and can be neglected in the equation [1.25](#) and the equation [1.25](#) can be rewritten as:

$$H_g l_g + H_m l_m = 0 \quad (1.26)$$

Using Gauss's Law given by the equation [1.3](#), the flux through the magnetic circuit can be calculated by:

$$\int_A \vec{B} \cdot d\vec{A} = \varphi$$

$$\varphi = B_g A_g = B_m A_m = B_c A_c \quad (1.27)$$

Substituting the equation [1.26](#) in [1.27](#), it can be defined:

$$B_m = -\mu_0 \left(\frac{l_m}{l_g} \right) \left(\frac{A_g}{A_m} \right) H_m \quad (1.28)$$

The influence of variations on the magnet geometry on the result achieved by the equation [1.29](#) on the total result achieved is illustrated below without considering any modification on the air gap geometry:

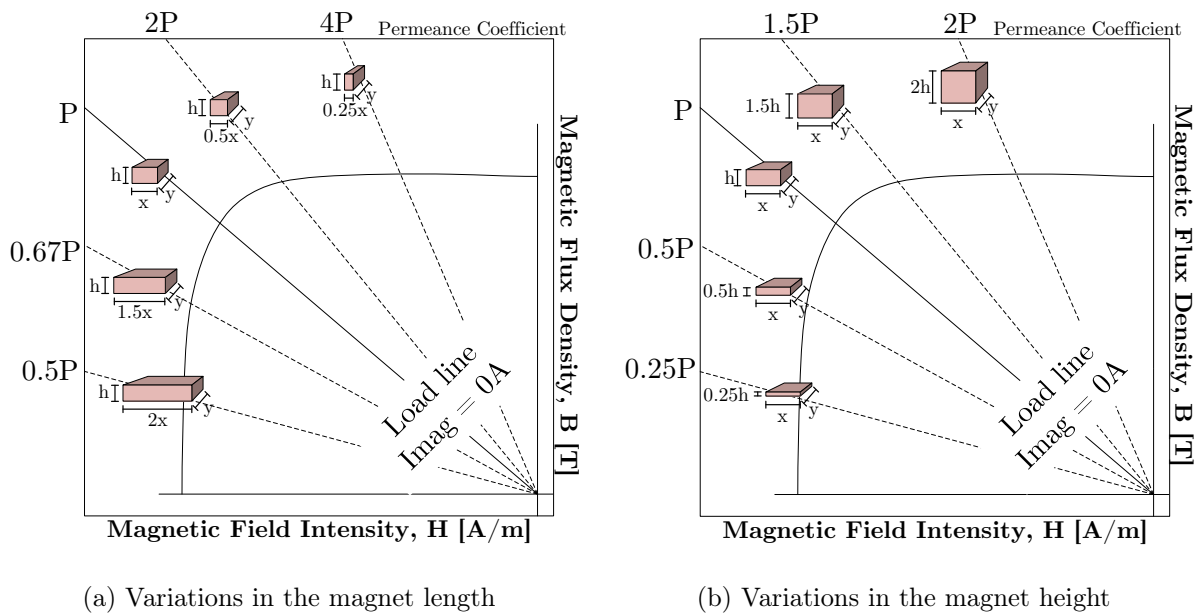


Figure 1.21: Variation of the Permanence Coefficient according to the magnet geometry, considering variations on the magnet dimensions.

The equation [1.28](#) models the load line when no magnetization currents supply the machine ($I_{mag} = 0$) as linear equation function $B(H) = k \cdot H$, where k_1 represents the slope (also known as Permeance Coefficient (PC)) of this load line. As can be observed, this parameter purely depends on the machine and the magnet geometry in open circuits. For operations at nonzero magnetization current, the equation [1.28](#) is rewritten as:

$$B_m = -\mu_0 \left(\frac{l_m}{l_g} \right) \left(\frac{A_g}{A_m} \right) H_m + \mu_0 \left(\frac{1}{l_g} \right) \left(\frac{A_g}{A_m} \right) NI_{mag} \quad (1.29)$$

The equation [1.29](#) defines $B(H) = H(PC) + k_2 NI_{mag}$, where PC is the same previously calculated for $I_{mag} = 0A$ as the geometry remains unchanged. The constant k_2 displaces the load line to the left or right respectively according to the the amplitude of the magnetization current pulse, negative ($I_{mag} < 0$) or positive ($I_{mag} > 0$). Shifting this mentioned load line, the magnetization current modifies the point in the BH plan in which the intersection with the hysteresis loop occurs. The Figure [1.22](#) illustrates this described behavior.

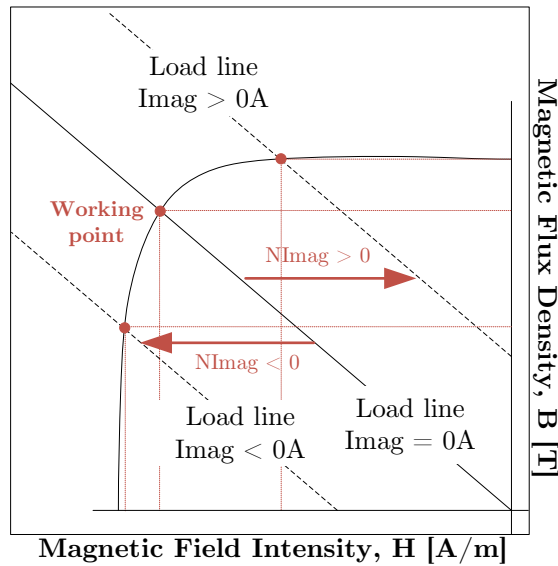


Figure 1.22: Variation in the load line placement according to the magnetization current supplying the armature windings.

Based on the simplifying assumption of linear modeling of the hysteresis loop, discussed in the section [1.1.4.2](#) and presented in Figure [1.4](#), the demagnetization curve on the second quadrant can be described by the equation [1.10](#):

$$\vec{B} = \mu_0 \mu_r \vec{H} + B_r \quad (1.30)$$

Using the equation [1.29](#) and [1.10](#), the working point of the magnet can be calculated by:

$$B_m = \frac{(A_g l_m B_r + \mu_0 \mu_r A_g (NI_{mag}))}{(A_g l_m + \mu_r l_g A_m)} \quad (1.31)$$

For electrical machines, because distributed windings compose each phase in the armature

geometry, the term NI_{mag} in the equation 1.29 representing the MMF generated by currents crossing a single slot can be rewritten in terms of q , the number of slots per pole and per phase and of p , the number of pole pairs, which defines:

$$B_m = \frac{(A_g l_m B_r + \mu_0 \mu_r A_g (pqNI_{mag}))}{(A_g l_m + \mu_r l_g A_m)} \quad (1.32)$$

Figure 1.23 exhibits the theoretical variation of the working point, and therefore of the magnetization state, according to the magnetization current amplitude. From the saturation of the magnet ($MS = 100\%$) in point 1, the working point moves along the external demagnetization curve until point 2 when the magnetization current is suppressed. The working point 2 defines the intersection of the major hysteresis loop and the load line for $I_{mag} = 0A$. This point must be preferentially placed at the linear region of the demagnetization curve for achieving a high air gap flux density which allows the machine to deliver high torques at low speeds [41]. From this point, when the currents exceed the base speed, the magnet flux can be reduced via negative d-axis current pulses ($I_{mag} < 0A$) injected in the armature windings. The demagnetizing field (H_n) generated by the term NI_{mag} in the equation 1.29 displaces the load line to the left because k_2 is inherently positive and $H_n = NI_{mag}$ is negative in this condition. The MS is reduced and the new working point intercepts the BH loop at point 3. When the current is released, the trajectory of the working point does not retrace the path defined by points 2-3. Instead of it, it moves along a recoil line until point 4. A portion of the initial MS of the magnet is conserved even after the demagnetization ($B_4 > B_3$), which defines the memory of this machine. From point 4, positive magnetization current pulses ($I_{mag} > 0A$) create a positive external field ($H_p = NI_{mag}$), and displace the load line to the right. The working point traces the path defined by points 4-5 and then moves to point 6 when the current is suppressed. Again, the initial MS is partially conserved ($B_6 < B_5$). The amplitude of the magnetization current required for re-magnetizing the magnet is higher than the one required during the demagnetization [12] [16].

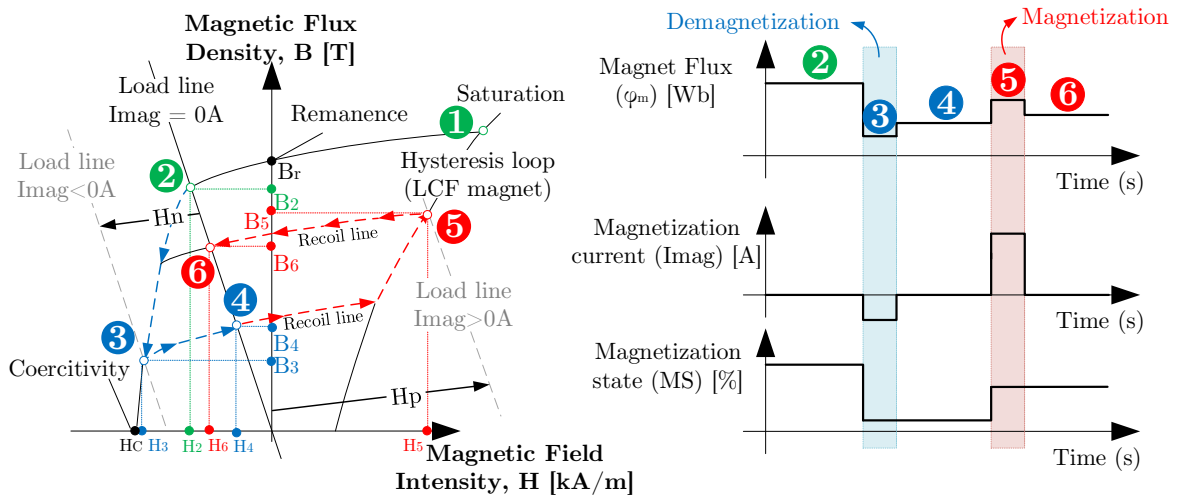


Figure 1.23: On the left, theoretical working points are placed in the hysteresis loop of a LCF material according to the magnetization current supplying the machine. On the right, the behavior of the magnetization state/magnet flux for these different operating conditions.

1.3.5 Characteristics of the magnetization process

1.3.5.1 Strategies of magnetization of Variable Flux Memory Machines

The variation of the MS can be achieved via two strategies, usually subsequently applied:

- **Standstill magnetization** A d-axis current injected through the drive to the motor terminal at zero rotor speed (or at mechanical speed $\Omega = 0rpm$) defines a standstill magnetization [39]. In this strategy, the low coercive magnet inserted in the VFMM, initially demagnetized, has its level of magnetization enhanced from the injection of positive short-duration d-axis current pulses (usually a few milliseconds for negligible Joule losses). As a consequence, the working point of the magnet in its hysteresis curve moves along the initial magnetization curve until a set point, defined according to the amplitude of I_{mag} used for supplying the machine. Once the current is released, this working point takes the path described by a specific recoil line and settles at the intersection of this recoil line and the load line $I_{mag} = 0$. A regime is then established in the machine, allowing it to measure the back-EMF and estimate the flux linkage through the stator windings and the magnetization state achieved by the magnet. A demagnetization procedure follows this estimation to ensure that all the magnetization state is analyzed from the same referential. Authors in [12, 17, 31, 39] explore the use of the standstill magnetization. Results obtained from this strategy are used for establishing the behavior of the flux linkage according to the magnetization current ($\varphi_s = f(I_{mag})$), which defines the lookup tables later used as a reference for the dynamic strategy.
- **Running magnetization** The running (or dynamic) magnetization corresponds to the capacity of adjusting the magnetization state in the machine by supplying it with d-axis magnetization currents pulses while it is running (at $\Omega \neq 0$ rpm) [109]. During this process, the working point initially placed at the intersection between the load line $I_{mag} = 0A$ and a specific recoil line in the hysteresis curve has the option of being displaced to the left (in case of a demagnetization) or to the right (in case of a remagnetization). For both procedures, the level of current required to change the magnetization state is sufficient to lead the working point beyond the intersection of this mentioned recoil line and the major hysteresis loop. Because the load line $I_{mag} = 0A$, which defines the working point at the initial magnetization condition, is placed on the second quadrant, the amplitude of current (or the external field) required for the demagnetization of this magnet is lower than the one required for the remagnetization (usually several times of the rated current). Authors in [27, 39, 40, 41, 89] explore the running magnetization.

Results achieved via standstill and running magnetization procedures will be explored in the next chapters of this thesis.

1.3.5.2 The magnetization current pulses

The flux adjustment is the most important feature of Variable Flux Memory Machines. To achieve it, pulses of current are injected into the armature windings aiming to create an external field in the magnetization axis. Some insights about the characteristics of these current pulses and how this affects the magnetization process of VFMMs have been presented in different studies. In [39], authors present an analysis of different magnetization pulse widths and magnetization methods on the back-EMF. This research provides insights to evaluate the minimal duration of the current pulse required for magnetizing the VFMM at a certain level. It is observed that the fundamental back-EMF achieved after a standstill magnetization realized by different pulse widths is quite similar, but the total harmonic distortion (THD) varies especially due

to the 3rd-order harmonic that changes for each pulse duration. Authors in [31] investigate the energy injected into the machine using different current pulse profiles. In this study, it is observed that most of the energy is injected into the machine during the transient of the pulse (rise and fall portions). Therefore, minimizing the energy consumption during the magnetization/demagnetization procedure requires the minimization of these transients. Finally, [17] indicates the possibility of applying several successive pulses of currents to achieve a certain level of magnetization. According to this study, the duration of the magnetization current pulses required for adjusting a defined MS depends on the current settling time and, therefore, on the electrical time constant of the motor. No in-depth study regarding the possible power electronics architectures for the generation of the current pulses is going to be discussed in this present thesis. For the application considered in this research, a DC/AC inverter previously developed at IFP Energies nouvelles is used to control the VFMM. A topology software is adapted to propose a DC/DC magnetization mode without requiring supplementary components and with no neutral access. This system is going to be presented in Chapter 2. In the Appendix A.6, some other examples of possible topologies for generating the current pulses are introduced.

1.3.6 First challenge on the use of Variable Flux Memory Machines: the armature reaction

By the theoretical definition of VFMMs presented in [23], only magnetization current pulses should be able to create a magnetic field passing through the LCF magnets used in VFMMs. Therefore, only the d-axis current pulses are expected to modify the MS [23]. Unintentionally, although, and depending on the machine geometry, the perpendicular magnetic field created by the injection of load currents (q-axis currents) into the machine can also contribute to the variation of the magnetic flux. In this case, as both magnetic and excitation fields cross the magnet simultaneously, the resultant magnetic field is distorted. The consequence is the establishment of regions of field-enhancing and field-weakening in the magnet. Figure 1.24 illustrates this phenomenon in a VFMM composed of a massive LCF-based rotor. If the amplitude of the q-axis current is sufficient to create an external field that shifts the working point beyond the knee in the second quadrant, a demagnetization is the result of this process.

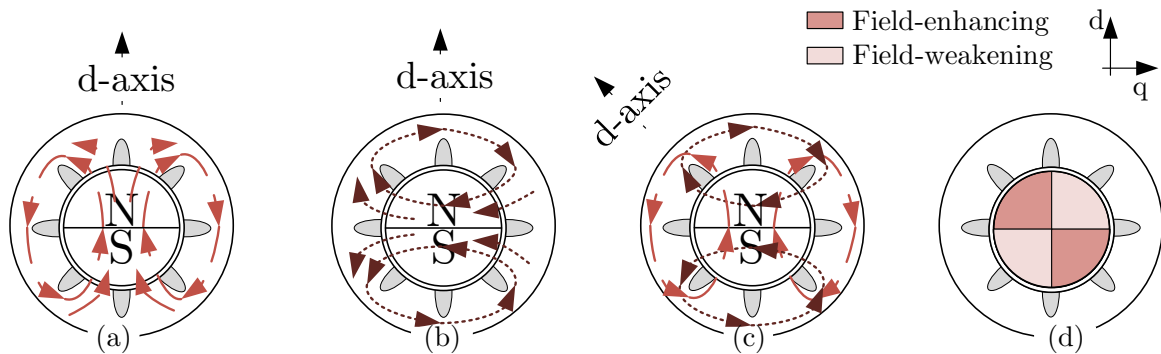


Figure 1.24: Illustration of the armature reaction - Excitation field generated by (a) d-axis currents and (b) q-axis currents and (c) interaction between excitation and armature field that creates (d) regions of field-weakening and field-enhancing in the magnet.

The armature reaction is a key challenge regarding VFMMs. The use of q-axis flux barriers is usually the methodology proposed to limit these effects, as authors discussed in [27, 31, 19] and so many other papers. Their design is strongly dependent on machine and magnet geometry.

1.3.7 The classification of the Variable Flux Memory Machines

Since the first VFMM was presented by [23], multiple designs have been investigated in the literature. According to the excitation method used [19, 20, 37, 110], VFMMs can be classified as DC-magnetized, for which specific coils are disposed in the stator for injecting the magnetization current (I_{mag}), or as AC-magnetized, if this current is directly injected in the armature windings. This classification is summarized in the Figure 1.25

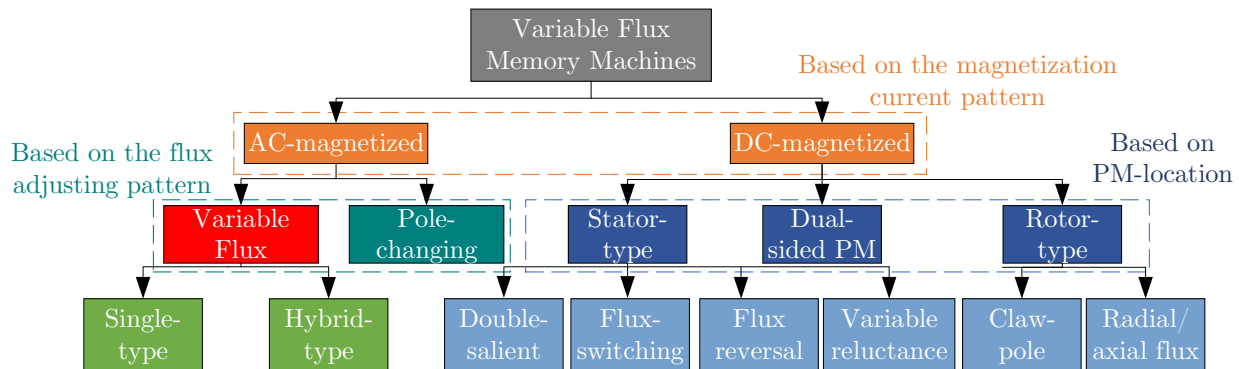


Figure 1.25: Categories of Variable Flux Memory Machines - Adapted from [19].

Remark: Because the first design of VFMM proposed in the literature by [23] is classified as AC-magnetized, multiple papers simplified the aforementioned classification, do not consider the information about the DC-magnetized machines. Also, it is observed that unless the geometry is specified as pole-changing, the terms "Variable Flux Memory Machines" or "Memory machines" are both used in the literature for classifying machines with a fixed number of poles. This remark avoids possible misconceptions about the classification of the machines presented by some authors.

Remark: In [111], an alternative classification of VFMMs is presented based on the flux adjusting pattern. To this paper, machines designed with an additional coil (previously presented as DC-magnetized VFMMs), are considered hybrid, rather than categorized according to the placement in the rotor or stator of the magnetization coil. The choice for the classification presented in Figure 1.25 against this one is mainly justified by the fact that this mentioned coil is being used for adjusting the magnetization level of the magnet, not for effectively exciting the machine.

1.3.7.1 DC-magnetized Variable Flux Memory Machines

DC-magnetized VFMMs are sub-classified conforming to the PM-location, being the stator-type ones the most commonly mentioned in the literature [21, 111, 20, 110]. Authors in [20] remark that DC-magnetized VFMMs conserve the merits of good rotor mechanical robustness and easy heat dissipation from conventional stator PM machines. Some examples of machine geometry are going to be introduced in this section.

Until in [20], a flux-switching memory machine composed of a partitioned stator is presented. The Figure 1.26 exhibits the machine geometry. The design proposes magnets (PM and LCF) placed in the inner stator, to ensure that the LCF magnets are free from the severe on-load magnetic saturation on the outer stator. The demagnetization risk caused by either PM or armature fields is reduced. Despite the results presented in this paper explicit a good performance of this machine, its complex design can be unattractive.

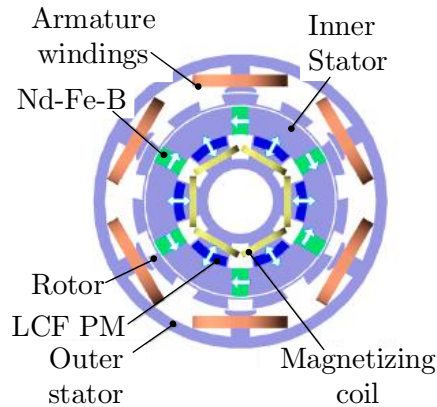


Figure 1.26: Partitioned stator switched flux hybrid magnet memory machine - Adapted from [20].

By exposing some drawbacks concerning the use of stator-type Double-Salient Memory Machines (DSMMs), as the non-sinusoidal back-EMF when under heavy magnetic saturation, which causes a high torque ripple, authors in [21] propose a comparison between the flux-switching memory machines (FSMMs) and the variable reluctance memory machines (VRMMs), both designed with extra windings to vary their magnetization state. Figure 1.27 presents them, which are differentiated by the position of the Nd-Fe-B magnets with respect to the armature windings. It is observed that FSMMs deliver a higher output torque and LCF magnets can resist the demagnetization when submitted to the armature field (armature reaction).

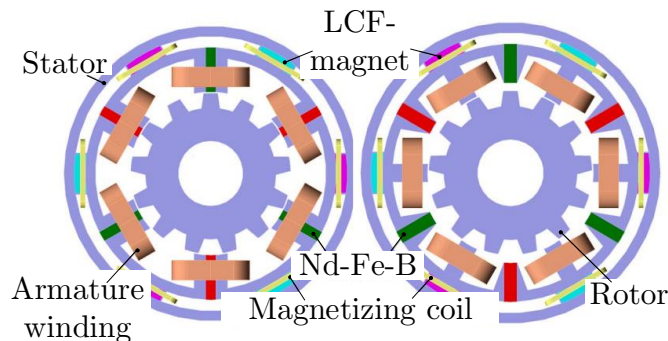


Figure 1.27: Flux-switching memory machine design (left) and Reluctance memory machines (right) [21].

Some more demerits and challenges related to the use of DC-magnetized VFMMs can be studied [111], as well as propositions for improving their performances.

1.3.7.2 AC-magnetized Variable Flux Memory Machines

For reducing the weight and manufacturing complexity of the machine, the AC-magnetization approach is usually preferred to the DC one [12]. This class of machines can be divided into pole-changing machines and VFMMs and will be the focus of this research work.

Pole-changing machines were introduced by [22] as a machine in which the magnets can be grouped in different forms. Figure 1.28 exhibits the cross-sectional view of this machine in two

states of magnetization. First, the magnets are exposed to a magnetization procedure in the same direction. Then, the stator windings are reconnected into a different pole configuration, forcing the magnetization of the rotor to fit in. The change of the rotor structure is required to ensure the equal pole number principle between the stator and rotor. This principle also explored in squirrel-cage induction machines, is described by the author as necessary for ensuring an average electromagnetic torque over the whole air gap periphery different from zero. In [19], more designs belonging to this class of VFMM are presented.

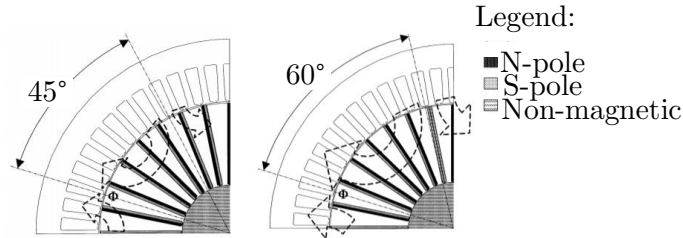


Figure 1.28: Cross-sectional view of an eight-pole magnetized(left) and six-pole magnetized(right) pole-changing memory motor [22].

The complexity involved in manufacturing pole-changing machines and their dependence on having multiple poles can justify their rare use. Most parts of AC-magnetized VFMMs are designed with a fixed number of poles and can be classified as single and hybrid types.

Single-type VFMMs ([19, 24, 27, 23, 40]) use only LCF magnets to produce the magnetic flux through the air gap. Hybrid topologies ([17, 19, 12, 33, 46, 38]) have their air gap flux generated by a combination between HCF and LCF magnets, disposed in order to ensure that fluxes of these both magnets contributes in series, parallel or in a mixed configuration to each other.

The first model of VFMM introduced in [23] illustrated by Figure [1.29] can be used as an example of a single-type VFMM. Composed of tangentially magnetized Al-Ni-Co magnets, the rotor in this machine is designed as a sandwich of magnets, soft iron, and nonmagnetic material. The geometry is defined to guarantee the controllability of the magnetization level of the magnet from the injection of short-duration armature currents in the magnetization axis (d-axis). As the flux created by the q-axis currents does not cross the magnets the magnetization state initially set from d-axis current pulses is not modified.

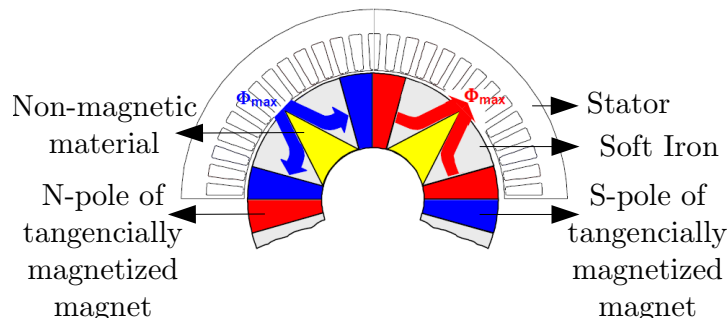


Figure 1.29: First Variable Flux Machine presented in the literature - Cross-sectional view in a full magnetized condition [23].

As overviewed by [19], several authors as [32], [37], and [89] investigate the benefits of

combining the features of a flux intensified (FI) synchronous machine, for which the d-axis inductance is higher than the q-axis one ($L_d > L_q$) and the variable flux property as strategy. Three main interests justify the use of this machine geometry: first, a positive reluctance torque and the unintentional demagnetization effect caused by the armature reaction can be avoided when $L_d > L_q$, which is especially challenging for classical machines designed with $L_d < L_q$ [37, 89]; second, a sufficient power conversion capability is achieved by using LCF magnets with a remanence equivalent to the ones of HCF magnets; and third, a large torque-speed envelope is achieved with reduced losses. As an example, authors in [27] introduce the six-pole Al-Ni-Co-based single-type VFMM presented in Figure 1.30. A set of analytical equations are presented for properly designing the magnet. Simulations via Finite Element Analysis are used for optimizing multiple parameters of the stator and rotor geometry, including the design of q-axis barriers in order to ensure that inductances respect the premise $L_d > L_q$. The same geometry is studied in [24], now focusing on optimizations related to the dimension magnet geometry for achieving improvements in machine performance. Authors suggest that the definition of the magnet width requires an analysis of a trade-off between the magnetization current and the no-load operating point of the magnet, and of the magnet length, the study of a trade-off between the machine torque and the operating point achieved by the magnet in presence of a q-axis field. It should be mentioned that the discussed results cannot be directly applied in other geometries, but the study highlights the methodology that can be used to improve other machine designs.

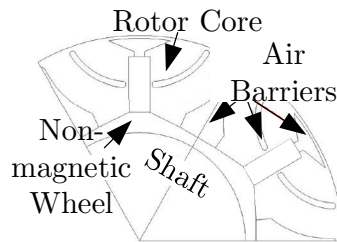


Figure 1.30: Single-type Al-Ni-Co-based Variable Flux Machine - Adapted from [24].

Hybrid topologies ([17, 19, 12, 33, 46, 38]) have their air gap flux generated by a combination of HCF and LCF magnets. As exposed by [12] and [33], these topologies are proposed to boost the torque density of VFMMs, as their design is defined considering a constant magnetic flux source (a HCF magnet, e.g.) combined with a variable one (a LCF magnet), that can be enhanced or weakened according to the d-axis current pulses supplying the machine. The link of both magnetic fluxes depends on the placement of the magnet in the machine geometry proposed. When the same flux through the LCF and the HCF magnets cross also the air gap, the hybrid VFMMs are classified as series-type. By the same reasoning, parallel-type machines have their air gap flux composed of the sum of the HCF and LCF magnets.

Hybrid topologies are not the focus of this research, but some characteristics of these geometries can be highlighted. For series-type machines, the load line $I_{mag} = 0$ is displaced to the right. Hence, its intersection with the hysteresis loop occurs in a more stable region, located in the linear portion of the demagnetization curve (See the figure 1.4 for better representation). As mentioned by [12], this characteristic helps to avoid the armature reaction and consequently the necessity of the flux barriers, which makes simpler the design of single-type VFMMs. In the case of parallel geometries, the load line $I_{mag} = 0$ is shifted to the left. The working points are consequently more unstable in these designs, especially during the demagnetization, which requires lower negative d-axis currents than the one demanded by a series-type geometry. In ideal operating conditions, fluxes of both magnets in parallel designs should be independent of

each other. However, if the level of magnetization of LCF magnets is too low, the magnetic flux and a short circuit of HCF magnetic flux via the LCF magnets branch can be observed. The consequence of this phenomenon is a potential demagnetization of the LCF magnets [12, 33]. Barriers of flux are mentioned in [33] as a strategy for preventing this effect, but no developments concerning their geometry are presented by the authors. Recently, new layouts have been presented in the literature ([38] and [46]) aiming to explore the benefits of both parallel and series geometries. These machines are composed of a dual-layer PM configuration and are characterized by a wide range of flux adjustments by the parallel-type portion and resistance to demagnetization under load thanks to the series-types portion.

1.4 Conclusion of Chapter 1

This first chapter was dedicated to presenting the State of the Art for positioning the Variable Flux Memory Machine investigated in this thesis research in relation to the electrical machines used for transportation electrification applications. As discussed, Permanent Magnetic Synchronous Machines have been for years considered the most attractive for traction drives used in electrical vehicles (EVs). Nevertheless, the long-term use of the rare-earth magnets producing the flux in these machines has been increasingly questioned. First, because of the economic control established by the major producer countries (e.g., China), which regulates the supply chain and, as a consequence, the price of these materials (which exposes the risks of the availability of the magnetic materials on a large scale). Second, due to environmental challenges related to the extraction, refinement, and recycling of these magnets, which are associated not only with high requirements of energy and water and high levels of air/soil pollution but also with a relatively low rate of recycling, hampered by the complexity of the magnets reuse and their long life cycle, incompatible with the growing demand.

In the pursuit of developing more sustainable electromotive systems, Variable Flux Memory Machines have been investigated as an option based on the use of low coercive force magnets for producing the magnetic flux. As discussed, a flux variation can be achieved in these machines by the injection of short-time current pulses, which allows operations in a wider torque-speed range while reducing or avoiding the use of rare-earth permanent magnets. The magnet options explored in the literature for these applications are multiple. High coercive force magnets such as Ferrites can be advantageous in terms of price, but their magnetic hysteresis profile with a knee close to the H-axis can make the regulation of their magnetization state difficult for applications in VFMMs. Low force magnets characterized by their narrow BH-loops and levels of remanence comparable to those of rare-earth materials, are considered more adapted to the realization of these machines. Nevertheless, their use in the literature is usually limited to Al-Ni-Co magnets, being Fe-Cr-Co up until now rarely explored. Indeed, a lack of information about these last mentioned alloys, their properties, and hysteresis curves was noticed despite their advantages when compared to the preferred Al-Ni-Co magnets: better mechanical/corrosion resistance, contributing to low-cost shaping possibilities, and a lower content of Cobalt, which is expected to impact positively on their price. In this context, this thesis research proposes as an object of study an AC-magnetized Fe-Cr-Co-based VFMM for which the standstill and running magnetization and the torque control will be explored in the next chapters.

Chapter 2

Standstill Magnetization Strategy of a Fe-Cr-Co-based Variable Flux Memory Machine

2.1 Introduction

In the State of Art introduced in Chapter 1 the most important concepts concerning Variable Flux Memory Machines were presented. In this chapter, the magnetic behavior of an AC-magnetized single-pole pair VFMM is investigated. A proof of concept is proposed from a PMSM, by replacing the Nd-Fe-B-based rotor with a cylindrical massive Fe-Cr-Co-based rotor (the stator geometry is conserved). This geometry is chosen to allow an easy adaptation to different stator designs as well as a lower fragility in case of high-speed operations.

The magnetic and analytical characterization of the Fe-Cr-Co of grade 36/5 itself and when inserted in a magnetic circuit (the machine) are discussed. Due to the anisotropy exhibited by this alloy, a hysteresis behavior dependent on the magnetization axis is observed. Hence, two studies were demonstrated to be required: a first one, based on an initially manufactured rotor, in which the flux crosses the magnet in the hard magnetization axis, and a second one, in which a second magnetic rotor was proposed for ensuring a the flux passing through the easy magnetization axis. Whereas the major BH-loop characterizing this second-mentioned magnet is similar to the ones observed for low-coercive force magnets commonly used for producing the magnetic flux in VFMMs, the one characterizing the first magnet is distinguished by an absence of a well-defined knee in the second quadrant, as going to be discussed throughout this chapter.

A standstill magnetization methodology is described for analyzing the variation of the magnetization state of the Fe-Cr-Co magnet inserted in a magnetic circuit (in this case, the machine environment). For generating a field in the magnetization axis (usually, the d-axis), current pulses obtained via an inverter in DC/DC mode are used. The experimental results achieved in these studies are presented, discussed, and finally used as a reference for developing a methodology aiming to define the magnetic behavior of the Fe-Cr-Co in both easy and hard magnetization axes in the case of partial magnetizations. Simulations via Finite Element Analysis are also considered for these studies. The internal hysteresis loops obtained are then compared to the intrinsic ones achieved via an ideal equipment of measurement, a HysteresisGraph, to evaluate the effects of the nonlinearities (e.g. stator saturation and design) in this magnetic behavior described by the Fe-Cr-Co. The differences observed are evaluated and a strategy for the compensation of the effects resulting especially from the stator saturation and design is developed and investigated.

2.2 Presentation of the system analyzed

The object of study of this research is a non-salient single-pole pair machine designed by IFP Energies nouvelles. The stator, initially proposed for the PMSM described in [112], is composed of standard COGENT NO20 electrical steel forming 12 teeth connected by closed slot wedges. The armature windings are exclusively positioned on the outer diameter of the slots to evacuate the heat via an axial airflow without requiring a water cooling system. A massive cylindrical Fe-Cr-Co-based rotor allowing regimes up to $200krpm$ is designed to replace the Nd-Fe-B magnet used in the PMSM design. Figure 2.1 exhibits the e-turbo prototype including the VFMM described. No dedicated winding is defined for regulating the magnetization state of the Fe-Cr-Co-based rotor, which classifies this machine as a single-type AC-magnetized VFMM according to the characterization presented in the section 1.3.7

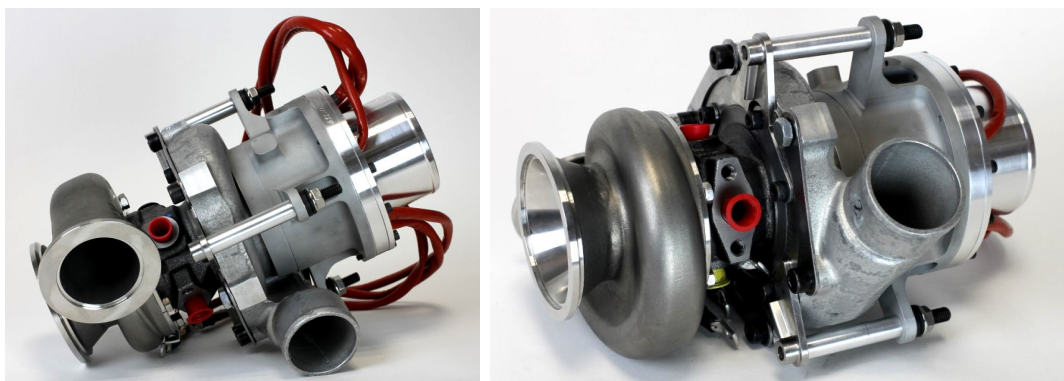
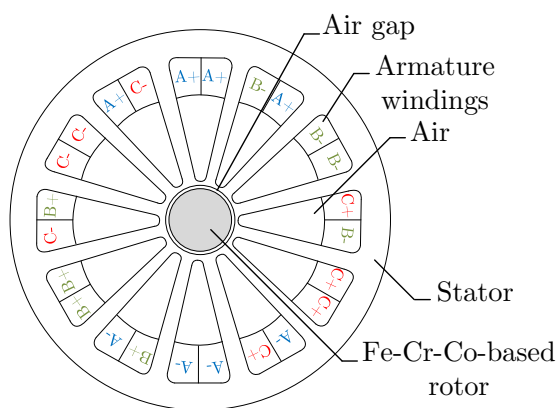


Figure 2.1: E-turbo system prototype including Variable Flux Memory Machine.

The distribution of the phases in the slots is presented in Figure 2.2a. The design specifications of the machine are introduced in Table 2.2. In Figure 2.3, the magnetic characterization of steel composing the stator is exhibited.



(a) Cross-sectional view

Description	Symbol	Value
Total number of slots	-	12
Air gap thickness [mm]	t_g	0.5
Fe-Cr-Co magnet height [mm]	h_m	18.1
Fe-Cr-Co magnet diameter [mm]	l_m	17
Number of spires per phase	N	1
Number of pole pairs	p	1
Number of slots per pole and per phase	q	4

(b) Specifications

Figure 2.2: Design of the Variable Flux Memory Machine.

Remark: Because $p = 1$, the electrical (ω) and mechanical (ω_m) speeds, in in [rad/s], are equal (as $\omega = p\omega_m$). The term Ω is going to be used for defining this mechanical speed in rpm.

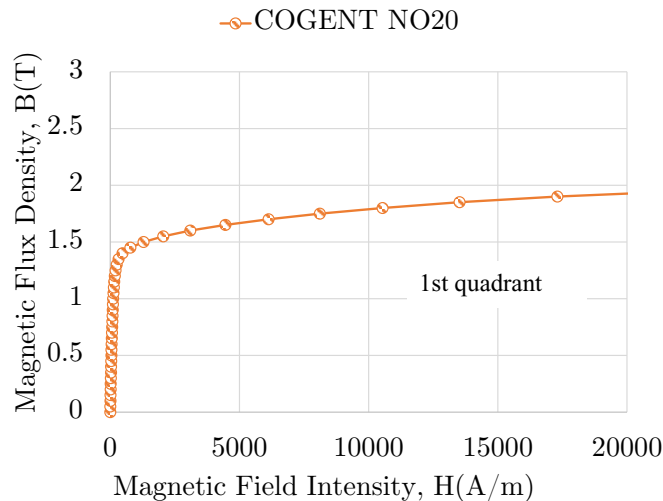


Figure 2.3: Magnetic characteristic of the electric steel COGENT NO20 composing the stator.

2.2.1 The power electronics system

Concepts discussed in the section [1.3.1](#) elucidated that the variation of the magnetization state of a LCF magnet inserted in a VFMM is achieved by supplying the machine with currents that create a field in the d-axis. Either for the magnetization process realized at standstill or running operating condition, these currents are controlled via a power electronic drive. Overall, the objective of a power electronic drive is the interconnection of different voltage sources to different loads, adapting the ratio voltage/current according to the system requirements, being often limited in terms of cost, volume, and weight [\[13\]](#). For the application considered in this research, a DC/AC inverter developed at IFP Energies nouvelles is used to control the AC electrical machine according to a DC voltage source. To allow the magnetization of the machine, the topology software is adapted to propose a DC/DC magnetization mode without requiring supplementary components and with no neutral access.

Figure [2.4](#) illustrates the proposed power electronics architecture. The complete system consists of a (1) DC voltage source, a (2) capacitive filter bus, (3) six switches (in this case, MOSFETs) arranged in three branches of two switches each, and (4) the electrical machine (in this case, the VFMM), whose the (5) three-phase stator windings are star-connected with no neutral access. In the magnetization mode, a (6) pulse-width modulation (PWM) is used as a switching strategy for generating the command signal used for controlling the MOSFETs (signal S_A controls the MOSFET of phase A in the Figure [2.4](#)) considering a classic Field-Oriented Control algorithm (see [1.3.5](#)). The magnetization mode (or DC/DC mode) is set via software as formerly mentioned and uses the stator windings as the inductor for regulating the magnetization current level similar to a buck converter. Therefore, the magnetization current I_{mag} is regulated by controlling one of the inverter's branches (for instance, the one of phase A) while the low-side components of one of the other phases are forced turned on. Assuming d being the duty cycle of the first inverter's branch switches, the Proportional-Integral (PI) controller can be designed according to the state equation of I_{mag} defined by:

$$2L \frac{d}{dt} I_{mag} = -2R I_{mag} + V_{DC} d \quad (2.1)$$

This later equation leads to the following transfer function between I_{mag} and d according to the

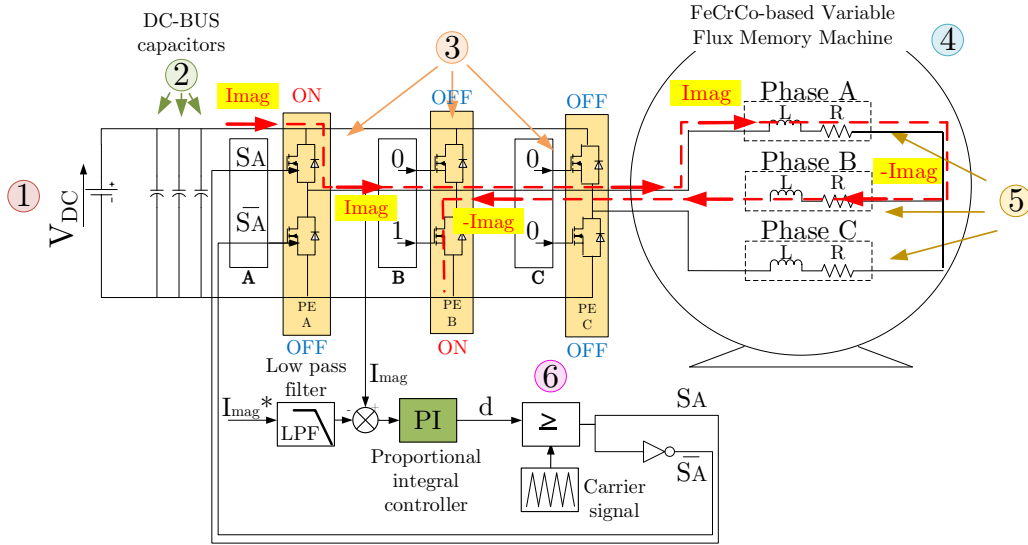


Figure 2.4: Presentation of the power electronics architecture proposed for supplying the armature windings during the experimental tests.

Laplace variable s for small variation around the operating point:

$$G(s) = \frac{I_{mag}}{d} = \frac{V_{DC}}{2R} \frac{1}{1 + \frac{L}{R}s} \quad (2.2)$$

Assuming a Proportional-Integral controller transfer function as $H(s) = K \frac{(1+\tau s)}{\tau s}$, with K being the proportional constant and $\frac{K}{\tau}$ the integral constant, the open loop transfer function (OLTF) can be defined by a compensation poles method and considering a the time constant $\tau = \frac{L}{R}$ as below:

$$OLTF = G(s)H(s) = \frac{V_{DC}}{2R} \frac{1}{1 + \frac{L}{R}s} K \frac{(1 + \tau s)}{\tau s} = K \frac{1}{\tau s} \frac{V_{DC}}{2R} \quad (2.3)$$

The closed-loop transfer (CLTF) function can be obtained from the equation 2.3 by:

$$CLTF = \frac{K \frac{1}{\tau s} \frac{V_{DC}}{2R}}{1 + K \frac{1}{\tau s} \frac{V_{DC}}{2R}} = K \frac{V_{DC}}{2R} \frac{1}{\tau s + K \frac{V_{DC}}{2R}} = \frac{1}{1 + (\frac{2R}{KV_{DC}})\tau s} = \frac{1}{1 + \tau' s} \quad (2.4)$$

The transfer function obtained in the equation 2.4 indicates a first-order system characterized by a time constant $\tau' = \frac{2R\tau}{KV_{DC}}$. Considering the time required for the transient state to reach 95% of the set point value given by settling time $t_{5\%} = 5\tau'$, the proportional parameter K can be calculated from the DC gain by:

$$K = \frac{5\tau}{t_{5\%} \frac{V_{DC}}{2R}} \quad (2.5)$$

For a settling time of $1ms$, with $V_{DC} = 48V$, $L = 5\mu H$, and $R = 5m\Omega$, results in $\tau = 0.001$ and $K = 0.001$.

As mentioned before, the direction and amplitude of the resultant magnetic field varies according to the controlled current I_{mag} flowing through the armature windings. Considering, for example, that in the schema formerly exhibited in Figure 2.4 the current I_{mag} is controlled

by the up-side switch of phase A, generating a magnetic field NI_A , where N is the number of spires per phase. If only the low-side switch of phase B is turned on (representing case I of the study), the three-phase current pattern is defined as $I_A = I_{mag}$, $I_B = -I_{mag}$ and $I_C = 0A$. Figure 2.5a exhibits the ampere-turns generated by these mentioned currents per phase (NI_A for phase A and NI_B for phase B, where $I_A = -I_B = I_{mag}$) and the resultant magnetic field ($NI_{res} = \sqrt{3}NI_A = \sqrt{3}NI_{mag}$). If, however, both low-side switches of phases B and C are turned ON (Case II), a three-phase current pattern $I_A = I_{mag}$, $I_B = -I_{mag}/2$, $I_C = -I_{mag}/2$ defines the ampere-turns of phases A, B and C, respectively as NI_A , $(-1/2)NI_B$ and $(-1/2)NI_C$. The Figure 2.5b exhibits this magnetic fields and the result one ($NI_{res} = (3/2)NI_A = (3/2)NI_{mag}$). Therefore, comparing both cases, it can be observed that Case I is expected to generate 15% stronger resultant ampere-turn than the one obtained by Case II. Especially for magnets characterized by a low remanence, the choice for a current pattern that produces a stronger field can be important. A magnet such as the Fe-Cr-Co in the hard magnetization direction is one example of a magnet for which this consideration is important, as later sections will discuss.

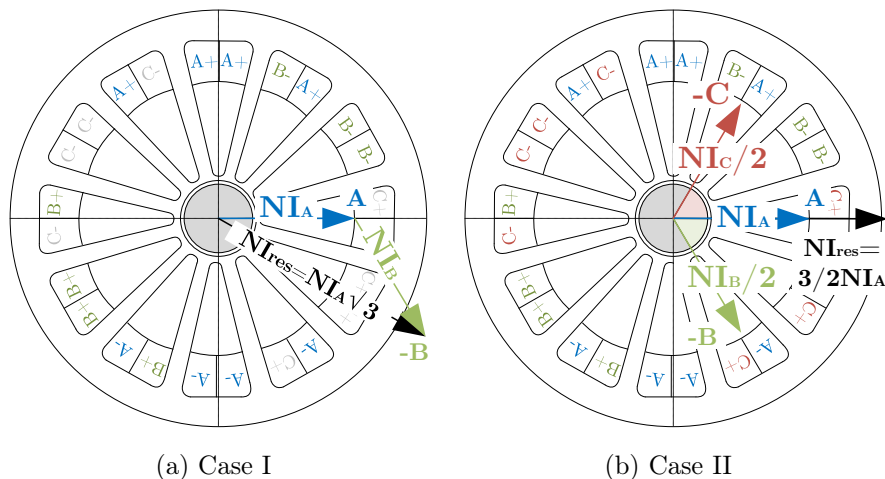


Figure 2.5: Resultant flux crossing the machine according to different three-phase current patterns.

2.3 Initial study concerning the magnetic behavior of the Fe-Cr-Co magnet: analysis of the hard magnetization direction

As formerly introduced, a Fe-Cr-Co-based magnet of grade 36/5 is manufactured for composing the rotor in the VFMM studied in this research. The analyses of the proprieties of this magnetic material, as also of other alloys, can be realized from different methodologies, as described in the literature by authors [51, 114, 115]. A HysteresisGraph (also known as Hystograph) is the one used in this thesis research. In essence, a HysteresisGraph is a complete setup used for measuring and recording hysteresis loops of soft and hard magnets [51, 116]. It corresponds to an equipment classified as a closed magnetic circuit as all the flux lines crossing the magnetic specimen analyzed also pass through the equipment core due to its high permeability, which limits the possible leakage flux. From this setup, the intrinsic proprieties (as the remanence, coercivity H_{cB} or H_{cJ} , the maximum energy product, and others) are measured with minimal influence of the medium in which the magnet is inserted. Effects such as the ones causing the internal demagnetizing field H_d [114], for example, are negligible in this type of equipment.

The setup is composed of a vertical electromagnet dedicated to varying the magnetization

level of the specimen analyzed, a set of measuring coils, and fluxmeters to integrate the voltages induced in the coils [117, 118]. The measuring principle of a HysteresisGraph, overviewed in [51, 114, 116, 118, 119], is based on the placement of the specimen to be analyzed in a controlled magnetic environment. The intensity of \vec{H} is slowly changed (to avoid Eddy currents effects [51]) and recorded simultaneously with the response obtained by \vec{B} . The poles composing the electromagnet form two faces of equal magnetic potential for a homogeneous magnetization of the specimen. As \vec{B} exists only inside the magnet, it cannot be directly measured. Instead, a fluxmeter coil placed around the sample or in one of its faces can be used for achieving this measure. This described fluxmeter consists of an integrating voltmeter that estimates \vec{B} from the equation $u(t) = -NA \times d\vec{B}/dt$, where $u(t)$ is the induced voltage, A is the cross-sectional area of the sample and N is the number of turns composing the mentioned fluxmeter. The accuracy achieved by this method is directly related to the uniformity of \vec{H} within the gap, being greatest when the measurements are made as close as possible to the specimen.

For characterizing the magnets studied in this present thesis work, a HysteresisGraph HG 200 (datasheet available in [120]) acquired from the supplier Brockhaus Group is used. The machine is certified according to International Standard IEC 60404-5. Figure 2.6 presents the test bench installed at IFP Energies nouvelles. The specifications of this measuring equipment can be consulted in Appendix B.1. A PC is used for data acquisition. A bar-shaped sample of FeCrCo36/5 of dimensions 24.9mm x 15.9mm x 4.1mm (length x width x height) is used as a specimen for the intrinsic magnetic characterization. Figure 2.7 presents this specimen, as well as the cylinder of 17mm x 18.1mm (diameter x height) composed of this same material of the rotor of the VFMM studied. The easy and hard magnetization directions of this specific magnet sample are also identified. In-depth discussions about these axes are going to be discussed in the next sections.

Remark: Figure 2.7 exhibits the first rotor designed for the VFMM investigated in this thesis. The magnetization axes indicated in this Figure 2.7 represent therefore the ones identified by using the HysteresisGraph for this first manufactured rotor. As later studies will introduce, a second rotor of the same dimensions was manufactured for being crossed by the flux in the easy magnetization direction. In this case, the easy and hard magnetization directions are, therefore inverted when compared to the ones in Figure 2.7.

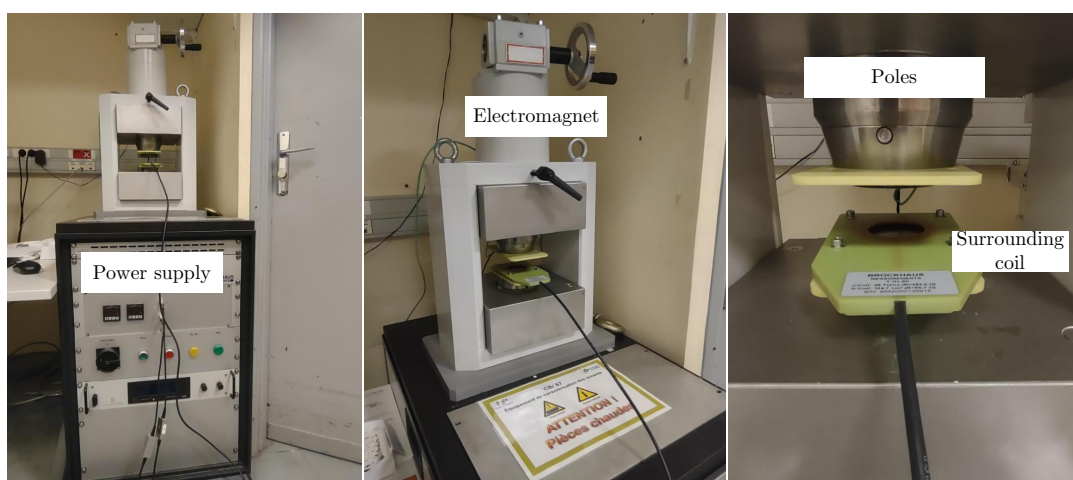


Figure 2.6: Hystograph HG 200 - Test bench for magnet characterization at IFP Energies nouvelles.

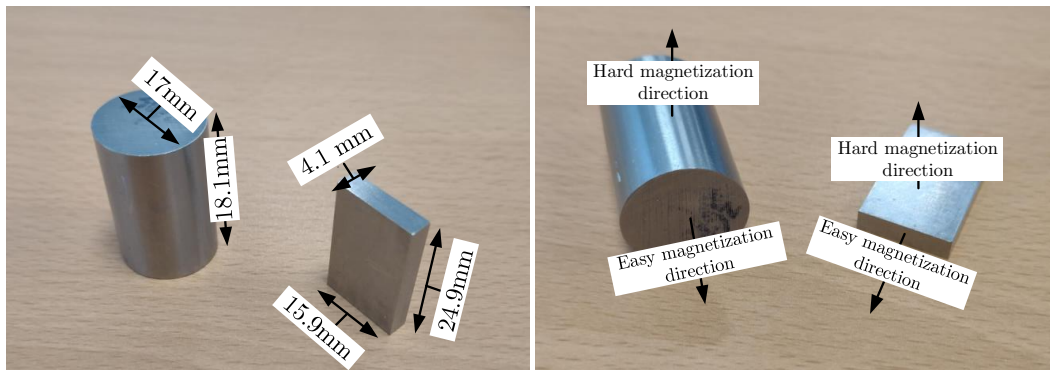


Figure 2.7: Magnet specimen used for characterizing the material in the Hystograph HG 200.

The hysteresis loop obtained from the characterization of the magnet sample presented in Figure 2.7 is exhibited in Figure 2.8a. A remanence $B_r = 0.45T$ and a coercivity $H_c = -24.4kA/m$ can be identified. These data will be incorporated into a Finite Element Analysis software for exploring the magnet behavior when inserted into VFMM studied in this thesis research.

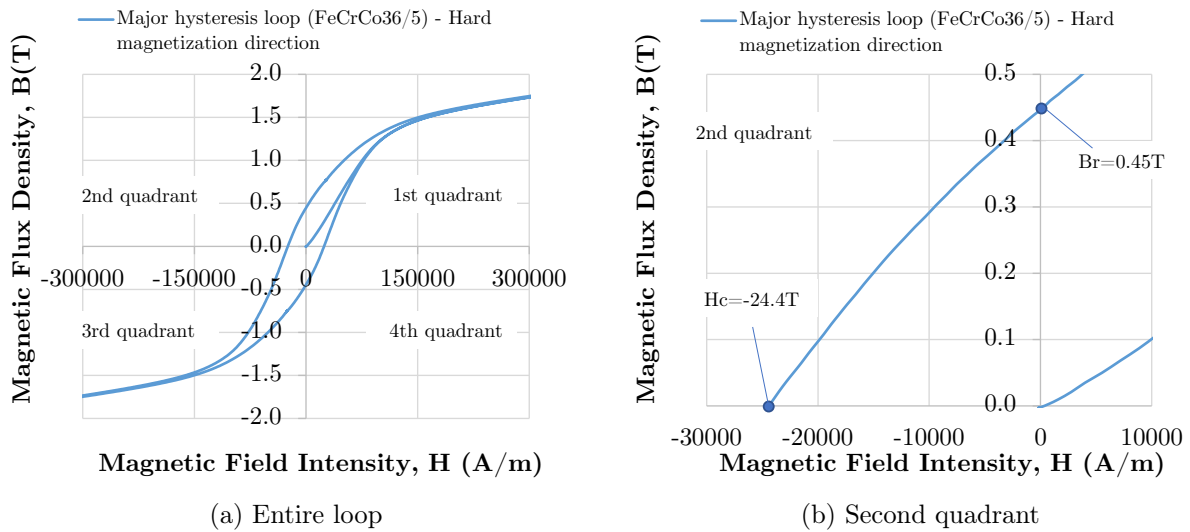


Figure 2.8: External hysteresis loop of the FeCrCo36/5 magnetized in the hard magnetization direction obtained using the HysteresisGraph HG 200.

In Appendix B.2 the major hysteresis loop obtained by characterizing the FeCrCo36/5 in each one of its three magnetization directions is exhibited. The anisotropy of this grade of magnet mentioned in the section 1.2.2.1 (see Table 1.6) is verified by these results. Indeed, the magnetic material properties are directional-dependent. In an easy magnetization direction, it is observed that a well-defined knee in the second quadrant and a level of remanence comparable to the one of a rare-earth magnet. As previously mentioned, this magnetic profile is similar to the one usually presented in the literature on the Al-Ni-Co magnets composing VFMMs. However, which concerns the two other magnetization directions, this knee is not observed in the hysteresis curve anymore and the level of remanence is reduced. Especially because the current literature regarding VFMM only investigates LCF magnets characterized by a well-defined knee

on the second quadrant of the hysteresis curve, this thesis work proposes to explore the VFMM designed with a magnet for which the BH-loop does not present this mentioned knee. As going to be later explored, this particularity changes the model used for characterizing the variation of the magnetization state of the LCF magnet.

Some other important observations regarding the magnet proprieties identified using the HysteresisGraph can be highlighted:

- The coercivity identified in the hysteresis loop of the FeCrCo36/5 in the hard magnetization direction allows its classification as a low coercive force (LCF) magnet. Indeed, an $H_c = -24.4kA/m$ corresponds to about 1,5% of the H_c typically characterizing the commercial available Nd-Fe-B (for which $H_c = 1500kA/m$ [121]). A similar conclusion is noticed for the FeCrCo36/5 in the easy magnetization direction, as results will later demonstrate.
- The low level of remanence ($B_r = 0.45T$) when compared also to one of commercially available Nd-Fe-B magnets ($B_r = 1.52T$) makes the FeCrCo36/5 when magnetized in hard magnetization direction not optimal for producing torque. The interest in this magnet can be, however, justified by the observation that this observed absence of a knee in the second quadrant of the BH-loop is also a characteristic of other magnet grades potentially interesting for VFMM applications. This is the case of the FeCrCo12/4 in both hard and easy magnetization direction, as presented by results in Appendix B.3. In the literature, alloys exhibiting this described magnetic profile are not explored until the moment.

Therefore, this section will be focused on better investigating the magnetic behavior of magnet manufactured for being crossed in the hard magnetization direction in the machine environment (magnetic circuit). The major objective is to explore a VFMM in which the magnetic field is generated by a magnet of a highly nonlinear hysteresis profile, which approximates the magnetic behavior to the one typically observed for electrical steels. Later in this Chapter 2, a complementary study is going to be proposed by the analysis of the same grade of magnet now manufactured to ensure a flux path in the easy magnetization direction. Thereby, a comparison can be established between the VFMM proposed and the ones usually explored in the literature (as mentioned, composed of Al-Ni-Co magnets).

2.3.1 Analytical calculation of the magnet working point

The mathematical model established for analyzing the VFMM proposed in this thesis is based on the conclusions obtained in Chapter 1 (section 1.3.4). Using the simplifying assumption of a linear hysteresis loop behavior for characterizing the magnet in the second quadrant, the hysteresis curve in this region can be mathematically described by a linear function of form $B(H) = (PC)H + B_r$ (see section 1.3.4.1). Considering the intersection of each load line and this mentioned linear function, it can be defined as:

$$B_m = \frac{(A_g l_m B_r + \mu_0 \mu_r A_g (pqN I_{mag}))}{(A_g l_m + \mu_r l_g A_m)} \quad (2.6)$$

The parameters characterizing the machine are illustrated in Figure 2.9. Details of the rotor shaft are not represented and do not interfere with the magnetization.

Due to the cylindrical geometry of the rotor of the machine proposed and the parallel profile of the magnet flux lines (identified via Finite Element Analysis), the average magnetic path taken is different by each infinitesimal portion of the magnet crossed by the flux lines (the magnet length l_m is not the same for each portion magnetized). In this context, three simplifying assumptions are preliminarily considered for these studies:

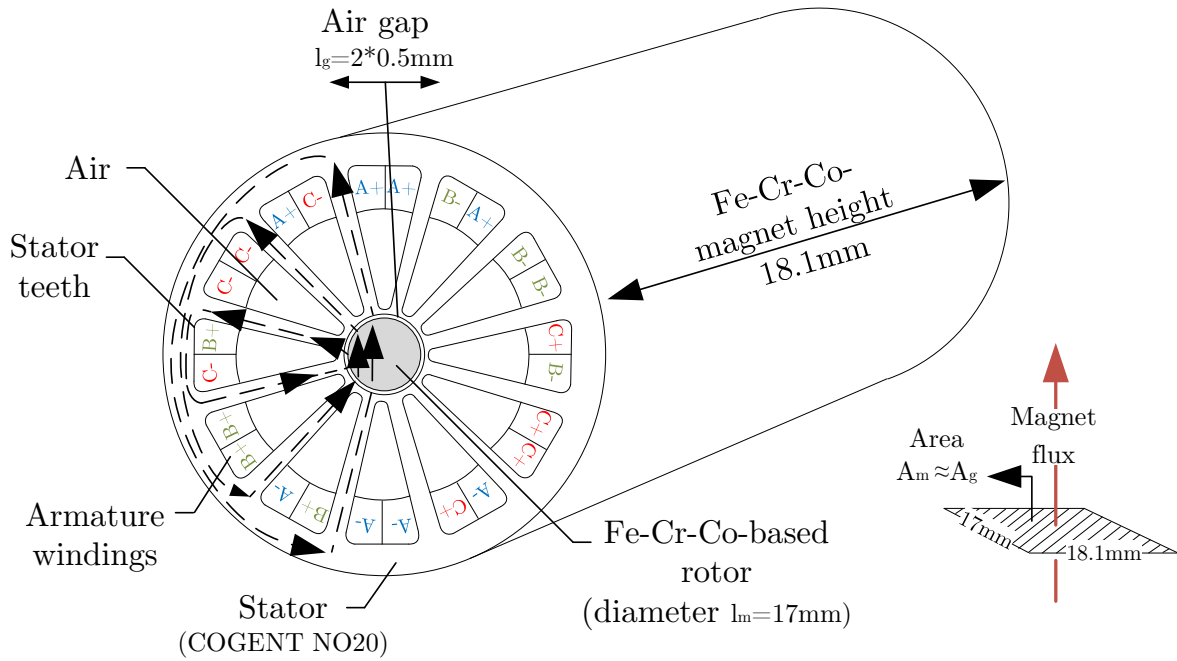


Figure 2.9: Identification of parameters for calculating the magnetic flux density characterizing each working point (rotor shaft not represented).

- Ideally, infinitesimal portions of the magnet should be individually considered for precisely calculating the working point. For simplicity, an assumption of six major portions of homogeneous magnetization is set for the study proposed in this chapter. These regions, defined according to the stator teeth distribution, are presented in Appendix B.4 and will be used as a reference for defining mathematically the magnetic behavior of the machine.
- As presented in this same Appendix B.4, the magnetic flux density is uniform in the majority of the magnet. However, effects of non-uniformity are especially observed in the regions closer to the teeth. Although for equations used for calculating the working points, this effect is ignored, for the investigations realized via Finite Element Analysis software, in which the integral of \vec{B} over the rotor is used for estimating the level of magnet magnetic flux density, these non-uniformity effects are taken into account. For this reason, some differences between the results obtained via equation 2.6 and the ones achieved in the simulations are expected.
- It can be also observed that due to the cylindrical shape proposed for the rotor, the extremities of the magnet (regions with the lower magnet length crossed by the flux lines) are encircled by low ampere-turns. Hence, these portions of the Fe-Cr-Co are expected to be poorly magnetized and will induce very low back-EMF while the machine is running.

Figure 2.10a illustrates three of the regions defined in the rotor for the study proposed. As formerly discussed, they are defined according to the stator teeth design, which guides the flux lines path in the stator (high permeability of the material). All flux lines crossing the same region are assumed to take a similar path in the stator core. This assumption is important for limiting the regions to specify the magnet length in each case. By symmetry, the ones crossed by the flux on the right side of the machine are similar, as exhibited in the zoom of the rotor proposed in Figure 2.10b.

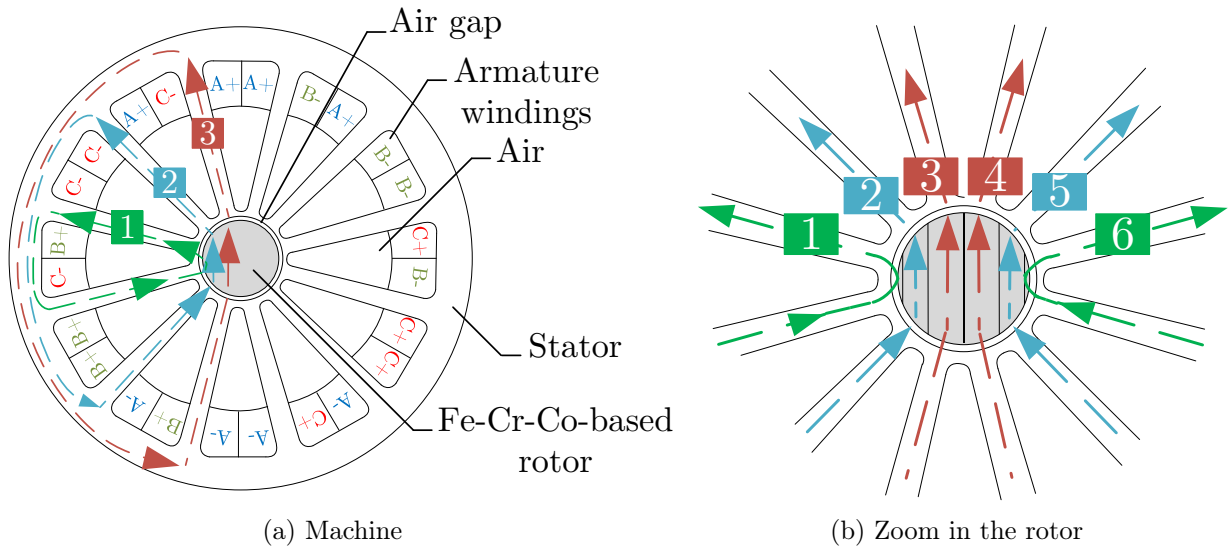


Figure 2.10: Illustration of the path traced by the flux lines through the rotor.

As mentioned, the magnetic flux density is considered constant in each defined region (B_{m_i} , for $1 \leq i \leq 6$) and calculated using the equation 2.6. The ampère-turns encircled by the magnetic flux lines tracing each path, considering that the single stator winding of each phase ($N = 1$) is divided by 4 slots, is given by the $pqNI_{mag}$ (in [A]), where q is the number of slots per pole and per phase and of p , the number of pole pairs. The magnet and the air gap areas (A_m and A_g) are considered equal for simplifying the equation, due to the low air gap thickness ($t_g = 0.5mm$, as presented in Table 2.2). The air gap is crossed twice for each flux line (top and bottom portion of the magnet) and, for this reason, the air gap length l_g is double the air gap thickness ($l_g = 2t_g$). To define the magnet length (l_m), an average path taken through the center of each region is utilized. This enables the calculation of the magnetic flux density for each of these regions using the equation 2.6 above presented. A hypothesis is set for calculating the total magnetic flux density B_m used for defining the working point placement in the hysteresis loop by the average B_m obtained in the six regions illustrated in Figure 2.10b. Therefore, B_m is calculated by:

$$B_m = \sum_{i=1}^6 \frac{B_{m_i}}{i} \quad (2.7)$$

Aiming to define the intersection between the external hysteresis loop on the second quadrant and the load line for $I_{mag} = 0A$, the hysteresis loop is first assumed linear. The slope of this curve (or the permeability, μ) can be calculated according to the equation 2.8, knowing that $\mu = \mu_0\mu_r$, where μ_0 is the permeability of the free space and μ_r the relative permeability. Using the design specifications presented in the Table 2.2, it can be obtained a $\mu_r = 14.65$:

$$\mu_r = \frac{\Delta B}{\mu_0 \Delta H} = \frac{-B_r}{\mu_0 H_c} = 14.65 \quad (2.8)$$

Considering each one of the regions 1 to 6 delimited according in Figure 2.10b, the magnet length calculated in the mean path traced by the flux lines as, respectively, $l_{m1} = l_{m6} = 4.2mm$, $l_{m2} = l_{m5} = 11.7mm$ and $l_{m3} = l_{m4} = 16mm$. Concerning the air gap, it should be noticed that this region is crossed twice by the flux lines, between the superior and inferior portions between the rotor and the stator. Thus, $l_g = 2 * t_g = 1mm$, because the air gap thickness $t_g = 0.5mm$ as specified in the Table 2.2. By the equation 2.6, the magnetic flux density calculated in

each region is $B_{m1} = B_{m6} = 0.1T$, $B_{m2} = B_{m5} = 0.2T$ and $B_{m3} = B_{m4} = 0.24T$ when $I_{mag} = 0A$. Therefore, an average level of induction of $B_m = 0.18T$ is defined at the intersection of the load line $I_{mag} = 0A$ and the external hysteresis loop considering all these regions. Using these same equations, the level of current required for total demagnetization of the magnet can be calculated (here considered for an average magnetic flux density measured in the magnet $B_m < 0.05T$). The six regions above presented are again used for this study. By the equation 2.6, for a relative permeability $\mu_r = 14.65$, $N = 1$, $p = 1$ and $q = 4$, the demagnetization current calculated for a $B_m < 0.05T$ in each one of these regions is of $I_{demag1} = I_{demag6} = -13.42A$ for regions 1 and 6 are respectively, $I_{demag2} = I_{demag5} = -54.16A$ for regions 2 and 5 and $I_{demag3} = I_{demag4} = -77.52A$, for regions 3 and 4. As expected, the magnet portions of lower length are demagnetized with higher amplitudes of currents. These results provide a mean current amplitude of $I_{demag} = -48.4A$ for demagnetizing the magnet. These results provide an order of magnitude expected currents and a reference for the studies realized via simulation using Finite Element Analysis.

2.3.2 Study of the magnetic behavior of the FeCrCo36/5 in the hard magnetization direction via simulations

The machine geometry exhibited in Figure 2.2a and magnetic characterization presented in Figures 2.3 and 2.8a are incorporated in the FEA (Finite Element Analysis) software for a 2D analysis of the magnetic behavior of the proposed VFMM. A magnetization current (I_{mag}) is used to supply the machine by the armature windings for generating a field in the magnetization direction (d-axis). The current pattern $I_A = I_{mag}$, $I_B = -I_{mag}$, $I_C = 0A$ is used for ensuring a higher magnetic field produced during the simulations.

First, a study is proposed for placing the working points at the initial magnetization curve of the Fe-Cr-Co, according to different amplitudes of magnetization current injected in the armature windings. The Figure 2.11a exhibits the achieved results. When I_{mag} increases from 100A to 1500A, the magnetic field \vec{H} in the Fe-Cr-Co-based rotor does not increase proportionally. The reason is the saturation of the stator teeth, which absorb a part of the ampère-turns generated by injection of I_{mag} in the stator windings. In the Appendix B.5, the level of magnetic flux density (B_{exc} , in [T]) and the magnetic field intensity (H_{exc} , in [A/m]) characterizing each of these working point achieved during the excitation of the magnet is presented.

Second, the demagnetization portion of the BH-loop presented in Figure 2.8a is incorporated in the simulations for studying the behavior of the load lines which intersection with the hysteresis loop defines the working points at each operating condition. As previously introduced in the section 1.3.4, the slope of the load line depends on the machine geometry. Because that remains unchanged, all the obtained recoil lines will be characterized by the same slope as the one at $I_{mag} = 0A$. Simulations considering different amplitudes of magnetization currents are carried out, shifting the working point initially obtained at $I_{mag} = 0A$ is shifted to the right or the left, if positive or negative d-axis currents are, respectively, used for supplying the machine. The Appendix B.5 describes the procedure used for defining each load line exhibited in Figure 2.11b. From these studies, some conclusions can be achieved:

- The excitation field (H_{exc} , in [A/m]) for saturating the magnet is around $H_{exc} = 95kA/m$ and is achieved when $I_{mag} = 1500A$ (which defines a magnet flux density $B_m > 1.30T$).
- For excitation fields obtained for magnetization currents approximately up to $I_{mag} = 100A$ ($H_{exc} = 29.9kA/m$, $B_m = 0.937T$) the magnet cannot be properly magnetized. This characteristic can be justified by the relative permeability ($\mu_{r_{mag}}$) of the BH loop in this region. Being $\mu_{r_{mag}}$ low when compared to the one of the steel composing the stator

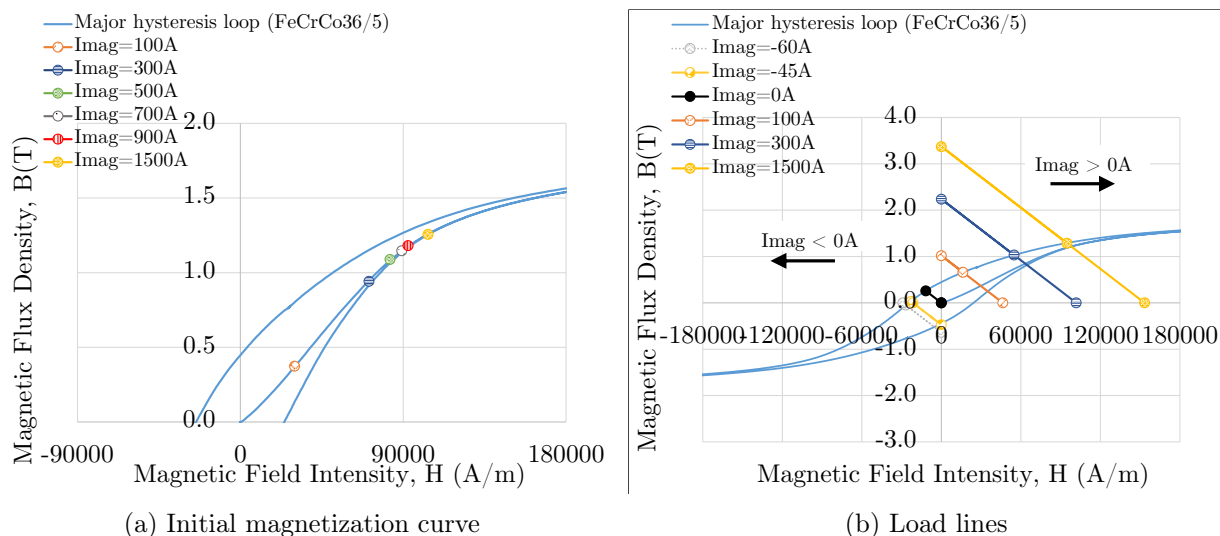


Figure 2.11: Analysis of the working points of the Fe-Cr-Co in its hard magnetization direction for different magnetization current amplitudes obtained via FEA simulations.

($\mu_{r_{steel}}$), the flux lines tend to be enclosed directly on the stator without passing through the magnet.

- By these results, a magnetic flux density of $B_{m_{LL}} = 0.25T$ is identified at the intersection of the load line $I_{mag} = 0A$ and the major hysteresis loop. By the theoretical equation [2.6](#), the level of magnetic flux density expected for this same working point is $B_{m_{LL}} = 0.18T$.
- A negative magnetization current of amplitude $I_{mag} < -42A$ is required for demagnetization the magnetic rotor ($B_m < 0.05T$) according to the simulations realized. Analytically, this same level of induction was obtained for $I_{mag} < -48A$, which indicates that the equations proposed provide a good order of magnitude for evaluating the demagnetization current (approximately a 10% error compared to the value obtained through FEA.).
- Inaccuracies are observed between the results calculated using the equation [2.6](#) and the ones obtained via simulations. These differences can be a consequence of the neglected effects of flux spreading or fringing outside the common area of the stator and of the modeling of the external hysteresis curve of the Fe-Cr-Co as linear.

2.3.3 Investigations concerning the armature reaction in the machine studied

An additional study is proposed for investigating the magnetic behavior of the VFMM studied when currents are injected in the armature windings for creating a field in the q-axis. Theoretically, this field should not promote a variation in the magnetization state of the magnet. Via FEA simulations, a three-phase current pattern is adjusted to supply the machine with different current amplitudes. A comparison is proposed by analyzing the magnetic behavior of the VFMM initially proposed considering a rotor composed of a LCF magnet (the FeCrCo36/5, which hysteresis loop was formerly presented in Figure [2.8a](#)), and the one of a PMSM, which is designed with a hypothetical HCF magnet in the rotor (characterized by a relative permeability $\mu_r = 1.6$, a coercivity $H_c = -140kA/m$ and remanence $B_r = 0.28T$). These parameters are defined to ensure in the PM-based rotor the same level of induction as the one achieved in the LCF-based rotor at no load (the intersection with the load line $I_{mag} = 0A$ occurs at the same

working point for external hysteresis curves characterizing both magnets). The Figure 2.12 shows the magnetic behavior of the HCF and LCF magnets in both dq-axis. It can be observed that both magnets are characterized by the same magnetic profile in both directions, but the absence of remanence in the q-axis makes the curves cross the origin. The stator properties and the machine geometry are the same for both machines studied, being the same already introduced in the section 2.2.

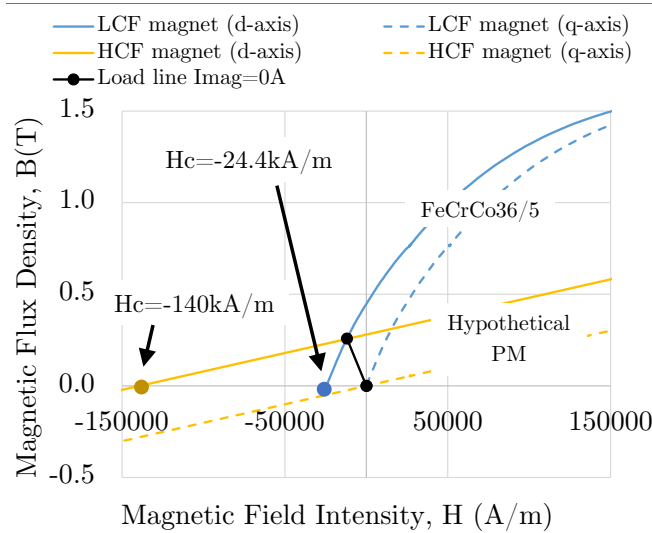


Figure 2.12: Hysteresis profile of the low (FeCrCo36/5) and the high (hypothetical PM) coercive force used for studying the effects of the armature reaction via FEA simulations.

An analysis of the magnetic flux crossing these machines is proposed for two amplitudes of regulated currents: $I_{ref} = 0A$ and $I_{ref} = 200A$. Figure 2.13 exhibits this mentioned current vector in the rotating reference frame (dq , related to the rotor), obtained from a Park transformation applied to the stationary reference frame ($\alpha\beta$, related to the stator). The rotor position θ is identified, as also the torque angle δ , defined about the q-axis, used to characterize the dq-axis current components supplying the machine ($I_q = I_{ref} \cos(\delta)$ and $I_d = -I_{ref} \sin(\delta)$). Because of the non-salient machine geometry (the dq-axis inductances are assumed equal, or $L_d = L_q$), the electromagnetic torque equation is reduced to $\Gamma_e = (3/2)p\varphi_s I_q$ and, consequently, the maximal torque is achieved for $I_q = I_{ref}$, or in other words, $\delta = 0^\circ$.

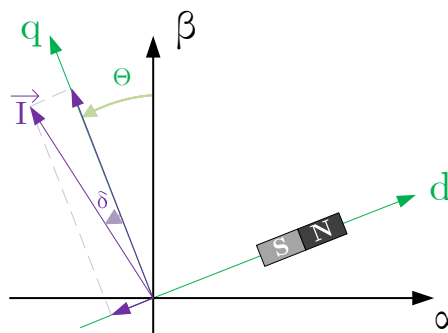


Figure 2.13: Vector diagram, being θ the rotor position.

First, considering $I_{ref} = 0A$, the results presented in the Figures 2.14a and 2.14b are obtained. Similar magnetic behavior is achieved in both machines, as expected due to the intersection of both major hysteresis loops at $I_{mag} = 0A$ in Figure 2.12. For reference currents $I_{ref} \neq 0A$, e.g. $I_{ref} = 200A$, despite the non-salient machine geometry, it is noticed that the maximal torque is not anymore measured at $\delta = 0^\circ$ for the VFMM, but at $\delta = 4^\circ$ according to the obtained results. This displacement is observed as a consequence of the q-axis currents field generated in the VFMM, as elucidated in the State of Art (see section 1.3.6). Using this same amplitude of current for supplying the HCF-based machine, this displacement is not visualized, and a maximal torque is obtained at $\delta = 0^\circ$. The Figures 2.14d and 2.14c present the profile of the magnetic flux through both machines for $I_{ref} = 200A$, considering the δ for maximal torque.

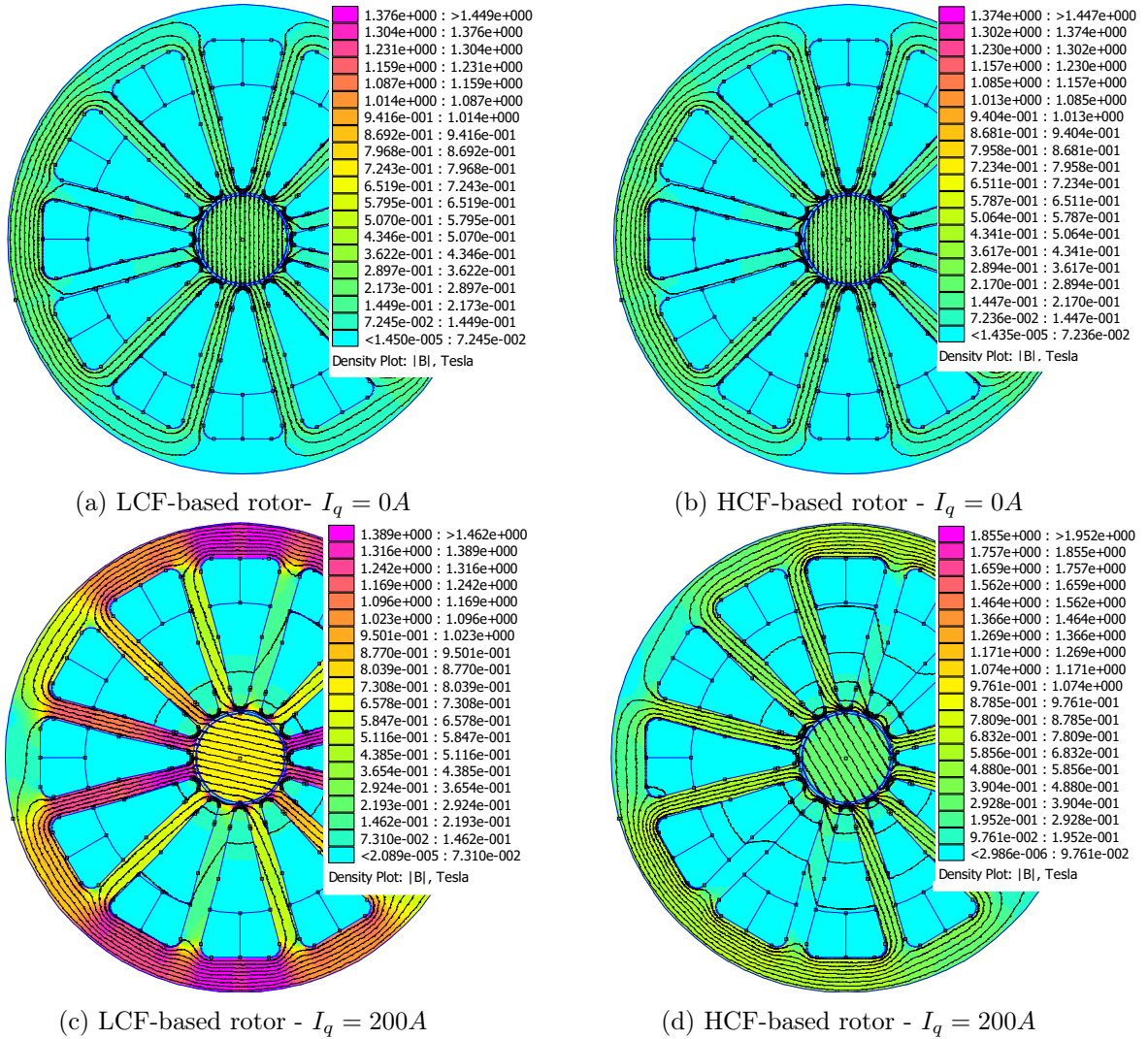


Figure 2.14: Magnetic flux density distribution via FEA simulations considering the supply of the LCF-based machine (a) $I_{ref} = 0A$ for $\delta = 0^\circ$ and (c) $I_{ref} = 200A$ for $\delta = 4^\circ$ and of the HCF-based machine (b) $I_{ref} = 0A$ for $\delta = 0^\circ$ and (d) $I_{ref} = 200A$ for $\delta = 0^\circ$ for a HCF-based machine (Magnetization axis in the Cartesian y-axis).

Due to the high relative permeability of the LCF magnet ($\mu_{r_{LCF}}$) used in rotor of the VFMM ($\mu_{r_{LCF}} = 14.65$, as previous results demonstrated, and so $\mu_{r_{LCF}} \gg 1$), the flux lines tends to prioritize the path passing through the LCF magnets. Nevertheless, this same path tends to be avoided when HCF magnets (for which the relative permeability $\mu_{r_{HCF}} = 1.6$, and so

$\mu_{r_{HCF}} \approx 1$) are used in the rotor. Hence, stronger effects of interaction between this excitation field (q-axis) and the magnetization field (d-axis) are, thus, observed in the LCF-based machines. This behavior justifies the displacement of the torque angle for which the maximal torque is generated when the amplitude of the q-axis current amplitude is increased. The more the q-axis field is enhanced (for higher I_q), the more interactions are expected with the magnetization field, resulting in the establishment in the magnet of regions of flux-enhancing (north pole) and flux-weakening (south-pole). If the level of q-axis current supplying the machine is sufficiently high, this described effect of flux-weakening can lead the working point in the hysteresis loop beyond the knee in the second quadrant, causing a demagnetization in the magnet (when the currents are suppressed the working point will move along a lower recoil line). For the PM-based machine, as these interactions are negligible, also it is the displacement observed in the magnetization axis due to the injection of q-axis currents in the armature windings.

For clarifying the affirmations above discussed, the Figure 2.15 exhibits the normal component of the air gap flux density ($\vec{B} \cdot n$) in the air gap along the rotor surface considering the two scenarios of current formerly described: (1) $I_d = 0 = I_q = 0A$ and (2) $I_d = 0A, I_q = 200A$ for both machines studied. The air gap flux density is expected to be positive to a magnet surface from 0° to 180° due to the north pole defined by the magnetization axis and negative from 180° to 360° , as the south pole is defined in this portion of the magnet surface, in case of no external field. When currents $I_q \neq 0A$ are, however, used for supplying the machines, effects of flux-enhancing (defining a north pole) will appear in portions of both magnets in regions initially expected to be a south pole and, for the same reason, effects of flux-weakening (defining a south pole) will be present in regions expected to be a north pole. It can be observed that this effect is almost negligible for the stronger PM-based machine, but is strong in the case of a LCF-based machine. The triangular spikes observed in the obtained curves are a consequence of the saturation of the closed slot wedges. Following the exposed in section 1.3.6, flux barriers are the strategy the most commonly proposed in the literature for avoiding or reducing the armature reaction. Proposing a new machine geometry is not the focus of this research but remains a perspective for future works.

Remark: The flux lines in Figure 2.14 are defined by the interaction between the magnetization axis (the d-axis, placed in the y-axis) and the q-axis. The magnetic flux density levels measured in the VFMM are subject to saturation effects of the stator yoke and teeth.

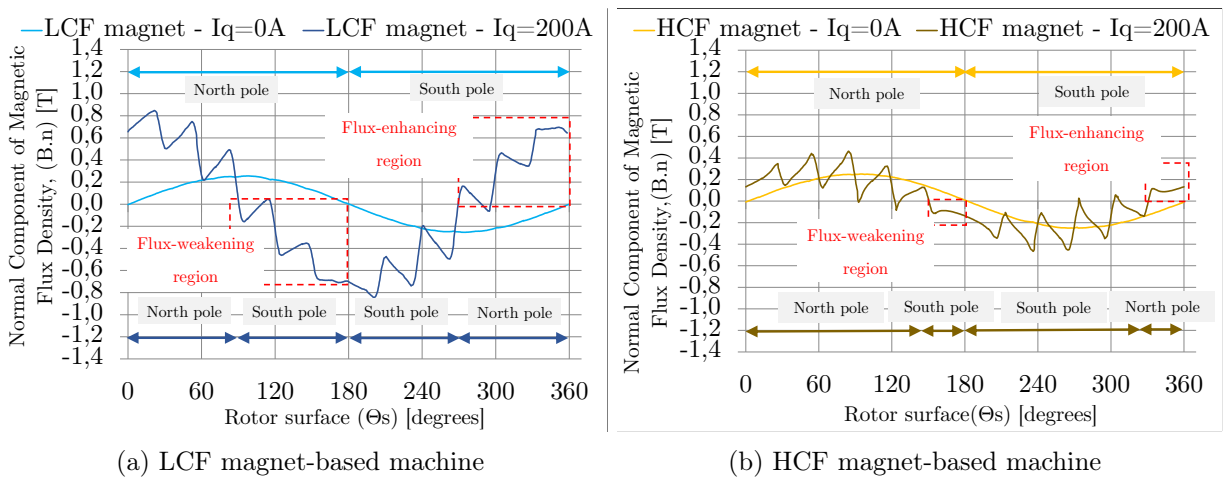


Figure 2.15: Normal component of the magnetic flux density ($B \cdot n$) measured in the air gap via simulations according to the rotor surface (θ_s).

2.4 Proposal of replacement of the magnet composing the rotor

The magnet FeCrCo36/5 composing the rotor whose magnetic behavior was investigated in the previous sections was manufactured or being crossed by the flux lines in its hard magnetization direction (see Figure 2.7). The objective of this section is to expose the magnetic behavior of the rotor composing the same grade of Fe-Cr-Co manufactured now in the easy magnetization direction to:

- First, validate the linear model exposed in the section 1.3.4 usually applied for the machines using Al-Ni-Co magnets (usually AlNiCo9 and AlNiCo5) as source of magnetic field (being single or hybrid type machines);
- Second, propose the study of Fe-Cr-Co-based rotor having similar levels of induction as the Nd-Fe-B and Al-Ni-Co magnets.

The hysteresis loop obtained from the HysteresisGraph test bench exhibited in Figure 2.6 is exhibited in Figure 2.16a. It corresponds to the curve already exhibited in the Appendix B.2. A remanence $B_r = 1.36T$ and a coercivity $H_c = -49.6kA/m$ can be identified. In the next sections, these data will be incorporated into a Finite Element Analysis software for exploring the magnet behavior of the VFMM implemented in the eTurbo proposed in Figure 2.2a.

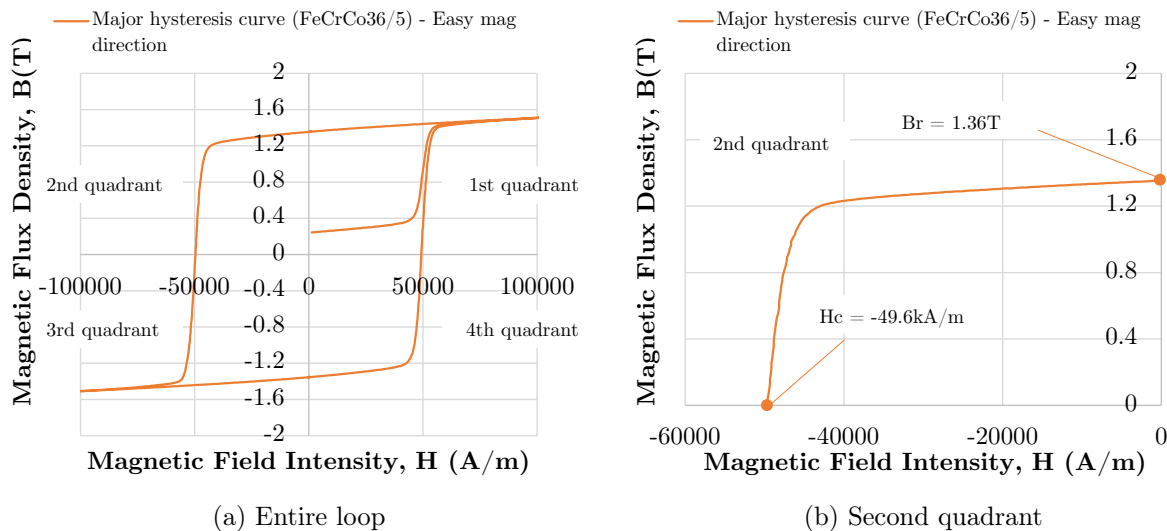


Figure 2.16: External hysteresis loop of the FeCrCo36/5 magnetized in the easy magnetization direction obtained using the Hystograph HG 200.

2.4.0.1 Validation of the magnet behavior of the FeCrCo36/5 in the easy magnetization direction via simulations

Simulations via FEA carried out are now considering the rotor characterized by the hysteresis behavior exhibited in Figure 2.16a. No modifications are made in the stator (already presented in Figure 2.2a) in terms of geometry and material used. Similarly to the investigations proposed for the magnet in the hard magnetization direction, the amplitude of the magnetization current supplying the armature windings is adjusted considering a current pattern $I_A = I_{mag}$, $I_B = -I_{mag}$, $I_C = 0A$. First, the initial magnetization curve is analyzed for defining the working points as much as I_{mag} is increased. The results are exhibited in Figure 2.17a. Second, the major BH-loop is incorporated into the rotor for studying the working point placed in the

demagnetization curve when the magnetization current amplitude is varied. Figure 2.17b shows the achieved results and the load lines that cross each working point, obtained from negative, positive, and zero magnetization currents supplying the machine. The method for calculating these load lines as well as the characteristics of working points placed on the initial magnetization and demagnetization curves are presented in Appendix B.6.

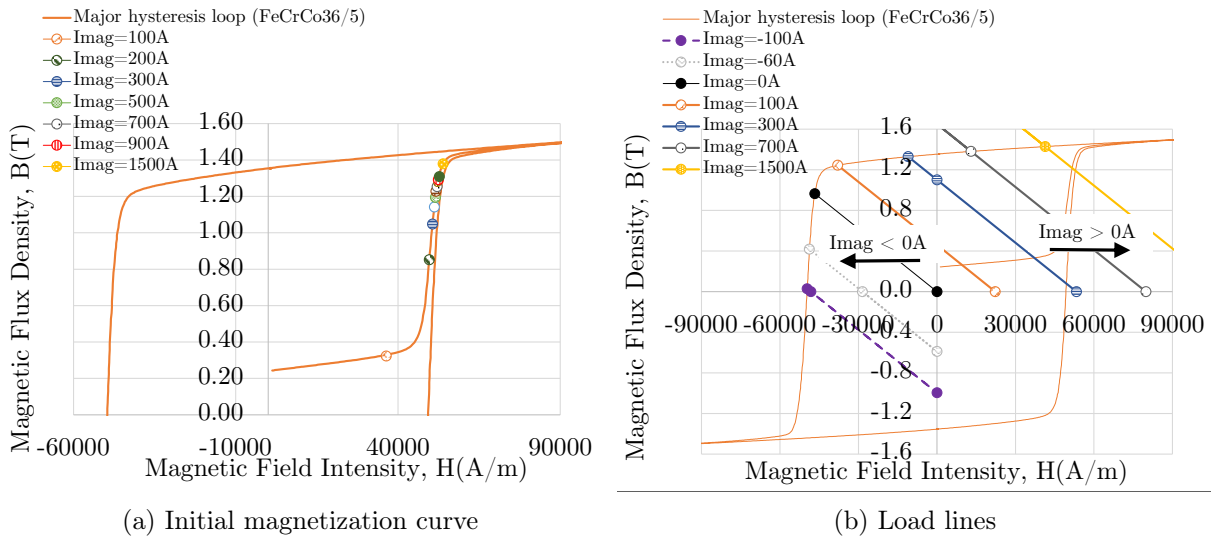


Figure 2.17: Analysis of the working points of the FeCrCo36/5 in its easy magnetization direction for different magnetization current amplitudes obtained via simulations.

Some conclusions about the results obtained are presented below:

- The excitation field (H_{exc} , in [A/m]) required for shifting the magnet to the saturation is approximately equal to $H_{exc} = 53.9kA/m$ and is obtained when $I_{mag} = 1500A$ (which defines a magnetic flux density $B_m > 1.26T$).
- For excitation fields obtained for magnetization currents up to $I_{mag} = 200A$ ($H_{exc} = 49.6kA/m, B_m > 0.85T$), where is observed a knee on the initial magnetization curve, the magnet cannot be properly magnetized. This behavior can be justified by the low permeability of the magnet in this region when compared to the one of the steel composing the stator.
- It can be observed that a negative magnetization current of amplitude $I_{mag} = -100A$ is required for the complete demagnetization of the magnetic rotor. This condition is considered achieved when $B_m < 0.03T$.

2.5 Proposal of experimental methodology and experimental tests at standstill

The main objectives for these experimental tests are:

- The investigation of magnetization level reached after magnetization via different amplitudes of current pulses supplying the machine. In other words, these tests allow to identify the working point placed at the load line $I_{mag} = 0A$ after each magnetization procedure.

- The investigation of recoil lines behavior for describing the path taken by the working points in the internal hysteresis loops, to validate the reliability of applying for a FeCrCo-based magnet the model presented in the literature for the Al-Ni-Co magnets.

2.5.1 Presentation of the setup and description of the procedure used

Experimental tests are proposed for studying the standstill magnetization of the Fe-Cr-Co-based VFMM. The setup used for this experimental validation can be analyzed in Figure 2.18. The inverter introduced in the section 2.2.1 is used to supply the machine windings with DC magnetization current pulses (I_{mag}) at $\Omega = 0rpm$. An oscilloscope, a differential voltage probe, a high-precision current sensor, and a PC are used for data acquisition.

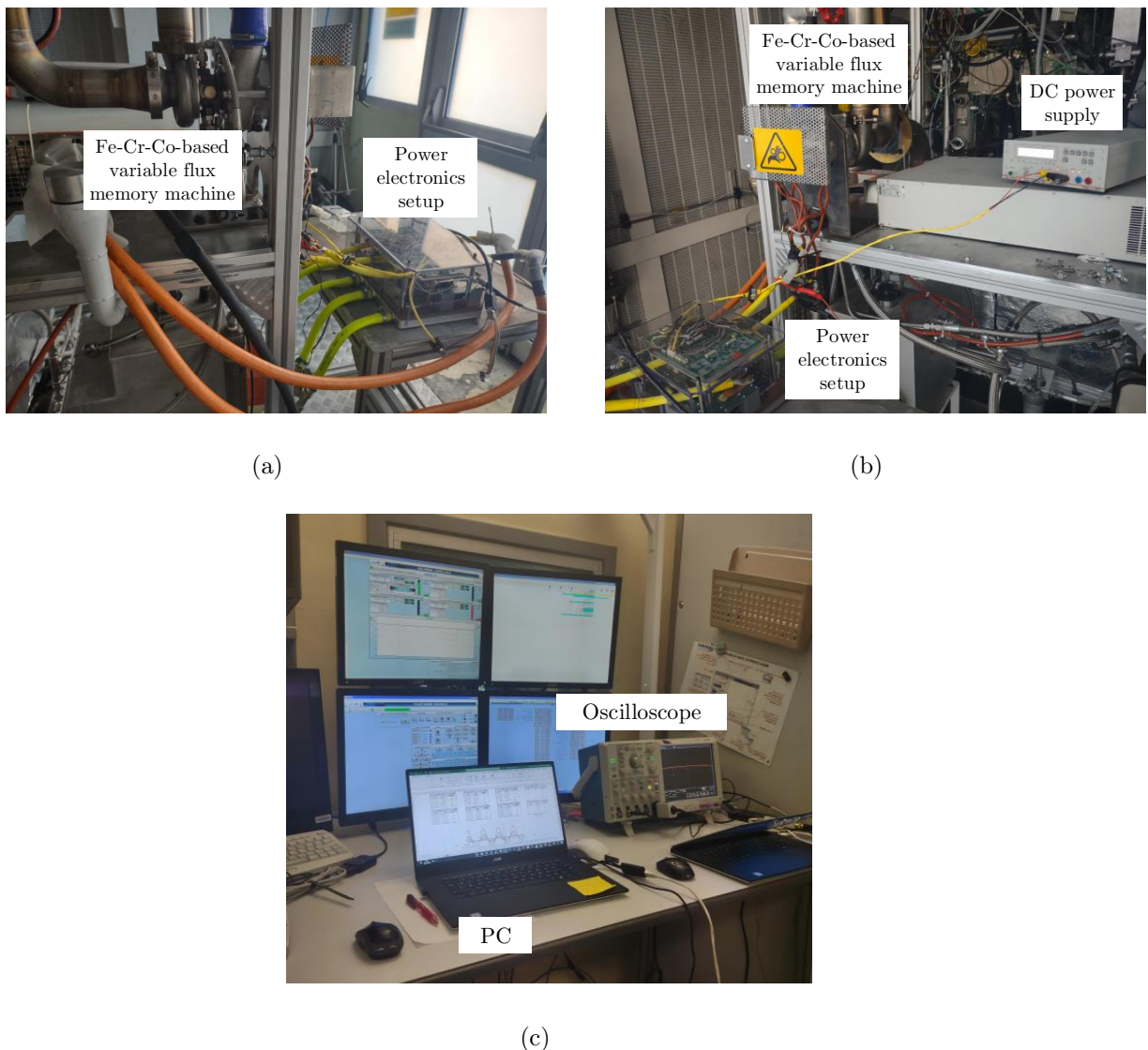


Figure 2.18: Experimental setup.

The magnetization state of the Fe-Cr-Co-based rotor increases according to the excitation field created by the currents used to supply the machine, as the field created by the d-axis current aligns the magnetization axis with the one of the current injection. For each amplitude of I_{mag} , a maximal magnetization level can be reached in the magnet. From this state, lower amplitudes

of currents will not be able to modify this magnetization, unless the external field is generated in an opposite direction.

As previously exposed, the working point of the Fe-Cr-Co-based magnet in the hysteresis loop is modified by injecting magnetization current pulses in the armature windings. The displacement of the load line $I_{mag} = 0A$ to the right or the left, according to the amplitude of magnetization current supplying the armature windings, defines the new placement of these mentioned working points. When currents generating the excitation field are suppressed, the working points return to the load line $I_{mag} = 0A$ by a specific recoil line, related to the magnetization state achieved by the magnet during the excitation procedure.

The methodology applied for these tests is the one previously described in the section [1.3.5](#). For estimating the MS achieved by the magnet after each magnetization procedure, the back-EMF (e , per phase, in [V]), supposed to be sinusoidal, is measured by running the machine at a set speed $\Omega \neq 0rpm$. The flux linkage through the armature windings (φ_s) can be calculated using the equation [2.9](#) introduced in the section [1.3.3](#) and presented below:

$$\varphi_s = \frac{e}{\omega} = \frac{V_{pp}}{2\sqrt{3}f} \quad (2.9)$$

where f is the frequency of the signal measured, which defines the electrical rotor speed ($\omega = 2\pi f$, in [rad/s], equivalent to the mechanical speed ω_m as the machine has one pole pair $p = 1$), and V_{pp} the measured peak-to-peak value of the line back-EMF. From this equation, it can be noticed that for a defined regime, the back-EMF is a direct image of the flux crossing the machine. Experimentally, an oscilloscope will be used to measure this mentioned back-EMF.

After each magnetization test, the magnet is completely demagnetized to ensure that all the magnetization procedures are realized from the same level of magnetization state. At this point, it should be remembered that the literature introduces multiple methodologies for this demagnetization procedure, as introduced in the section [1.3.1](#). According to these authors, the weakening of the flux crossing the armature windings of a VFMM can be achieved by supplying the machine with negative d-axis current pulses or via a continuous injection of a negative d-axis current in the armature windings. This second case, even if more practical because the regulation of the pulse is not required, introduces Joule losses to the system, similar to what is observed for PMSMs in classic flux-weakening operations. For this reason, the current pulses are going to be preferred for the experimental tests proposed in this thesis. Because no position sensors are used for identifying the direct and quadrature axis, an intermediary step of axis alignment is required during this demagnetization procedure. For this, multiple pulses of positive current first supply the machine at standstill for alignment of the magnetization axis with the axis of the field created by the d-axis currents. Second, a negative pulse of current is applied without changing the rotor position. A field counteracting the magnetization one initially set is therefore expected to be established. This described methodology for adjusting the working points is synthesized in Figure [2.19](#).

Remark: In practical terms, the axis alignment during the demagnetization procedure cannot be ensured. Indeed, the machine should not turn after being supplied by these positive current pulses, otherwise, the position of the d-axis would be unknown when the machine was stopped for the demagnetization step. Because the injection of a negative current pulse generates an opposite field to the magnetization one depends on the knowledge of the d-axis, when this axis alignment is not effective, the demagnetization will also not be. More insights regarding the demagnetization procedure will be discussed in the next sections.

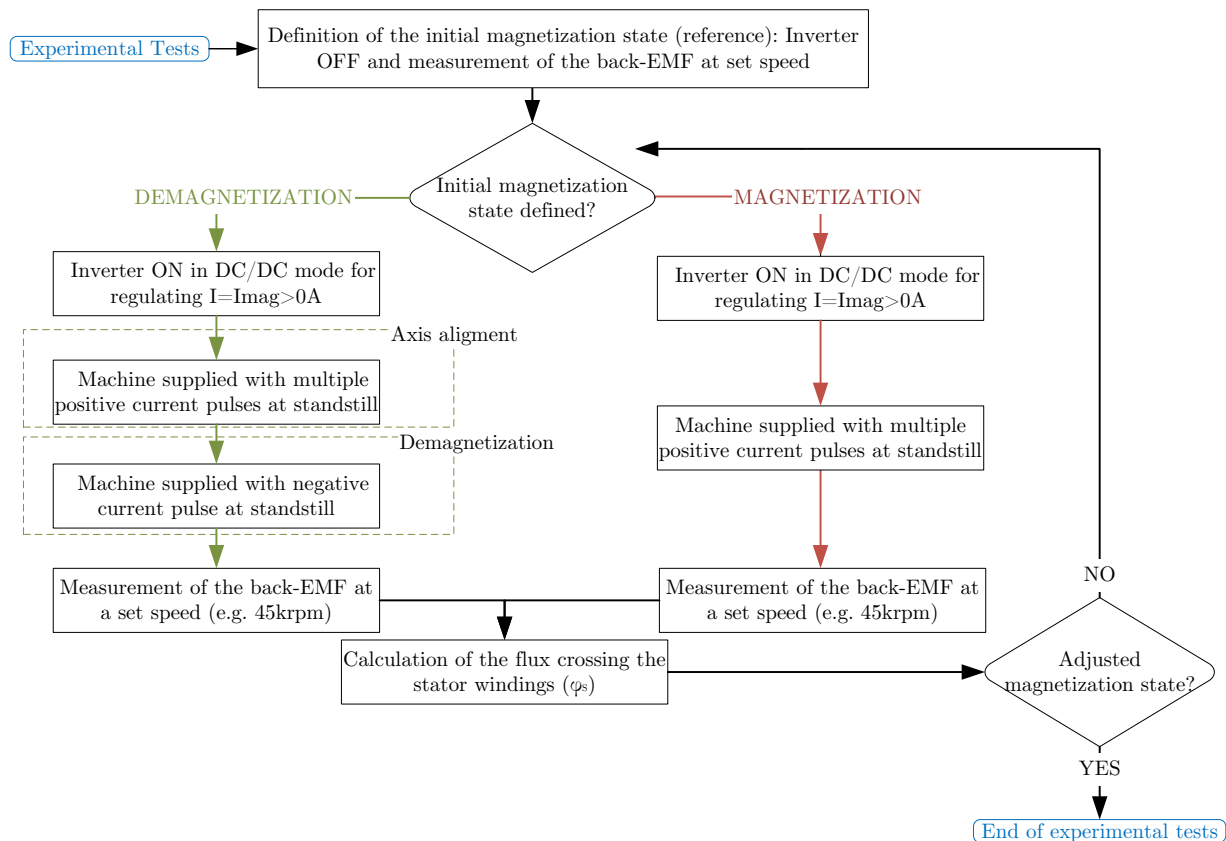


Figure 2.19: Standstill magnetization method proposed.

2.5.2 Results obtained via experimental tests

This section is focused on the presentation of the experimental results achieved by applying the standstill magnetization method overviewed in Figure 2.19. An investigation into the magnetic behavior of the machine when subject to external fields is therefore proposed. The power electronics architecture introduced in the section 2.2.1 is used in DC/DC mode for generating the current pulses used for varying the magnetization state (MS) of the Fe-Cr-Co magnet. Figure 2.20 exhibits some examples of current pulses injected in the armature windings during the experimental tests. In this present research, these square current pulses are going to be modified in terms of amplitude (as observed in the Figure 2.20a) and time duration (t) (Pulses of $t=0.5s$ are presented in the Figure 2.20a as of $t=2.0s$ in the Figure 2.20c).

Remark: The focus of this research is not the optimization of the magnet pulse used for varying the magnetization state. This topic is one of this thesis's future perspectives. For this reason, The time duration of the magnetization current pulses is defined for ensuring the establishment of the magnetic field in the magnet (due to Eddy currents).

Magnetization and demagnetization tests are realized in this study. For evaluating this increment in the magnetization state of the magnet due to the presented current pulses, the back-EMF before and after each procedure is measured. The later sections will more deeply explore the relation between this back-EMF and the MS, in addition to proposing a methodology for validating these results in comparison to the ones provided by the HysteresisGraph.

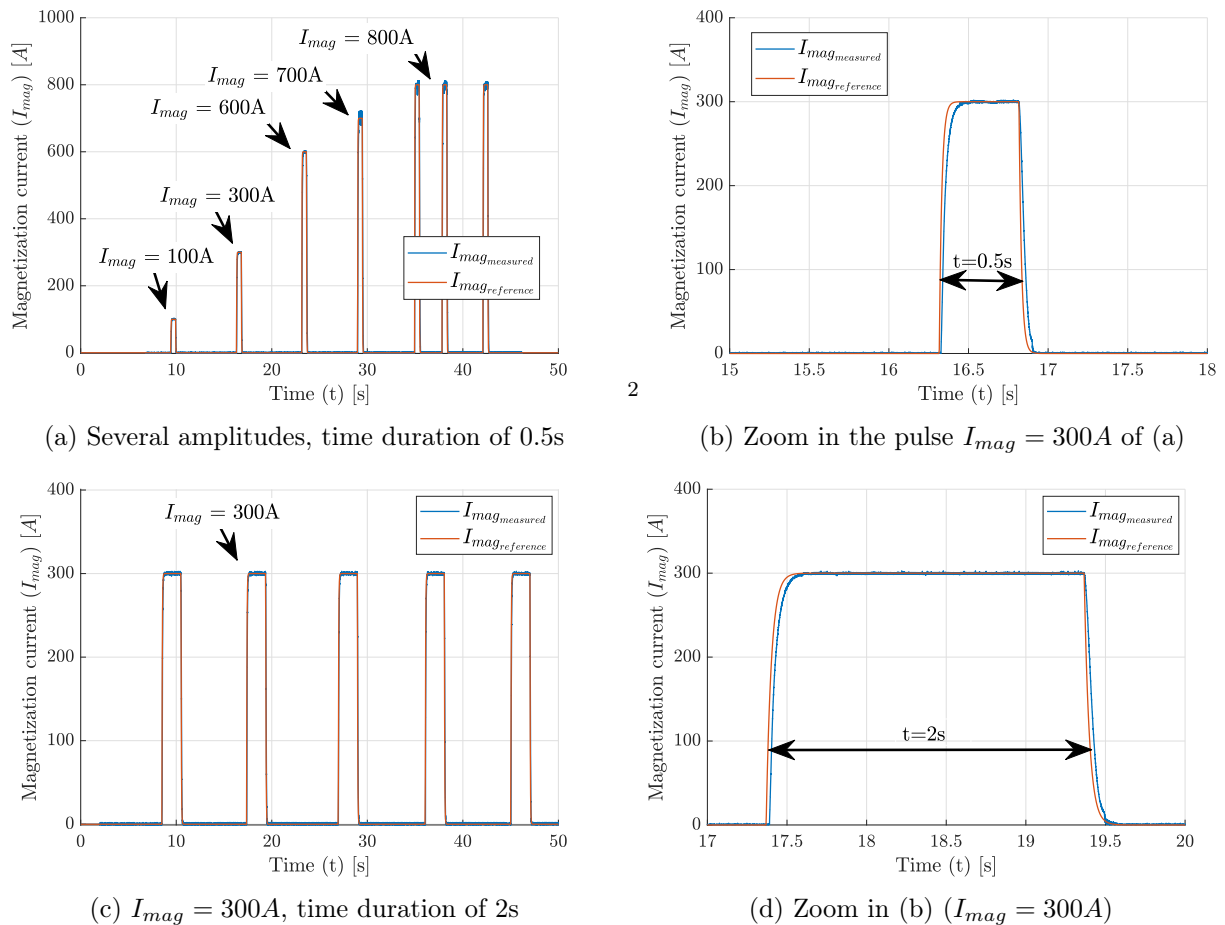


Figure 2.20: Current pulses of several amplitudes generated by the inverter in DC/DC mode for promoting the variation of the magnetization state of the Fe-Cr-Co-based rotor.

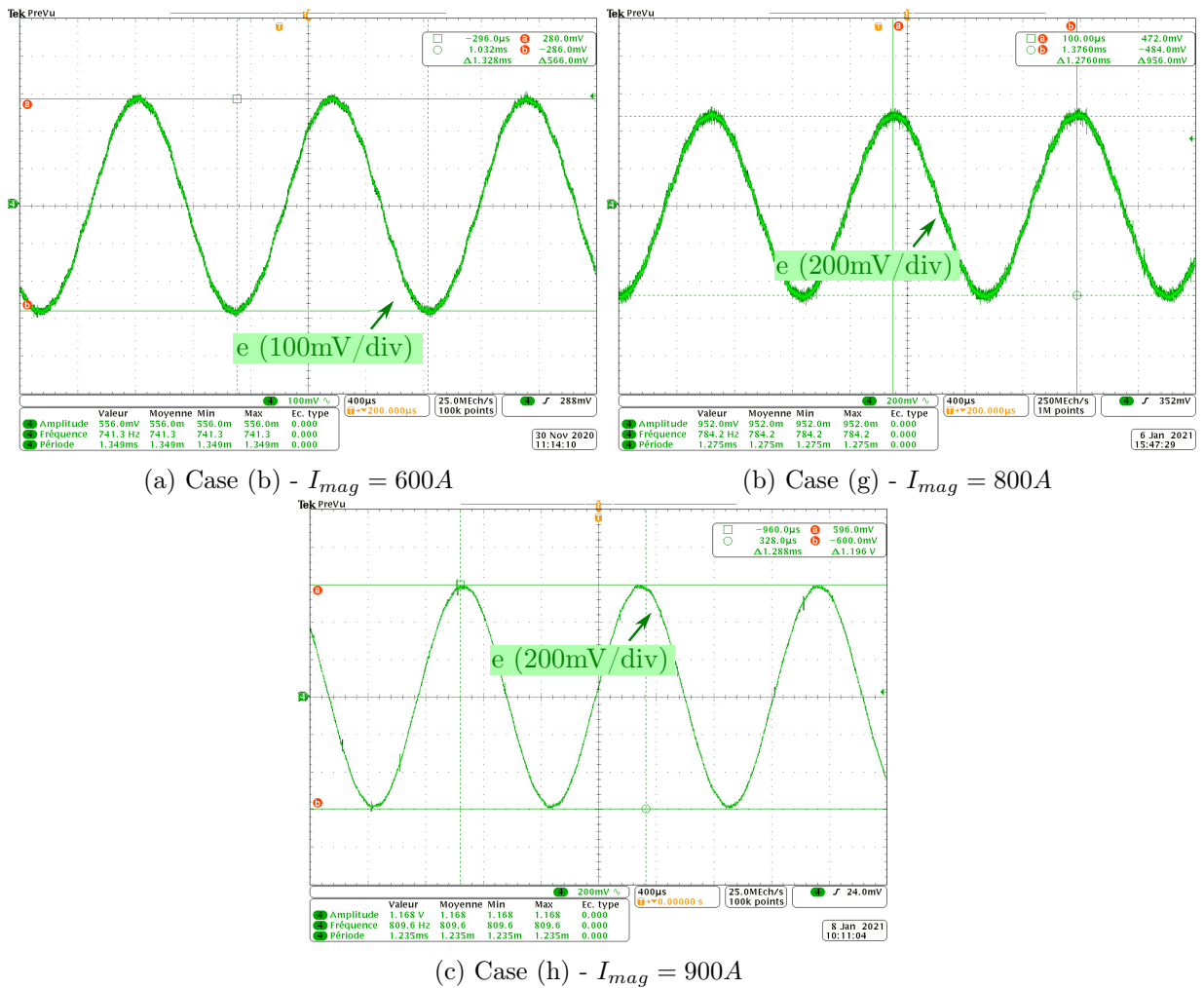
2.5.2.1 Experimental results considering the machine manufactured to ensure a magnet flux through the rotor in the hard magnetization direction

This section is dedicated to presenting the first experimental results obtained in the studies developed for understanding the magnetic behavior of the Fe-Cr-Co-based VFMM. Current pulses similar to the ones presented in the Figure 2.20 are used for modifying the magnetization state of the magnet at standstill. A current pattern $I_A = I_{mag}$, $I_B = -I_{mag}$, and $I_C = 0A$ is defined for creating a stronger external magnetization field. The back-EMF is measured considering different regimes, at $\Omega = 10krpm$ and $\Omega = 45krpm$. Because the regime in the VFMM proposed is not controlled, being imposed through a turbocharger by airflow drive, Ω varies around these references.

Table 2.1 presents the experimental results achieved by the magnetization of the VFMM from different amplitudes of current levels, considering $I_{mag} > 500A$. Lower amplitudes of currents were demonstrated to be insufficient for magnetizing the machine. Figure 2.21 shows as an example the back-EMF measured in the experimental tests using an oscilloscope for a regime around $\Omega = 45krpm$, considering three amplitudes of current for magnetizing the machine: $I_{mag} = 600A$, $I_{mag} = 800A$ and $I_{mag} = 900A$ (limit of the inverter used). As expected, magnetization procedures realized with higher amplitudes of I_{mag} will generate higher levels of back-EMF.

Table 2.1: Magnetization procedure via injection of positive current pulses in the armature windings at standstill.

Experimental Results					
Case	Magnetization			Amplitude of phase-to-phase back-EMF measured after magnetization around $\Omega = 10krpm$ around $\Omega = 45krpm$	
	Magnetization current	Quantity of pulses	Time Duration	e [V _{pp}]	e [V _{pp}]
	I_{mag} [A _{pk}]	P [unity]	t [s]		
(a)	500	10	0.5	0.104	0.468
(b)	600	3	0.5	0.110	0.566
(c)	700	6	0.5	0.155	0.700
(d)	750	6	0.5	0.192	0.876
(e)	800	10	0.5	0.193	0.956
(f)	900	10	0.5	0.208	1.200


 Figure 2.21: Back-EMF measured for a regime around $\Omega = 45krpm$ considering a magnetization procedure via injection of positive current pulses of different amplitudes in the armature windings at standstill.

An investigation of the effects of using different quantities of magnetization pulses on the back-EMF measured is also proposed by analyzing the results shown in Table 2.2. For this study, the VFMM is (1) magnetized using 6 pulses of $I_{mag} = 700A$ and (2) magnetized using 10 pulses of $I_{mag} = 700A$. The same time duration of 0.5ms is set for all these pulses. The Figure 2.22 shows the back-EMF measured at $\Omega = 10krpm$ after magnetization procedures (1) and (2). It can be noticed a back-EMF 18% higher when 10 pulses are used to magnetize the machine instead of 6. These results indicate that multiple pulses are preferred for ensuring the magnetization of the machine.

Table 2.2: Magnetization procedure via injection of positive current pulses in the armature windings at standstill.

Experimental Results				
Case	Magnetization			Amplitude of phase-to-phase back-EMF measured at 10krpm after magnetization
	Magnetization current	Quantity of pulses	Time Duration	
	I_{mag} [A_{pk}]	P [unity]	t [s]	e [V_{pp}]
(a)	700	6	0.5	0.167
(b)	700	10	0.5	0.197

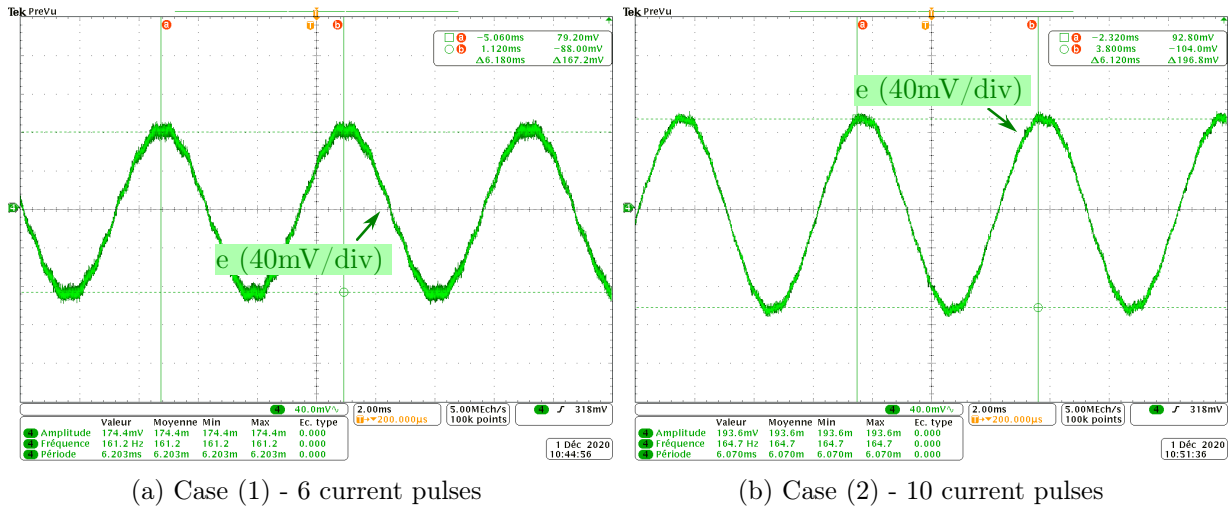


Figure 2.22: Back-EMF measured at $\Omega = 45krpm$ considering a magnetization procedure via injection of different quantity of positive current pulses in the armature windings at standstill.

Regarding the demagnetization procedure, experimental tests propose the investigation of two possible methodologies formerly introduced. In case (1), at standstill, positive current pulses are injected in the armature windings aiming to ensure the detection of the d-axis. The amplitude of these currents is lower than the ones used for setting the initial magnetization state of the machine, aiming to avoid a re-magnetization of the rotor (e.g., considering a VFMM initially magnetized via $I_{mag} = 700A$, positive currents of amplitude $I_{mag} < 700A$ are used). Then, a negative pulse is used for supplying the machine aiming to reduce the magnetization state of the magnet. Table 2.3 exhibits some results achieved by using this strategy. Figure 2.23 shows the profile of the current pulses for (b) a demagnetization via a single pulse of $I_{mag} = -50A$ and (d) multiple pulses of $I_{mag} = -300A$.

Table 2.3: Demagnetization procedure via injection of negative current pulses in the armature windings at standstill, considering pulses of time duration $t=0.5s$ for cases (a)-(c) and $t=1s$ for case (d).

Experimental Results						
Case (1)	Detection of the d -axis		Demagnetization		Phase-to-phase back-EMF measured at $\Omega = 45krpm$	
	Magnetization	Quantity of	Magnetization	Quantity of	before demag.	after demag.
	current	pulses	current	pulses	$e [V_{pp}]$	$e [V_{pp}]$
	$I_{mag} [A_{pk}]$	$P [unity]$	$[A_{pk}]$	$P [unity]$		
(a)	200	1	-50	1	0.620	0.566
(b)	200	6	-50	1	0.704	0.406
(c)	200	1	-100	1	0.566	0.410
(d)	600	4	-300	1	0.744	0.350

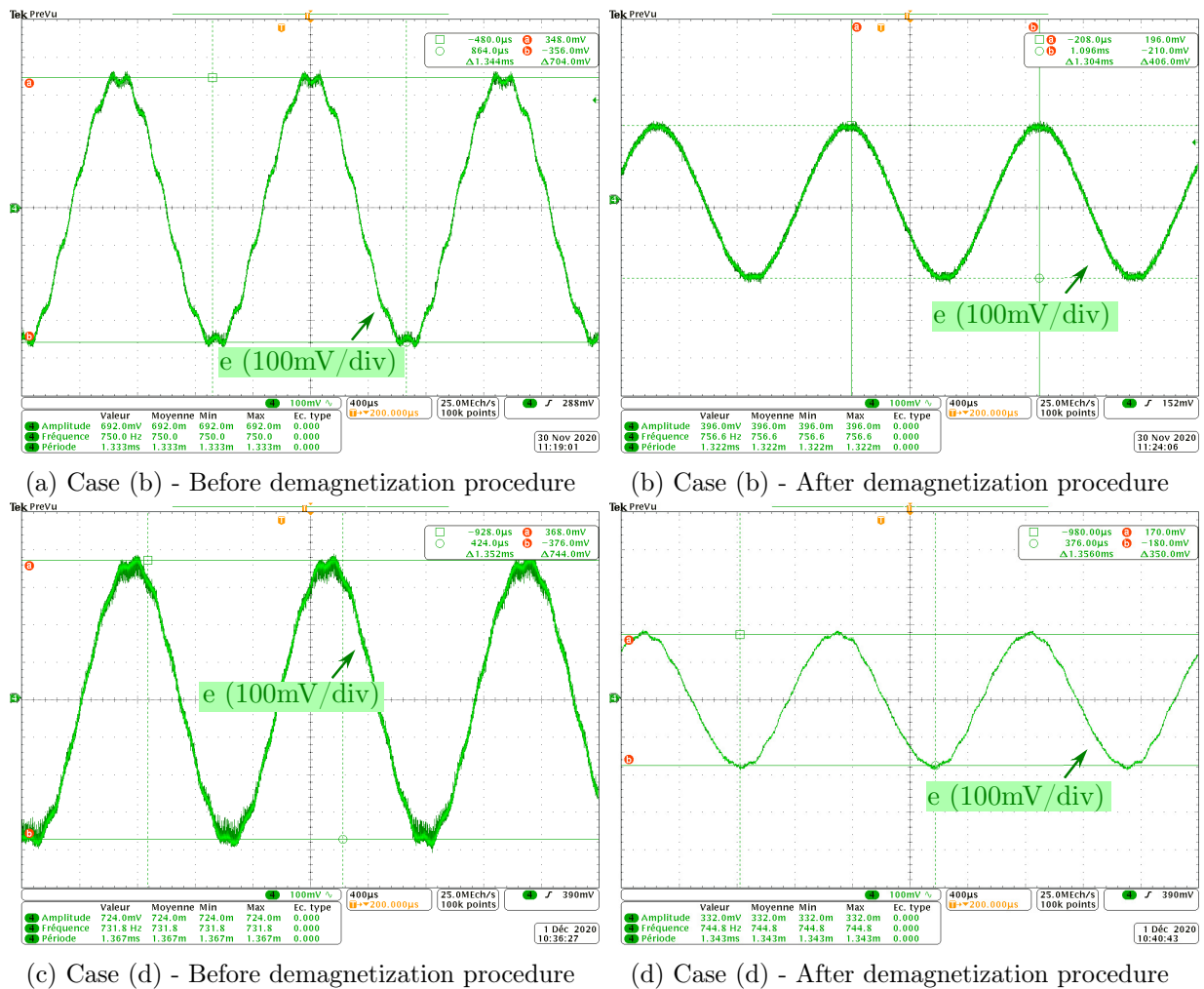


Figure 2.23: Back-EMF measured considering a demagnetization procedure via injection of negative current pulses in the armature windings at standstill.

Case (2) suggests a new strategy to simplify the demagnetization process. For it, the VFMM is first magnetized at standstill from multiple current pulses aiming to establish an initial magnetization state. Second, in a given regime, a continuous current is used to supply the

machine. The back-EMF is measured and this current amplitude is increased. This procedure is repeated until a complete demagnetization. An example of its application can be observed in Figure 2.24. A back-EMF $e = 808mV$ is measured at $\Omega = 45krpm$ after the injection of multiple pulses of $I_{mag} = 700A$ at standstill. Then, the machine is run and the amplitude of the current used for supplying the machine is continually increased to promote the rotor demagnetization. It is observed that for $I_{mag} > 140A$, a back-EMF to less than 200mV as exhibited in Figure 2.24b.

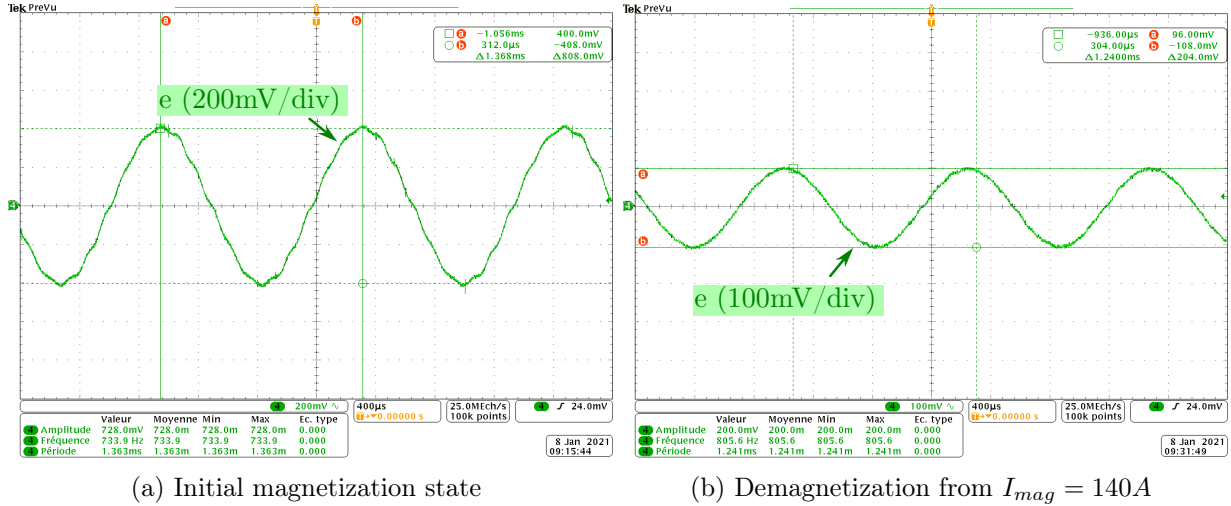


Figure 2.24: Back-EMF measured considering a demagnetization procedure via injection of positive current amplitudes in the armature windings while $\Omega \neq 0$.

The level of back-EMF measured according to the experimental results obtained at standstill magnetization are summarized in Figure 2.25. These results, which are going to be evaluated in the following sections, can be used as a reference for estimating the machine behavior and the working point placement at the hysteresis curve during a running magnetization procedure. Some conclusions regarding these experimental tests can be mentioned:

- The use of multiple pulses of the same amplitude for magnetizing the machine increases back-EMF measured. However, this back-EMF is limited to maximum amplitude, which cannot be exceeded without an increment in the magnetization current. As reference, for $I_{mag} = 900A$, which represents the maximum amplitude of magnetization current that can be supplied by the power electronics setup used, a maximal back-EMF of $e = 956mV$ can be measured.
- A strong harmonic distortion is observed especially for partial magnetizations from lower amplitudes of I_{mag} , as example $I_{mag} < 500A$. This behavior can be justified by insufficient magnetization, as the analysis for these current levels considered the injection of a single pulse in the armature windings. When results are obtained considering a higher quantity of pulses for supplying the machine, the waveform of the counter-FEM is approximated to a sinusoid.
- The demagnetization of a magnet inserted in a VFMM can be achieved via injection of negative current pulses (see Table 2.3) or by the injection of a positive current in the armature windings while the machine is running (see Figure 2.25). For the total demagnetization of the machine, this last-mentioned methodology is preferred due to its simplicity. For partial ones, the controllable demagnetization of the FeCrCo36/5 in the hard magnetization direction was demonstrated to be challenging especially due to the highly nonlinear profile of the major hysteresis loop (see Figure 2.8a).

- Finally, it should be reinforced that the results presented in this section are the very first ones obtained in the studies of the Fe-Cr-Co-based. Although they demonstrate that improvements are necessary in the magnetization and demagnetization methodologies, it allows to develop the first conclusions about the magnetic machine behavior.

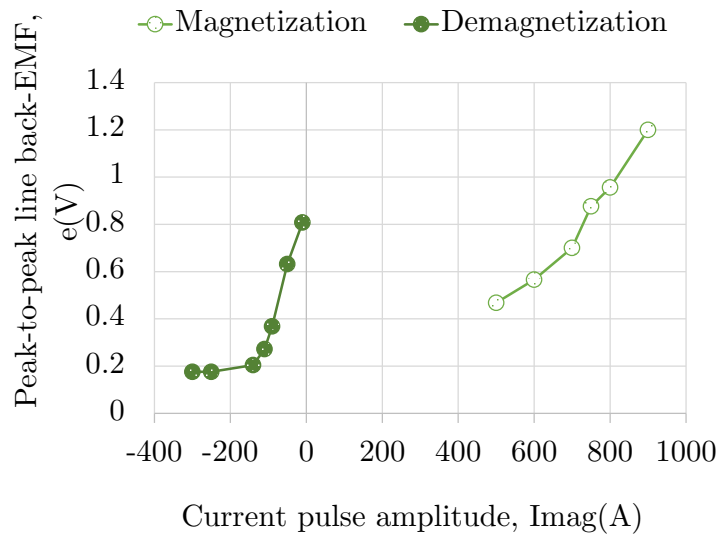


Figure 2.25: Magnetization behavior for a VFMM considering the flux crossing the hard magnetization direction of the magnet - Experimental tests at $\Omega = 45krpm$.

2.5.2.2 Experimental results considering the machine manufactured to ensure a magnet flux through the rotor in the easy magnetization direction

Similar investigations as the ones described in the section [2.5.2.1](#) are proposed for analyzing the magnetic behavior of the FeCrCo36/5 manufactured for being crossed by a magnetic flux in the easy magnetization direction. Due to the high remanence of the magnet (see its hysteresis loop in Figure [2.16a](#)), higher levels of back-EMF are expected to be measured from the experimental tests realized with this new machine. The same current pattern previously used for experimental tests is used for these studies.

The Tables [2.5](#) and [2.4](#) exhibit the experimental results achieved by the magnetization of the VFMM from different amplitudes of current levels considering a fixed number of 6 pulses, that demonstrated to be, for this machine, sufficient for maximizing the magnetization state for each amplitude of current used to supply the machine.

Two different regimes are investigated for measuring the back-EMF after each magnetization procedure: $\Omega = 18krpm$ and $\Omega = 45krpm$. Because the speed is not regulated, being controlled by an axial airflow crossing the machine (see section [2.2](#)), slight variations in the regime can be observed between measures. A normalization of the measured back-EMF is proposed for the results presented according to the expected regime in which the experimental tests were realized. For a regime $\Omega = 45krpm$ a frequency $f = 750Hz$ is used for this normalization. For the one at $\Omega = 18krpm$, $f = 300Hz$. The standard values of back-EMF are going to be used as a reference for estimating the path described by the working points in BH plan, as the next sections will clarify.

In complement to the Tables [2.4](#) and [2.5](#), Figure [2.26](#) exhibits the back-EMF measured experimentally after some standstill magnetization via different amplitudes of magnetization

Table 2.4: Magnetization procedure via injection of positive current pulses in the armature windings at standstill - Back-EMF measured at $\Omega = 18krpm$.

Experimental Results						
Case	Magnetization			Phase-to-phase back-EMF		
	Magnetization current	Quantity of pulses	Time Duration	Measured amplitude	Measured frequency	Calculated at $18krpm/300Hz$
	I_{mag} [A _{pk}]	P [unity]	t [s]	e [V _{pp}]	f [Hz]	e [V _{pp}]
(a)	250	6	0.5	2.80	307	2.74
(b)	300	6	0.5	3.23	306.5	3.16
(c)	350	6	0.5	3.34	301.3	3.33
(d)	400	6	0.5	3.54	304.7	3.48
(e)	500	6	0.5	3.68	301.9	3.65

Table 2.5: Magnetization procedure via injection of positive current pulses in the armature windings at standstill - Back-EMF measured at $\Omega = 45krpm$.

Experimental Results						
Case	Magnetization			Phase-to-phase back-EMF		
	Magnetization current	Quantity of pulses	Time Duration	Measured amplitude	Measured frequency	Calculated at $45krpm/750Hz$
	I_{mag} [A _{pk}]	P [unity]	t [s]	e [V _{pp}]	f [Hz]	e [V _{pp}]
(f)	250	6	0.5	7.08	751.4	7.07
(g)	300	6	0.5	7.62	748.3	7.64
(h)	350	6	0.5	8.10	747.4	8.13
(i)	400	6	0.5	8.50	747.9	8.52
(j)	500	6	0.5	8.88	746.6	8.91
(k)	600	6	0.5	9.12	745.6	9.17

current considering the two regimes studied: $\Omega = 45krpm$ and $\Omega = 18krpm$.

For demagnetizing the rotor, the strategy used is the one formerly presented in Figure 2.19. For example, the magnet is initially magnetized at standstill using multiple pulses of $I_{mag} = 250A$ for a duration of $t=0.5s$ each. A level of back-EMF $e = 7.22V$ is measured by running the machine at $\Omega = 45krpm$. Once the machine is stopped, the demagnetization process is proposed in two steps: first the d-axis alignment by applying 2 pulses of $I_{mag} = 50A$ followed by the application of a negative current pulse without modifying the rotor position for reducing the magnetization state of the machine. The amplitude of this demagnetization current is increased at each demagnetization procedure. The standstill magnetization results achieved by the experimental tests are summarized in Figure 2.27. These results provide a reference for the analysis of this machine during the running magnetization, as going to be presented in Chapter 3. Some final conclusions regarding these experimental tests can be mentioned:

- The amplitudes of the back-EMF measured at $45krpm$ can be compared to the ones obtained for the previously studied machine (considering the hard magnetization direction of the FeCrCo36/5, as presented in the section 2.5.2.1). The results from $I_{mag} = 600A$ for the magnet manufactured for being crossed by the magnetic flux in the easy magnetization direction indicates a back-EMF more than 16 times higher than the one measured in the magnet crossed in the hard magnetization direction in the same regime ($\Omega = 45krpm$). For

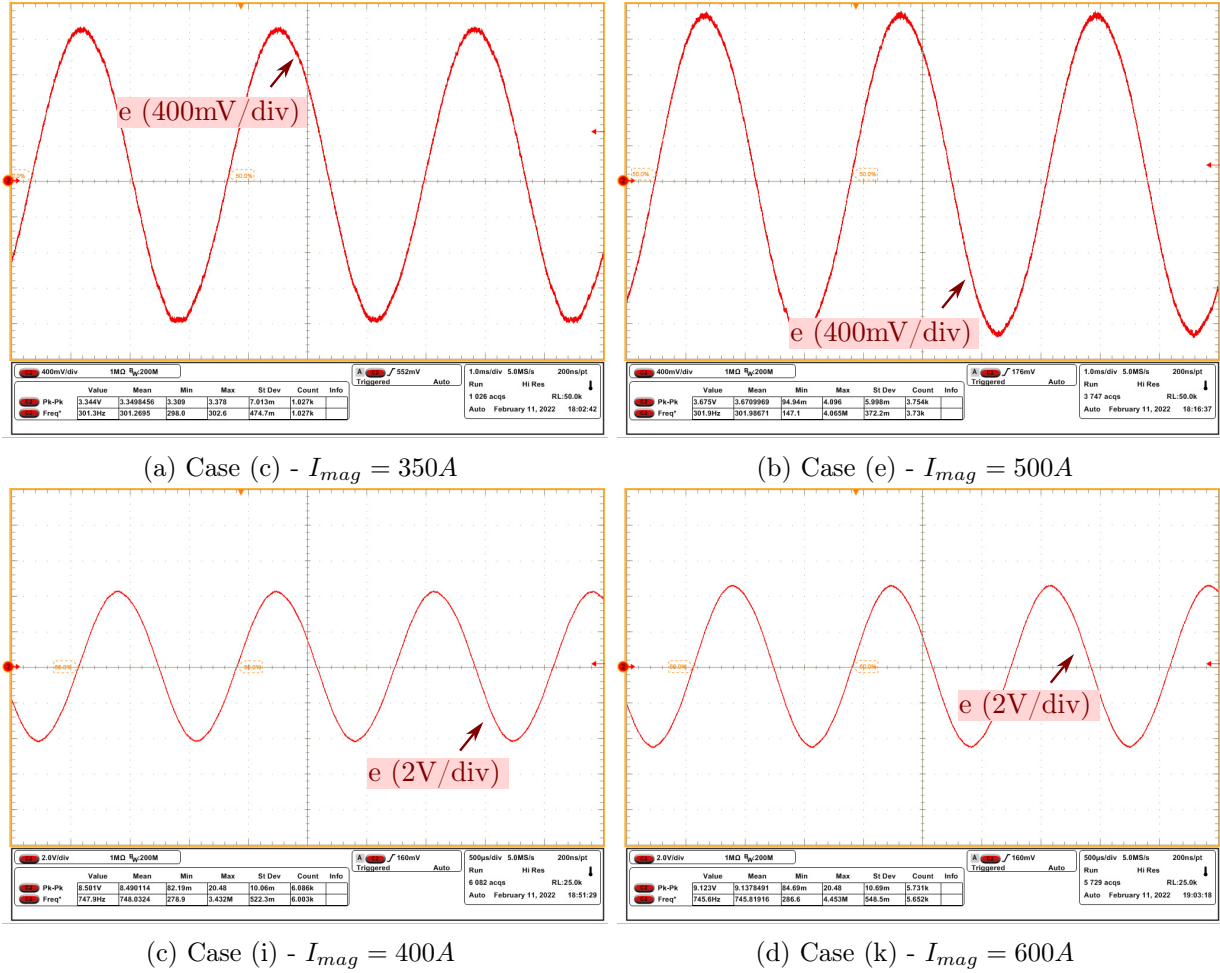


Figure 2.26: Back-EMF measured at $\Omega = 18krpm$ ((a) and (b)) and $\Omega = 45krpm$ ((c) and (d)) considering a magnetization procedure via injection of positive current pulses of several amplitudes in the armature windings at standstill.

$I_{mag} = 500A$, the back-EMF is almost 19 times higher for the machine designed with the magnet in the easy magnetization direction, also at $\Omega = 45krpm$. For this reason, most part on the studies are going to be focused in the machine composing this new magnet.

- Magnetizations realized from $I_{mag} < 200A$ provides unstable results. This magnetic behavior can be justified by observing Figure 2.17a which estimates the placement of the working points at the initial magnetization curve for several magnetization current amplitudes. For working points below the knee in the initial magnetization curve (characterized by $H_{exc} \leq 40kA/m$, achieved for $0A < I_{mag} < 200A$), the relative permeability of the magnet is low ($\mu_r \approx 1$). As a consequence, the flux lines tend to cross the stator without passing through the magnet, by the closed slot wedges observed in the geometry (see 2.2a). This magnetic behavior poorly magnetizes the Fe-Cr-Co-based rotor for these levels of current.
- For reducing the magnetization state of the magnet, the procedure considering the injection of negative pulses in the armature windings provides controllable results, that will be evaluated by FEA in the next sections.
- The difficulties observed for the magnet manufactured in the hard magnetization axis

related to a poor variation of the magnetization level in some attempts of magnetization during experimental tests are not visualized for this new magnet.

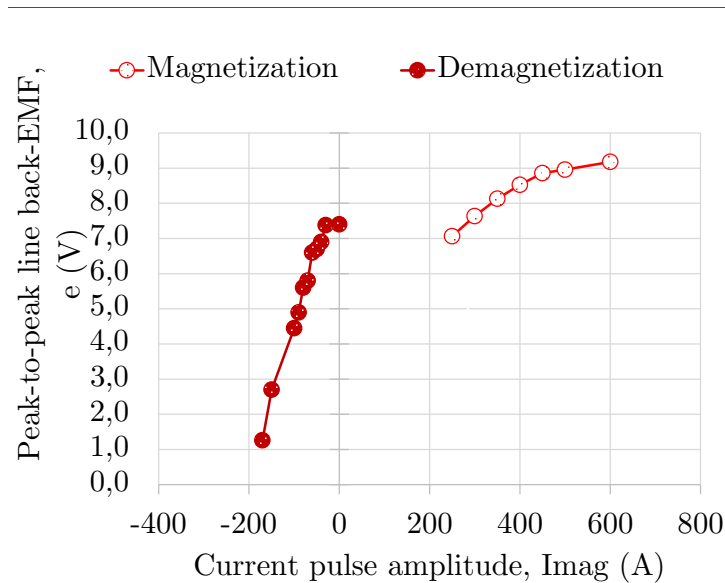


Figure 2.27: Magnetization behavior for a VFMM considering the flux crossing the easy magnetization direction of the magnet - Experimental tests at $\Omega = 45krpm$.

2.6 Analysis of the magnetic behavior of the internal hysteresis loops via HysteresisGraph

As previous concepts exposed, during the variation of the magnetization state in a VFMM, the working points initially placed at the intersection of the recoil lines describing the internal hysteresis loops and the load line $I_{mag} = 0A$, move along these mentioned recoil lines according to the currents supplying the machine. Using the HysteresisGraph previously presented in the section [2.3](#), the internal BH-loops characterizing the FeCrCo36/5 in its hard and easy magnetization direction can be obtained. Two profiles are observed:

- For hard magnetization direction, which magnetic behavior is exhibited in Figure [2.28a](#), the internal hysteresis loops have each a different coercivity. As a consequence, moving a working point from a recoil line to another can be challenging. Especially for a demagnetization, high levels of current will be required to allow the magnet to change of recoil line, as the connection between the internal curves is in the third quadrant. The internal hysteresis loops present a parallel behavior in the first and second quadrants.
- According to Figure [2.28b](#), it can be observed that the magnetic behavior of the recoil lines in the easy magnetization direction is similar to the one described for the Al-Ni-Co magnets in [\[3, 12, 18\]](#). The internal curves have approximately the same coercivity and exhibit a profile approximately parallel, as described in the literature. This hysteresis profile facilitates a controllable variation of the working points placement because the major hysteresis loop works as a bridge between the recoil lines in the first and second quadrants.

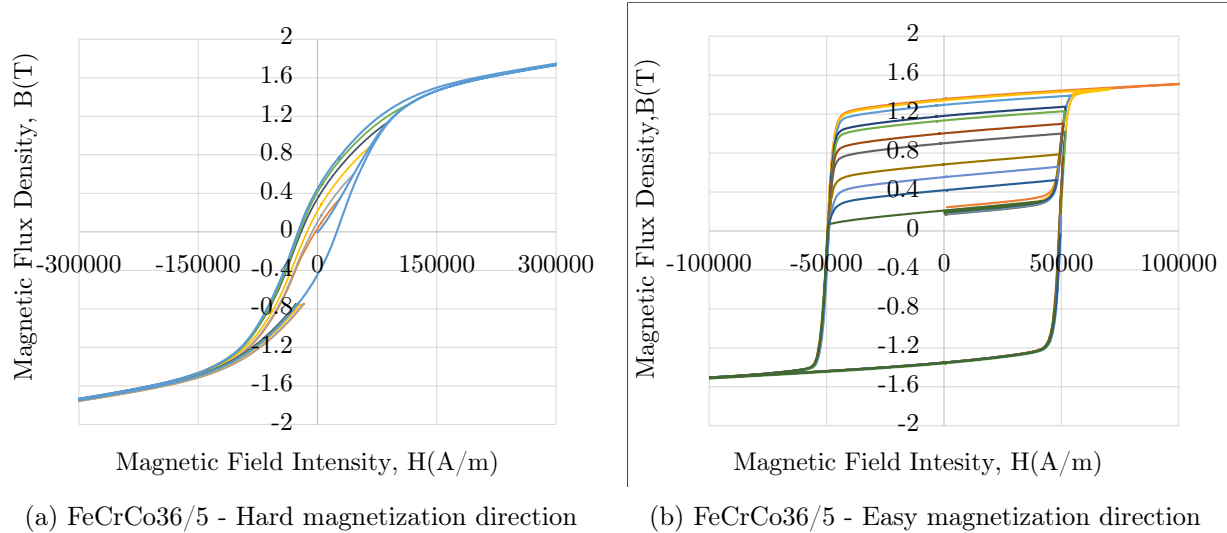


Figure 2.28: Internal hysteresis loops via HysteresisGraph.

2.7 Evaluation of the magnetic behavior of the FeCrCo36/5 considering a standstill magnetization

This section is dedicated to evaluating the internal hysteresis curves obtained according to the experimental test results presented in the section 2.5.2. The main objective is to propose a reliable model that describes the path traced by the working points when the magnetization level of the magnet is modified, that can be used as a reference for the running magnetization studies.

Indeed, the behavior of the recoil lines in the studied magnets is expected to be similar to the one described using the HysteresisGraph (Figures 2.28a and 2.28b). In real applications, however, a HysteresisGraph is an expensive measuring equipment rarely available in the industry, being typically restricted to the research institutes or laboratories dedicated to materials characterization. For this reason, most part of studies in the literature propose the use of a model that estimates the recoil lines without requiring the use of a measuring equipment. For magnets having no knee in the second quadrant of the BH-loop, the scientific literature investigating VFMMs until the moment does not introduce an adapted model for determining the recoil lines. In this context, this section will be dedicated to validating the use of the linear model for characterizing the FeCrCo36/5 (easy magnetization direction). In complement to this study, the results in Appendix B.7 will propose a model that fits with the behavior observed when flux lines cross the hard magnetization direction of this same magnet.

2.7.1 First estimation of the magnetic behavior of the magnet when magnetized in the easy magnetization direction

Assuming the hypothesis of parallelism of the recoil lines to the linear portion of the demagnetization curve in the BH-loop (between the positive saturation and the knee), this section has as objective the estimation of the back-EMF that would be produced in the magnet at different magnetization states. First, the relative permeability (μ_r) of each recoil line is calculated according to the slope of the linear external demagnetization curve by the equation 2.10. Using the hysteresis loop presented in Figure 2.16a, a $\mu_r = 1.25$ is obtained.

$$\mu_r = \frac{\Delta B}{\mu_0 \Delta H} \quad (2.10)$$

Next, by using FEA software, the working point placement in the initial magnetization curve of the FeCrCo35/5 is estimated for the machine supplied via several amplitudes of I_{mag} , aiming to define the behavior of the recoil lines in the first quadrant. A current pattern of $I_A = I_{mag}$, $I_B = -I_{mag}$, $I_C = 0A$ is set for reproducing in simulations the same conditions of the experimental tests previously realized. The results are presented in Table 2.6.

Table 2.6: Characterization via FEA of the recoil lines considering a parallelism to the major hysteresis loop ($\mu_r = 1.25$) - FeCrCo36/5 magnetized in the easy magnetization direction.

Recoil lines							
Magnetization current	Coercivity	Remanence	Magnetization state	Points in the load line $I_{mag} = 0A$		Points in the initial magnetization curve	
I_{mag} [A _{pk}]	H_C [kA/m]	B_r [T]	MS [%]	H_m [kA/m]	B_m [T]	H_{exc} [kA/m]	B_{exc} [T]
200	-49.6	0.77	57.16	-34.94	0.72	49.61	0.85
250	-49.6	0.89	66.07	-40.23	0.83	50.23	0.97
300	-49.6	0.97	71.49	-43.63	0.90	50.66	1.05
350	-49.6	1.02	75.41	-46.00	0.95	50.95	1.10
400	-49.6	1.06	78.32	-46.82	0.97	51.52	1.14

As discussed in the section 1.1.4.1, the remanence characterizing each recoil line (assumed linear) can be calculated by the equation 2.11, considering the values obtained via simulation $H_m = H_{exc}$ and $B_m = B_{exc}$, as shown in the Table 2.6:

$$B_m = (\mu_0\mu_r)H_m + B_r \quad (2.11)$$

These remanences can be used for estimating the magnetization state expected after each magnetization process realized by the ratio $MS[\%] = B_r/B_{r_{max}}$, where $B_{r_{max}}$ is the remanence of the major hysteresis loop. Figure 2.29 illustrates the recoil lines obtained by the described methodology, all supposed to have the same coercivity.

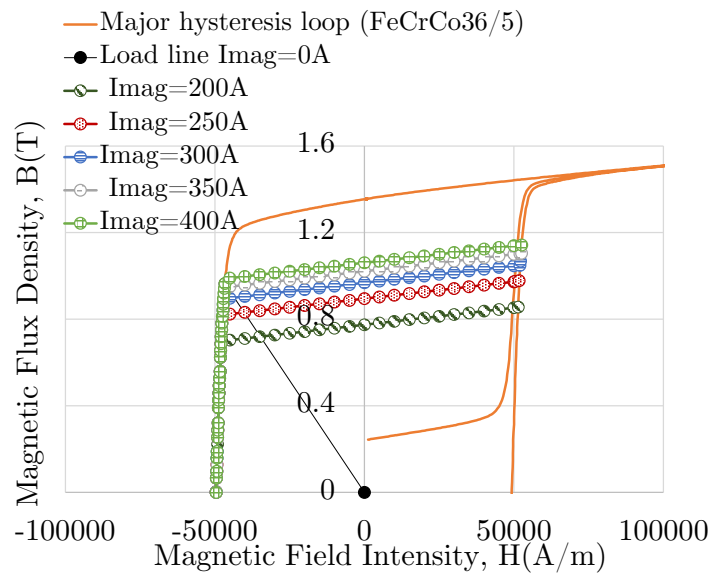


Figure 2.29: Recoil lines estimated via simulations considering a parallel behavior to the major hysteresis loop ($\mu_r = 1.25$) - FeCrCo36/5 magnetized in the easy magnetization direction.

Finally, the intersection of these recoil lines with the load line $I_{mag} = 0A$ can be estimated. Using these working points, the magnet flux density at standstill can be evaluated as also the flux linkage (φ_s) through the stator windings.

The slope of load line $I_{mag} = 0A$ or the Permeance Coefficient (PC) is calculated according to the magnetic circuit geometry, as exposed in Chapter 1 and rewritten below:

$$B_m = -\mu_0 \left(\frac{l_m}{l_g} \right) \left(\frac{A_g}{A_m} \right) H_m = (PC)H_m \quad (2.12)$$

being the cross-sectional area of the air gap and the magnet respectively given by A_g and A_m (in $[m^2]$) and the air gap and the magnet length by l_g and l_m (in $[m]$). By equating the equations 2.11 and 2.12, magnetic field intensity at the intersection of each recoil line with the load line $I_{mag} = 0$ is given by:

$$H_m = -\frac{B_r}{(PC) - (\mu_0\mu_r)} \quad (2.13)$$

The magnetic flux density B_m at this same point can be calculated by applying this result in the equation 2.11. The calculated values of H_m and B_m are exposed in the Table 2.7. By the recoil lines exhibited in Figure 2.29, it can be concluded that the highest level of induction is achieved when the magnet inserted in the VFMM is magnetized via $I_{mag} \approx 400A$. For magnetizing current amplitudes that exceed this limit ($I_{mag} > 400A$), the recoil lines will lead the working point to stabilize at the load line $I_{mag} = 0A$ in the same placement as the one defined to $I_{mag} = 400A$.

Table 2.7: Estimation of the back-EMF for parallel recoil lines - FeCrCo36/5 magnetized in the easy magnetization direction ($B_r = 1.36T$, $H_c = -49.6kA/m$).

Estimation of the back-EMF for parallel recoil lines				
Magnetization current	Estimations via FEA		Experimental tests	
	Line back-EMF estimated at 18krpm	Flux through the stator windings	Line back-EMF measured at 18krpm	Flux through the stator windings
$I_{mag}[A_{pk}]$	$e_{est} [V_{pp}]$	$\varphi_{est} [\mu Wb]$	$e_{mes} [V_{pp}]$	$\varphi_s [\mu Wb]$
200	4.95	759	-	-
250	5.74	879	2.96	453
300	6.29	963	3.16	484
350	6.65	1020	3.33	510
400	6.78	1040	3.85	534
500	6.78	1040	3.65	559

The hypothesis of a sinusoidal back-EMF measured in the VFMM during the experimental tests can be evaluated also using simulations via FEA. For this study, the recoil lines presented in Table 2.6 are incorporated in the rotor and the flux linkage per phase is calculated at no magnetization current condition according to the mechanical position of the rotor (θ , in [radians]). Then, using Faraday's Law, the back-EMF at $\Omega = 18krpm$, the same regime defined during the experimental tests, can be calculated by:

$$e = -N \frac{d\varphi_s}{dt} = -N \frac{d\varphi_s}{d\theta} \frac{d\theta}{dt} = -N \frac{d\varphi_s}{d\theta} \omega \quad (2.14)$$

The Figure 2.30 exhibits the back-EMF calculated considering the magnets characterized using two of the recoil lines, specifically the ones for $I_{mag} = 300A$ ($B_r = 0.97T$, $H_c = -49.6kA/m$

and $\mu_r = 1.25$) and for $I_{mag} = 400A$ ($B_r = 1.06T$, $H_c = -49.6kA/m$ and $\mu_r = 1.25$). The phase-to-phase values of e are presented to facilitate the comparison with the experimental results. The results are summarized in Table 2.7 for all the recoil lines studied. It can be noticed that the estimated amplitudes of voltage are considerably higher than the one measured during the experimental tests, around 100% higher for a magnetization via $I_{mag} = 300A$ and 80% for a magnetization via $I_{mag} = 400A$. This difference indicates that the model used for the recoil lines is not adapted to describe the real behavior of the magnet inserted in the machine. Thus, a new methodology is proposed for characterizing the working point behavior in case of partial magnetization conditions.

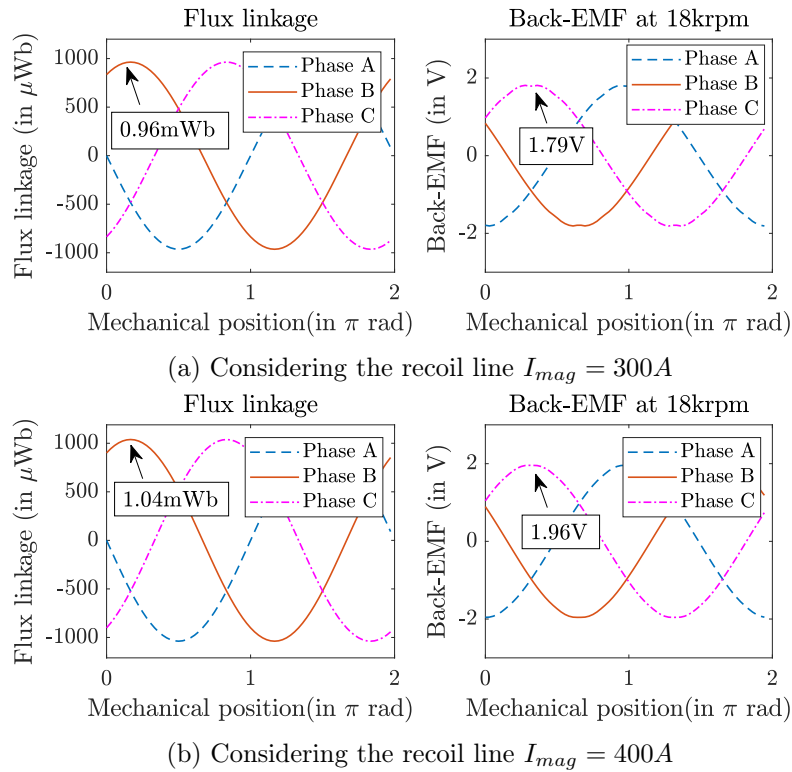


Figure 2.30: Validation via simulations of the estimated recoil lines.

2.7.2 Proposition of an adapted model for describing the behavior of the recoil lines

This section aims to propose a methodology for defining the profile of the recoil lines characterizing the Fe-Cr-Co magnet inserted in the machine environment. In this context, from the results obtained via standstill magnetization, the partial magnetization states of the VFMM are studied for estimating the path traced by the working points considering variations in the magnetization state of the magnet. The methodology used and related conclusions considering the easy magnetization direction are going to be presented in this section. A similar approach, introduced in Appendix B.7, will be considered for evaluating the magnetic behavior of the magnet in the hard magnetization direction.

2.7.2.1 Description of the methodology proposed

The steps composing the methodology proposed for describing the recoil lines are overviewed in Figure 2.31.

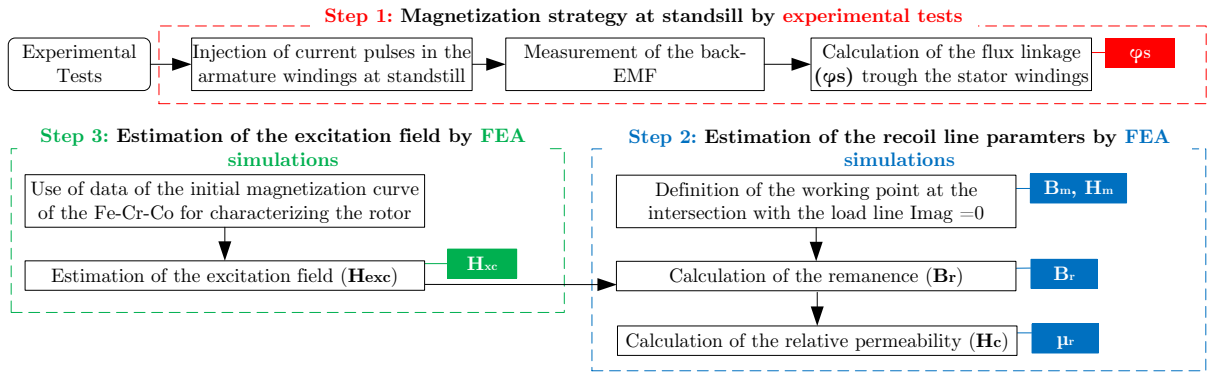


Figure 2.31: Overview of the methodology proposed for validating of the working point placement of the Fe-Cr-Co magnetized in the easy magnetization direction.

Three steps can be identified in this methodology:

1. From each back-EMF measured during the experimental tests (see section 2.5.2), the flux linkage through the stator windings is calculated by the equation 2.9, rewritten below:

$$\varphi_s = \frac{e}{\omega} = \frac{V_{pp}}{2\sqrt{3} \cdot 2\pi f} \quad (2.15)$$

2. Then, the working points at the load line $I_{mag} = 0A$ can be estimated. To this end, FEA simulations are proposed conserving the stator material (COGENT NO20) but modifying the rotor one by different hypothetical magnetic materials characterized by a linear function ($\vec{B} = \mu_0\mu_r\vec{H}$, considering a low μ_r for avoiding saturation). The coercivities of these materials are chosen to ensure in the armature windings a similar magnet flux to the ones calculated from step 1. The 2.8 shows the results achieved and the Figure 2.32 exhibits the linear curves as also the intersection of these with the load line $I_{mag} = 0A$.

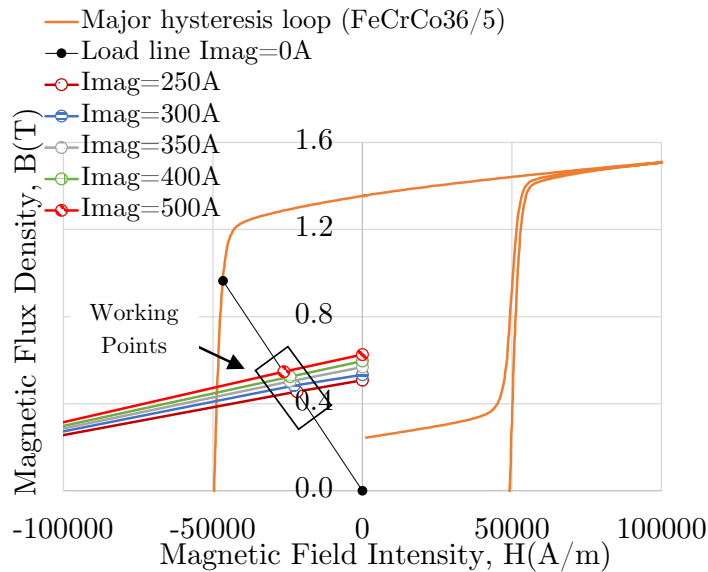


Figure 2.32: Methodology proposed - Definition of the working point placement at the load line $I_{mag} = 0A$ via FEA.

3. Once the working points in the second quadrant are defined, the focus is to estimate the excitation field in the initial magnetization curve. For these investigations, FEA simulations are proposed by characterizing the rotor using the initial magnetization curve measured by the HysteresisGraph (see Figure 2.17a). A current pattern identical to the one used during the experimental tests is used for reproducing the same excitation condition in the machine and the one experimentally defined. The results obtained by this study also exhibited in the section 2.7.1 (see Table 2.6), are represented in Table 2.8

Table 2.8: Characterization of the recoil lines - FeCrCo36/5 magnetized in the easy magnetization direction ($B_r = 1.36T$, $H_c = -49.6kA/m$).

Experimental Tests		Recoil lines					Initial magnetization curve - by FEA simulations	
Magnetization current	Flux linkage	Remanence	Magnetization state	Relative permeability of the linear curve	Points in the load line $I_{mag} = 0A$		Points in the initial magnetization curve	
I_{mag} [A _{pk}]	φ_s [μ Wb]	B_r [T]	MS [%]	μ_r [unitless]	H_m [kA/m]	B_m [T]	H_{exc} [kA/m]	B_{exc} [T]
250	453.0	0.61	44.80	5.78	-21.44	0.45	50.23	0.97
300	483.9	0.66	48.19	6.17	-22.63	0.48	50.66	1.05
350	509.9	0.69	50.91	6.39	-23.66	0.50	50.95	1.10
400	533.6	0.73	53.32	6.47	-24.69	0.52	51.23	1.14
500	559.3	0.76	55.86	6.72	-25.57	0.54	51.52	1.19

Finally, the recoil lines connecting the working points estimated in the initial magnetization curve (H_{exc} and the corresponding B_{exc}) to the ones placed at the load line $I_{mag} = 0A$ are set. Figure 2.33 illustrates these results. Supposed linear, these curves are defined by the hypothesis of the same coercivity to the one of the external loop. The slope of each recoil line representing the partial magnetization of the Fe-Cr-Co is calculated below. These results are later applied in the equation 2.11 for calculating the remanence.

$$\frac{\Delta(B_{exc} - B_m)}{\Delta(H_{exc} - H_m)} = \mu_0 \mu_r \quad (2.16)$$

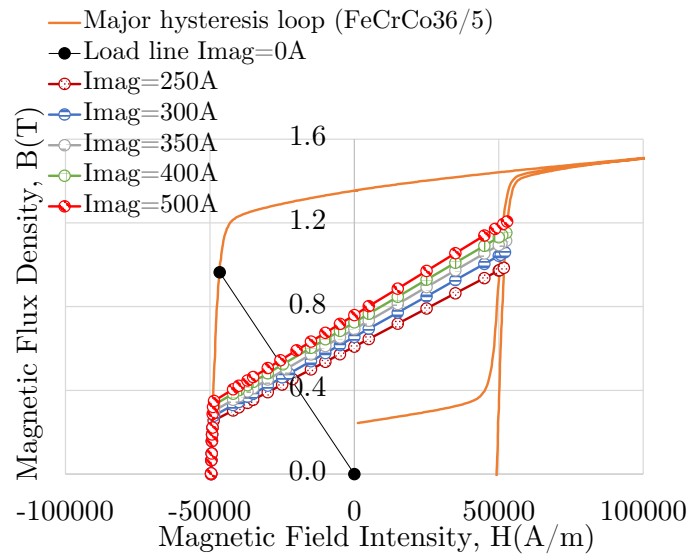


Figure 2.33: Recoil lines estimated via FEA for characterizing the FeCrCo36/5 magnetized in the easy magnetization direction ($B_r = 1.36T$, $H_c = -49.6kA/m$).

Characterizing the rotor in FEA simulations by each of these recoil lines, the flux linkage through the stator windings for $I_{mag} = 0A$ can be estimated. These results can be applied to the equation 2.14 for estimating the induced back-EMF. The Figures 2.34a and 2.34b show the flux and back-EMF at $\Omega = 18krpm$, considering, respectively, the recoil line obtained for $I_{mag} = 300A$ ($B_r = 0.66T$, $H_c = -49.6kA/m$ and $\mu_r = 5.78$) and for $I_{mag} = 400A$ ($B_r = 0.73T$, $H_c = -49.6kA/m$ and $\mu_r = 6.47$). The peak phase back-EMF of $e = 0.89V$ in Figure 2.34a and one of $e = 0.98V$ in Figure 2.34b are used for calculating the peak-to-peak line back-EMF $e = 3.09V$ and $e = 3.40V$ for these two working conditions. These amplitudes represent, respectively, 2.2% and 2.3% of error with regard to the ones obtained via experimental tests.

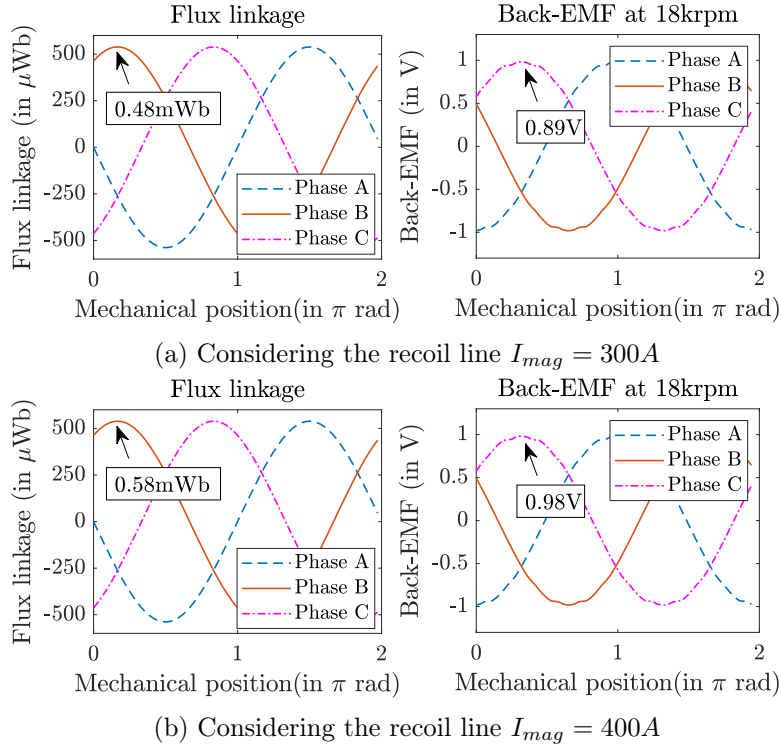


Figure 2.34: Validation of the sinusoidal profile of the back-EMF via simulations considering the estimated recoil lines.

2.7.2.2 Evaluation of the results obtained from the methodology proposed

Recoil lines model the path traced by the working points during the variation of the magnetization state. In this context, aiming to obtain a reliable hysteresis model describing the FeCrCo36/5 inserted in the machine, the recoil lines estimated from the experimental results according to the methodology introduced in the previous section and in Figure 2.33 are going to be evaluated. A comparison is proposed between them and the ones estimated considering the hypothesis of a parallelism of the internal demagnetization curves to the external one (major hysteresis loop), as formerly discussed in the section 2.7.1. It should be remembered that the general literature uses this last mentioned methodology for characterizing LCF magnets composing VFMMs and that these results can be considered similar to the ones obtained via a HysteresisGraph, equipment that provides the intrinsic magnetic material representation. The Figures 2.35a, 2.35c and 2.35e show the profile of the curves hysteresis loops obtained using, respectively, the HysteresisGraph, the methodology applied considering parallelism to the major hysteresis loop and finally, the one proposed in this thesis research according to the experimental results.

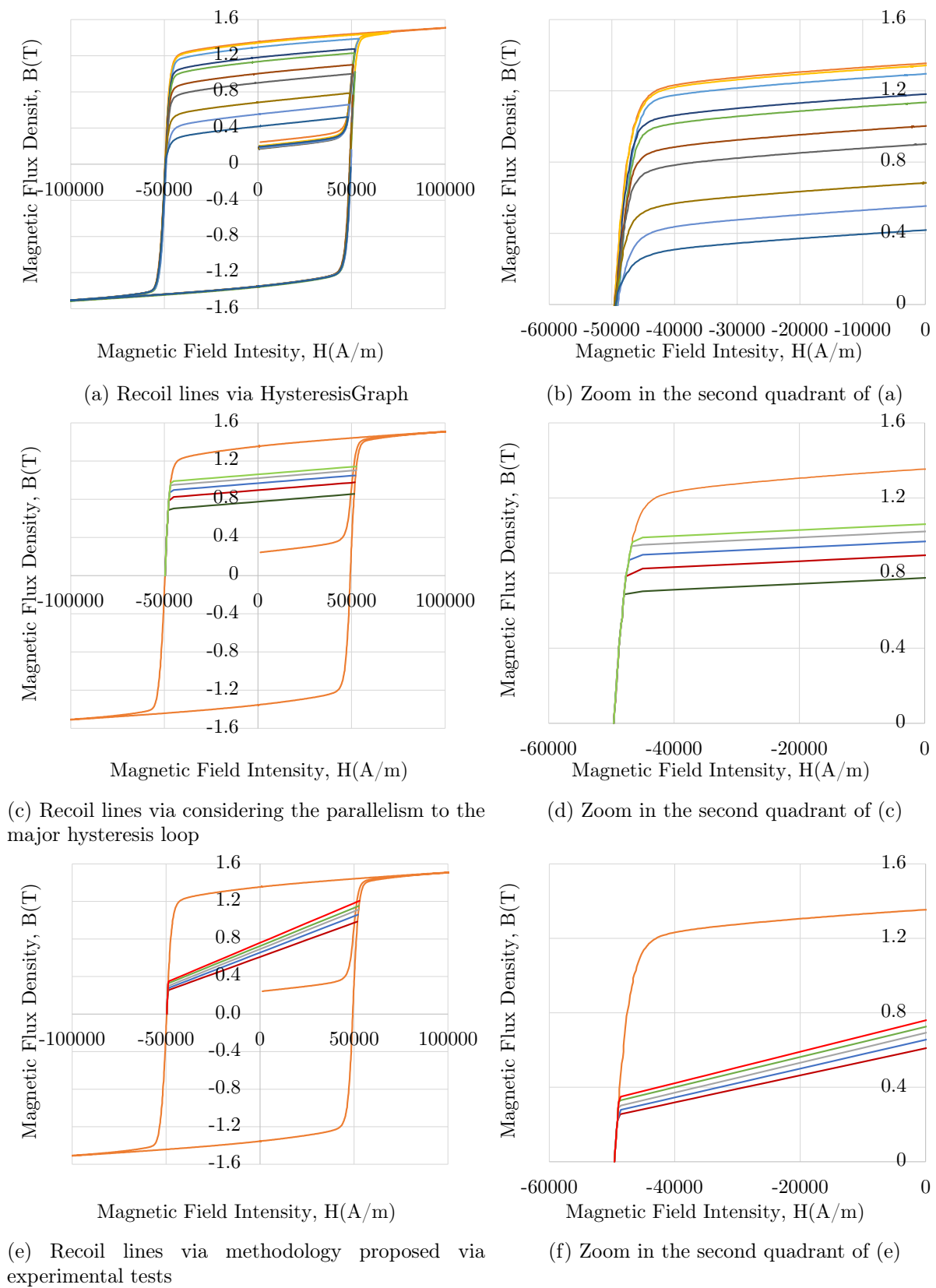


Figure 2.35: Recoil lines obtained via multiple strategies.

The most important conclusion observed from these curves is the higher slope (higher μ_r) of the demagnetization curves that characterize the partial magnetization states (internal BH-loops) of the Fe-Cr-Co estimated from the proposed methodology. A lower magnetic flux density characterizes the working points at the load line $I_{mag} = 0A$ considering these curves. Figure 2.36 exhibits a comparison proposed between these aforementioned recoil lines and the ones considering the parallelism to the external BH-loop. Results achieved after magnetization via currents pulses of amplitude $I_{mag} = 250A$ and $I_{mag} = 350A$ are going to be analyzed. In the case of a magnetization procedure via $I_{mag} = 350A$, for example, it can be noticed that a magnetization state of $MS = 50.9\%$ is achieved according to the results coming from the experimental tests (which defines a recoil line characterized by $Br = 0.69T$, $H_c = -49.6kA/m$ and $\mu_r = 6.39$), whereas $MS = 75.4\%$ was expected by using the hypothesis of a parallel hysteresis model (which defines a recoil line characterized by $Br = 1.02T$, $H_c = -49.6kA/m$ and $\mu_r = 1.25$).

Remark: The results obtained by the HysteresisGraph cannot be directly compared to the ones estimated by the methodology proposed in this thesis. This is because the correspondence between the amplitude of the current and the created magnetic field that crosses the sample in this measuring equipment is not known *a priori*. For this reason, the comparison proposed in Figure 2.36 exhibits the results obtained from the model considering the parallelism of the internal recoil lines to the major loop (a mathematical estimation of any recoil line, from any point of the initial magnetization curve, can be obtained by the knowledge of the external loop).

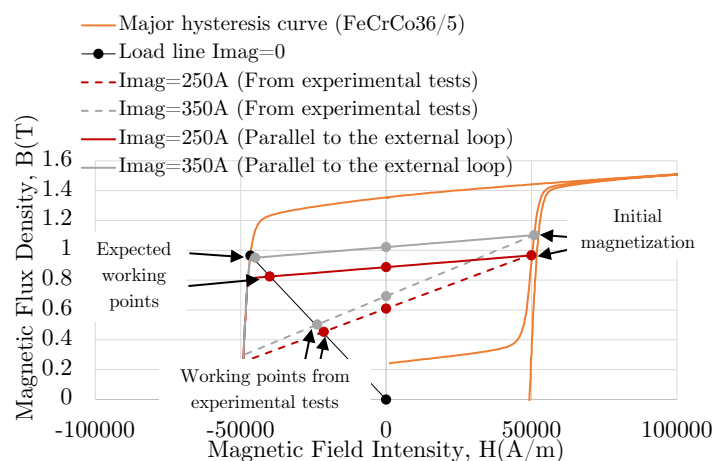


Figure 2.36: Recoil lines estimated by simulations after magnetization via $I_{mag} = 250A$ and $I_{mag} = 350A$, using as methodology the parallelism to the external loop and the experimental tests results.

2.7.2.3 Studies for analyzing the differences observed between the results achieved by the methodologies discussed

Figure 2.36 exposed the difference between the recoil lines traced using the parallel model (similar to the one provided by the HysteresisGraph) and the ones described from the analyses of the magnet in the machine environment. Investigations were carried out by FEA simulations for justifying these differences. The following key conclusions are obtained:

- First, results show that the closed slot wedges in the stator geometry, when not saturated, can represent an alternative path for the flux lines during the initial magnetization process.

As a consequence, the majority of flux lines will pass through the rotor allowing an effective magnetization only when the excitation field is sufficient to saturate these regions. However, this saturation procedure requires higher ampere-turns for ensuring the same flux crossing the magnet than the ones expected in an ideal circuit of measurement as the HysteresisGraph. Aiming to better understand this behavior, the excitation of the VFMM studied is compared to the one of a similar geometry in which the slot wedges are opened, as presented in Figure 2.37. The rotor characteristics are preserved, as well as the material used in the stator. It can be concluded via simulations that for achieving the same magnet flux density, lower ampere-turns (in this case, lower I_{mag}) are required for the machine designed with open slot wedges. These results can be analyzed in the Table 2.9. They define a strategy to approximate the characteristics of the recoil line in the first quadrant of the magnet inserted in the VFMM to those characterized via a HysteresisGraph (or via the parallelism proposed by the current literature).

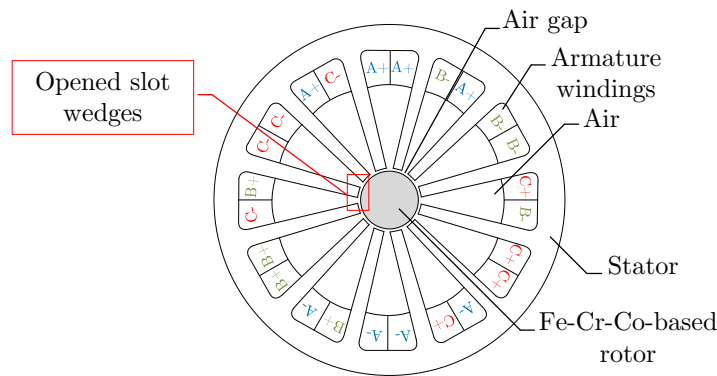


Figure 2.37: Machine geometry considering opened slot wedges.

Table 2.9: Study by FEA simulations of the effects of a stator geometry designed with closed slot wedges.

Working points in the initial magnetization curve			
Both geometries		Closed slot wedges	Opened slot wedges
Magnetic flux strength	Magnetic flux density	Magnetization current	
H_{exc} [kA/m]	B_{exc} [T]	I_{mag} [A _{pk}]	
0.97	50.23	250	240
1.05	50.66	300	275
1.10	50.95	350	330
1.14	51.23	400	350
1.19	51.52	500	410

- Until regarding the behavior of the magnet during the initial magnetization, effects of saturation on the yoke and stator teeth are observed even when low amplitudes of magnetization currents are used for supplying the machine (e.g., $I_{mag} = 250A$, which represents a considerably lower amplitude than the one required for saturating the magnet, around $I_{mag} = 1500A$). To demonstrate these phenomena, Figure 2.38a exhibits the level of induction measured in different portions of the machine when a $I_{mag} = 250A$ is injected in the armature windings considering the same current pattern used during the

experimental tests. Due to this described saturation of the stator material, the ampere-turns required for achieving the expected level of magnet flux density are considerably higher than would be without these effects. For a magnet inserted in the HysteresisGraph, however, the saturation of the core does not interfere with the achieved results, as the equipment is designed to measure the intrinsic properties of a magnet without the influence of the medium in which this magnet is inserted. For this, a high permeability non-saturable core is used. Therefore, to correct these saturation effects observed in the VFMM by approximating the conditions of magnetization in the machine to the ones of the HysteresisGraph, new simulations were carried out. In these, not only the open slot wedges in the stator geometry were considered, but also a modification of the stator material, that was replaced by a hypothetical ferromagnet saturating at a three times higher level of induction than the steel composing the real stator (COGENT NO20). Figure 2.38b exhibits the magnetic characteristics of this new material in comparison to that of COGENT NO20. The results in Table 2.10 demonstrate that by replacing the COGENT with this hypothetical material, the magnetization current required to achieve a certain level of excitation during the initial magnetization is reduced. By using them, the behavior of the recoil lines in the first quadrant can be corrected to be closer to the ones obtained using the HysteresisGraph.

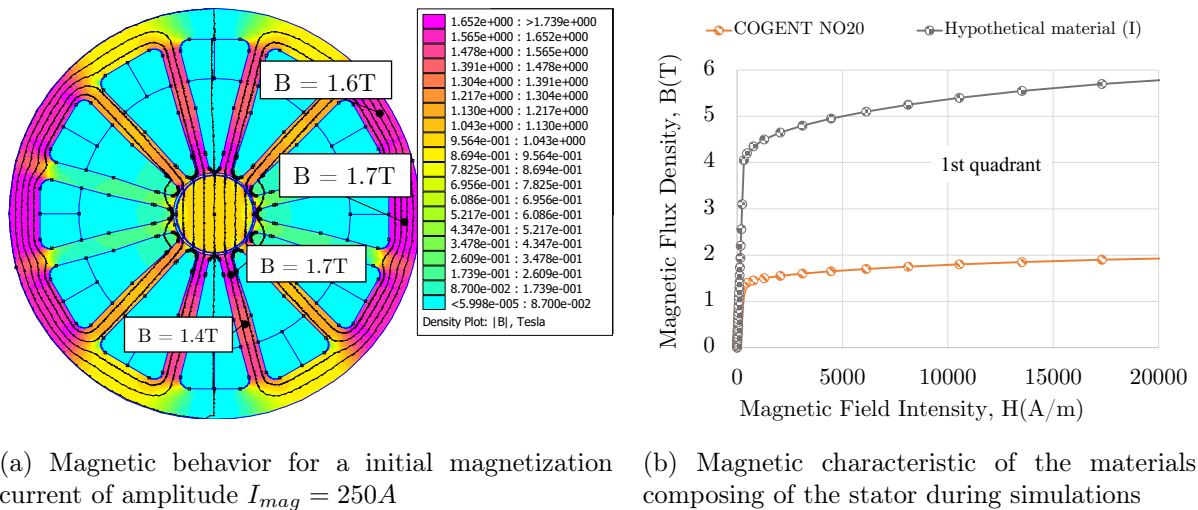


Figure 2.38: FEA simulations results regarding effects of stator material saturation.

Table 2.10: Study by FEA simulations of the effects of the stator material saturation.

Working points in the initial magnetization curve			
Both geometries		Closed slot wedges and saturable steel	Opened slot wedges and non-saturable steel
Magnetic flux strength	Magnetic flux density	Magnetization current	
H_{exc} [kA/m]	B_{exc} [T]	I_{mag} [A_{pk}]	
0.97	50.23	250	223
1.05	50.66	300	234
1.10	50.95	350	242
1.14	51.23	400	249
1.19	51.52	500	257

- Next, an investigation focused on the induction of the back-EMF while the machine is running ($\Omega \neq 0rpm$) is proposed. Once the magnet is initially magnetized at standstill and the external field is suppressed ($I_{mag} = 0A$), all the flux lines crossing the rotor are expected to induce in the armature windings a flux linkage and, consequently, a back-EMF in a set regime. For the VFMM studied in this research, it is observed that the presence of non-saturated closed slot wedges in the stator can provide an alternative path for the magnet flux that is short-circuited instead of crossing the stator windings. Hence, the portion of the magnet that contributes to the generation of back-EMF ("active" portion of the magnet) is reduced. Figure 2.39 presents this effect in the VFMM at $I_{mag} = 0A$ for which the rotor is characterized considering an initial magnetization at $I_{mag} = 250A$ (therefore, the load line presented in Table 2.8 for $I_{mag} = 250A$ defines the magnetic rotor properties). Analyses demonstrate that the leakages represent almost 12% of the total magnet flux.

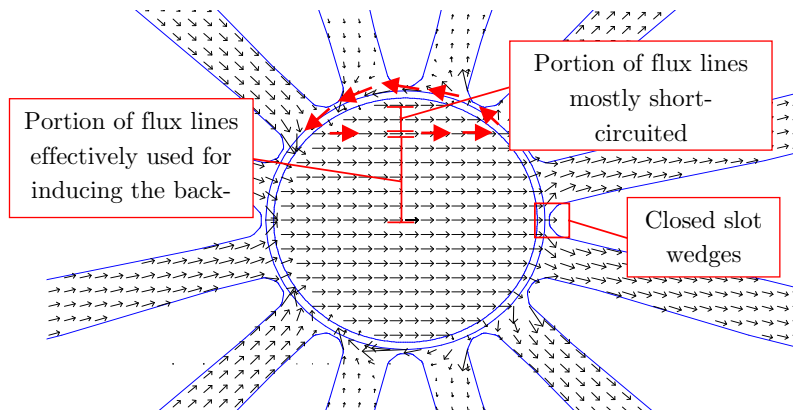


Figure 2.39: Short-circuit of the magnet flux lines at no-load observed from simulations by the vector plot for the magnet manufactured for being magnetized in the easy magnetization direction (zoom in the rotor).

Table 2.11 exhibits the flux leakage observed considering the magnet characterized by the other recoil lines described in Figure 2.35e. Compensating these leakages, the flux through the stator windings is hypothetically enhanced and the new working point placement in the second quadrant of the hysteresis loop can be estimated by the same methodology described in Figure 2.31. These results allow correcting the working point placement on the second quadrant of the hysteresis loop and approximate the magnetic behavior observed in the recoil lines to the one observed in the HysteresisGraph. It should be remembered that the stator geometry designed for the VFMM studied in this research was initially designed for a PMSM. The Nd-Fe-B magnet equipping this PMSM has a high level of remanence (around 1.2T) for all the working conditions, which is normally sufficient to saturate the closed slot wedges present in the stator geometry when the machine at standstill. Nevertheless, because of the low remanence of the Fe-Cr-Co when the magnet is in partial magnetization conditions (as the ones describing the internal hysteresis loops studied in Figure 2.35e), these slot wedges are not saturated, and the flux leakage effects are consequently observed.

- Due to the parallel magnetization of the cylindrical rotor used in the VFMM studied, the magnet length crossed by the flux lines changes for each portion of the rotor studied. The section 2.3.1 exposed this magnetization characteristic and mentioned the simplifying assumption of defining the magnetic flux density of each working point by using the integral of \vec{B} over the rotor. The slope of the load line $I_{mag} = 0A$ used in the studies presented

Table 2.11: Study by FEA of the effects of the short-circuit of magnetic flux lines.

		Working points in the load line $I_{mag} = 0A$					
Magnetization current	% of losses due to flux leakage	Before corrections			After corrections		
		of short-circuit effects (experimental tests)			of short-circuit effects (simulations)		
		Flux linkage	Relative permeability	Remanence	Flux linkage	Relative permeability	Remanence
I_{mag} [A _{pk}]	[%]	φ_s [μWb]	μ_r [unitless]	B_r [T]	φ_s [μWb]	μ_r [unitless]	B_r [T]
250	12	453.0	5.78	0.61	514.7	4.39	0.64
300	12	483.9	6.17	0.66	549.9	4.26	0.67
350	11	509.9	6.39	0.69	572.9	4.17	0.70
400	11	533.6	6.47	0.73	599.6	3.99	0.72
500	11	559.3	6.72	0.76	628.4	3.87	0.74

in the evaluation of the magnetic behavior of the FeCrCo36/5 was calculated according to this level of magnetic flux density obtained using this described integral. However, because as mentioned, the magnet length changes, a more precise study of the working points would require load lines defined for each one of these magnet portions and the use of the methodology proposed for each one of these cases.

- The last item to be discussed refers the shape anisotropy. In the section [1.1.2](#) this propriety is described as the reason for an internal demagnetizing field (H_d , in [A/m]) that reduces the effective field (H_{eff} , in [A/m]) on a magnet body exposed to an external magnetization field (H_{ext} , in [A/m]). This reduction can be quantified by the equation below:

$$\vec{H}_{eff} = \vec{H}_{ext} - \vec{H}_d = \vec{H}_{ext} - N_d \vec{M} \quad (2.17)$$

where N_d is the coefficient that represents the demagnetizing factor, assuming values between 0 and 1 according to the magnet shape [57](#). Studies presented in [61](#) and [122](#) are focused on the calculation of the demagnetizing factor for different sample shapes.

When a magnet is characterized using a HysteresisGraph, a closed magnetic circuit of measurement, the applied ampere-turns are totally absorbed by the sample studied (uniform magnetization). Hence, the external field is equal to the effective one crossing the sample [114](#), [119](#), or $N_d = 0$. For a magnet inserted in the VFMM studied, however, due to the leakage flux and saturation effects in the stator, this uniformity is not present. The magnetic behavior observed in the machine environment is closer to one of the open magnetic circuits of measurement, in which the sample properties are affected by the demagnetizing field that varies according to the sample geometry [123](#), [124](#). This might explain the last differences between the experimental and the HysteresisGraph results. In [58](#) authors present the distinctions between BH-loops of hard magnets obtained using open (a vibration sample magnetometer) and closed magnetic circuits of measurement. For the system studied by these authors, a difference in the order of 25kA/m is observed between the measures realized using these two methods (closed and open). The measurement time is also mentioned as a source of the differences observed between these two experimental results that are strictly related to the magnet geometry used.

Multiple authors investigated methods for correcting possible differences between measurements realized via open and closed magnetic circuits. In [123](#), authors are focused

on describing a method based on a mathematical function repeatedly modified in a finite-element method in computer calculation. The authors in this paper mention the difficulties of reproducing an intrinsic magnetization curve by deforming an open magnetic circuit curve, especially due to the complexity of the spatial distribution of the demagnetizing field in the sample. In [124], a methodology is described considering a variable demagnetizing factor dependent on the differential susceptibility and the length-to-diameter ratio of a cylindrical magnetic sample. The use of these methods, however, extrapolates the objective of this thesis. The correction of effects regarding the anisotropy shape will not be considered in this present research but remains a future perspective.

Remark: The demagnetizing effect is only important for the VFMM studied in this thesis because the machine was not originally designed for LCF magnets and was adapted from a PMSM geometry by replacing the Nd-Fe-Br-based rotor by a Fe-Cr-Co-based rotor. Machines designed for VFMMs are specifically manufactured to avoid the saturation and flux leakage effects, and consequently, the demagnetizing effects are reduced. For this reason, future work foresees the development of new machine geometry, considering adaptations such as the use of a less saturable iron and open slot wedges composing the stator design and flux barriers in the rotor one.

Figure 2.40 exemplifies the impact in the definition of the recoil lines of correcting the effects above discussed for placing the working points in the first and second quadrants. An example considering the magnetization procedure via current pulses of amplitude $I_{mag} = 350A$ is presented. It can be noticed that the corrected recoil line is characterized by a lower level of magnetic flux density in the initial magnetization curve, while a higher \vec{B} is observed for the working point at the intersection with the load line $I_{mag} = 0A$. The relative permeability characterizing the corrected recoil line is thus reduced in comparison with the one obtained before the correction of the effects discussed. Hence, the slope of this corrected recoil line is closer to the one observed in the major hysteresis loop.

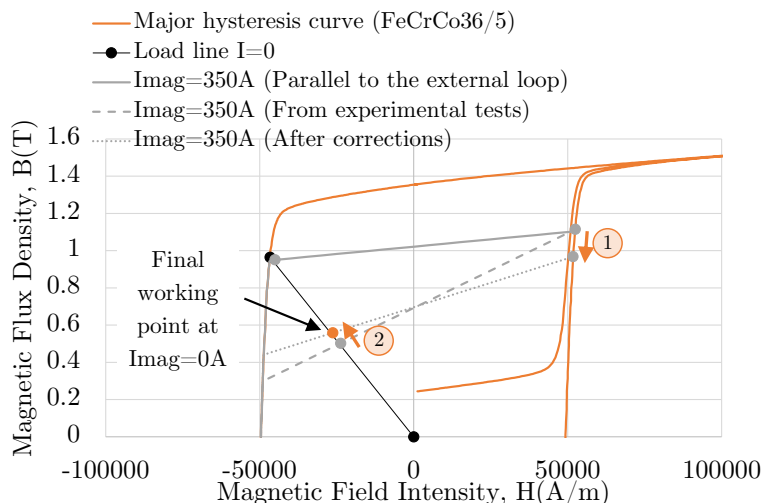


Figure 2.40: Examples of recoil lines obtained by simulations for magnetization via $I_{mag} = 350A$, where the hysteresis model is corrected considering (1) the effects of saturation and closed slot wedges during the initial magnetization and (2) the flux leakage during back-EMF induction.

Table 2.12 shows the difference between the relative permeability provided by the external demagnetization loop measured via HysteresisGraph, the one calculated considering the

experimental results and the one calculated considering the experimental results after corrections. Figure 2.41 exhibits these corrected recoil lines for some magnetization current amplitudes. As discussed before for the recoil lines estimated for $I_{mag} = 350A$, it can be observed that for all current amplitudes, the corrections proposed allow the reduction of the relative permeability and, consequently, the approximation of the profile obtained to the one observed by results provided via HysteresisGraph. Differences are still observed between these curves, probably due to some aspects of the proposed investigations that are not optimized, such as the demagnetization effect due to the shape anisotropy, the saturation profile of the iron used in the stator (that is not intrinsically characterized), and the analysis of different load lines for each portion of the magnet. Nevertheless, these investigations provide a good estimation of the magnet behavior when inserted in the machine environment and open perspectives for future improvements in the model proposed.

Table 2.12: Estimation by FEA of the recoil lines.

Relative permeability characterizing the recoil line				
Magnetization current	Reference (HysteresisGraph)	Calculated from experimental tests	After corrections on the initial magnetization	After corrections on the back-EMF induction
I_{mag} [A _{pk}]	μ_r [unitless]	μ_r [unitless]	μ_r [unitless]	μ_r [unitless]
250	1.25	5.78	5.19	4.39
300	1.25	6.17	5.07	4.26
350	1.25	6.39	4.93	4.17
400	1.25	6.47	4.76	3.98
500	1.25	6.72	4.64	3.87

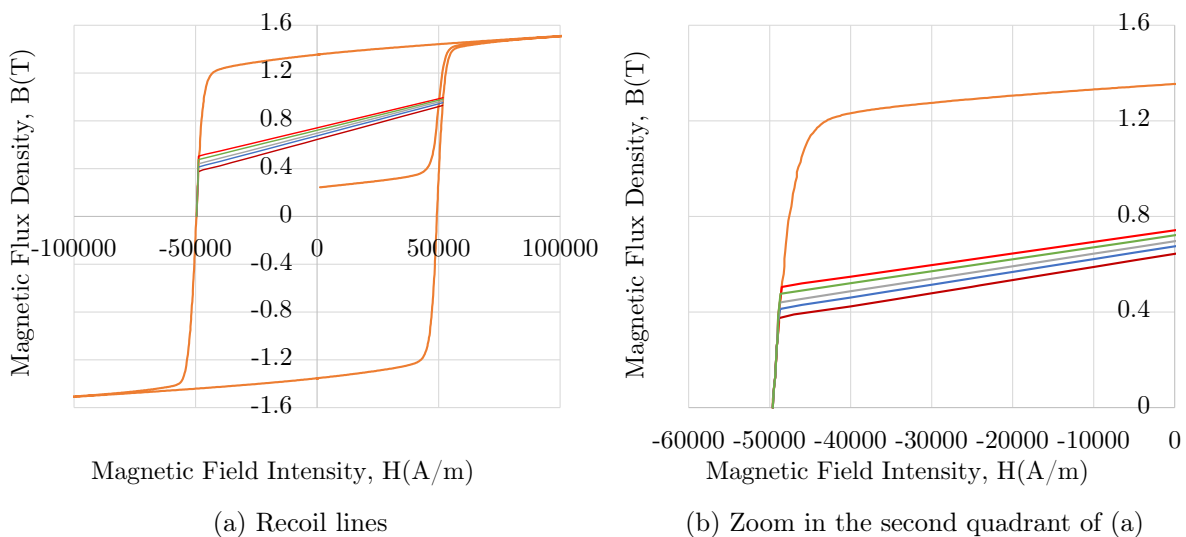


Figure 2.41: Recoil lines obtained correcting the methodology proposed for approximating the magnetic behavior of the machine to the one of the HysteresisGraph.

2.7.3 Evaluation of the demagnetization results

By the same methodology proposed in the section 2.4.0.1, FEA simulations are carried out in this present section for evaluating the demagnetization results experimentally obtained (they are

reminded in the Figure 2.42b). The importance of this study is related to the identification of the negative d-axis current amplitude that leads the working points initially placed at the load line $I_{mag} = 0A$ to the intersection with the major hysteresis loop. From this point, minimal increments of the excitation field generate a strong demagnetization, as the relative permeability of the hysteresis loop in this region is considerably higher than the one characterizing the internal recoil line. Knowledge of this level of current is particularly critical for evaluating two possible effects in the machine: (1) the armature reaction of the machine and (2) in case of reluctance, the amplitude of negative d-axis currents that are allowed to be regulated in the machine before a demagnetization of the Fe-Cr-Co-based rotor. This last-mentioned effect is part of the studies proposed in Chapter 3.

Within this context, simulations are going to be realized in this section for investigating the machine behavior when exposed to an external field created by negative d-axis currents supplying the armature windings. The recoil line estimated according to the methodology presented in the section 2.7.2.1 for $I_{mag} = 250A$ (therefore a $B_r = 0.61T$ and $\mu_r = 5.78$), is going to be incorporated to the rotor for the proposed simulations. This level of initial magnetization is chosen for reproducing in these simulations the same condition as imposed during the experimental tests. Supplying the machine with $I_{mag} < 0A$ for creating a d-axis field contrary to the magnetization one, the results summarized in Figure 2.42a are obtained. It is observed that an amplitude of $I_{mag} = -78A$ is theoretically required for displacing the recoil line $I_{mag} = 0A$ to the intersection with the major loop. Therefore, only pulses of current exceeding this current limit would be expected to lead the working point to a lower recoil line (so a lower magnetization state) after the suppression of currents. These lower recoil lines can be estimated by the assumption of a parallelism to the one defined for $I_{mag} = 250A$, and, therefore, considering that the same relative permeability ($\mu_r = 5.78$). The working point at the external magnetization loop (defining a pair B_m, H_m), achieved for different negative d-axis current amplitudes, is used for calculating the remanence characterizing the estimated recoil lines. For this, the equation $B_r = B_m - \mu_r \mu_0 H_m$ is used. FEA simulations for $I_{mag} = 0A$ are then proposed using each one of these recoil lines in order to calculate the flux through the stator windings and, finally, to estimate the back-EMF expected to be measured. The results obtained are exhibited in Figure 2.42b and compared to the ones experimentally achieved. It can be observed that the demagnetization effects are observed in these experimental tests for current pulses of amplitude $I_{mag} < -30A$, not $I_{mag} < -78A$ as expected via simulations using the recoil line proposed.

At this point, it should be reminded that the parallelism between the recoil lines proposed by the linearization of the recoil lines is a simplification of the real behavior of these curves that does not take into account the existence of a knee connecting these mentioned recoil lines and the external hysteresis loops. Hence, for recoil lines such as the one presented in Figure 2.42a, amplitudes of demagnetization current higher than $I_{mag} = -78A$ are expected to provide the same back-EMF when the currents are suppressed because the return path taken by the working points is always the same one. The Figure 2.43 illustrates this case. A working point initially placed at the intersection with the load line $I_{mag} = 0A$ in point 1 is shifted to the external BH-loop in point 2 for a demagnetization current $I_{mag} = -78A$ and returns to point 1 when this demagnetization current is suppressed. The presence of knees, however, modifies the relative permeability of the recoil lines and consequently, in the case of a current suppression, the working points trace a return path by a new recoil line. Figure 2.43 illustrates this path via the working points 1-3. The return to the intersection with the load line $I_{mag} = 0A$ occurs by 3-4, defining a reduced level of magnetization when the demagnetization current is suppressed.

Because of the exposed difference between the experimental results and the ones achieved via simulation using the linear recoil line, an optimization of the model for defining this curve

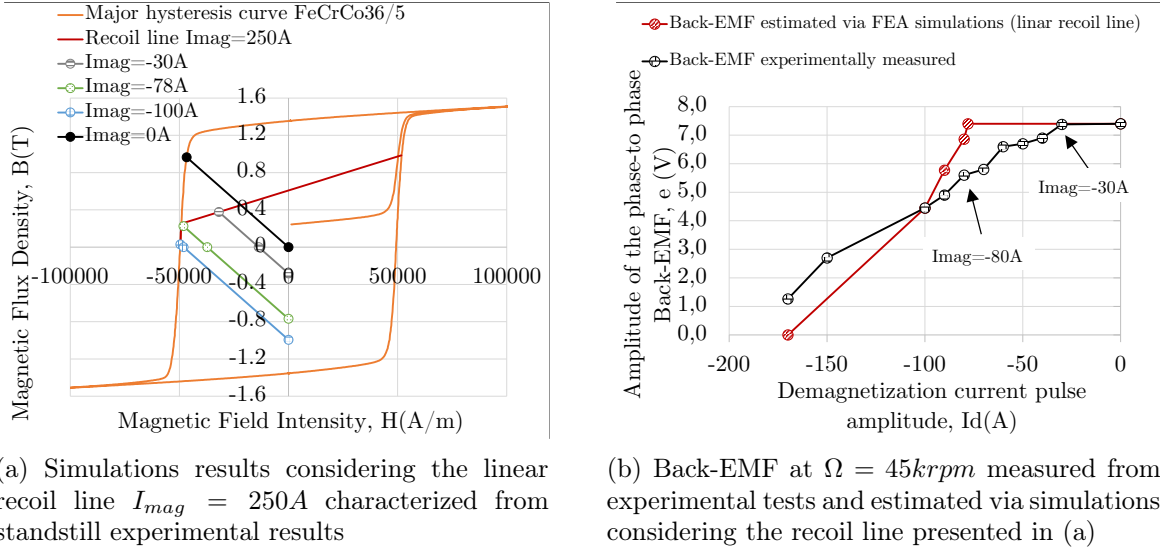


Figure 2.42: Studies of the magnetic behavior of the VFMM during demagnetization procedures.

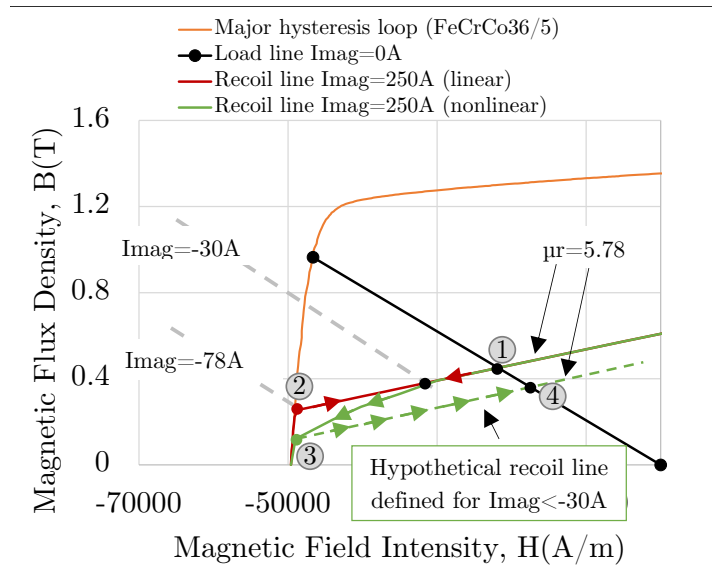


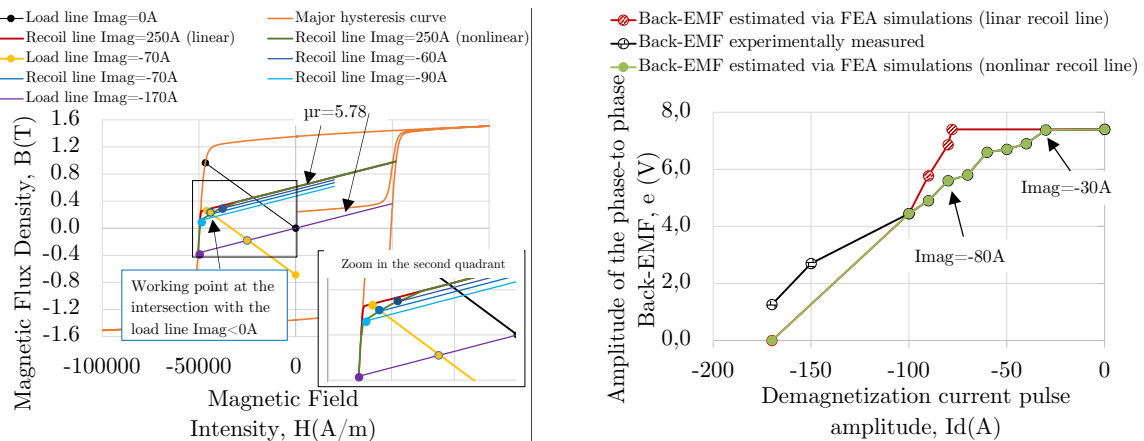
Figure 2.43: Illustration of the path traced by the working point considering the linear and nonlinear recoil lines.

is proposed. The methodology used for characterizing the knee from the experimental results is based on the one proposed in the previous sections (see section [2.7.2.1](#), which describes these steps). First, the back-EMF experimentally measured is used for calculating the flux crossing the armature windings. Using this reference, simulations are carried out considering hypothetical magnetic materials incorporated into the rotor considering that the relative permeability remains unchanged ($\mu_r = 5.78$). Each BH pair (B_m and H_m) characterizing the working point at the intersection with the load line $I_{mag} = 0A$ can therefore be identified. The equation $B_m = \mu_0\mu_r H_m + B_r$ is then used for calculating the remanence B_r of each recoil line. Finally, a hypothetical knee is estimated from the points of intersection of these different recoil lines and the load line corresponding to each current amplitude used to demagnetize the machine.

Attention is also given to the level of current required for the complete demagnetization of the

VFMM studied. For ensuring a null back-EMF when the currents are suppressed, simulations demonstrate that a demagnetization current pulse of $I_{mag} < -170A$ is required. Experimentally, the amplitude of demagnetization current sufficient to reduce the magnetization state of the magnet to zero is $-200A < I_{mag} < -170A$. This similarity between the results demonstrates that the model proposed for the recoil lines provides a good order of magnitude for estimating the experimental currents. The Figure 2.44a exhibits the complete hysteresis cycle obtained considering FEA simulations.

Remark: The precise level of current that provides $e = 0V$ is hard to be identified experimentally. For this reason, a range of currents is presented here ($-200A < I_{mag} < -170A$) as a reference.



(a) Internal recoil lines estimated considering nonlinear recoil line $I_{mag} = 250A$ proposed by methodology described

(b) Back-EMF at $\Omega = 45krpm$ measured from experimental tests and estimated via simulations considering the linear and nonlinear recoil lines

Figure 2.44: Studies of the magnetic behavior of the VFMM during demagnetization procedures.

Remark: As exposed, the knee proposed in Figure 2.44a is defined according to the experimental results obtained during the demagnetization procedure. This approach is the same as that used in the former sections for the definition of the recoil lines. Without previous knowledge of these results, an additional option for estimating the mentioned knee for the internal curves would be to consider that they have a similar profile as the one exhibited by the external one. By this assumption, it is expected that the back-EMF estimated via simulation would be slightly different from the one experimentally measured, but by a good order of magnitude.

2.8 Conclusions of Chapter 2

The second chapter of this thesis work was focused on developing a comprehension of the magnetic behavior of the proposed Fe-Cr-Co-based Variable Flux Memory Machine. Based on the concepts introduced in Chapter 2, this chapter explores the magnetization of the proposed AC-magnetized Fe-Cr-Co-based VFMM at standstill ($\Omega = 0rpm$). For supplying the machine with the short-time current pulses required for modifying the rotor magnetization state, a power electronics setup is presented in the section 2.2. This system, developed at IFP Energies nouvelles, is designed as a two-level voltage source inverter (VSI) embedded with customized software allowing magnetizations in DC/DC mode without requiring supplementary components and with no neutral access. Also in this section, the geometry specifications of the VFMM are described.

As a result of the rotor magnetic anisotropy, verified using a HysteresisGraph, the differentiation of the two possible magnetic responses of the FeCrCo36/5 when submitted to an external field demonstrated to be particularly important: first, a hysteresis loop exhibiting no well-defined knee in its second quadrant for the rotor manufactured for being crossed by the magnetic flux in its hard magnetization direction and second, a hysteresis loop described by this well-defined knee in its second quadrant, presenting, therefore, a magnetic behavior similar to the ones observed for grades AlNiCo5 and AlNiCo9 commonly used in VFMM applications, for the rotor in which the easy direction defines the magnetization axis.

For this mentioned hard magnetization direction, the major hysteresis loop presents a high relative permeability in all portions of the demagnetization curve, which leads to challenges regarding the regulated variation of the magnetization state and enhanced effects of the armature reaction. Also, a low torque capacity is observed as a consequence of the low remanence (around 38% of that of typical Nd-Fe-B magnets). Despite these inconveniences, the interest in studying this magnet arises from the fact that some other low coercive magnet grades, such as the FeCrCo12/4, whose magnetic profile is described in Appendix B.3, are characterized in both easy and hard magnetization directions by this absence of knee in the hysteresis loop. Therefore, the objective of these studies was to address the lack of research exploring this magnetic profile based on experimental results and simulation via Finite Element Analysis. For easy magnetization direction, a similar approach is proposed from an in-depth study investigating the standstill magnetization of a machine supplied by different amplitude and time-duration d-axis currents. It is noticed that for the same magnetization current amplitude supplying these both machines, the one composed of the rotor magnetized in the hard magnetization direction generates a substantially lower back-EMF (for $I_{mag} = 600A$, as an example, a 16 times lower back-EMF is measured).

The investigation of internal hysteresis loops for characterizing the partial magnetization of the FeCrCo36/5 is also analyzed in this chapter for both magnetization directions. This study will be used as a reference for the running magnetization in the next chapters. First, the intrinsic BH-loops (major and minor) obtained using a HysteresisGraph are presented. Because this measuring equipment is expensive and rarely available in the industry, it is typically restricted to research institutes or laboratories dedicated to materials characterization. Practical applications require an accurate model that estimates the behavior of the recoil lines. For magnets having no knee in the second quadrant of the BH-loop, the scientific literature investigating VFMMs until the moment does not introduce an adapted model for determining the recoil lines. Within this context, the Appendix B.7 is dedicated to these studies, describing a model based on the hypothesis of parallelism between both major and minor hysteresis loops for defining the behavior of the recoil lines, as observed by the results provided by the HysteresisGraph. Next, the use of the same parallelism hypothesis is proposed for describing the recoil lines of the magnet manufactured for being crossed by the flux lines in the easy magnetization direction. This model, as formerly mentioned, is expected to provide results similar to the ones obtained using the HysteresisGraph demonstrated not to be capable of describing the recoil lines of the FeCrCo36/5 inserted in the VFMM environment, as the levels of back-EMF experimentally obtained for both machines investigated are considerably lower than expected by these models. Studies revealed that four major factors can be used to justify the low levels of magnetization obtained for both machines. First, analysis demonstrated that a higher excitation field is measured in the magnet inserted in the considered machine than in a measuring equipment, as a consequence of using closed slot wedges in the stator geometry. These regions should be saturated before the flux lines excite the magnet in the machine, but this process is not required in a HysteresisGraph. Also, because of the stator geometry and the presence of closed slot wedges, a magnet leakage flux is present during the measurement of the back-EMF at standstill. This reduces the flux linkage

that effectively passes through the stator windings. An additional reason for the difference observed between the results can be justified by the saturation of the material composing the stator. The magnetic characteristic of this material leads the stator yoke and stator to saturation during the initial magnetization of the magnet. Because this effect is present in the VFMM but not in the measuring equipment, higher levels of ampere-turns are required for magnetizing the magnet inserted in the machine. Additionally, the simplification proposed for calculating the magnetic flux density used for describing the slope of the load line $I_{mag} = 0A$ does not take into account the magnet flux length that varies according to each portion of the magnet considered. This assumption can contribute to the errors observed between the results obtained from the methodology proposed and the ones observed from the HysteresisGraph. Finally, the reduction of the excitation field estimated by the methodology discussed can be justified by the effects of the self-demagnetization of the magnet equipping the machine (which represents an open circuit of measurement). Given all these conclusions, a methodology for compensating these phenomena is proposed for adapting the results achieved by experimental tests to the ones obtained by the HysteresisGraph. Based on these results developed at standstill, the next chapter will propose the running magnetization of the Fe-Cr-Co-based VFMM.

Finally, a study is realized to evaluate the experimental results provided by the demagnetization of the VFMM. A comparison between the back-EMF experimentally measured after injection of current pulses of negative amplitude (dedicated, in this case, to creating a field in the opposite direction of the magnetization one) and the one estimated from FEA simulations, demonstrate that adjustments are necessary for the recoil lines initially proposed. Investigations demonstrated that this difference can be corrected by supposing a nonlinear behavior for these recoil lines. For this reason, a knee in the second quadrant of the hysteresis loop is proposed for a more accurate description of the magnetic behavior of the Fe-Cr-Co.

Chapter 3

Running Magnetization Strategy of a Fe-Cr-Co-based Variable Flux Memory Machine

This chapter is focused on the investigation of the running magnetization strategy applied to the Fe-Cr-Co-based Variable Flux Memory. The machine geometry in which the magnetic flux crosses the rotor in its easy magnetization direction is going to be used. Operations on-load are described in this chapter. As the injection of the currents into the armature windings of VFMMs depends on the knowledge of the direct-axis and quadrature-axis for promoting, respectively, the magnetization or torque control in the machine, the identification of the rotor position has been demonstrated to be critical. More specifically for the machine geometry proposed, which is dedicated to high applications and for which the regime is driven by an axial airflow (no torque control at low speeds), a sensorless strategy is chosen. In this context, this research proposes the development of a phase-locked loop-based algorithm for estimating the rotor position and speed from the output voltages measured in the machine. An additional stage is also developed for composing this system with the correction of angles that can affect this estimated position. The study of the adjustments of these angles for different working conditions is also discussed.

3.1 Introduction of sensorless strategies

A dynamic manipulation of the current vector ($I = I_d + jI_q$) feeding stator windings of a VFMMs (when $\Omega > 0rpm$) is realized using the well-known Field Oriented Control (FOC) (see section [1.3.5](#)). This control strategy is based on the transformation of the electrical variables related to the stationary reference frame (the stator) into ones related to the flux reference frame (the rotor) [\[125\]](#), as already exposed in the section [1.3.3](#). The decoupling of the torque and the magnetization control is the most interesting achievement of this methodology.

The basis of using an FOC is described in [\[126\]](#) by the analysis of the separately excited DC machine. For this machine, the armature current and the stator flux can be independently adjusted. First, the flux is regulated by the magnitude of the field excitation current. For a constant flux, the torque can be calculated according to the current supplying the rotor windings, which are managed using a mechanical commutator to ensure a flux production orthogonal to the stator field (or current). For PMSMs, as also for VFMMs, torque, and flux are coupled, and therefore a FOC is required to allow their separated control. Because the armature windings are positioned within the stator, an electronic commutation is used via a switching circuit and a three-phase inverter topology [\[127\]](#). In this methodology, the rotor position (θ) information

is critical for an efficient current/torque control (which affects directly the produced/consumed energy) [25, 126]. The angle θ characterizing the rotor position is usually mechanically obtained from the use of incremental or absolute encoders or resolvers. Nevertheless, some inconveniences are related to the use of these sensors, as additional costs, maintenance requirements, and sensitivity increase [42, 128, 43]. Particularly for high-speed machines as the one considered the object of study for this present thesis, the use of these sensors can be considered unpractical. For similar applications, multiple sensorless methods are introduced in the literature for extracting the rotor position information. Two main categories are often presented for classifying the sensorless strategies dedicated to PMSMs [46, 42, 128, 43]:

- Model-based methods (also known as back-EMF-based methods): generally related to the observation of the flux associated with the fundamental excitation ([129, 130]) or the back-EMF, via several types of observers, as the Luenberger observers [131, 132], sliding-mode observers (SMOs) [133, 134], or others, as presented in [135, 136]. These models are dedicated to high-speed applications [129, 137] since the back-EMF measured is proportional to the speed. At low or zero speed, especially during the system initialization, the use of them is consequently limited. Model-based methods can still be subdivided into open- and closed-loop methods, assuming for both a sinusoidal air gap flux density (spatial harmonics and their effects are neglected) [138]. For open-loop, a direct integration of the back-EMF is realized for estimating the rotor position without considering corrections terms, whereas a closed-loop method is going to take into account the error between the estimated and measured quantities as feedback for achieving better algorithm performance.
- Inductance variation methods (also known as saliency-based methods): For these methods, the rotor position is estimated by tracking inductance variations caused by a magnetic saturation and/or effects of geometrical saliency [133]. They are characterized by a good performance in a wide speed range but can generate torque ripples and power losses, besides being sensitive to parameter variations or measurement noises [133, 139]. Saliency-based methods can be divided into signal injection-based models [139, 140] and fundamental pulsewidth modulation (PWM) excitation (FPE)-based methods, [137, 141]. These methods are, however, limited to salient machines [129].

The description of each aforementioned sensorless strategy is out of the scope of this thesis research. A complete overview of the methods above mentioned can be studied in [43] and [137].

3.2 The use of sensorless strategies in VFMM applications: proposition a sensorless PLL-based strategy for the Fe-Cr-Co-based VFMM

Regarding VFMMs, the definition of the direct-axis and quadrature-axis is particularly critical. As previously discussed, not only does the variation of the magnetization state (MS) depend on the injection of currents to create a flux in the magnetization axis (or d-axis), but the torque control depends on the injection of currents in the q-axis. Unintentional demagnetizations can happen when the rotor position is not well known. Because of the importance of this information, most of the setups presented in the literature consider the use of a position sensor [74, 34, 31, 142]. Nevertheless, as the Fe-Cr-Co-based machine proposed by this present research is dedicated to high-speed applications, for which the least unbalance on the rotor shaft is very harmful, the use of sensorless strategies is required [25, 44, 45]. Additionally, due to the pre-defined regime imposed on the machine by an external axial airflow (no operations at zero speed), a simplified

model-based algorithm is used. Within this context, this thesis research adapts a sensorless strategy initially developed at IFP Energies nouvelles (see [25]) for estimating the speed and rotor position of the Fe-Cr-Co-based VFMM. This section is dedicated to presenting this system structure as well as its integration with the machine control strategy.

By using a PI-PLL (Proportional-Integral Phase-Locked Loop), the rotor position and speed can be estimated from the three-phase output voltages measured in the machine. The information about the voltage angles (θ_v) is included in these measures as described by:

$$V_{abc} = V_{max} \begin{bmatrix} \sin(\theta_v) \\ \sin(\theta_v - \frac{2\pi}{3}) \\ \sin(\theta_v - \frac{4\pi}{3}) \end{bmatrix} \quad (3.1)$$

where V_{max} is the peak voltage of each phase. As introduced in Chapter 1, three-phase quantities can be represented in a two-axis orthogonal stationary reference frame ($\alpha\beta$) by using a Clarke Transformation (see 1.3.3). By Park Transformation, this last-mentioned stationary reference frame can be converted into an orthogonal rotating reference frame. Due to the use of a PLL for estimating the rotor position, an additional estimated reference frame is also defined. Using a voltage vector as reference ($\vec{V} = [V_a \ V_b \ V_c]$), the following reference frames can be therefore established:

- the stationary $\alpha\beta$ -reference frame, related to the stator/machine quantities, expressed as $\vec{V} = [V_\alpha \ V_\beta]$.
- the rotating dq-reference frame, related to the rotor, expressing $\vec{V} = [V_d \ V_q]$.
- the \widehat{dq} -reference frame or dq_{PLL} -reference frame, regarding the estimated quantities by the PLL-based sensorless algorithm, expressed as $\vec{V} = [V_{d_{PLL}} \ V_{q_{PLL}}]$.

which defines:

$$\begin{aligned} V_{dq} &= P(-\theta)V_{\alpha\beta} \\ V_{dq_{PLL}} &= P(-\theta_{est})V_{\alpha\beta} \end{aligned} \quad (3.2)$$

Therefore, by Clark (C_{23}) and Park ($P(-\theta_{est})$) transformations, $V_{dq_{PLL}}$ are calculated by:

$$V_{dq_{PLL}} = \begin{bmatrix} V_{d_{PLL}} \\ V_{q_{PLL}} \end{bmatrix} = P(-\theta_{est})C_{23}V_{abc} = V_{max} \begin{bmatrix} \sin(\theta_v - \theta_{est}) \\ -\cos(\theta_v - \theta_{est}) \end{bmatrix} \quad (3.3)$$

being $V_{dq_{PLL}}$ the dq-PLL voltages and θ_{est} the angle estimated. This angle θ_{est} is going to be equal to the voltage vector angle θ_v when $V_{d_{PLL}}$ is null, or more specifically, if $\Delta\theta = \theta_v - \theta_{est} = 0$. The PI-PLL is therefore used to regulate $V_{d_{PLL}}$ to the reference $V_{d_{PLL}}^* = 0$. Figure 3.1 illustrates the PLL formerly described. The rotor speed is directly obtained from this algorithm, but the complete definition of rotor position requires also the compensation of phase shift generated by the estimation system. The next sections will better describe these angles and characterize the global compensation phase shift ($\Delta\theta_c$) to be considered for the precise estimation of the rotor position.

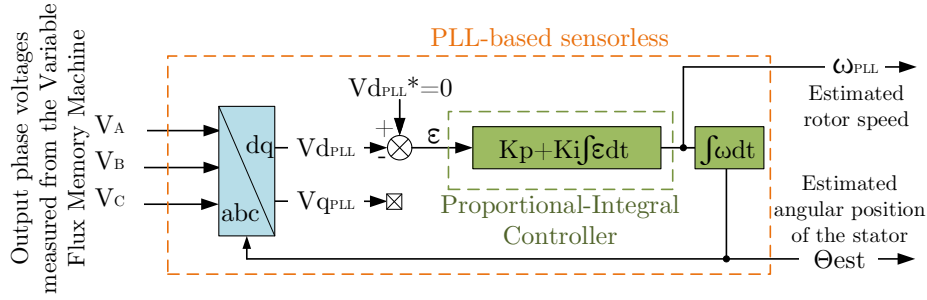


Figure 3.1: Block diagram of the PLL-based algorithm.

Remark: The use of sensorless techniques for VFMMs is still little explored. The first study discussing this topic was very recently presented for the first time in [46], which proposes a saliency-based sensorless control for a dual-layer AC-magnetized hybrid VFMM. A high-frequency voltage signal injection is used via a pulsating square-wave voltage injected in the rotor reference frame.

3.2.1 The global angle compensation

As introduced, the use of a FOC in electrical machines has as a major objective the independent control of the flux and the torque. While for PMSM, this magnet flux is fixed by a permanent magnet (PM), in the VFMM it varies according to the magnetization state of a low coercive force-based (LCF-based) magnet. In both cases, the magnet flux axis is aligned with the d-axis. The torque (Γ_e) is calculated by $\Gamma_e = 3/2[p\varphi_s I_q + p(L_d - L_q)I_d I_q]$, as discussed in the Chapter 1. In the case of a non-salient machine, only currents flowing in the quadrature axis will interact orthogonally with the magnetic axis, and this equation is reduced to $\Gamma_e = 3/2[p(\varphi_s I_q)]$.

Due to the requirements of the sensorless system used for estimating the rotor position and speed, three phase shifts define the global offset angle ($\Delta\theta_c$, also known as global correction angle) to be compensated for the precise identification of the real rotor angle: the PLL (θ_{PLL}), the filtering (θ_{filter}) and the calculus phase shifts. Figure 3.2 exhibits them (all angles are considered positive the counterclockwise), according to the different reference frames. The calculus angle was previously implemented in the sensorless software and will not be externally corrected. Also in this Figure 3.2, the vector \vec{V}_{BF} is used for representing the physical voltage measured before being filtered, as \vec{V} represents the output voltage vector to be aligned with the q_{PLL} -component considering a convergence of the PLL sensorless strategy. For representing the current vector, a general case in which the torque angle (δ) is non-null (and consequently $\vec{I} = \vec{I}_d + j\vec{I}_q$) is presented. For a non-salient machine, $\delta = 0^\circ$ (or $\vec{I} = \vec{I}_q$ for maximal torque) and the angle θ_{PLL} is given by the phase shift between the voltage and current vectors.

The global correction angle can be calculated by:

$$\Delta\theta_c = \theta_{PLL} - \theta_{filter} \quad (3.4)$$

The rotor position (θ) considering this global correction angle is given by:

$$\theta = \theta_{est} + \Delta\theta_c \quad (3.5)$$

Figure 3.3 below exhibits the PLL-based sensorless considering this angle compensation stage.

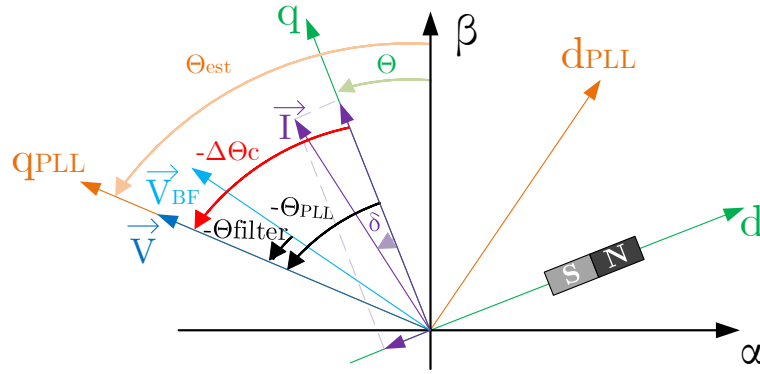
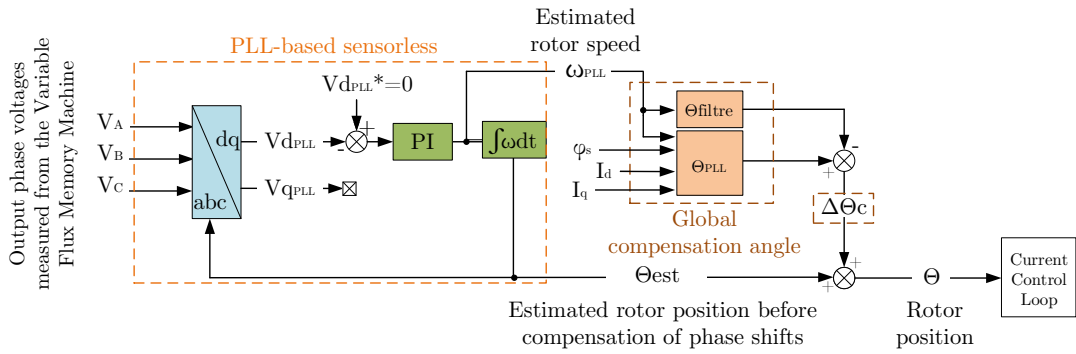

 Figure 3.2: Vector diagram for defining the global offset angle $\Delta\theta_c$.


Figure 3.3: Block diagram of the PLL-based sensorless algorithm and the global offset angle to be compensated.

3.2.2 The description of the PLL angle (θ_{PLL})

From the PLL-based sensorless strategy previously introduced, a first estimation of rotor position is obtained from the output voltage vector in the PLL reference frame (defining the dq_{PLL} -axis), for a $\Delta\theta = \theta_v - \theta_{est} = 0$. The angle between this estimated and the real rotating reference frame, represented by θ_{PLL} , establishes a requirement of angle compensation for allowing the PLL to correctly provide the rotor position. The machine equations presented in the section [1.3.3](#) (Chapter [1](#)) can be rewritten as a flux model by:

$$\begin{cases} v_d = R_s i_d + \frac{d}{dt} \varphi_d - \omega \varphi_q \\ v_q = R_s i_q + \frac{d}{dt} \varphi_q + \omega \varphi_d \end{cases} \quad (3.6)$$

where the dq flux linkages are defined by $\varphi_d(i_d, i_q) = L_d(i_d, i_q) i_d + \varphi_s$ and $\varphi_q(i_d, i_q) = L_q(i_d, i_q) i_q$. The shifting angle can be calculated from the machine flux model in steady-state considering the static inductances L_d and L_q by:

$$\theta_{PLL} = \text{atan} \left(\frac{v_d}{v_q} \right) = \text{atan} \left(\frac{R_s i_d - \omega \varphi_q}{R_s i_q + \omega \varphi_d} \right) = \text{atan} \left(\frac{R_s i_d - \omega L_q i_q}{R_s i_q + \omega (L_d i_d + \varphi_s)} \right) \quad (3.7)$$

Because the real rotor speed ω cannot be directly measured, θ_{PLL} is calculated using the one estimated from the PLL ($\omega = \omega_{PLL}$ in the equation [3.7](#)).

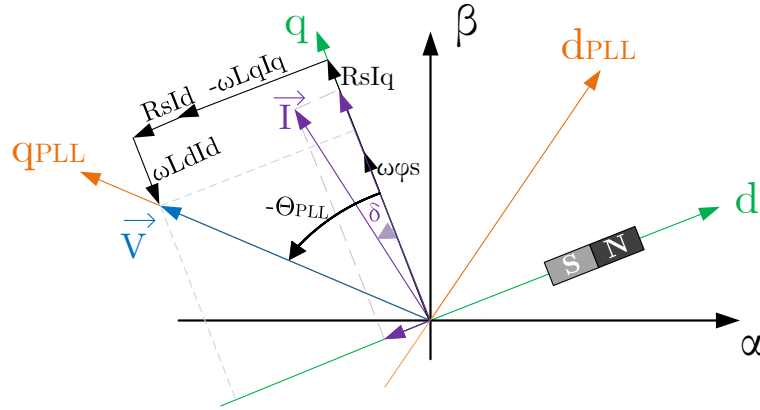


Figure 3.4: Vector diagram for defining angle θ_{PLL} established between the estimated and the rotating referential frames.

3.2.3 The description of the filtering angle (θ_{filter})

The estimation of the rotor speed and position by the PLL-based sensorless described in the section [3.2](#) is based on the measurement of the output phase voltages (V_{aN} , V_{bN} and V_{cN}). The signal processing for adapting these three-phase voltages to the DSP (Digital Signal Processor) requirements demands the use of a filtering chain that introduces a phase shift between the physical input signal and digital output values. This is because neutral access is not available in the machine and the phase voltages cannot be directly measured. The signals are reconstituted from the measures available using the inverter. Figure [3.5](#) exhibits the definition of the referential for the voltage measured in phase A. The same logic is applied to phases B and C. Considering the signal between the local ground (connected to the negative access of the DC voltage source) and the point between the two switches composing each inverter branch (voltages V_{aM} , V_{bM} and V_{cM}), the phase-neutral voltages can be obtained by:

$$\begin{cases} V_a = V_{aN} = V_{aM} - V_{NM} \\ V_b = V_{bN} = V_{bM} - V_{NM} \\ V_c = V_{cN} = V_{cM} - V_{NM} \end{cases} \quad (3.8)$$

Because the system is balanced and presents a star connection, $V_{aN} + V_{bN} + V_{cN} = 0V$ the system of equations above presented can be rewritten considering $V_{NM} = \frac{1}{3}(V_{aM} + V_{bM} + V_{cM})$. Replacing this relation in the equation [3.8](#):

$$\begin{cases} V_a = V_{aN} = V_{aM} - \frac{1}{3}(V_{aM} + V_{bM} + V_{cM}) \\ V_b = V_{bN} = V_{bM} - \frac{1}{3}(V_{aM} + V_{bM} + V_{cM}) \\ V_c = V_{cN} = V_{cM} - \frac{1}{3}(V_{aM} + V_{bM} + V_{cM}) \end{cases} \quad (3.9)$$

Details about this filtering chain are not being presented due to confidentiality issues. Each filtering stage composing the chain can be simplified by a first-order filter which correspondent

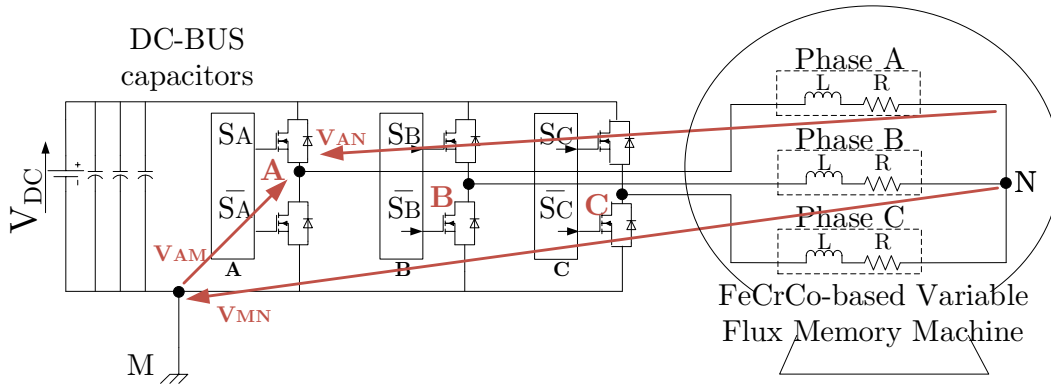


Figure 3.5: Schema presenting the reference of voltages measured - Definition of filtering angle.

offset angle can be calculated as:

$$\theta_{filter_1} = atan(\theta_{num_1} - \theta_{den_1}) = atan(-\omega(R_1C_1)) \quad (3.10)$$

where θ_{num_1} and θ_{den_1} are respectively the phase of the numerator and denominator of the transfer function characterizing the filter at the stage 1, being R_1 and C_1 respectively the resistance and capacitance defining the cutoff frequency as $\omega_0 = 1/R_1C_1$. For multiple stages composing this mentioned filtering chain, the angle θ_{filter} representing the total angle generated can be calculated by:

$$\theta_{filter} = \sum_1^n atan(-\omega(R_nC_n)) \quad (3.11)$$

where the parameters R_n and C_n represent, respectively, the resistance and capacitance composing each n th filtering stage. The rotor electrical speed ω (or the signal frequency (f , in [Hz]), as $f = \omega/2\pi$) impacts on the value obtained. For low frequencies, the behavior of θ_{filter} can be simplified using a linear function dependent only on signal frequency, defined by the rotor speed ($\theta_{filter} = K\omega$, where K is a constant). As for θ_{PLL} , the filtering angle is calculated from the estimated speed, and consequently, ω in the equation 3.11 is ω_{PLL} .

3.2.4 The description of the calculus angle (θ_{cal})

The implementation of the control strategy algorithm is based on the use of interruption sequences for the correct signal acquisition and processing. Four steps describe the procedure of calculation used [25]:

1. Three-phase voltages and currents measurement (ADC registers).
2. Rotor position and speed estimation using the PLL formerly described considering the three output phase voltages previously measured.
3. Three-phase voltages and currents measurement (ADC registers).
4. According to the angle estimated in step (2) and the three-phase currents measured in step (3), current regulation in dq reference frame. Finally, the calculation of the duty cycles.

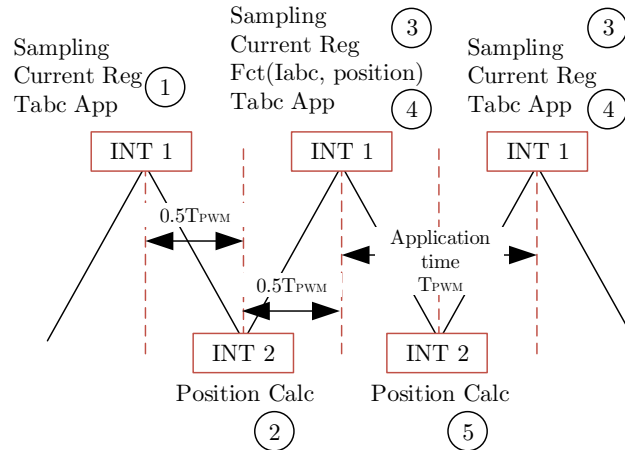


Figure 3.6: Schema for presenting the control algorithm interruption sequences - Definition of calculus angle - Adapted from [25].

Two interruptions (INT_1 and INT_2), triggered with a delay of $0.5T_{PWM}$ (where T_{PWM} is the switching frequency), are used for allowing these four calculation steps to be realized. While INT_1 is used for measuring the current and voltage (1), for the current regulation and the duty cycle calculation (4), INT_2 is dedicated to the position and speed estimation. The switching frequency T_{PWM} is used for calculating the delay caused by the calculus time can be obtained as below:

$$\theta_{cal} = \omega T_{PWM} \quad (3.12)$$

This described angle is compensated automatically in the software used and for this reason it is not represented in the previously presented Figure 3.10. As a result, the angle θ_{cal} is not considered in the calculation of the global correction angle ($\Delta\theta_c$).

3.2.5 Parametric sensitivity: first insights

As formerly presented, the definition of $\Delta\theta_c$ depends not only on the rotor speed but also on the machine parameters. In this context, this section has as its major objective the investigation of the effects of parametric uncertainties or modeling errors in the calculation of θ_{PLL} and θ_{filter} , and, as a consequence, of $\Delta\theta_c$.

For these studies, some considerations should be presented. The VFMM geometry described in the section 2.2 is designed considering a cylindrical massif rotor. No reluctance is, therefore, expected in the machine, and the dq-axis inductances (L_d and L_q) are supposed similar. The values initially setting these parameters ($L_d = L_q = 5\mu H$) are based on the machine modeling realized at IFP Energies nouvelles considering the PMSM for which the stator used in the VFMM studied in this thesis research used was initially designed. The stator windings resistance (R_s) is also considered well known, assuming the value $R_s = 5m\Omega$. The rotor speed (Ω) and the flux linkage through the stator windings (φ_s) are defined based on the results achieved by magnetizing the machine at standstill. As introduced in the section 2.5, the magnet flux for different conditions of initial magnetization varies between $453\mu Wb$, for a magnetization via $I_{mag} = 250A$, and $559.3\mu Wb$, for $I_{mag} = 500A$, as presented in the Table 2.8). The average value of $\varphi_s = 500\mu Wb$ is considered for the proposed studies. As regards the rotor speed, a regime $\Omega = 45krpm$ is considered.

Remark: As formerly mentioned, because the number of pole pairs characterizing the Fe-Cr-Co-based VFMM is $p = 1$, the electrical and mechanical speeds, respectively given by ω and ω_m , in [rad/s], are equal. To avoid misunderstandings, it should be mentioned that ω is used for calculating the correction angles, but the results of the sensitivity study are presented in terms of Ω (in [rpm]).

The parametric sensitivity of the correction angle is investigated below according to the possible variations on the mentioned machine parameters (L_d , L_q , R_s), for different flux linkage crossing the armature windings (representing different magnetization states) and different regimes. Because the filtering angle θ_{filter} is not calculated from these mentioned machine parameters, the impact of this angle on the $\Delta\theta_c$ is only observed when the regime varies. Therefore, for a constant regime, differences observed in $\Delta\theta_c$ are caused by θ_{PLL} . Results obtained are exhibited in Figure 3.7. They propose the study of the global correction angle for variations of -50% , 100% and 150% on the machine parameters initially considered well known: the dq-axis inductances $L = L_d = L_q = 5\mu H$ (non-salient machine) and the stator resistance $R_d = 5m\Omega$. The analyses are realized for two conditions: (1) torque control, simulated by supplying the machine via $I_q = 50A$ and $I_{mag} = I_d = 0A$, which reduces the equation 3.7 defined for calculating θ_{PLL} to $\theta_{PLL} = atan((- \omega L_q I_q) / (R_s I_q + \omega \varphi_s))$; (2) magnetization control, simulated via $I_{mag} = I_d = 50A$ and $I_q = 0A$, for which $\theta_{PLL} = atan((R_s I_d) / (\omega (L_d I_d + \varphi_s)))$. For both cases, θ_{filter} is similarly calculated by the equation 3.11 formerly introduced. The impact of these above-described parametric errors strictly in θ_{PLL} can be analyzed in the Appendix C.2

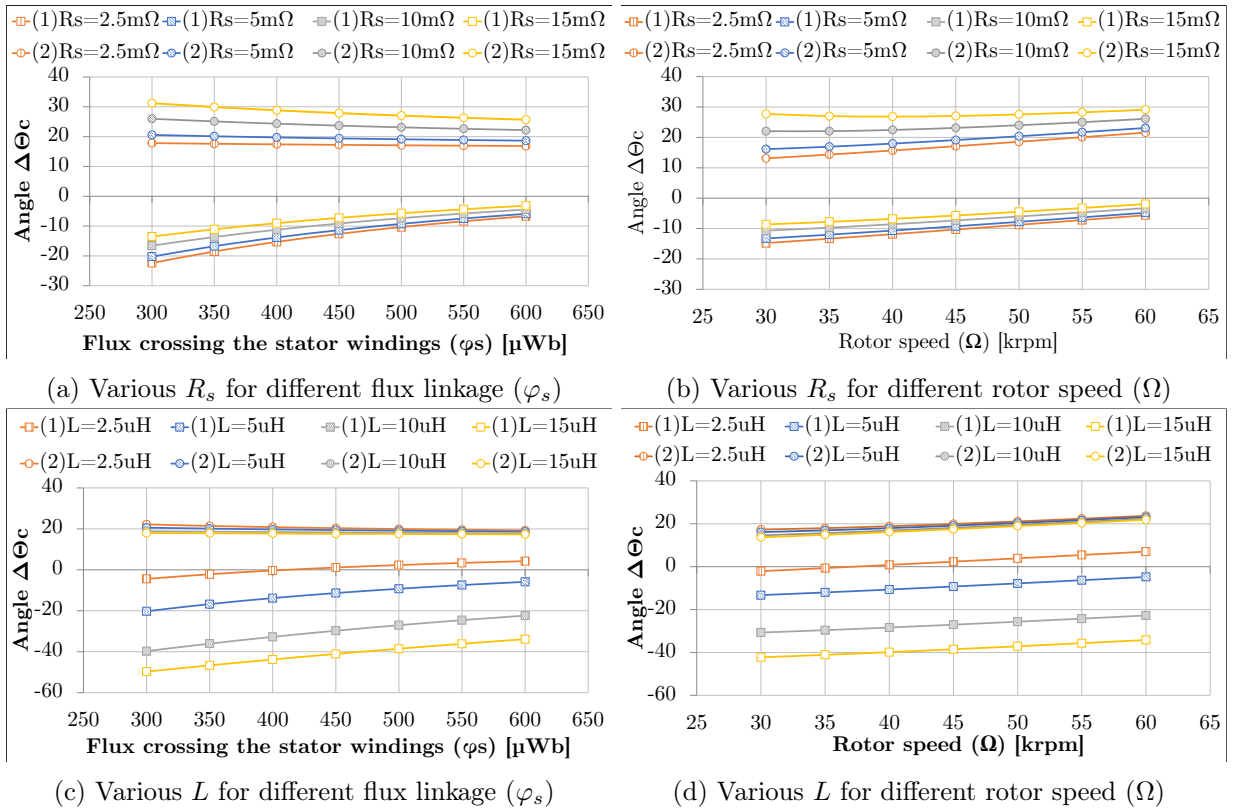


Figure 3.7: Study by simulation of parametric sensitivity of $\Delta\theta_c$ for different system parameters considering: (a) and (c) different flux linkage conditions and (b) and (d) different regime - Case (1) torque control and Case (2) magnetization control.

The conclusions obtained are summarized below:

- In case (1), describing a torque control, it can be identified that the sensitivity of $\Delta\theta_c$ is higher to variations on the inductances ($L_d = L_q = L$) than to variations on the stator resistance, considering the same Ω and φ_s (see Figure 3.7b and 3.7d). Indeed, the dominant term on the equation of θ_{PLL} is $\omega(L_q I_q)$, and variations on this parameter are therefore expected to be the one mostly affecting the obtained angle (as $I_{mag} = 0A$, L_d does not affect the correction angle). It can be also concluded that the total angle $\Delta\theta_c$ increases for increments in φ_s or Ω , being more negative for higher values of L_q and lower values of R_s . Increases in the rotor speed affect both θ_{PLL} and θ_{filter} , having a more important impact on this last-mentioned angle.
- In case (2), describing a magnetization control, $R_s I_d$ is the dominant term and $\Delta\theta_c$ is as high as R_s for the same regime and flux linkage. Increasing the inductance (in this case, only L_d is considered as $L_q I_q$ is null), also for a defined regime and flux linkage conditions, $\Delta\theta_c$ is reduced (see Figure 3.7c). When φ_s is enhanced, the global correction angle is reduced. Increments on Ω , however, have the opposite effect and contribute to enhancing $\Delta\theta_c$, as not only θ_{PLL} but also θ_{filter} are reduced.

Figure 3.8 exhibits the sensitivity of $\Delta\theta_c$ to variations in the flux linkage crossing the stator windings, for different rotor speeds, for the machine characterized by the initial model assumed well known ($L = L_d = L_q = 5\mu H$ and $R_d = 5m\Omega$). Two important conclusions can be obtained:

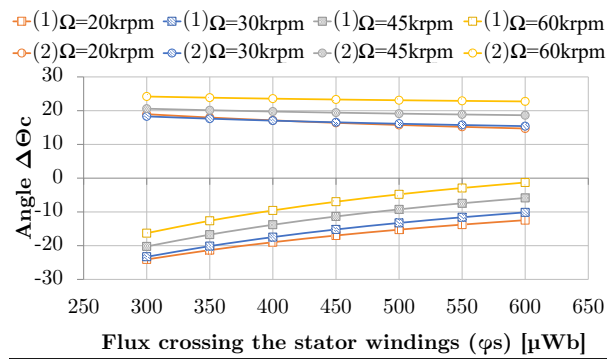


Figure 3.8: Study by simulation of sensitivity of the angle $\Delta\theta_c$ for different system parameters considering errors in the system parameters (φ_s , Ω). The case (1) represents the $I_{mag} = 0A$ and $I_q = 50A$ and (2) $I_{mag} = 50A$ and $I_q = 0A$.

- By analyzing a torque control (case (1)) it can be observed that for the same flux linkage (φ_s), higher regimes are expected to require a more positive $\Delta\theta_c$. **Remark:** As formerly introduced, q-axis currents are not expected to modify the magnetization state (or the flux linkage crossing the armature windings) of a VFMM in normal operating conditions.
- The results exhibited by a magnetization control (case (2)) demonstrate that for a defined regime, $\Delta\theta_c$ is not largely affected by variations on φ_s . For this reason, the global correction angle required to be adjusted during different magnetization procedures, that define different magnetization states in the machine (and different flux linkages φ_s) are expected to be similar. In other words, the range of variation expected for the angle $\Delta\theta_c$ for different I_{mag} is low.

The effects of parametric errors in the angle $\Delta\theta_c$ are evaluated for different regime and flux linkages (magnetization states) in this proposed study. Specially in which concerns torque

control, Figures 3.7c and 3.7d demonstrate that the global correction angle can be strongly impacted by errors in the machine inductances. Hence, the knowledge of these parameters can be seen as critical for estimating the rotor position by the sensorless algorithm proposed. Therefore, attention is going to be given in the next sections to propose a strategy for modeling the dq-axis inductances.

3.3 Presentation of the control strategy

A differential flatness control is proposed as the strategy for current control in the system studied in this thesis. The concepts related to a flat system have been presented and/or applied by many authors, as [113, 143]. In this context, a system of state x and command system u defined by:

$$\dot{x} = f(x, u) \quad x \in \mathbb{R}^n, \quad u \in \mathbb{R}^n \quad (3.13)$$

is characterized flat if it exists a function $y \in \mathbb{R}^m$ called flat output, given by:

$$y = h_y(x, u, \dot{u}, \dots, u^{(q)}) \quad (3.14)$$

where $x = h_x(y, \dot{y}, \dots, y^{(r)})$ and $u = h_u(y, \dot{y}, \dots, y^{(r+1)})$. The functions $h_y : \mathbb{R}^n \times (\mathbb{R}^m)^{q+1}$, $h_x : (\mathbb{R}^m)^{r+1} \rightarrow \mathbb{R}^n$ and $h_u : (\mathbb{R}^m)^{r+2} \rightarrow \mathbb{R}^m$ are regular. Hence, they are differentiable and their successive derivatives are continuous.

In the section 3.3, the mathematical model of the VFMM was described according to three key equations that will be rewritten below:

$$\begin{cases} \hat{L}_d \frac{d}{dt} i_d = -R_s i_d + p\Omega(L_q i_q) + v_d \\ \hat{L}_q \frac{d}{dt} i_q = -R_s i_q - p\Omega(L_d i_d + \varphi_s) + v_q \\ J \frac{d}{dt} \Omega = 3/2p[(L_d - L_q)i_d i_q + \varphi_s i_q] - \Gamma_{ch} - f\Omega \end{cases} \quad (3.15)$$

where \hat{L}_d and \hat{L}_q are respectively the dq-axis dynamic inductances and L_d and L_q the static ones.

By using these equations, two procedures can be considered for controlling the machine: a current and a mechanical speed regulation. In the system studied in this thesis research, however, the speed is not regulated, being externally guided by the axial airflow crossing the machine. More insights regarding the speed regulation are described in [113]. In which concerns the direct and quadrature-axis (dq) currents regulation, the major objective is to generate the voltages reference v_d^* and v_q^* in the dq-axis plan. These voltages define a command vector $v_{dq} = [v_d^*, v_q^*]$ for a flat output given by $y_{dq} = [i_d, i_q]$. By rewriting these mentioned equations according to the flat output as demonstrated below, the flatness properties of the current model are proven. It should be mentioned that the controller is expected to reject any errors, being considered non-saturated. Therefore, the dynamic and static inductances are equal in the command equations ($\hat{L}_d = L_d$ and $\hat{L}_q = L_q$).

$$\begin{cases} v_d^* = L_d \frac{d}{dt} i_d + R_s i_d - p\omega(L_q i_q) = h_{v_d^*}(i_d, \mu_d, i_q) \\ v_q^* = L_q \frac{d}{dt} i_q + R_s i_q + p\omega(L_d i_d + \varphi_s) = h_{v_q^*}(i_q, \mu_q, i_d) \end{cases} \quad (3.16)$$

The derived terms of highest order can be defined as $\mu_d = \frac{d}{dt} i_d$ and $\mu_q = \frac{d}{dt} i_q$. To consider a rejection of possible parametric uncertainties or modeling errors, the terms μ_d and μ_q are generated by the equation 3.17 described below, which are obtained from an input/output

linearization allowing to lead the dynamic behavior of the convergence of the errors $\epsilon_d = (i_d - i_d^*)$ and $\epsilon_q = (i_q - i_q^*)$ to zero. The terms i_d^* and i_q^* are, respectively, the dq-axis components of the reference stator currents (set points).

$$\begin{aligned}\mu_d &= \frac{di_d^*}{dt} + 2\xi_d\omega_d(i_d - i_d^*) + \omega_d^2 \int (i_d - i_d^*)d\tau \\ \mu_q &= \frac{di_q^*}{dt} + 2\xi_q\omega_q(i_q - i_q^*) + \omega_q^2 \int (i_q - i_q^*)d\tau\end{aligned}\quad (3.17)$$

The parameters ξ_d , ξ_q and ω_d , ω_q are, respectively, dq-axis components of the damping and the closed loop bandwidths of the current regulators. They are sized to respect load specifications, such as the current regulation bandwidth, for example.

An overview of the flatness control of a synchronous machine is illustrated in Figure 3.9. The output of this control is the machine control voltages (v_d^* , v_q^*) that can be rewritten, by applying the Clarke and Park transformations, as the three-phase voltages (v_a^* , v_b^* and v_c^*) used for generating the PWM control signals.

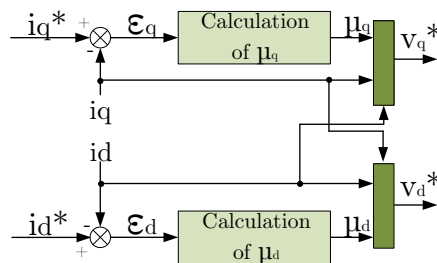


Figure 3.9: Overview on the flatness control for a PMSM.

3.4 Presentation of the final system

A microcontroller implemented in the voltage inverter is used in the control system, considering a switching frequency of 35 kHz. The three-phase output voltages are measured for estimating the speed and rotor position by using the PLL sensorless control introduced in the section 3.2, chosen due to its simplicity for being implemented and relative low computation time consumption [25]. Next, the methodology formerly presented in the section 3.2.1 for compensating the errors in the rotor position is used for calculating the phase shifts generated by the estimation method (θ_{PLL}) and the active filters (θ_{filter}). By these angles, the global correction angle to be compensated for the initially estimated rotor position is defined by $\Delta\theta_c = \theta_{PLL} - \theta_{filter}$. Figure 3.10 exhibits the block diagram of the machine control considering the sensorless strategy aforementioned. The flatness control described in the section 3.3 is also implemented in the current loop controller.

3.5 Validation of the control system via simulations

This section is dedicated to validating via MATLAB/Simulink the control system. The hypothesis that the machine parameters are well known, assuming the values introduced in the Appendix C.1 ($L = L_d = L_q = 5\mu H$ and $R_s = 5m\Omega$), is also used for these studies. A reference regime is imposed ($\Omega = 45krpm$) for reproducing in the simulations the same speed set for the machine in the experimental tests. With regards to the flux linkage, as exposed in the section 3.2.5, the mean value of $\varphi_s = 500\mu Wb$, defined according to the results obtained via

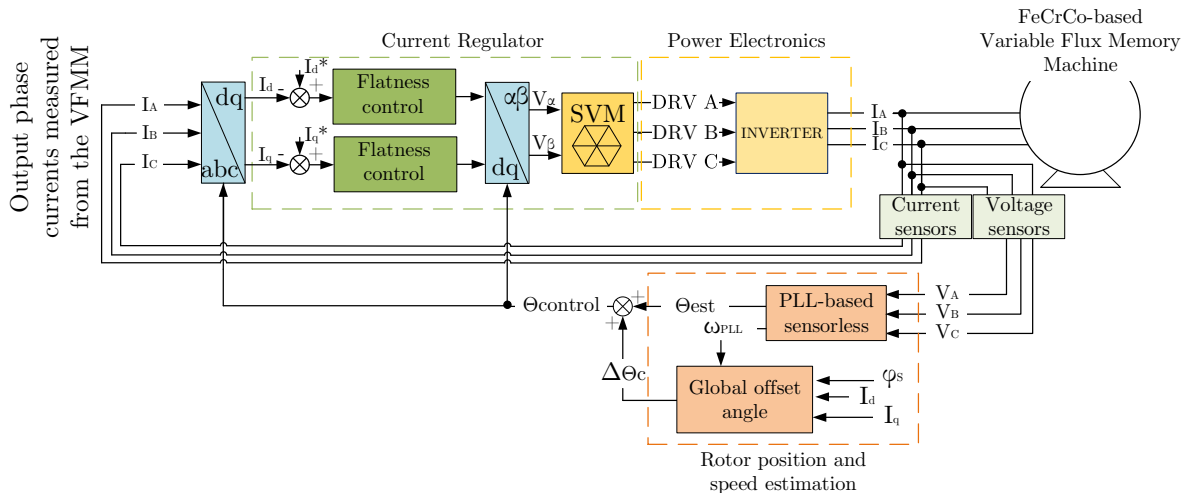


Figure 3.10: Block diagram of the control system proposed.

magnetization at standstill, is used for characterizing the magnetization state of the machine before the torque control studies. The VFMM is, therefore, for simplicity, simulated as a synchronous machine having a permanent flux.

3.5.1 Validation of the PLL-based sensorless strategy

This section is focused on the validation of the PLL-based sensorless algorithm previously proposed. The behavior of the system is analyzed via Matlab/Simulink for a better understanding of the dynamic response of the control methodology in different conditions. Each study considers one parameter changed at a time, between the q-axis current, for simulating a condition of torque control (id-null, because of the non-salient machine model), the d-axis current, for simulating a variation of the magnetization state (iq-null magnetization control), and finally, the rotor speed, for simulating the variation on the regime. The impact of these modifications on the angles θ_{PLL} , θ_{filter} and $\Delta\theta_c$ are also exhibited. For avoiding initialization errors in the simulations, the PLL is started at $t=0.05s$, when the regime at the machine is already established for estimating the rotor position and speed. In the running experimental tests, because a magnetization state is pre-defined in the machine at standstill, the PLL-based sensorless is expected to converge even for low regimes.

Three case studies are proposed in this section, all considering the machine parameters previously introduced: the dq-axis inductances $L_d = L_q = 5\mu H$ (non-salient machine) and a stator resistance $R_s = 5m\Omega$. First, the torque control is studied by modifying the amplitude of the q-axis current $I_q = 50A$, $I_q = 70A$ and $I_q = 100A$, as exhibited in the Figure 3.11, for a constant regime of $\Omega = 45krpm$ and as mentioned, $I_d = 0A$; second, the magnetization control via $I_d = I_{mag} = 200A$, $I_d = I_{mag} = 300A$ and $I_d = I_{mag} = 500A$ are investigated for $I_q = 0A$ and the same regime $\Omega = 45krpm$; finally, a variation on the rotor speed is analyzed from $\Omega = 20krpm$, $\Omega = 30krpm$ and $\Omega = 45krpm$, considering a torque current of $I_q = 50A$ and $I_d = 0A$. In the Appendix C.3, these two last-mentioned investigations concerning the variations in the magnetization current (I_d) and the speed (Ω) are presented. The Table 3.1 summarizes the angles (θ_{PLL} , θ_{filter} and $\Delta\theta_c$) calculated for some of these described working conditions.

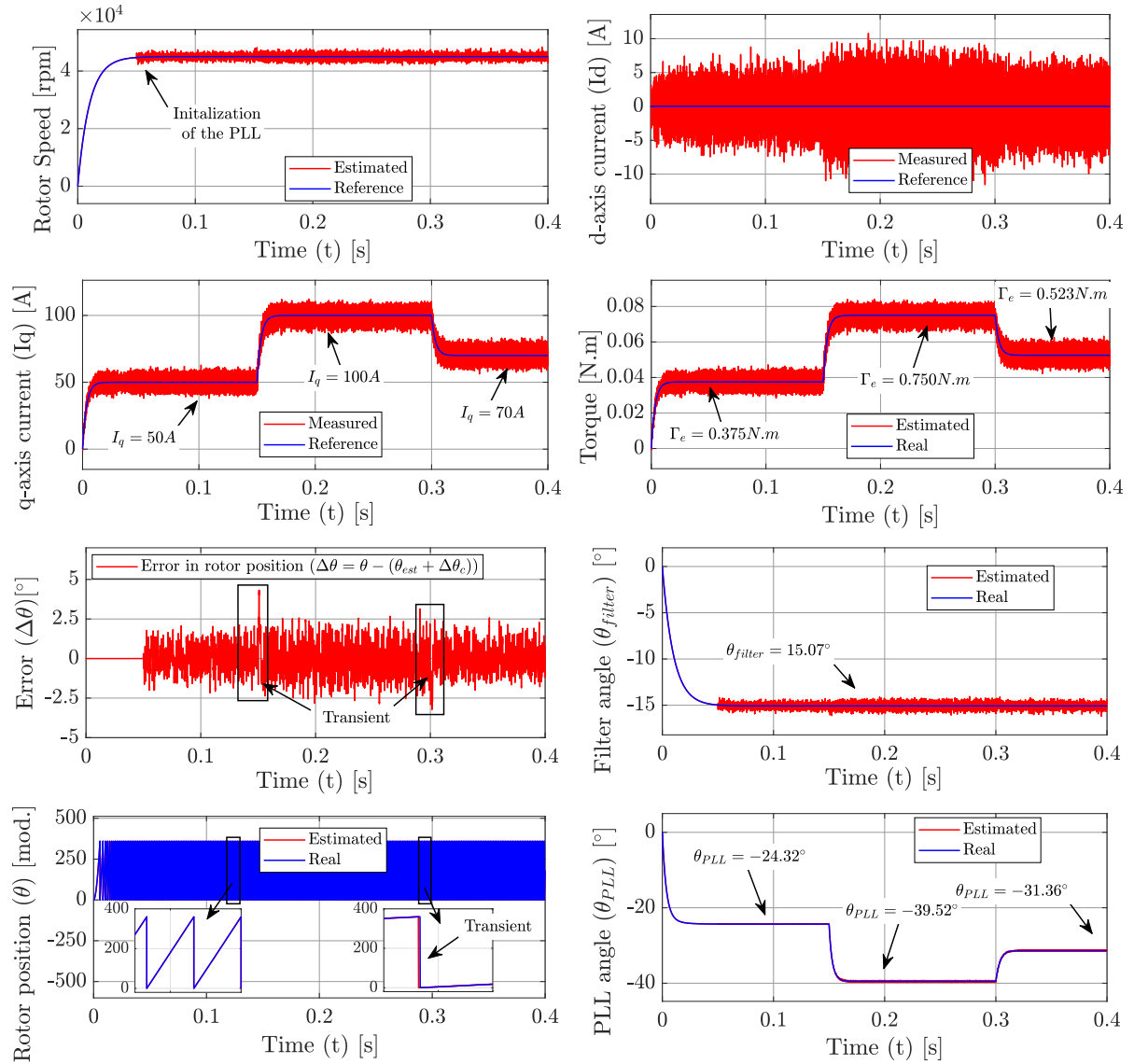


Figure 3.11: Validation of the sensorless strategy - q-axis current variation considering the rotor position and speed estimated via PLL - Study at $I_q = 50A$, $I_q = 100A$ and $I_q = 70A$.

Table 3.1: Study of the displacement angles.

Case	Magnetization current	Torque current	Rotor speed	Angle between voltage and current vectors	Filtering angle	Correction angle
	I_{mag} [A]	I_q [A]	Ω [krpm]	θ_{PLL} [°]	θ_{filter} [°]	$\Delta\theta_c$ [°]
Rotor speed	0	50	20	-21.98	-6.72	-15.26
variation	0	50	30	-23.33	-10.07	-13.26
q-axis current	0	50	45	-24.32	-15.07	-9.25
variation	0	100	45	-39.52	-15.07	-24.2
d-axis current	200	0	45	8.05	-15.07	23.1
variation	500	0	45	10.02	-15.07	25.1

3.5.2 Parametric sensitivity analysis

Figure 3.12 exhibits the system response in the case of $L_q = 2.5\mu H$, $L_q = 5\mu H$, and $L_q = 10\mu H$. In the Appendix C.4, the behavior of the control system for variations on the stator resistance and on the d-axis inductance are studied. Currents $I_q = 50A$ and $I_d = 0A$ are regulated for a regime $\Omega = 45krpm$ and a flux linkage $\varphi_s = 500\mu Wb$. Because the correction angles are calculated from the control currents and these parameters are kept constant, both θ_{PLL} and θ_{filter} are the same for all cases analyzed. However, it is noticed that parametric errors cause a divergence between the real (machine) and control currents. For this reason, the angle θ_{PLL} (as also the total correction angle $\Delta\theta_c$) is badly calculated about the real phase shift to be compensated. The rotor position obtained from the PLL (or $\theta_{est} + \Delta\theta_c$) is therefore different than the real one (θ) and an error $\Delta\theta \neq 0$ is observed. The q-axis field created by $I_q \neq 0A$ will not be placed at the real q-axis. Hence, a d-axis current component is observed, which can potentially compromise the magnetization state (MS) of the machine (MS can be enhanced, for $I_d > 0A$ crossing the machine or reduced, in case of $I_d < 0A$). Therefore, this section demonstrates that the global correction angle ($\Delta\theta_c$) is sensitive to parametric errors and that a precise estimation of the machine parameters, as previously discussed, is critical for the sensorless strategy used.

3.6 Investigation of the correction angle via experimental tests: description of results obtained by manually adjusting the angle $\Delta\theta_c$

By using the sensorless algorithm presented in the section 3.2, running experimental tests were carried out to investigate the Fe-Cr-Co-based VFMM in different working conditions. The global correction angles are calculated according to the equations formerly introduced considering the well-known non-salient machine model characterized by the inductances $L_d = L_q = 5\mu H$ and a stator resistance $R_s = 5m\Omega$. When these pre-defined calculated angles are manually adjusted in the experimental tests, divergences of the control system are observed for different regimes and current conditions studied. For this reason, this look-up table initially used for identifying the global correction angles demonstrated to be not adapted for modeling the system analyzed. This present section describes therefore the global correction angles identified directly via experimental tests for ensuring the convergence of the control system during (1) the magnetization control by different amplitudes of d-axis currents and (2) torque control by different q-axis current amplitudes ($I_d = 0A$ due the non-salient machine hypothesis). Later, these same angles are going to be compared to the ones initially calculated according to the non-salient machine model formerly described, to evaluate the differences that can be the reason for the observed divergence. Then, an optimization of the machine modeling will be proposed to allow the calculation of the correction angles independently of the experimental tests.

3.6.1 Studies of the running magnetization control

3.6.1.1 Study of the variation of the magnetization current amplitude

As described in the section 1.3, Variable Flux Memory Machines have their magnetization state modified by the injection of d-axis current (I_{mag}) pulses. This section presents experimental results achieved for different amplitudes of I_{mag} supplying the VFMM while $\Omega \neq 0rpm$.

From a magnet partially magnetized, the inverter is turned on to supply the machine with $I_{mag} = 400A$. An angle $\Delta\theta_c = 4^\circ$ is manually adjusted before the current pulse injection and defined to ensure the convergence of the control system. The Figure 3.13 exposes the achieved results. The amplitude of the output phase voltages V_A , V_B , and V_C enhances after the

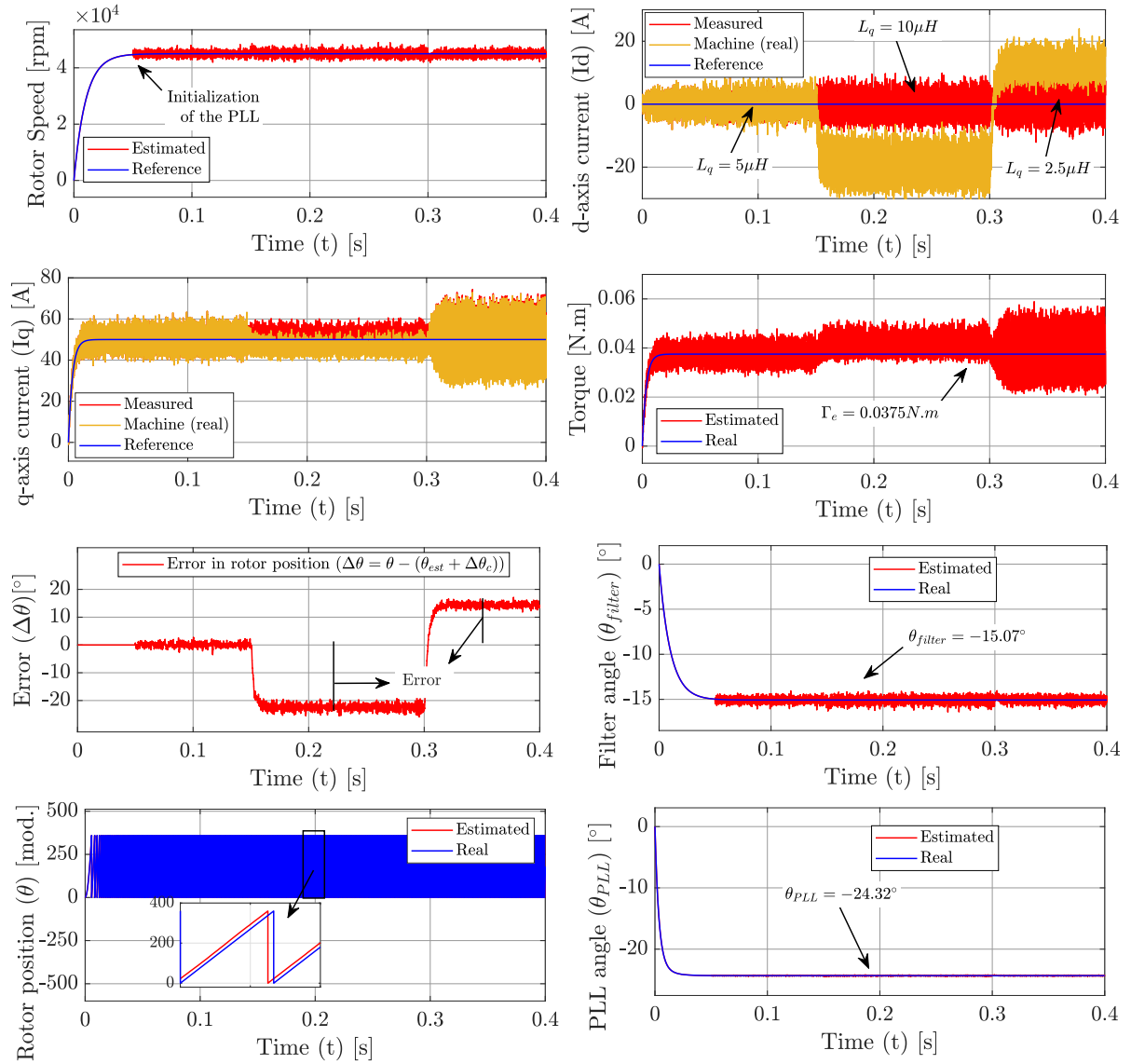


Figure 3.12: Investigation of the parametric sensitivity via simulation - Study considering a variation of the machine parameters $L_q = 5\mu H$, $L_q = 2.5\mu H$ and $L_q = 10\mu H$, for control dq-axis inductances $L_d = L_q = 5\mu H$.

current pulse injection, indicating a magnetization of the Fe-Cr-Co-based rotor. This conclusion is validated by turning off the inverter for measuring a back-EMF $e = 8.2V$. This measured amplitude of e represents 96% of the total one obtained as a result of the standstill magnetization procedure (see Table 2.5 in Chapter 2), which indicates that the maximal MS for $I_{mag} = 400A$ was achieved by this experimental test.

Remark: For the standstill magnetization studies in Chapter 2 (see section 2.5.2) multiple d-axis current pulses were required for achieving the maximal magnetization state (MS) from each amplitude of magnetization current because the magnet was completely demagnetized before the current pulse injection. In the running magnetization tests, however, one current pulse is identified as sufficient for this same procedure. Furthermore, once this maximal MS is achieved, increasing the time duration or quantity of pulses without modifying the current amplitude used has no impact on the magnetization level.

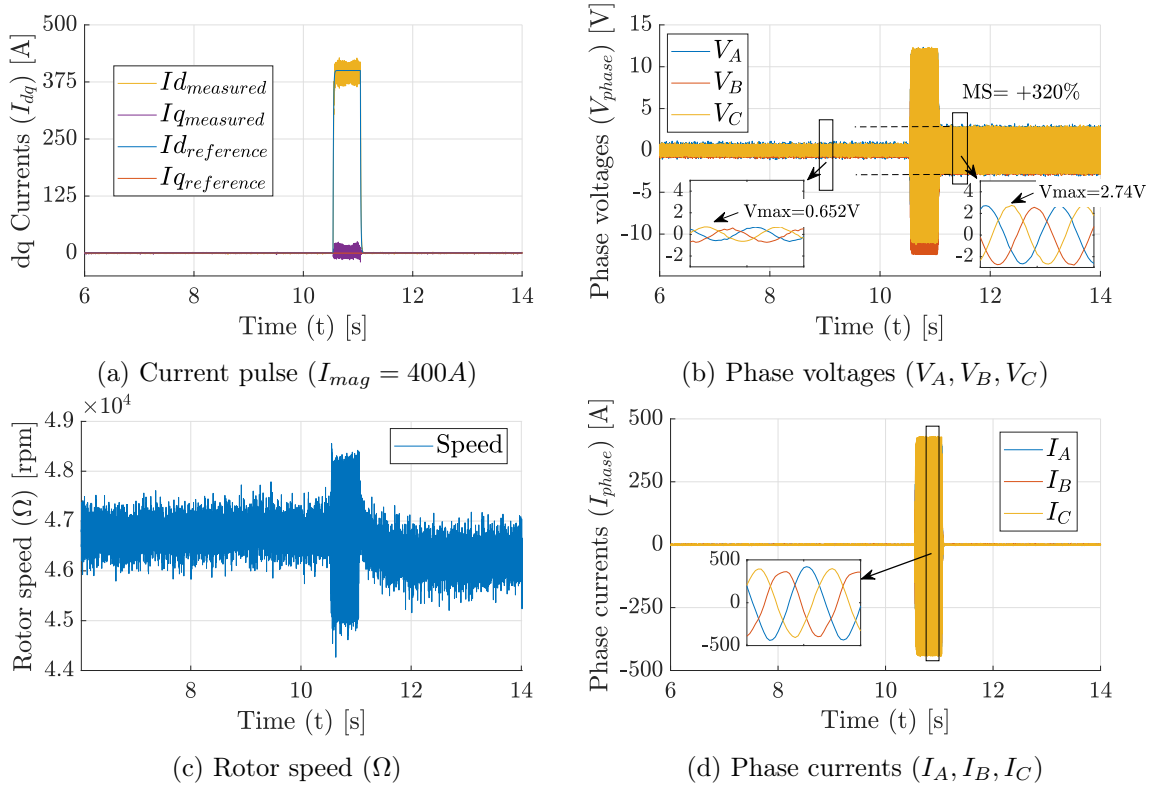


Figure 3.13: Variation of the MS via magnetization current pulse $I_{mag} = 400A$.

An increase in this magnetization level initially set via $I_{mag} = 400A$ is only expected in case of supplying the machine with higher magnetization current amplitudes. The theoretical behavior of the working points in the hysteresis curves clarifies this conclusion. The load line $I_{mag} = 0A$ and consequently the working point placed at its intersection with a defined recoil line moves to the right when the machine is supplied with a positive d-axis current pulses. If the amplitude of this current is sufficiently higher than the one used for setting the initial magnetization state, this working point reaches the major hysteresis loop. Consequently, when the currents are suppressed, the working point returns to the intersection with the load line $I_{mag} = 0A$ by a new recoil line, describing a higher magnetization state. The tests exposed in Figures 3.14 and 3.15 show this behavior, both considering a global correction angle adjusted via experimental tests for ensuring the convergence of the control system. As mentioned before, these angles are not the same as the ones calculated via the equations taking into account the well-known non-salient machine model. First, pulses of amplitude $I_{mag} = 300A$ are injected in the armature windings in an attempt to variation the magnetization state of the magnet initially magnetized via $I_{mag} = 400A$, as exhibited the Figure 3.14. The back-EMF remains unchanged after this magnetization procedure, demonstrating that this amplitude of current is not sufficient for changing the magnetization state. When, however, a magnetization current of $I_{mag} > 400A$, as it is the case presented in Figure 3.15 for $I_{mag} = 500A$, an increase of the phase voltages can be visualized. Switching off the inverter a back-EMF level of $e = 8.5V$, higher than the one measured before the current pulse injection, is measured, confirming the expected magnetization.

Remark: The increase of 4% observed in the back-EMF measured after the magnetization procedure via $I_{mag} = 400A$ compared to the one obtained via $I_{mag} = 500A$ is coherent with the results obtained at standstill in the Chapter 2, as presented in the Table 2.5

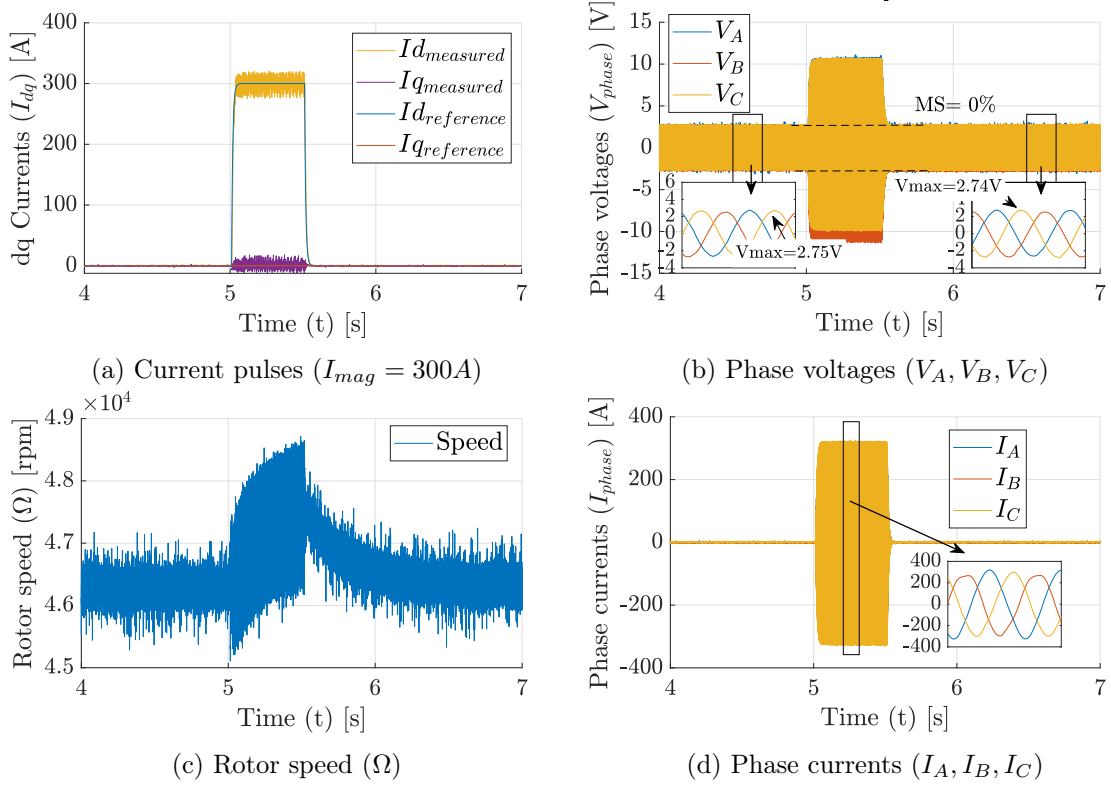


Figure 3.14: Variation of the via magnetization current pulse $I_{mag} = 300A$.

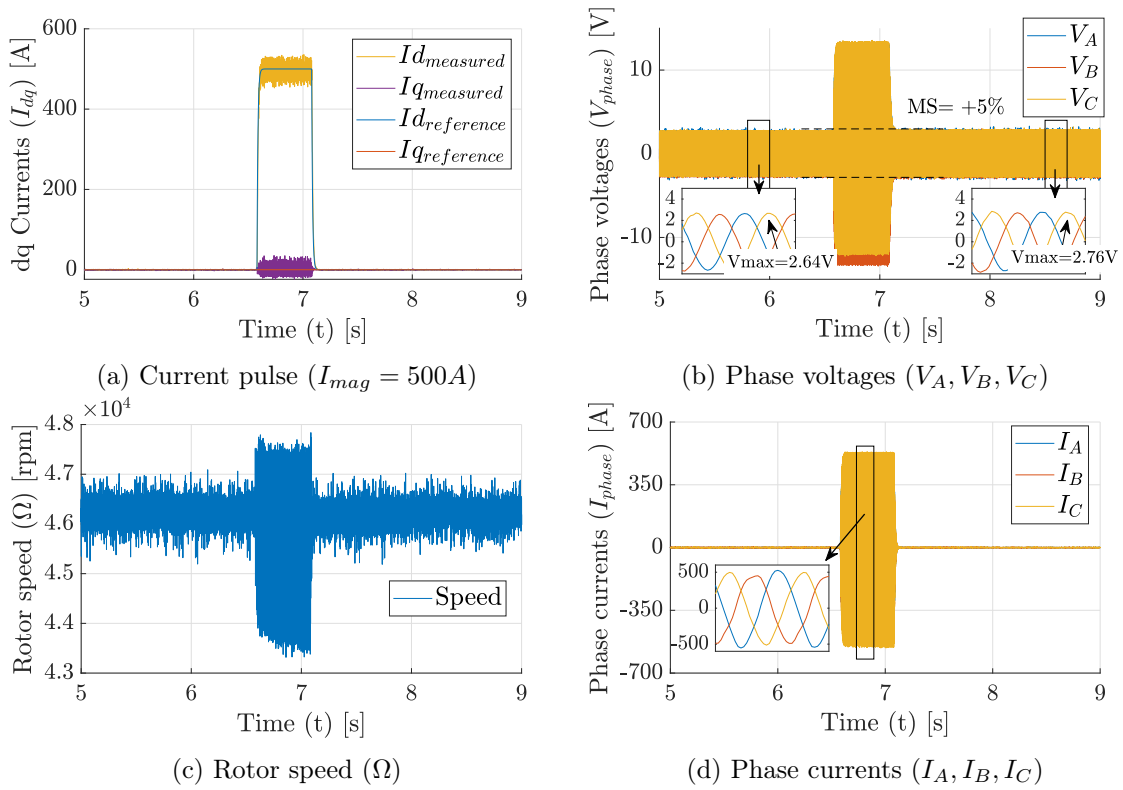


Figure 3.15: Variation of the via magnetization current pulse $I_{mag} = 500A$.

3.6.1.2 Study of the variation of the current loop regulation parameters

The effective variation of the magnetization state in the VFMM studied depends not only on $\Delta\theta_c$ but also on the controller parameters. If they are not well-designed, a divergence of the state variables and an unintentional demagnetization of the machine can be caused. Within this context, this section investigates the effects of adjusting the dq-axis current loop bandwidth (BW) during the magnetization procedures at $\Omega \neq 0rpm$.

For this present investigation, an initial magnetization state is set in the machine at standstill. Then, a rotor speed $\Omega = 45krpm$ is defined by the axial airflow system and the inverter is turned on to supply the machine with a current pulse $I_{mag} = 200A$, considering a current loop BW of about 6krad/s. The global correction angle is defined to ensure the control system convergence during the experimental tests. The Figure 3.16 exhibits this study. As can be observed, the currents diverge until they reach the limit of 900A, and the inverter switches off. By analyzing the phase voltages, it is also concluded that the described magnetization current pulse injection, contrary to expectations, causes a partial demagnetization of the machine.

Remark: As an example, it can be mentioned that the global correction angle calculated from the equations for $I_{mag} = 200A$ supplying the non-salient machine model is $\Delta\theta_c = 23.1^\circ$, as shown in the Table 3.1. This angle, however, is different from the one required for avoiding a divergence in the experimental tests, identified as assuming a value of around $\Delta\theta_c = 1^\circ$. A future section will evaluate this difference and propose a strategy for reducing it.

A second test is proposed by reducing BW to 4krad/s, for a similar rotor speed, correction angle, and magnetization current amplitude as before. Figure 3.17 shows these results. A convergence of the control system and an increase in the phase voltage amplitudes are observed.

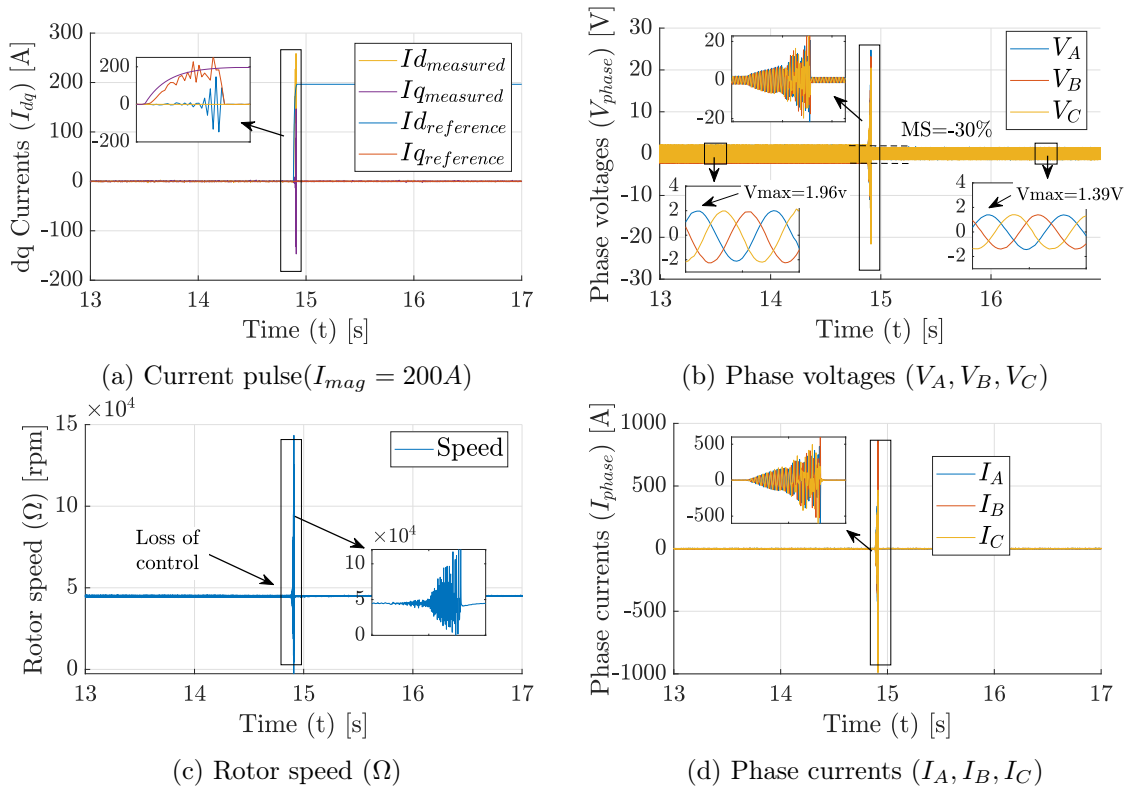


Figure 3.16: Variation of the MS via $I_{mag} = 200A$ for a current loop bandwidth $BW=6krad/s$.

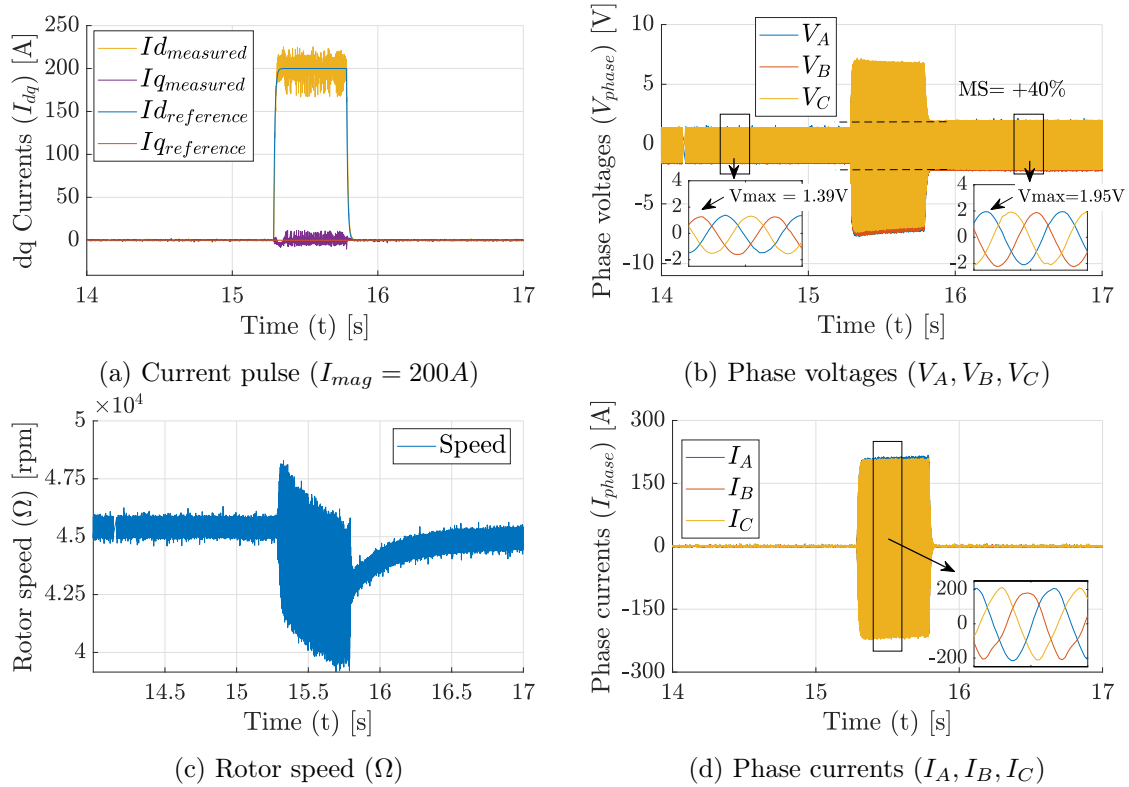


Figure 3.17: Variation of the MS via $I_{mag} = 200A$ for a current loop bandwidth $BW=4krad/s$.

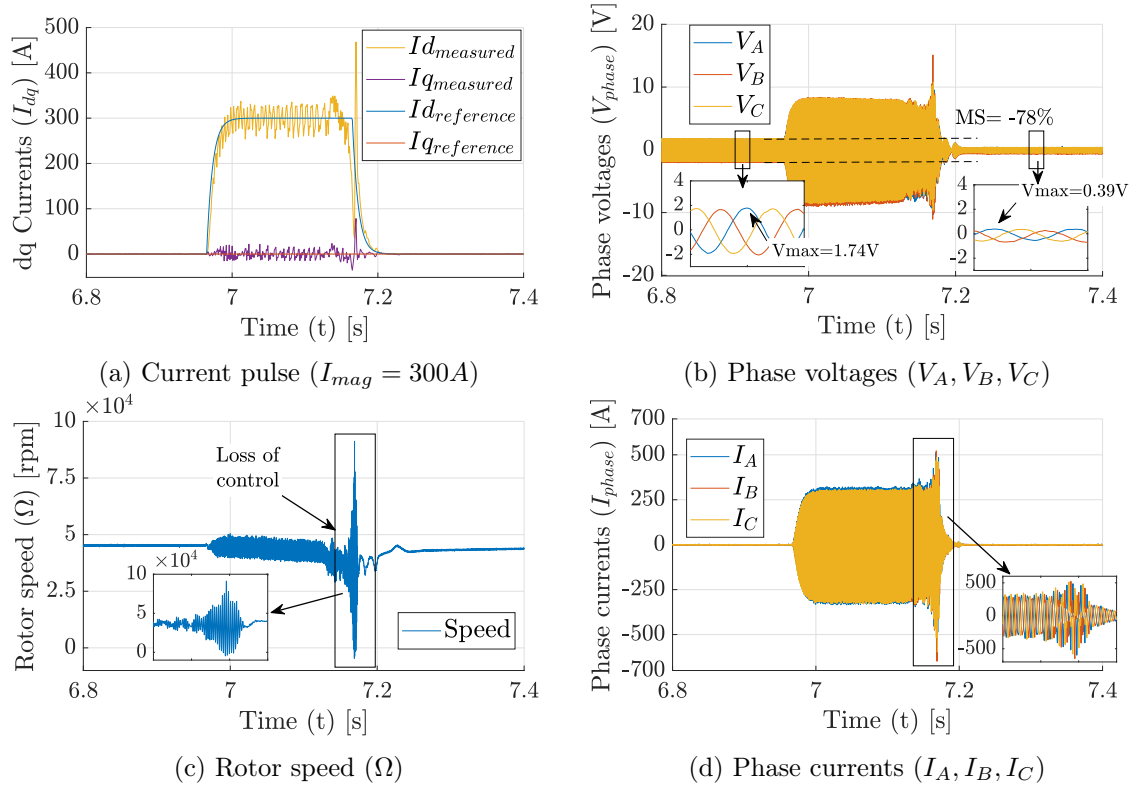
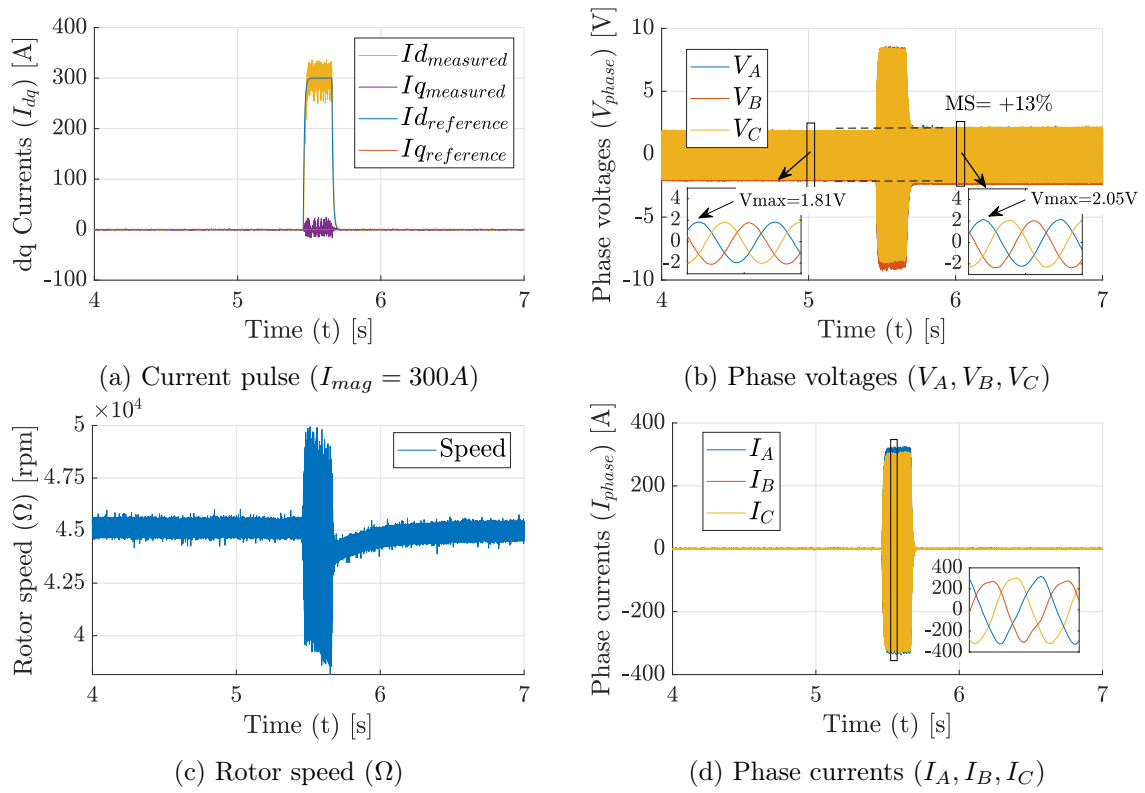
3.6.1.3 Study of errors on the global correction angle $\Delta\theta_c$

Effects of unintentional demagnetization can be introduced to the system when the global correction angle ($\Delta\theta_c$) is badly adjusted. Because of this mentioned error in $\Delta\theta_c$, the d-axis for the controlled currents will not be the same as the real d-axis and the convergence of the system cannot be ensured. This case of study is presented for the machine supplying via $I_{mag} = 300A$, as exhibited in Figure 3.18. A current loop bandwidth $BW = 4krad/s$ and a $\Delta\theta_c = 0^\circ$ (randomly defined) are manually adjusted for this magnetization test. It can be observed a divergence of the control system. Because the peak of magnetization current (of around $I_d = 500A$, which is injected in the machine creating a field in an axis different from the real magnetization) has a sufficient amplitude to lead the machine to an unintentional demagnetization, a reduction is observed in the phase voltages measured after the magnetization procedure.

A second study in Figure 3.19 presents the level of magnetization achieved when this same procedure is realized considering $\Delta\theta_c = 3^\circ$. The phase voltages measured after the current pulse injection are enhanced, which indicates a magnetization of the machine. By switching off the inverter after this mentioned magnetization, a back-EMF of $e = 8V$ is measured. This value is equivalent to the one obtained via standstill tests in Chapter 2 (see Table 2.5). The increase in the number of pulses used for supplying the machine considering this same correction angle $\Delta\theta_c = 3^\circ$ does not modify the back-EMF measured, as expected by the conclusions formerly discussed.

3.6.1.4 Conclusions obtained from these magnetization control tests

Some important insights are obtained from the studies above presented:


 Figure 3.18: Variation of the MS via $I_{mag} = 300A$ for a $\Delta\theta_c$ badly estimated.

 Figure 3.19: Variation of the MS via $I_{mag} = 300A$ for an optimal $\Delta\theta_c$.

- The magnetization test results confirm that similar levels of back-EMF are obtained for running or standstill magnetization procedures (see Table 2.5) considering the same amplitude of magnetization current supplying the VFMM. The results achieved are repeatable, demonstrating a stable behavior of the VFMM composed of the magnet crossed by the flux in its easy magnetization direction.
- The studies at standstill demonstrated the importance of supplying the machine with multiple current pulses to achieve a certain level of back-EMF (see section 2.5.2 in Chapter 2). For the running magnetization, however, because the magnet is already partially magnetized, the use of a single pulse was demonstrated to be efficient for achieving the maximal level of magnetization according to each magnetizing current amplitude.
- For an effective variation of the magnetization state, the amplitude of the d-axis current used for supplying the machine must create a field stronger than the one defining the initial magnetization state (before current supply). This is the reason because the magnet initially magnetized from $I_{mag} = 400A$ in Figure 3.13 only has its magnetization state modified when the machine is supplied with a current $I_{mag} > 400A$ (e.g. $I_{mag} = 500A$, as presented in the Figure 3.15).
- Two major reasons can justify the divergence of the sensorless algorithm proposed: (1) a wrong definition of the current control parameters (e.g. the current loop bandwidth, as seen in Figure 3.16) and (2) a wrong adjustment of the global correction angle, which results in an external field created in an axis differently to the magnetization one (as seen in the Figure 3.18).

3.6.2 Studies of the torque control

3.6.2.1 Studies for defining the global correction angle $\Delta\theta_c$

A similar approach to the one proposed for the magnetization studies is used for investigating, in this section, the torque control in the Fe-Cr-Co-based VFMM according to different amplitudes of q-axis currents used for supplying the machine, assumed to be non-salient. Although the criteria used for adjusting the correction angles via simulation was torque maximization, because the amplitude of torque expected for the machine studied is low, a highly sensible torque sensor would be required, which makes their use unpractical. For evaluating the torque maximization, the DC and AC power, available quantities by using a wattmeter, can be used. These powers are calculated by:

$$P_{DC} = P_{AC} + P_{losses_{sys}} = P_{em} + P_{losses_{mac}} + P_{losses_{sys}} \quad (3.18)$$

where the electromechanical power $P_{em} = \Gamma_e \omega_m = 3/2[p\varphi_s I_q + p(L_d - L_q)I_d I_q]\omega_m$ and ω_m , the mechanical rotor speed. The $P_{losses_{mac}}$ represents the machine losses, calculated by the sum of the Joule stator losses, the iron losses in the stator and rotor, and the mechanical losses. The $P_{losses_{sys}}$ are losses related to the drive system (inverter losses). For the analyses in this section, because the speed and amplitude of the current vector ($I_{ref} = \sqrt{I_d^2 + I_q^2}$) are constant for each test realized, the mechanical and system losses are also constant. Therefore, the equation 3.18 can be reduced to:

$$P_{DC} \approx 3/2[p\varphi_s I_q + p(L_d - L_q)I_d I_q]\omega_m + constant \quad (3.19)$$

The maximization of the P_{DC} and P_{AC} is therefore considered the maximization of the electromagnetic power or of the torque, as the rotor speed is constant. Hence, the DC and AC

power maximization will be the reference used for experimentally adjusting the correction angle in the experimental tests proposed. The machine is supplied via q-axis currents of different amplitudes in a regime $\Omega = 45krpm$. Figure 3.20 exhibits the results achieved by varying the q-axis current up to 50A, for a d-axis current regulated to zero. The correction angle is manually adjusted to maximize the P_{DC} and P_{AC} for each current level.

Results obtained for defining the global correction angle required for torque control are summarized in Table 3.2. In later sections, they will be compared to the ones theoretically obtained using the equations and the non-salient machine model formerly introduced.

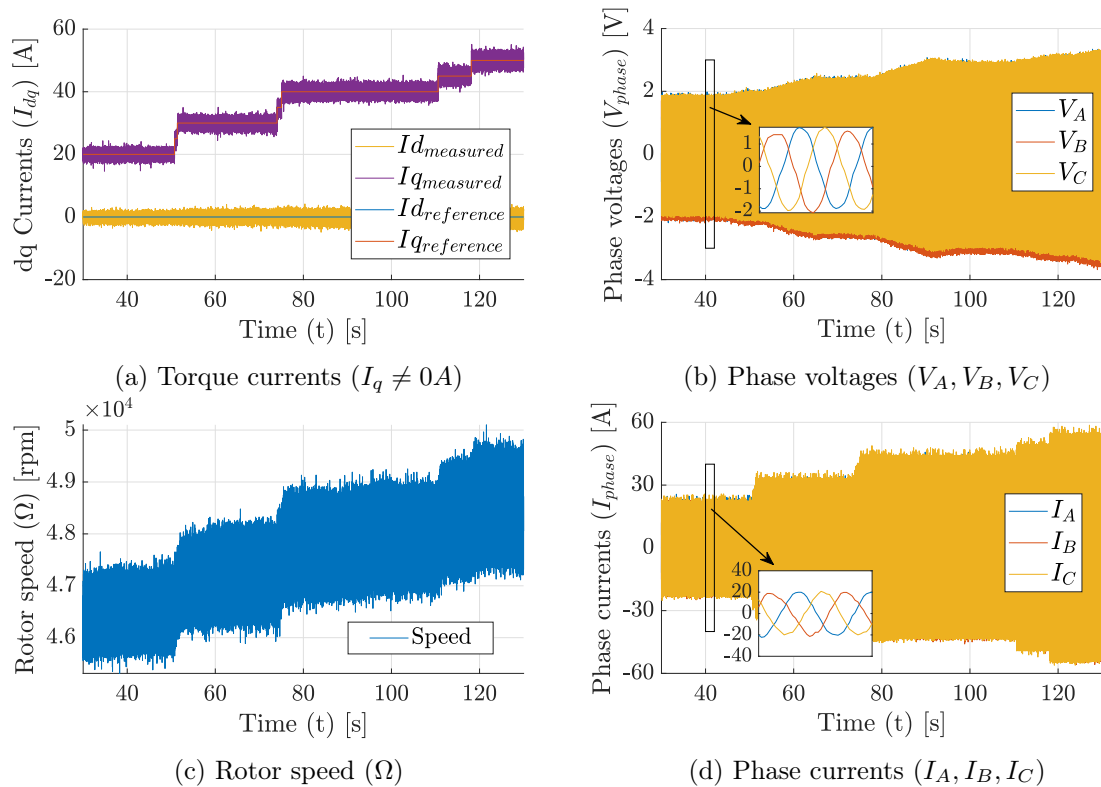


Figure 3.20: Torque control (multiple q-axis current amplitudes).

Table 3.2: Study of the correction angle via experimental tests (For $I_q \neq 0A$ and $I_d = 0A$).

Case	Magnetization current amplitude	Torque speed	Measured rotor current amplitude	DC/AC Power measured	Experimentally adjusted correction angle
	I_d [A]	I_q [A]	Ω [krpm]	P_{DC}/P_{AC} [W]	$\Delta\theta_c$ [o]
(a)	0	30	47.0	155/120	-34
(b)	0	40	47.5	195/157	-43
(c)	0	50	48.5	257/206	-45
(d)	0	60	50.0	300/240	-50
(e)	0	70	50.5	344/275	-54

3.6.2.2 Studies causing an unintentional control loss

A second study is introduced to illustrate a case of unintentional control loss. For these analyses, the q-axis current amplitude supplying the armature windings is continuously increased and the global correction angle is adjusted for respectively maximizing the AC and DC power. The Figure 3.22 exhibits these results. The angle at $\Delta\theta_c$ is initially adjusted to $\Delta\theta_c = -54^\circ$ for a maximum AC and DC power from $I_q = 70A$, and next, to $\Delta\theta_c = -55^\circ$, considering a $I_q = 75A$. From this point, a $I_q = 80A$ is set and a control loss is observed. Two hypotheses are presented to justify this described behavior. First, it should be remembered that an error in the global offset angle generates a divergence between the real currents (machine) and the ones controlled, as formerly discussed by the parametric sensitivity studies introduced in the section 3.5.2. Eventually, this error can lead to a negative d-axis real current, which can result in a demagnetization of the Fe-Cr-Co-based rotor. Because the global correction angle depends on the controlled currents, the divergence between these and the machine currents does not lead to a correction of $\Delta\theta_c$ by the system, and consequently divergence of the control system can be observed. Second, a demagnetization generated by armature reaction effects can also contribute to the same results aforementioned. In this case, for sufficiently high levels of load currents supplying the machine for creating a field in the q-axis, the effects of flux-weakening in the rotor can result in an unintentional reduction of the magnetization state.

Therefore, assuming these demagnetization effects as the reason for the control loss, a strategy is proposed for reducing them. Using the concepts discussed in Chapter 2, it is proposed to supply the machine with d-axis current for creating a field in the magnetization axis. The amplitude of this d-axis current is kept low to avoid a remagnetization of the magnet and also considerable extra Joule losses. The objective is to move the working point away to the knee in the second quadrant of the hysteresis loop, as illustrated in Figure 3.21 for $I_d = 10A$.

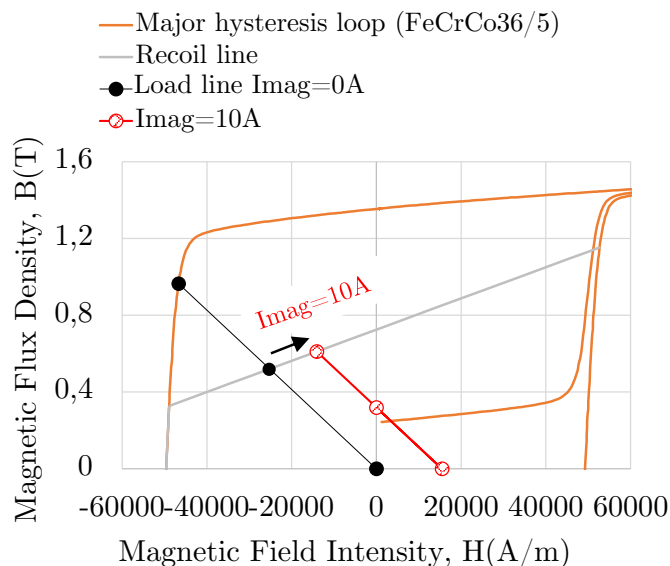


Figure 3.21: Displacement of the load line for $I_{mag} = 10A$.

In this context, a similar experimental test to the one previously presented in Figure 3.22 is proposed. A constant $I_d = 10A$ is regulated for reducing the demagnetization effects while the q-axis current amplitude is enhanced until a loss of control. The results are exhibited in Figure 3.23 and allow to observe that currents up $I_q = 90A$ can be regulated before a control loss, whereas this amplitude was limited to $I_q = 80A$ considering a $I_d = 0A$.

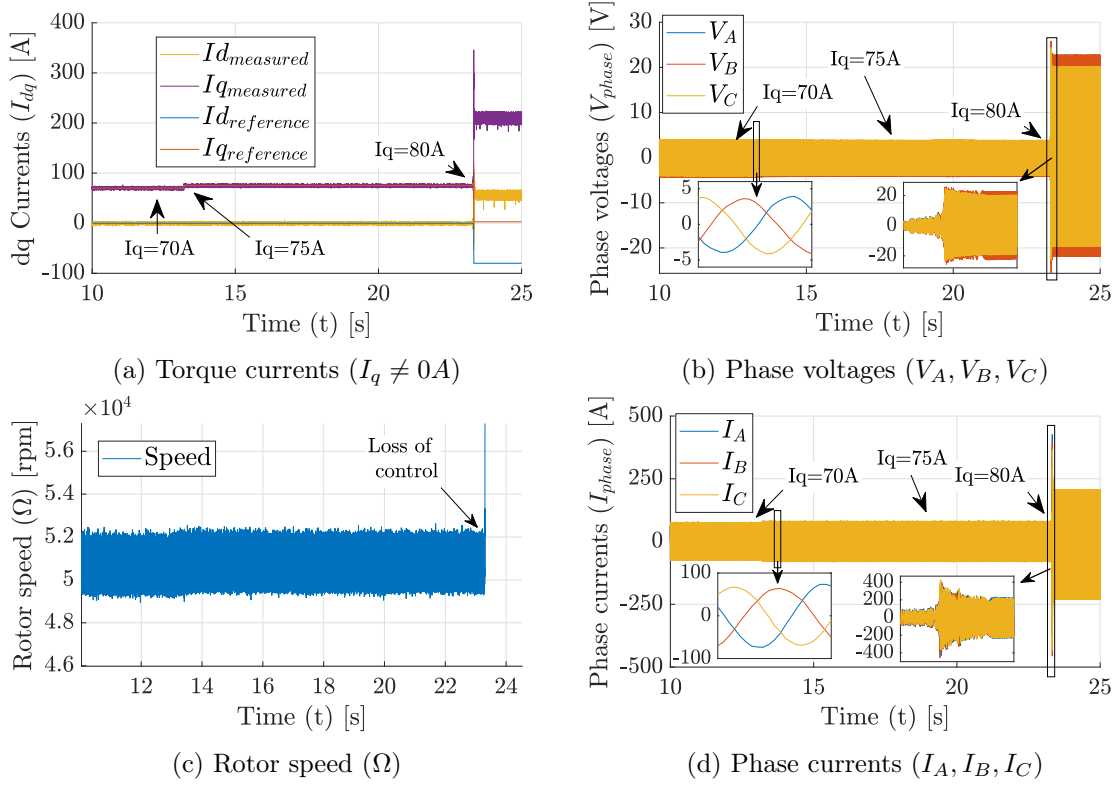


Figure 3.22: Torque control (multiple q-axis current amplitudes) - Analysis of control loss at $I_q = 80A$, for $I_d = 0A$.

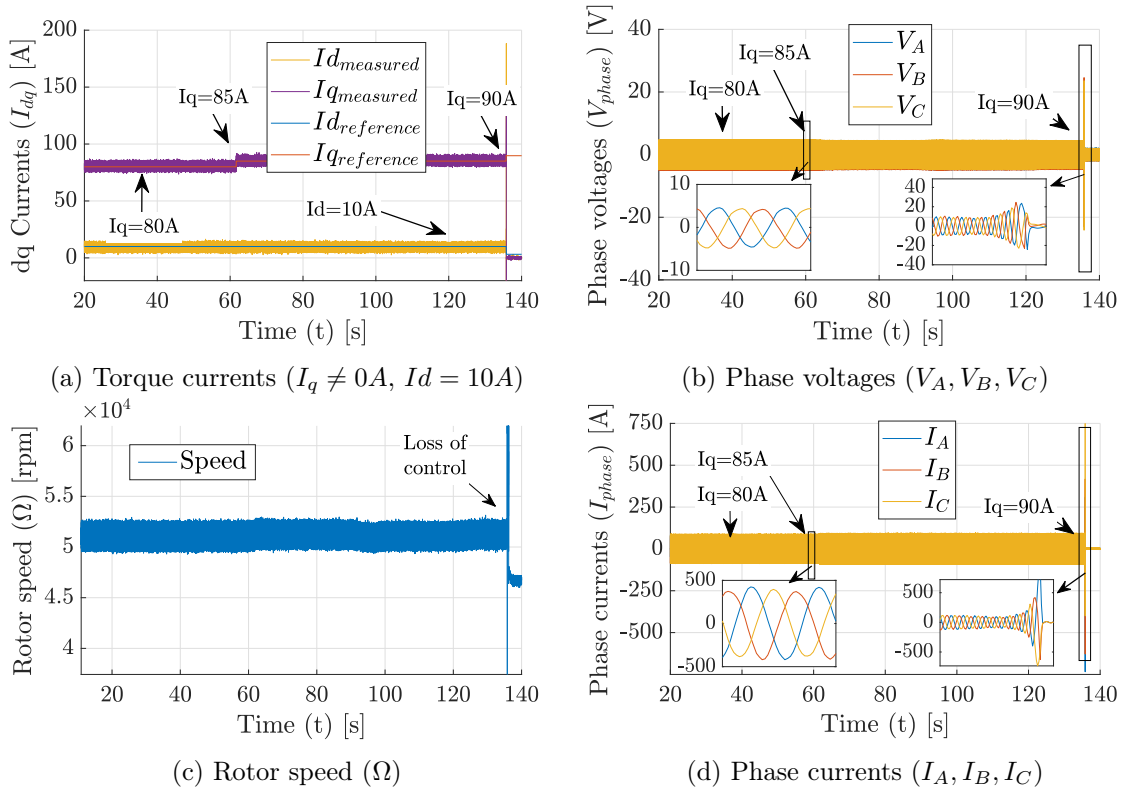


Figure 3.23: Torque control (multiple q-axis current amplitudes) - Analysis of control loss at $I_q = 90A$, for $I_d = 10A$.

3.7 Analyses of errors observed in the errors in the global correction angle

This section proposes, as formerly mentioned, a discussion for evaluating the differences observed between the manually adjusted global correction angle ($\Delta\theta_{cexp}$, experimentally defined) and the ones calculated using the formerly discussed equations ($\Delta\theta_{ccalc}$, which were validated via simulations) for different working conditions. Figure 3.24 summarizes the mentioned angles, considering the non-salient machine hypothesis for analyzing (1) the magnetization control by different amplitudes of d-axis currents and (2) torque control by different q-axis current amplitudes. The difference $\Delta = \Delta\theta_{cexp} - \Delta\theta_{ccalc}$ highlighted in this Figure 3.24 is expected to be null if angles experimentally obtained are the same achieved by the equations/simulations considering the machine parameters supposed known. For this reason, Δ is going to be used in the next sections to verify if the machine parameters are well estimated.

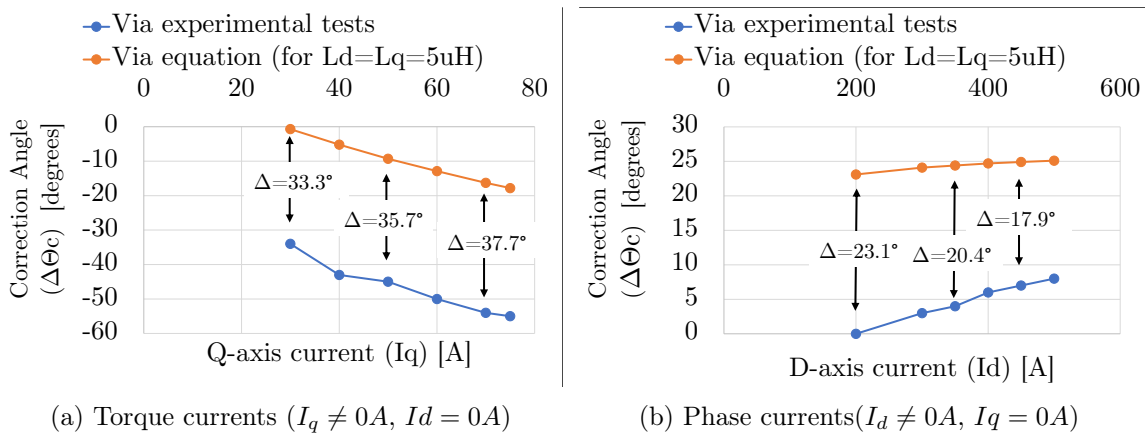


Figure 3.24: Comparison between correction angles obtained via equations ($\Delta\theta_{ccalc}$) and experimental tests ($\Delta\theta_{cexp}$) considering non-salient machine ($L_d = L_q = 5\mu H$ and $R_s = 5m\Omega$) at $\Omega = 45krpm$.

The error Δ in the Figure 3.24 can be justified by:

- No regulated speed during experimental tests: The global correction angles obtained via equations are calculated considering a set speed $\Omega = 45krpm$. However, in the experimental setup, the rotor speed is not regulated at this reference, being externally guided by the axial airflow crossing the machine. For this reason, during the experimental tests of torque control, variations on Ω can be observed. These variations have an impact on the real global correction angle (the one experimentally required for the control system convergence) with regard to the calculated one (considering a constant Ω).
- Parametric errors in the inductances: The global correction angles are calculated considering also the non-salient machine modeling characterized by $L_d = L_q = 5\mu H$. Errors in the estimation of these parameters can be however considered critical for a good estimation of the global correction angle via equations. This conclusion is provided by the parametric sensitivity study introduced in the section 3.2.5, which indicates that the machine parameter affecting the most $\Delta\theta_c$ during a torque control is L_q . Also, results exhibited in the section 3.5.2 indicate that a poor estimation of the inductances can lead to unintentional demagnetization of the Fe-Cr-Co-based rotor.
- Parametric errors in the stator resistance: Also from the conclusions obtained from the

parametric sensitivity studies, it can be observed that for magnetization control tests, the stator resistance R_s is the parameter that impacts the most $\Delta\theta_c$.

By the discussions above presented, it is noticed that parametric errors are probably the main reason for the error Δ between the manually adjusted global correction angle and the ones calculated using the formerly discussed equations.

3.8 The the dq-axis inductances modeling

The previous section justified the interest in a deeper analysis of the machine parameters for accurately defining $\Delta\theta_c$. In this context, this section is focused on characterizing the machine parameters, with a focus on describing the evolution of the dq-axis inductances.

3.8.1 Estimation of the dq-axis inductances according to the FeCrCo36/5 hysteresis curve

The methodology described in this section is based on the one introduced in [144] for a PMSM. Simulations by Finite Element Analysis are proposed by supplying the machine geometry introduced in the Chapter 2 by different current vector amplitudes (I_{ref} , where $I_{ref} = \sqrt{I_d^2 + I_q^2}$). The angle δ , defined with regard to the q-axis, is varied for characterizing the dq-axis current components ($I_q = I_{ref}\cos(\delta)$ and $I_d = -I_{ref}\sin(\delta)$) crossing the armature windings. The static dq-axis inductances (L_d and L_q , respectively) are then calculated according to each pair (I_d, I_q) by:

$$\begin{cases} L_d(I_d, I_q) = \frac{\varphi_d(I_d, I_q) - \varphi_s}{I_d} \\ L_q(I_d, I_q) = \frac{\varphi_q(I_d, I_q)}{I_q} \end{cases} \quad (3.20)$$

where φ_d and φ_q are the d- and q-axis flux linkage through the stator windings, calculated from the three-phase flux linkage by the Park and Clarke Transform-based introduced in the Chapter 1.

The key challenge involved in the analysis of the inductances via simulations is the anisotropy differentiating the easy and hard magnetization directions of the FeCrCo36/5 composing the rotor of the VFMM studied in this thesis. The recoil lines obtained from the methodologies presented in Chapter 2 will be used in this present section as a reference for magnetically characterizing the rotor in the simulations proposed. Figure 3.25 illustrates this characterization of the magnet in the dq-axis based on these mentioned recoil lines.

It should be remembered that from the results presented in Chapter 2 which concerns the easy magnetization direction (d-axis), each recoil line is characterized by a different relative permeability. As a consequence, the complete modeling of the d-axis inductances would require the characterization of the flux considering each one of these recoil lines separately. For simplicity, only one of these curves is proposed to be used for modeling the d-axis in this present study for the dq-axis inductances estimation: the one obtained from a standstill magnetization by $I_{mag} = 400A$ (d-axis relative permeability $\mu_{rd} = 6.47$), as this was the level of current used to set the initial magnetization state before the torque control tests exhibited in the section 3.6.2. In which concerns the characterization of the q-axis magnetic behavior, described as a hard magnetization direction of the FeCrCo36/5, the relative permeability of $\mu_{rq} = 14.65$ is defined for all the recoil lines according to the assumption of a parallelism between the internal and external hysteresis loop introduced in the Appendix B.7. The Fe-Cr-Co-based rotor is therefore characterized by the assumption of the constant $\mu_{rd} = 6.47$ and a constant $\mu_{rq} = 14.65$.

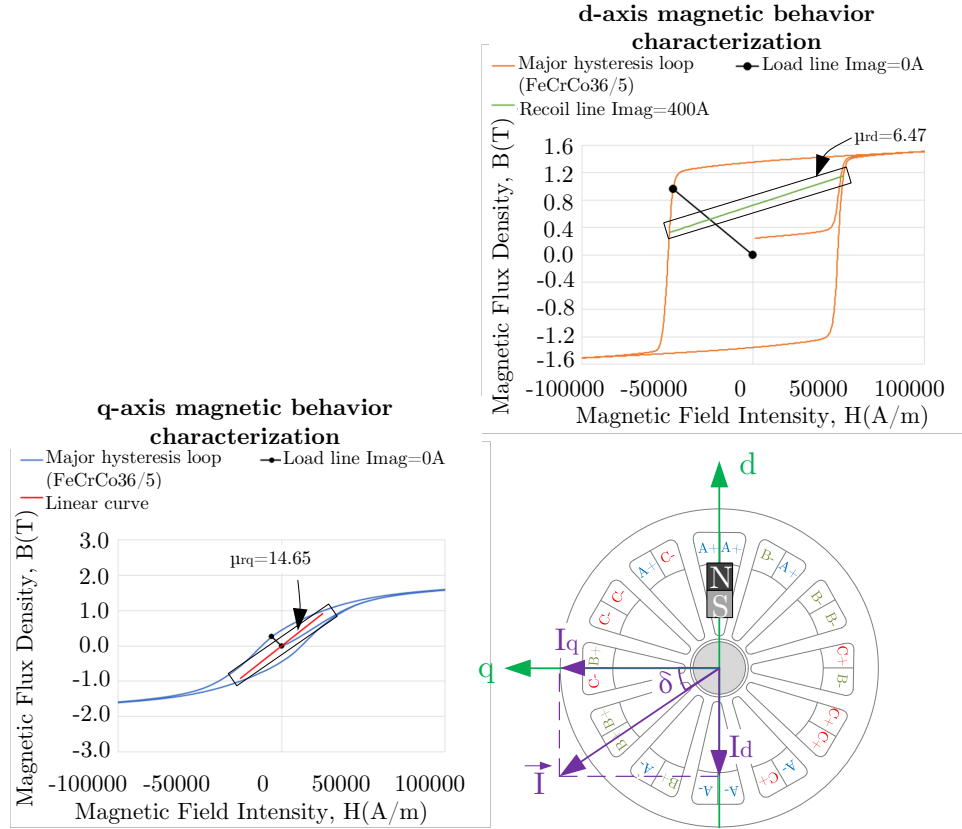


Figure 3.25: Magnet characterization for estimating the dq-axis inductances via FEA simulations - Identification of δ , the torque angle.

Simulations are carried out considering different amplitudes of currents supplying the machine from $\delta = 0^\circ$, in which only a q-axis field is created in the machine, to $\delta = 90^\circ$, in which only a d-axis field is present. Figure 3.26 exhibits respectively, the direct and quadrature axes flux linkages for current amplitudes of $0 < I_{ref} < 100A$ and a torque angle $0^\circ < \delta < 90^\circ$. The static inductances L_d and L_q are calculated using equations 3.20. The achieved results are presented knowing that q-axis currents of amplitude $30A < I_q < 80A$ supplies the machine in the proposed torque control and that a low amplitude of d-axis current ($-50A < I_d < -10A$) can eventually cross the armature windings. These results will be later used for calculating θ_{PLL} . The most important conclusion is the observation of q-axis inductances higher than the d-axis ones ($L_q > L_d$), which indicates that a reluctance is present in this machine.

Remark: The difference between the d- and q-axis inductances can be justified, as aforementioned, by the difference in the relative permeability describing the hysteresis loop of the magnet in these two axes. By applying Ampère's circuital law, it can be defined as:

$$L = \mu_0 \mu_r \frac{AN^2}{l} \quad (3.21)$$

where A (in $[m^2]$) represents the cross-sectional area, l (in $[m]$) the length of the path described by the flux lines (in $[m]$), N the number of turns of the solenoid generating the flux. Therefore, a proportionality is expected between μ_r and L . For the magnetic rotor composing the VFMM investigated in this thesis, as $\mu_{rq} > \mu_{rd}$, the inductances L_q are expected to be higher than L_d , as results obtained demonstrated.

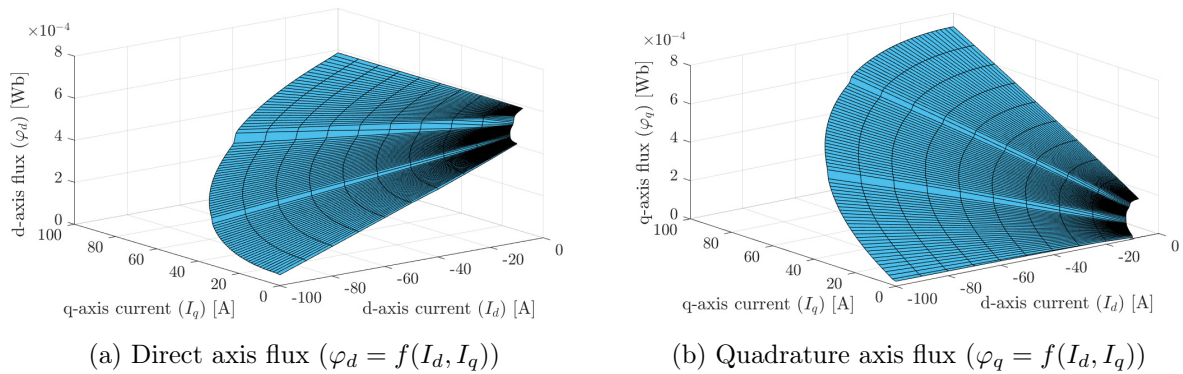


Figure 3.26: Flux estimated via FEA according to the dq-axis currents considering the anisotropic magnetic profile of the FeCrCo36/5.

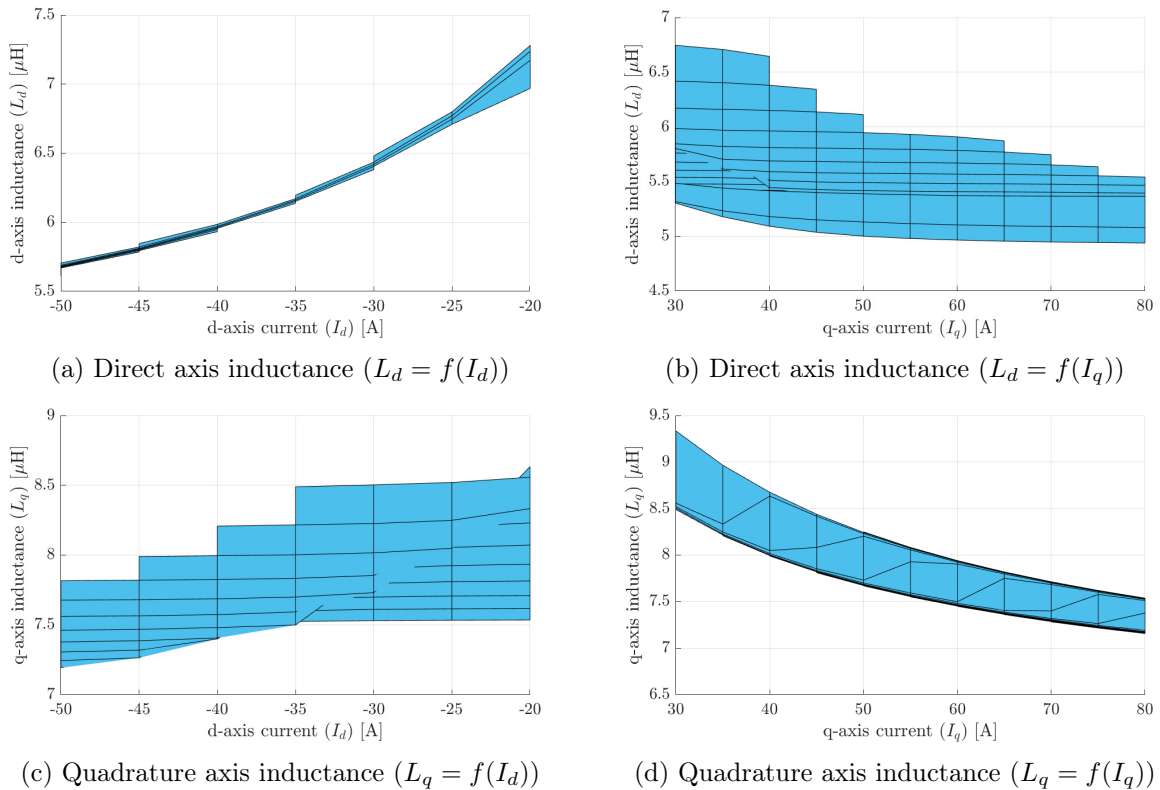


Figure 3.27: Static inductances estimated via FEA according to the dq-axis currents considering the anisotropic magnetic profile of the FeCrCo36/5.

3.8.2 Evaluation of the inductances estimated from the methodology described

An in-depth analysis of the dq-axis inductances estimated according to the methodology described allows to conclude that these both parameters are expected to present higher values than the ones initially considered ($L_d = L_q = 5\mu H$). Indeed, the parametric sensitivity study in the section [3.2.5](#) demonstrated that higher inductances are expected to reduce $\Delta\theta_c$ in the case of torque control and to enhance this angle in the case of magnetization control. For both cases,

higher inductances will approximate the angles $\Delta\theta_c$ calculated from the machine model to the ones experimentally obtained.

Also from these results, it is concluded that despite the non-salient geometry of the rotor, a reluctance exists in the machine due to the anisotropic magnetic behavior between the easy and the hard magnetization directions of the FeCrCo36/5. The next section is going to be dedicated to verifying the impact of these salient poles on the global correction angle.

Because of the differences between the d- and q-axis inductances, the torque angle defining the dq-axis current components for which the maximal torque is achieved is not null ($\delta_{max} \neq 0^\circ$). Considering the L_d and L_q assuming the mean values defined from the described results, the torque profile in Figure 3.28 can be obtained for different amplitudes of regulated current. It is noticed, for example, that a maximal torque $\Gamma_e = 0.65N.m$ is expected at $\delta_{max} = 18.5^\circ$ for a machine supplied by $I_{ref} = 70A$ and $\Gamma_e = 0.46N.m$ at $\delta_{max} = 15.5^\circ$ in case of $I_{ref} = 50A$.

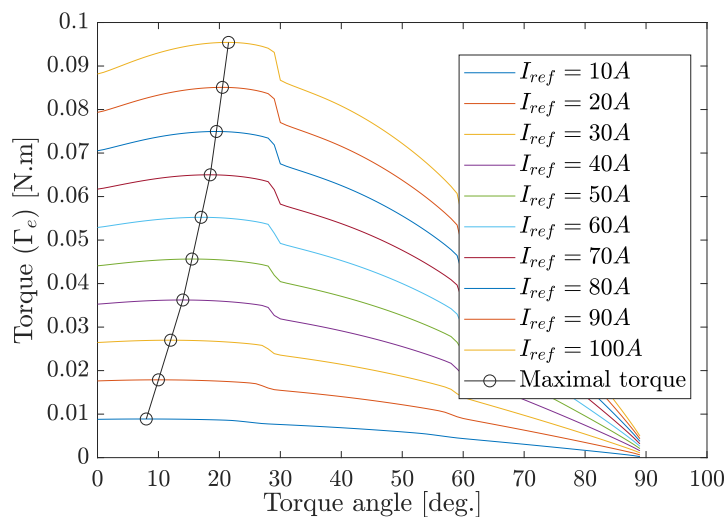


Figure 3.28: Torque measured for several amplitudes of current vector I_{ref} considering different torque angles δ ($\Gamma_e = f(\delta)$).

3.9 Study of the global correction angle ($\Delta\theta_c$) considering the reluctance effects

The conclusions obtained in the previous section demonstrated that although the geometric non-salience observed in the rotor, the magnetic anisotropy of the FeCrCo36/5 generates a reluctance effect. The dq-axis inductances are therefore different and the maximum torque per ampere is obtained with a torque angle different from zero (or $I_d \neq 0A$). This characteristic of the machine, not considered in the simulations formerly proposed for validating the system (see section 3.5), is the focus of this present section, especially dedicated to the study of torque control.

The inductances characterizing the machine assume mean values defined according to the results exhibited in Figure 3.27, in which $L_d = 6\mu H$ and $L_q = 8\mu H$ can be identified. Some modifications are proposed in the parameters used in the simulation system in accordance with the experimental behavior of the machine formerly observed in the torque control studies:

- The flux linkage crossing the armature windings is reduced to $\varphi_s = 450\mu Wb$ for taking into account the demagnetization effects when load currents supply the machine.

- The regime considered for simulations is increased to $\Omega = 50krpm$ for being approximated to the values measured during the experimental tests (see Table 3.2).
- As described in the section 3.2.3, for the studies presented in this thesis, filters of first order are considered for simplifying the filtering chain used. This simplification, as also the dependency of the angle delay generated by these filters on the rotor speed can represent a source of errors of around 5° in relation to the ones initially considered. For this reason, the filtering angle $\theta_{filter} = -15.07^\circ$ in the simulations formerly analyzed for $\Omega = 45krpm$ will assume the value $\theta_{filter} = -10.29^\circ$ for the next to ones at $\Omega = 50krpm$.

3.9.1 Analysis via simulation considering a defined amplitude of current: a case study at $I_{ref} = 70A$

Simulations are carried out considering the specifications above described for multiple amplitudes of regulated currents I_{ref} . The correction angle is regulated having as reference the maximization of the DC and AC power, for ensuring a similar operating condition to the one defined in the experimental tests. This section presents as example of this study for $I_{ref} = 70A$, as exhibited in Figure 3.29.

The torque angle is initially set to $\delta = 0^\circ$, as defined for the experimental tests presented in the section 3.6.2 due to the initial hypothesis of the non-salient machine. The correction angle $\Delta\theta_c$ is then calculated from θ_{PLL} and θ_{filter} according to the controlled currents ($I_d = 0A$ and $I_{ref} = I_q$). Considering that no parametric error exists between the machine parameters (real dq-axis inductances and stator resistance) and the ones used for defining the current loop control, a convergence is expected between the dq-axis real currents (machine currents), the controlled ones, and the set point (reference currents). This working condition is presented by Case (1), in Figure 3.29, and defines the correction angle of reference ($\Delta\theta_{c_{ref}}$, where the index *ref* is used for indicating that this the correction angle that allows the convergence of the control currents to both the reference and the machine currents). Because, however, a reluctance is observed in the machine model, the torque is not maximized when $\delta = 0^\circ$ (or $I_d = 0A$), as the reluctance torque component ($p(L_d - L_q)I_dI_q$) is null at this condition.

Variations in $\Delta\theta_c$ around the reference aforementioned ($\Delta\theta_{c_{ref}}$) are following proposed for investigating in which condition the torque is maximized. First, for $\Delta\theta_c < \Delta\theta_{c_{ref}}$, as exhibited in Case (2), a positive d-axis machine current component is observed although this current reference is null. The torque and both DC and AC power are reduced in relation to the one measured in (1), as a consequence of a negative reluctance torque that appears in the machine ($p(L_d - L_q)I_dI_q < 0$ because $I_d > 0$ and $(L_d - L_q) < 0$). However, for angles $\Delta\theta_c > \Delta\theta_{c_{ref}}$ as defined in (3), a negative d-axis machine current component is observed as also a positive reluctance torque, which increases the total torque and both DC and AC power. These parameters can be still enhanced for more positive correction angles, as presented in case (4). From this point, it is observed that an increase in $\Delta\theta_c$ has an effect of reduction in the total torque and both DC and AC power, as case (5) demonstrates. In case (6), the correction angle is again adjusted as in (4), for confirming the maximization of the torque and the DC and AC power at this working condition. Nevertheless, it is observed from cases (2)-(7) that the controlled currents do not converge to the machine ones, which can cause a divergence of the system even when the torque is maximized (case (4)). For ensuring this convergence, a rotation in the controlled current vector is required from the consideration of the torque angle for redefining the dq-axis currents. Case (7) exhibits the results achieved in this case, for a $\delta = \delta_{max} = 18^\circ$. The maximal torque (and the maximal torque and DC and AC power) as well as the convergence of the controlled to the machine and reference currents can be achieved in this operating condition.

Similar studies are presented in the Appendix C.5 for a current amplitude $I_{ref} = 50A$, for which the maximal torque is expected at $\delta_{max} = 15.5^\circ$.

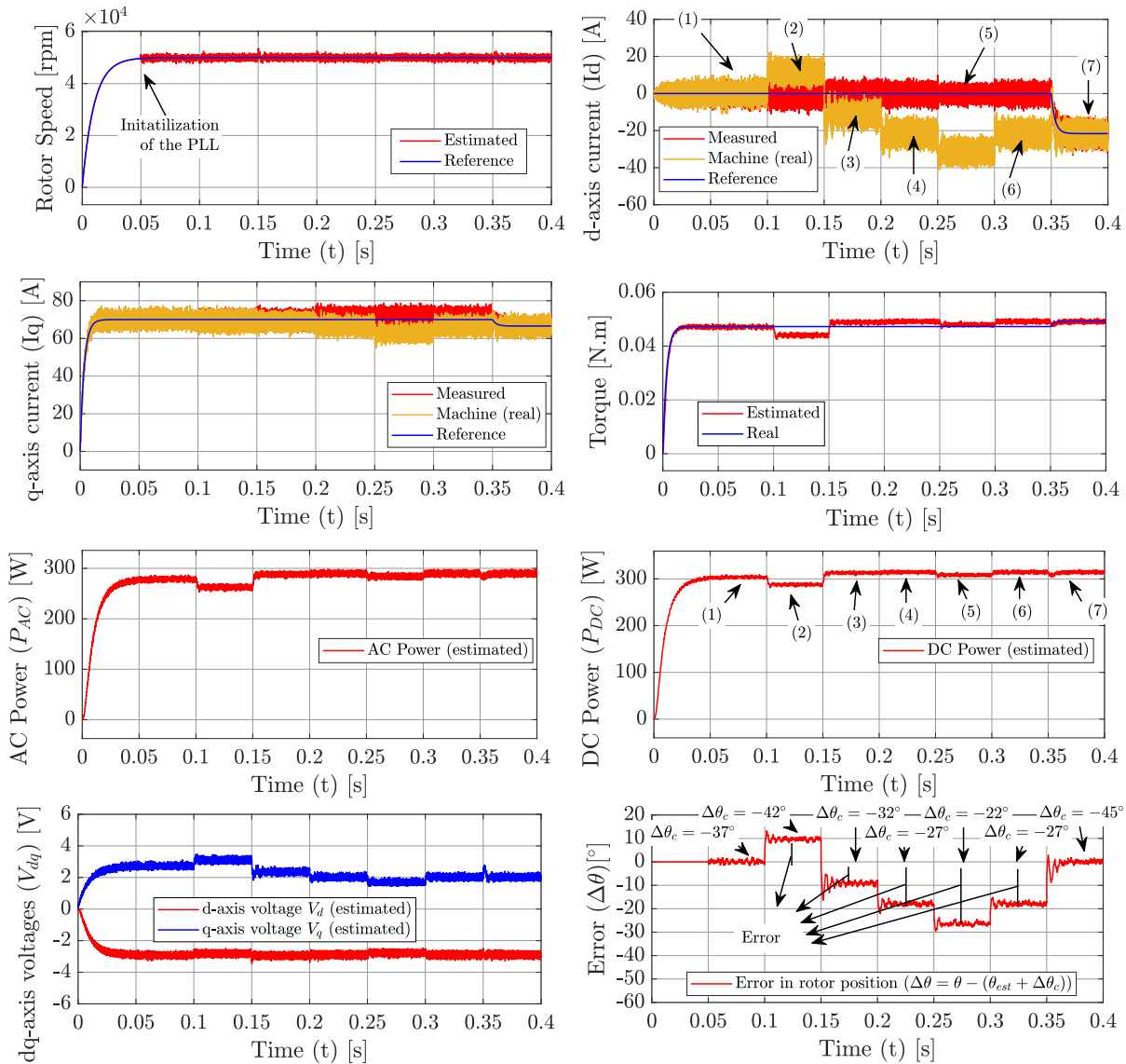


Figure 3.29: Effect of the variation of the correction angle ($\Delta\theta_c$) considering the hypothesis of a salient machine ($L_d = 6\mu H$ and $L_q = 8\mu H$) - Study for $I_{ref} = 70A$.

Remark: The real torque is calculated from the controlled currents. For this reason, because $\delta = 0^\circ$ for cases (1)-(6), $I_{dref} = 0$ and the reference torque is constant. In case (7), which considers $\delta = 18^\circ$ and therefore, an $I_{dref} \neq 0$, the reluctance torque reference is non-null and the total real torque is enhanced.

3.9.2 Definition of the equation calculating the global offset angle for a reluctance machine

As previously discussed, because the machine was initially assumed non-salient, the experimental tests presented in the section 3.6.2 were carried out for $\delta = 0^\circ$ and a manual adjustment of the correction angle using as reference the maximization of both DC and AC power. Assuming the hypothesis that the torque angle for maximal torque (δ_{max} , defined according to the Figure 3.28)

is well estimated from the simulations proposed, this information can be taken into account in this present section for defining the dq-axis current references. In this case, the correction angle $\Delta\theta_c$ is calculated from these new references of current by the same equation previously defined by:

$$\Delta\theta_c|_{\delta=\delta_{max}} = (\theta_{PLL} - \theta_{filter})|_{\delta=\delta_{max}} \quad (3.22)$$

For a non-salient pole machine $\delta_{max} = 0^\circ$ and the equation 3.22 becomes the equation 3.4 presented at the beginning of this present Chapter (see section 3.2.1).

In the case of the $\Delta\theta_c$ calculated for dq-axis current components regulated considering $\delta = 0^\circ$, if a salient machine is considered, the maximization of the DC and AC power cannot be directly obtained by the difference $(\theta_{PLL} - \theta_{filter})$. Instead, this equation has to be adapted taking into account the information of δ_{max} for each amplitude of reference current regulated. The equation below can be therefore defined as:

$$\Delta\theta_c|_{\delta=0^\circ} = (\theta_{PLL} - \theta_{filter})|_{\delta=\delta_{max}} + \delta_{max} \quad (3.23)$$

The study presented the Figure 3.29 is used as an example for validating this above-presented equation 3.23 considering as hypothesis that the torque angle ($\delta_{max} = 18^\circ$) is known from the FEA simulations. For $I_{ref} = 70A$, it is observed that the maximal DC and AC power are obtained for $\Delta\theta_c = (\theta_{PLL} - \theta_{filter}) = -45^\circ$, calculated when the dq-axis currents are defined using the torque angle knowledge. This same maximization can be achieved considering $\delta = 0^\circ$ (as it is the case of the experimental results presented in the section 3.6.2) but calculating $\Delta\theta_c$ from the equation 3.23. In this case, $\Delta\theta_c = -45^\circ + 18^\circ = -27^\circ$ (where $(\theta_{PLL} - \theta_{filter})|_{\delta=\delta_{max}} = -45^\circ$ and $\delta_{max} = 18^\circ$).

The same analyses discussed can be obtained from the results presented in the Appendix C.5 for $I_{ref} = 50A$. Defining the reference dq-axis currents from the torque angle $\delta_{max} = 15.5^\circ$, a correction angle $\theta_{PLL} - \theta_{filter} = -33.5^\circ$ can be calculated. For maximizing the torque and the DC and AC power at $\delta = 0^\circ$ and for being able to compare these results with the ones obtained via the experimental test formerly presented, a correction angle $\Delta\theta_c = -33.5 + 15.5 = -17^\circ$ is required. These results will be used as a reference for evaluating the inductance modeling proposed.

3.9.3 Evaluation of the global correction angle considering the reluctance machine

As previously proposed in the section 3.7, this present one discusses, from the results exhibited in Figure 3.30, the comparison between the global correction angle calculated from the estimated machine model, from which dq-axis inductances of $L_d = 6\mu H$ and $L_q = 8\mu H$ are identified, and the angles manually adjusted in the experimental tests. For both cases, the maximization of the AC and DC power at $\delta = 0^\circ$ is used as a reference for defining the angles. The calculated ones are obtained from the equation 3.23 by using the reluctance profile estimated via FEA simulations.

These results can be also compared with the ones presented in Figure 3.24, considering the initially investigated non-salient machine model (characterized by $L_d = L_q = 5\mu H$). It can be observed that the assumption of a reluctance machine reduces the error Δ between the calculated and the experimentally obtained correction angles of around 25%. It should be reminded that not only does the reluctance model contribute to these better results, but also the increase of the regime used for simulations (from $\Omega = 45krpm$ to $\Omega = 50krpm$) and the reduction of the filtering angle (from $\theta_{filter} = -16.73^\circ$ to $\theta_{filter} = -10.30^\circ$ at $\Omega = 50krpm$) and of the flux linkage (from $\varphi_s = 500\mu Wb$ to $\varphi_s = 450\mu Wb$).

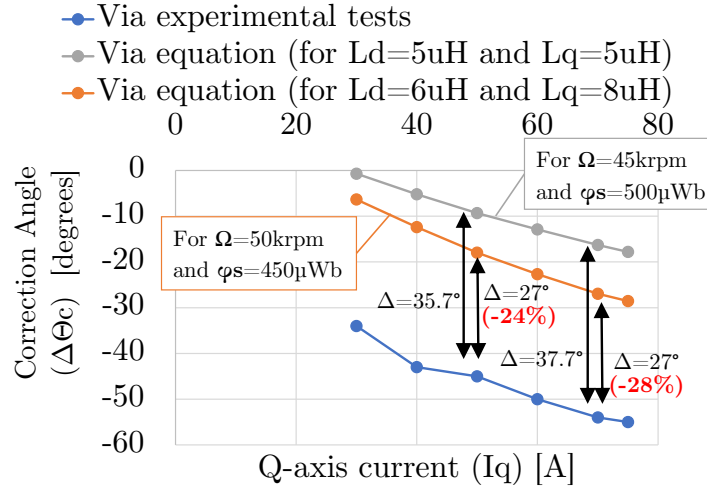


Figure 3.30: Comparison between correction angles for maximizing the torque and both DC and AC power via equations and experimental tests for multiple I_{ref} and $\delta = 0^\circ$.

3.10 Proposition of improvements in the dq-axis inductance modeling

3.10.1 Analysis of the impact of the stator material in the dq-axis inductance modeling proposed

Because the error Δ between the experimental and calculated global correction angles is still important, in-depth studies are proposed in this section to approximate the estimated working conditions to the real ones. The formerly introduced analyses were focused on better estimating the rotor speed, flux linkage, filtering angle, and dq-axis inductances due to the magnet anisotropy. In this present one, attention is given to the saturation of the material composing the stator. Simulations are proposed considering the stator composed of a hypothetical ferromagnet saturating in a three times higher level of magnetic flux density than the COGENT NO20 composing of the original stator. This hypothetical material, whose magnetic profile is reminded in Figure 3.31, is the same previously used for the saturation studies in the section 2.7.2.3

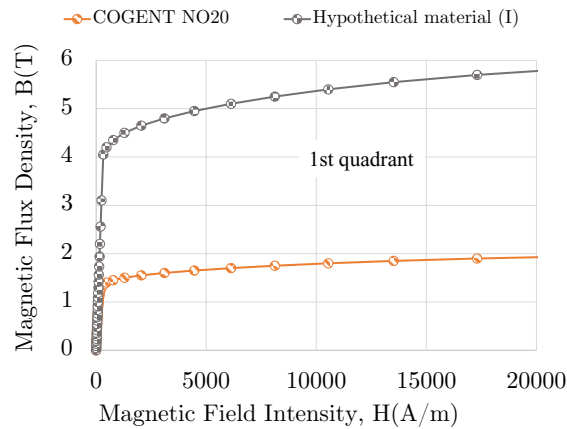


Figure 3.31: Magnetic profile of hypothetical material composing the stator during simulations.

For this study via FEA simulations, the characterization of the rotor is not modified, being described by an anisotropy characterized by a d-axis relative permeability $\mu_{rd} = 6.47$ and a q-axis relative permeability $\mu_{rq} = 14.65$. Figure 3.32 exhibits the estimated dq-axis flux and Figure 3.33 the estimated static inductances.

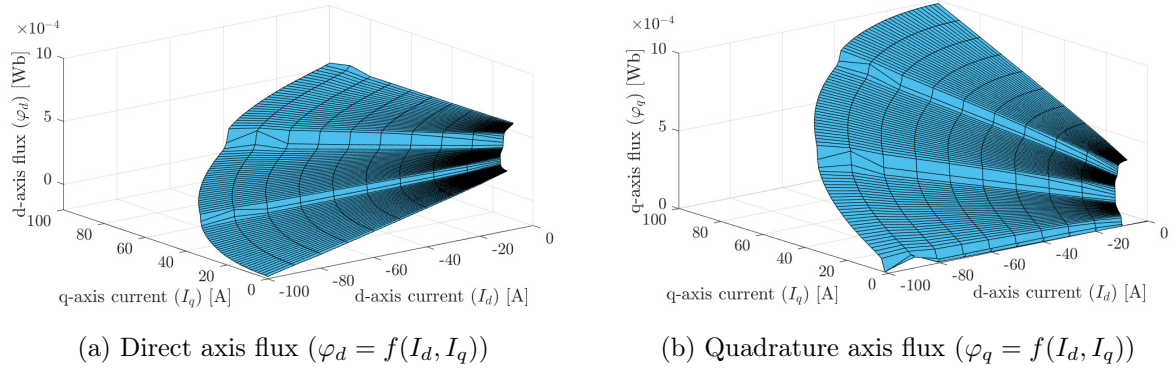


Figure 3.32: Flux estimated via FEA considering the anisotropic magnetic profile of the FeCrCo36/5 and a hypothetical ferromagnet material composing the stator.

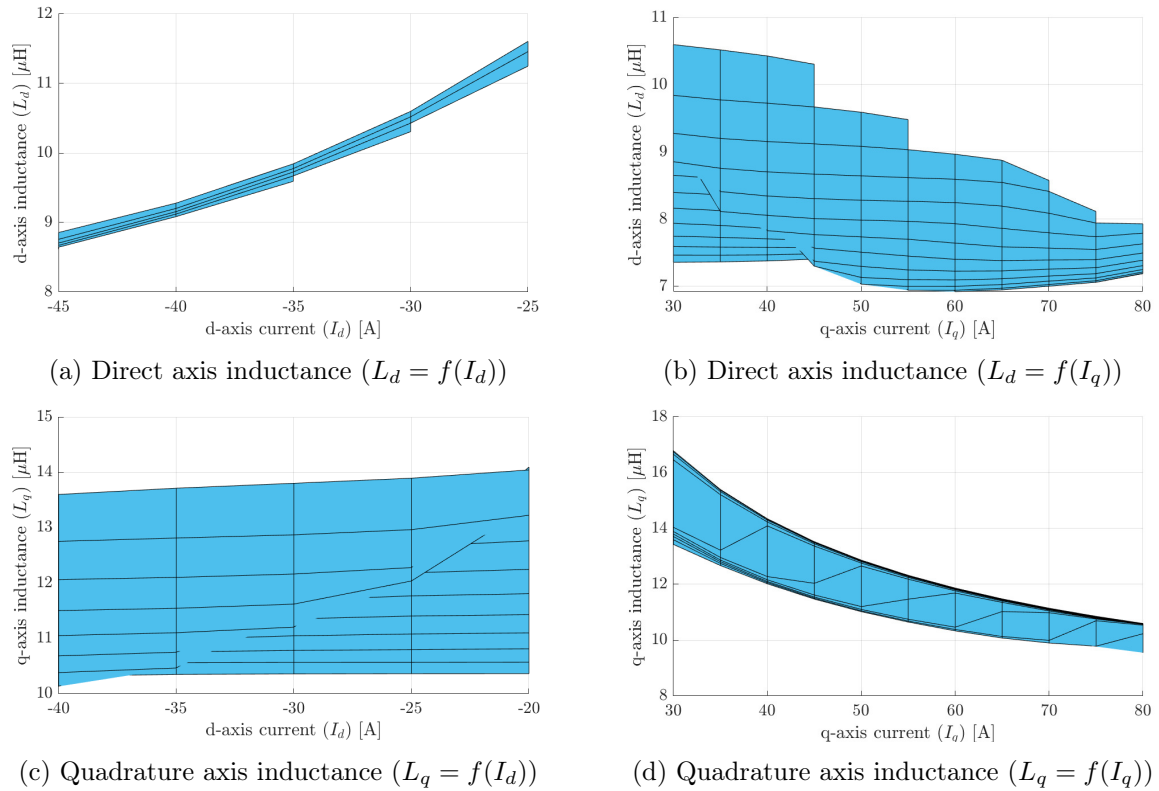


Figure 3.33: Static inductances estimated via FEA considering the anisotropic magnetic profile of the FeCrCo36/5 and a hypothetical ferromagnet material composing the stator.

The results presented in Figure 3.33 indicate that errors in the characterization of the stator material can also have an influence on the dq-axis inductances estimated. The mean value of these parameters increases considering the magnet inserted in this reduced saturation scenario,

assuming as observed values $L_d = 10\mu H$ and $L_q = 12\mu H$. The impact of the use of these new parameters in the calculation of the global correction angles for different working conditions is going to be discussed in later sections.

3.10.2 Evaluation of the global offset angle considering the improved model of reluctance machine

The parametric studies formerly introduced in the section 3.2.5 provide a conclusion that $\Delta\theta_c$ is particularly dependent on the values of the dq-axis inductances. Figure 3.34 exhibits the error Δ obtained by comparing the experimentally adjusted angles and the ones calculated using: (1) the non-salient model assumed well known and characterized by $L_d = L_q = 5\mu H$, (2) the dq-axis inductances estimated by taking into account the magnetic anisotropy of the material used in the rotor, which allowed to estimate $L_d = 6\mu H$ and $L_q = 8\mu H$, and (3) by taking also into account modifications in the saturation profile of the material composing the stator, which increase these inductances for $L_d = 10\mu H$ and $L_q = 12\mu H$. As can be noticed, the comparison of the global correction angle calculated considering these last mentioned dq-axis inductances model with the one calculated from a non-salient machine geometry allows to identify a reduction of around 65% lower in the error Δ . In comparison with the results obtained from the first proposed dq-axis inductances model, a reduction of around 55% is observed in the error Δ . Although errors of around 10° are still observed by the model proposed in relation to the experimentally adjusted angles, the order of magnitude achieved is sufficient for estimating the correction angle via the equations proposed. In this case, fine-tuning is still necessary in the experimental tests in order to maximize the torque in the machine.

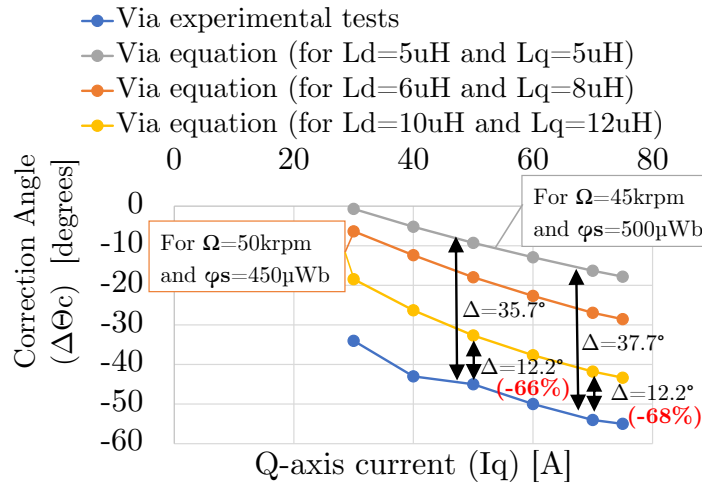


Figure 3.34: Comparison between correction angles for maximizing the torque and both DC and AC power via equations and experimental tests for multiple I_{ref} and $\delta = 0^\circ$.

Experimental tests similar to the ones initially proposed in the section 3.6.2 were realized considering the torque angle δ obtained from FEA simulation for maximizing the DC and AC power (Figure 3.28) of a machine characterized by the dq-axis inductances of $L_d = 10\mu H$ and $L_q = 12\mu H$. The Figures 3.35 and 3.36 present the experimental results achieved for a reference current $I_{ref} = 70A$. The dq-axis current components are regulated for a torque angle for maximal torque $\delta_{max} = 18^\circ$. It is observed that a manually adjusted correction angle of $\Delta\theta_c = -72^\circ$ is required in this working condition for maximizing the DC and AC power measured in this experimental test. The system was demonstrated to be stable and capable of operating for long

periods of time. An AC power $P_{AC} = 280W$ is measured. This amplitude is close (4% lower) to the one estimated via simulations (in which $P_{AC} = 290W$ could be measured). The dq-axis voltages provide also a reference for verifying if the angle is correctly adjusted. Via simulation, it can be identified $v_d = -4.2V$ and $v_q = -1.5V$, while the experimental tests (Figure 3.35) results in $v_d = -4.3V$ and $v_q = -1.2V$.

Additionally, a comparison is proposed by the presentation in Figure 3.37 of the control system behavior when the torque angle is not considered (then $\delta = 0^\circ$), for a machine supplied via the same amplitude of reference current as before ($I_{ref} = 70A$). The correction angle in this condition can be estimated according to the equation 3.23 previously proposed (which defines $\Delta\theta_c = -42^\circ$) and adjusted experimentally for achieving the maximal DC and AC power. In this condition, $\Delta\theta_c = -54^\circ$. A loss of control is observed when the system is left running for a long time.

By taking into account the torque angle, it is also noticed that the amplitude of reference

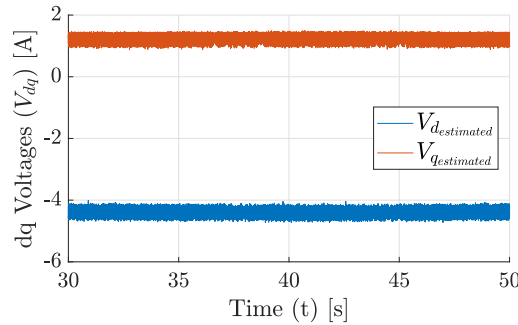


Figure 3.35: Estimated (control) dq-voltages (V_d, V_q) for $\delta = 18^\circ$ ($I_{ref} = 70A$).

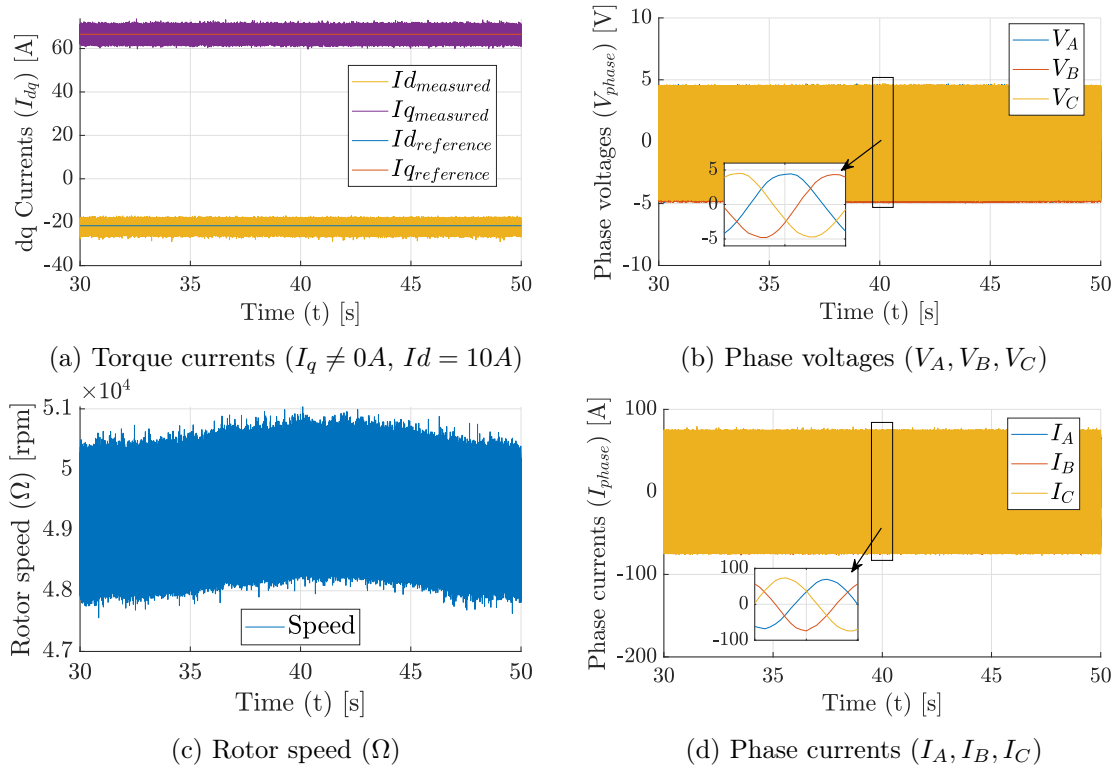
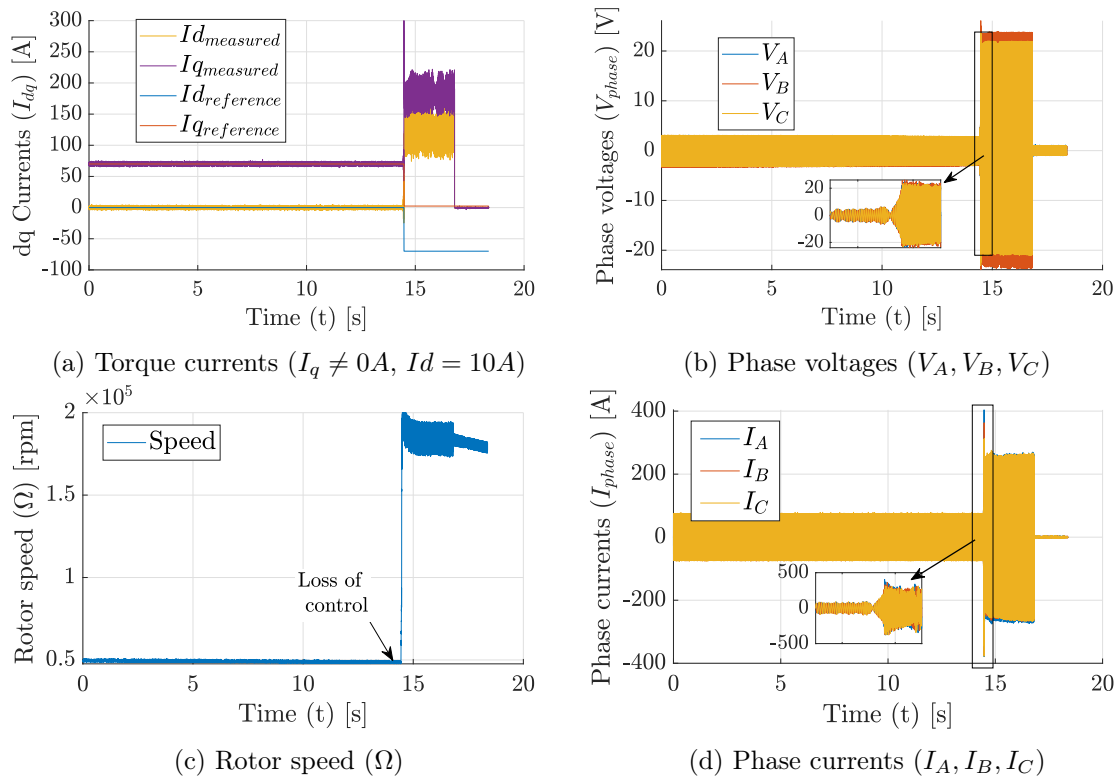


Figure 3.36: Torque control for $I_{ref} = 70A$ and $\delta = 18^\circ$.


 Figure 3.37: Torque control for $I_{ref} = 70A$ and $\delta = 0^\circ$.

currents that can be regulated in the machine increases, exceeding the limit of around 80A (see previously presented Figure 3.22) from which a loss of control is observed when this parameter was not considered. This control loss occurs when the d-axis current creates a field on a different axis than the real magnetization one, which can result in negative d-axis current components and lead to a potential destabilization (or even demagnetization) of the magnet.

Similar experimental analyses are proposed at higher levels of current. First, the Figure 3.38 exhibits the results achieved for $I_{ref} = 90A$ and $\delta = 21^\circ$. Again, this torque angle for which the maximal DC and AC power is achieved is defined from the torque profile exhibited in Figure 3.28. The Figure 3.39 exhibits the results for $I_{ref} = 100A$ and $\delta = 21^\circ$. In the figure 3.40, the estimated dq-axis voltages are presented for these two cases of study. Figure 3.41 presents the simulations considering these two last-mentioned levels of currents and respective torque angles. As before, the AC power and dq-axis voltages are also used as references for verifying the correction angles proposed according to the torque profile previously presented. For simulations considering $I_{ref} = 90A$, an angle $\Delta\theta_c = -68.5^\circ$ is calculated from $\theta_{PLL} - \theta_{filter}$ defining an estimated AC power of $P_{AC} = 396W$ and dq-axis voltages $v_d = -5.4V$ and $v_q = 1.2V$. Experimentally, it can be observed in Figure 3.38 that an AC power $P_{AC} = 370W$ (7% lower than the one simulated) and dq-axis voltages $v_d = -4.4V$ and $v_q = 1.5V$ are measured. By the same reasoning, now for $I_{ref} = 100A$, simulations exhibit an estimated AC power $P_{AC} = 455W$ and dq-axis voltages $v_d = -6V$ and $v_q = 1V$, whereas experimental results in the Figure 3.39 demonstrated that $P_{AC} = 404W$ (13% lower than the one simulated) and dq-axis voltages $v_d = -5V$ and $v_q = 2V$.

Remark: The "glitches" observed in Figure 3.38 are a consequence of the failures in the fast data acquisition.

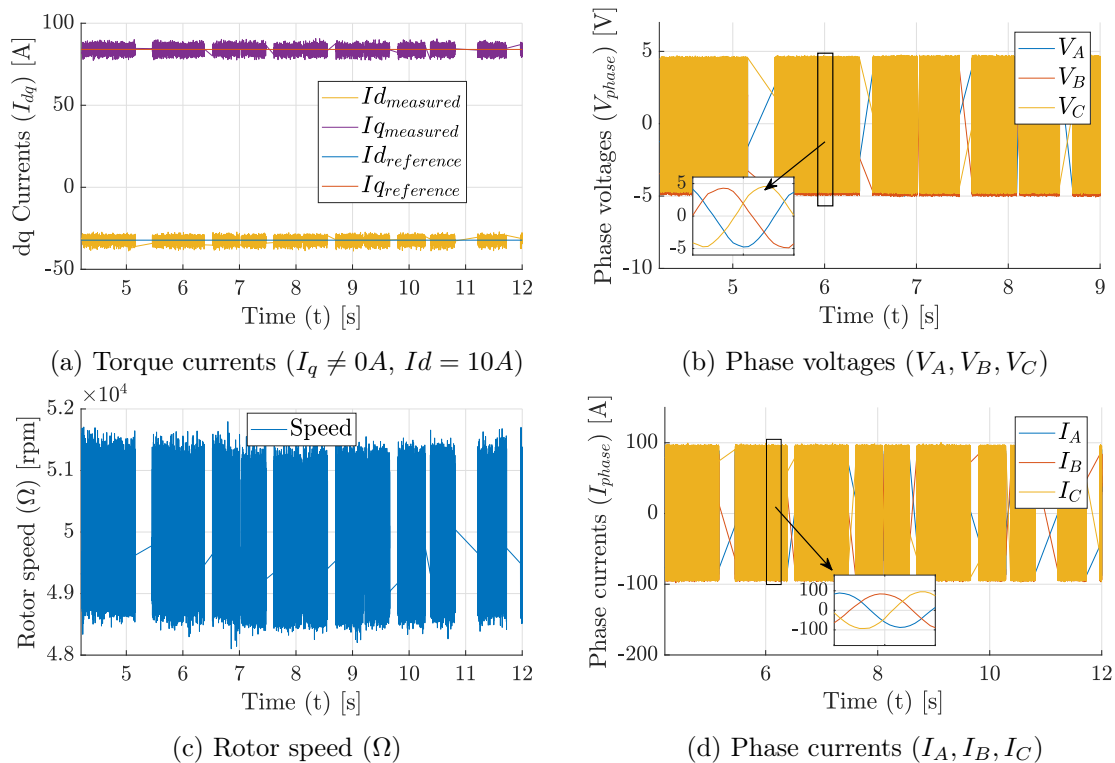


Figure 3.38: Torque control for $I_{ref} = 90A$ and $\delta = 21^\circ$.

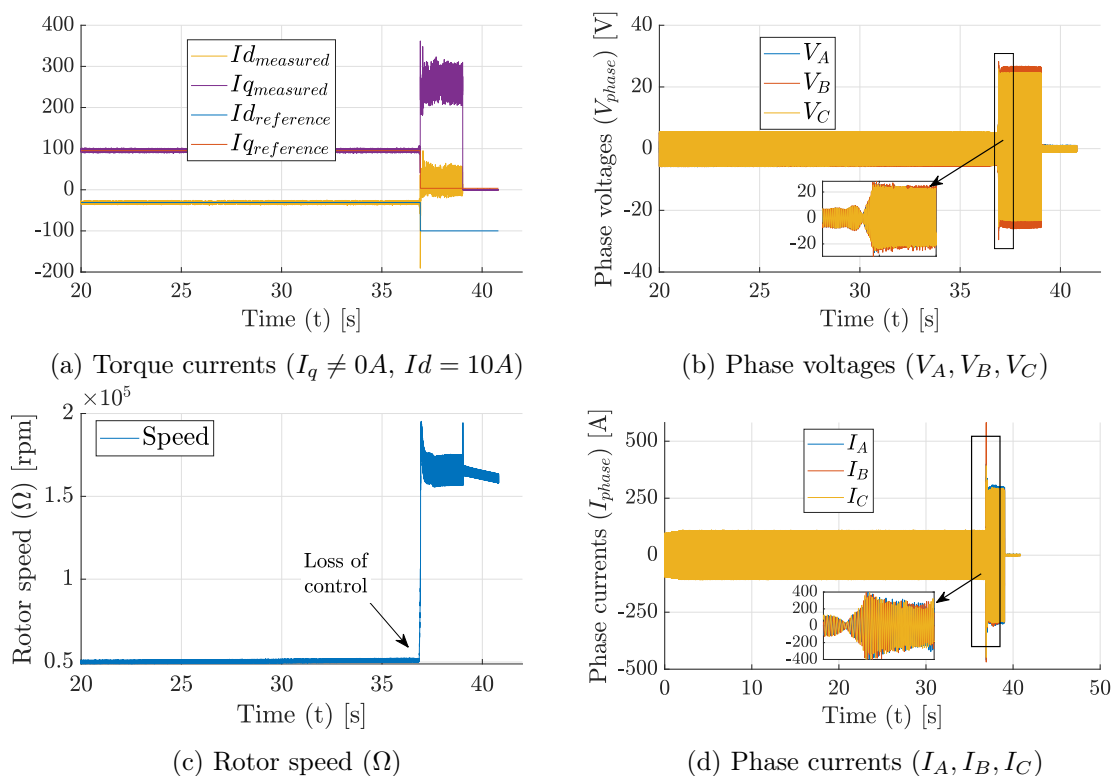
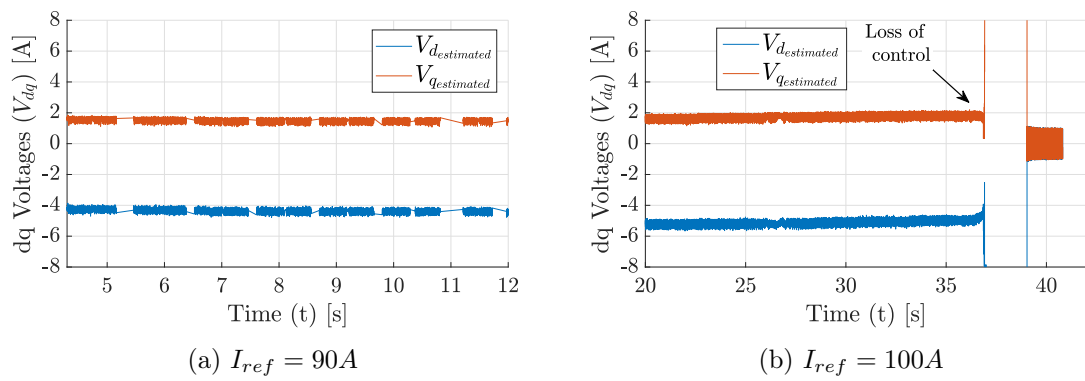
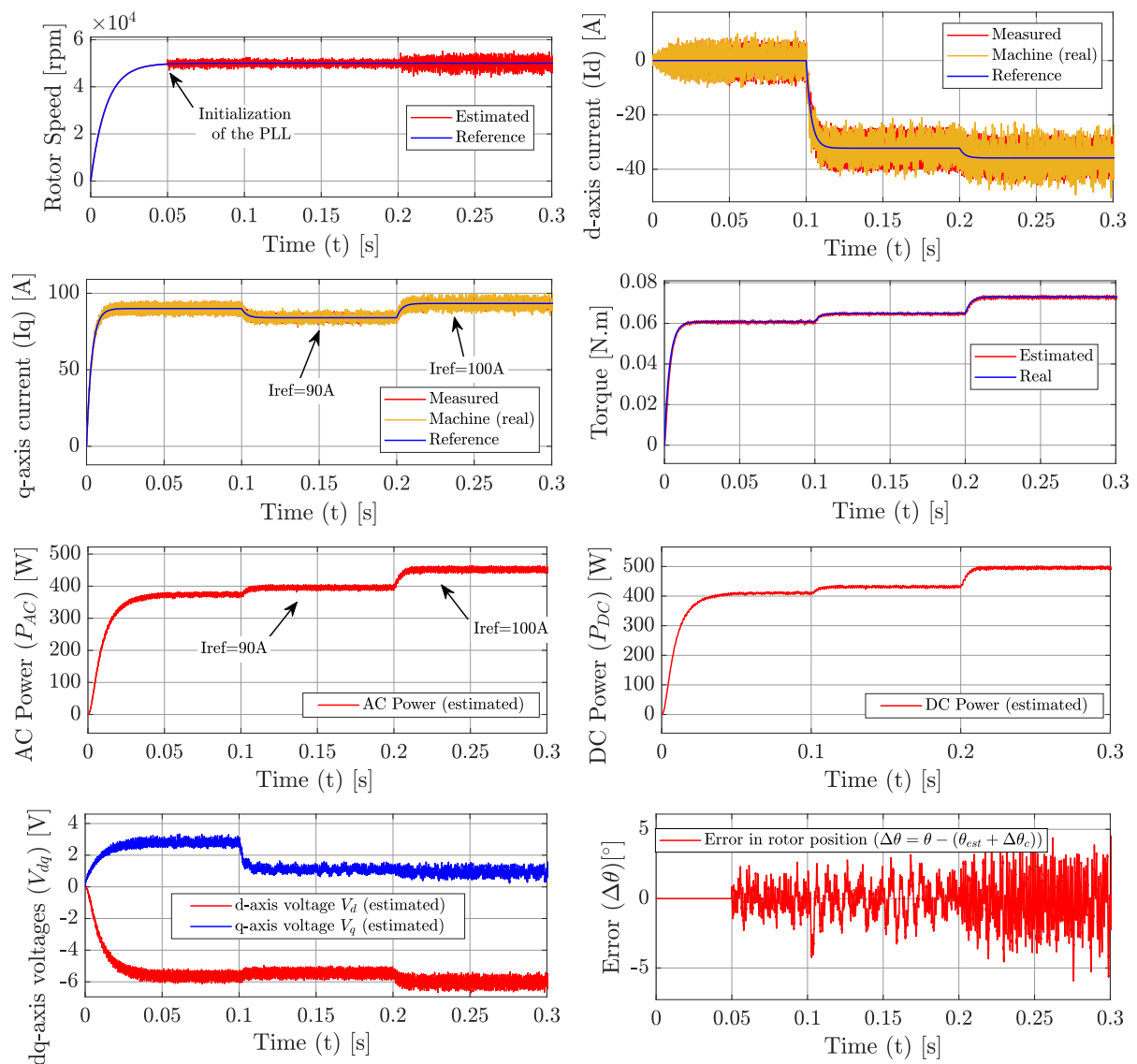


Figure 3.39: Torque control for $I_{ref} = 100A$ and $\delta = 21^\circ$.


 Figure 3.40: Estimated (control) dq-voltages (V_d, V_q) for $\delta = 21^\circ$.

 Figure 3.41: Study of the global offset angle considering the rotor reluctance for (1) $I_{ref} = 90A$ and (2) $I_{ref} = 100A$ - Study considering $\delta = 21^\circ$ according to the torque profile in the Figure 3.28. Theoretical correction angle from analytical formulation $\Delta\theta_c = \theta_{PLL} - \theta_{filter} = -67.9^\circ$ for $t=0.10s$ to $t=0.20s$ and (2) $\Delta\theta_c = \theta_{PLL} - \theta_{filter} = -70.9^\circ$ for $t=0.35s$ to $t=0.40s$.

Remark: The experimental test realized at $I_{ref} = 100A$ considering $\delta = 21^\circ$ in the Figure 3.39 indicates a control loss, although the real and controlled currents converge. This effect is justified by the level of negative d-axis current passing through the machine ($I_d = -100\sin(21^\circ) = -35.8A$). It should be reminded from the standstill magnetization results discussed in Chapter 2 that negative d-axis currents that exceed $I_d = -30A$ are expected to generate effects of demagnetization in Fe-Cr-Co-based rotor; consequently, because the flux linkage φ_s is expected to be reduced, the correction angle required is going to change, which requires also modifications of $\Delta\theta_c$.

3.10.3 Evaluation in different operating points (regime and current) of the results achieved via the improved reluctance model assumption

This section proposes an in-depth comparison between the experimental results with the ones obtained using the dq-axis inductances $L_d = 10\mu H$ and $L_q = 12\mu H$, estimated considering the less saturated stator material and the anisotropy characterizing the magnetic behavior of the rotor. Analyses are realized for several amplitudes of reference current (I_{ref}) and the respectively estimated torque angles for maximizing the DC and AC power are used for defining the dq-axis currents components. A regime $\Omega = 50krpm$ is set for simulations to take into account the machine acceleration when the currents are regulated during the experimental tests (proposed at $\Omega = 45krpm$). The maximal AC power and the global correction angle for each operating point are presented in Figure 3.42.

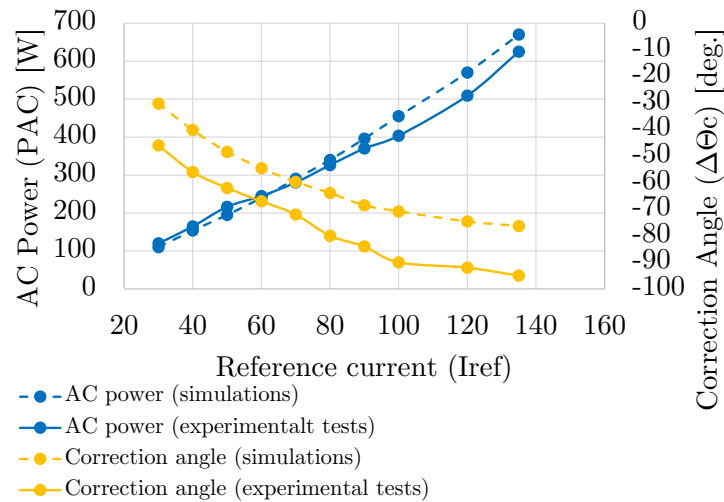


Figure 3.42: Comparison between the simulations and experimental results of the correction angles and AC power, for multiple I_{ref} and estimated $\delta = \delta_{max}$ - Study for experimental tests at $\Omega = 45krpm$.

Figure 3.43 exhibits these same results experimentally obtained for two other regimes, $\Omega = 30krpm$, and $\Omega = 55krpm$, and compares them with the ones achieved via simulations, also by taking into account the machine acceleration during the current regulation in the experimental tests. Again, it can be observed that the levels of AC power obtained via simulations are close ones experimentally measured. The most important differences (of around 12%) are observed for $\Omega = 30krpm$.

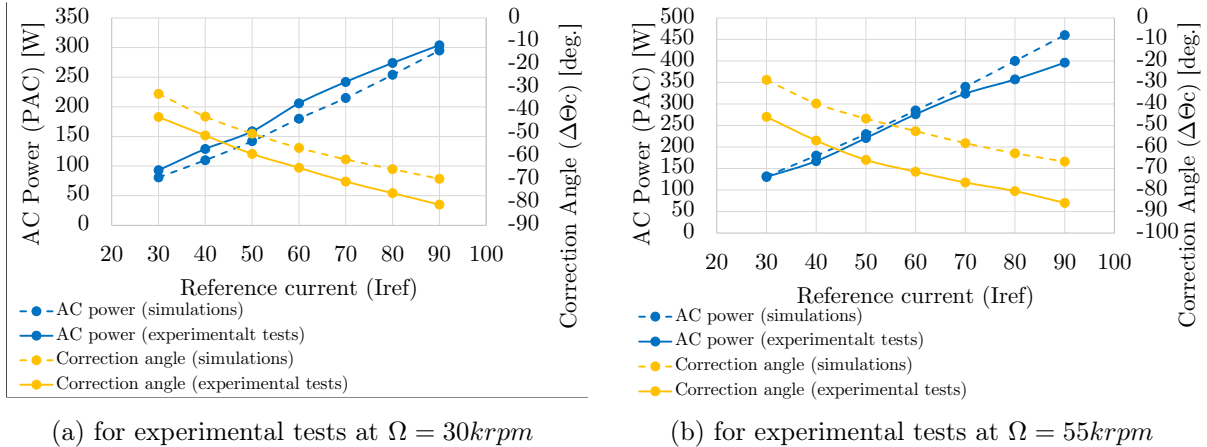


Figure 3.43: Comparison between the simulations and experimental results of the correction angles and AC power, for multiple I_{ref} and estimated $\delta = \delta_{max}$ - multiple regimes.

Remark: For experimental tests realized at $\Omega = 45krpm$ for $I_{ref} > 90A$ (Figure 3.42) as also for the ones at $\Omega = 55krpm$, for $I_{ref} > 70A$ (Figure 3.43), it is noticed that the difference between the AC power obtained by simulations and the experimentally measured increases. The reason is a slight demagnetization of the machine during the adjustment of the correction angle. By former studies already present (see Figure 3.18 in section 3.6.1), a wrong estimation of angle can lead to unintentional demagnetization of the magnet. Because the flux is estimated constant for simulations ($\varphi_s = 450\mu Wb$), this effect is observed in simulations. A flux estimator is envisaged for future studies to detect these variations and optimize the simulations realized.

3.10.4 Impact of the reluctance model in the global correction angle measured during the adjustment of the magnetization state

The previous sections investigated the global offset angle for loaded operating conditions. This present one is going to focus on the impact on using the inductance model proposed for estimating the correction angle during a magnetization procedure. This analysis considers the conclusions obtained from the experimental tests exhibited in section 3.6.1 and also the results achieved by the standstill magnetization studies described in Chapter 2. The flux linkage through the stator windings, although expected to be different as the magnetization state of the magnet changes, is considered for these simulations assuming the mean level $\varphi_s = 500\mu Wb$. Assuming a global correction angle well estimated for different magnetization current amplitudes, no impact is expected in the rotor speed during the magnetization control tests. Therefore, a rotor speed of $\Omega = 45krpm$ can be used for calculating the global correction angle in these proposed studies. Additionally, the filtering chain introduced in the section 3.9, defining a phase shift $\theta_{filter} = -9.27^\circ$ for $\Omega = 45krpm$ is considered.

The global correction angles calculated from the initial assumption of a non-salient machine geometry ($L_d = L_q = 5\mu H$) were compared for different magnetization current amplitudes in the Figure 3.24 (section 3.7) to the ones experimentally adjusted for ensuring the convergence of the control system. As formerly described, an important difference between these angles was observed. In this present section, similarly to the analyses proposed for the torque control, the global correction angles in the case of magnetization control are estimated considering: (1) the dq-axis inductances model defined according to the magnet anisotropy study, which resulted in $L_d = 6\mu H$ and $L_q = 8\mu H$ and (2) the dq-axis inductances obtained from the study of the less saturated stator material, defining $L_d = 10\mu H$ and $L_q = 12\mu H$. Figure 3.44 summarizes the

comparison proposed, presenting the error Δ between the experimentally and estimated results (these second, validated via FEA simulations). For $I_{mag} = 200A$, for example, the error Δ is reduced by 13% for a $L_d = 6\mu H$ and 36% for a $L_d = 10\mu H$, both considering the new filtering chain, compared to the one calculated for $L_d = 5\mu H$, for the initially presented filtering chain.

From these studies, it can be concluded that the use of the proposed model for characterizing the machine via $L_d = 10\mu H$ and $L_q = 12\mu H$ provides a good order of magnitude for estimating the correction angle to be experimentally adjusted in the machine also during the magnetization control.

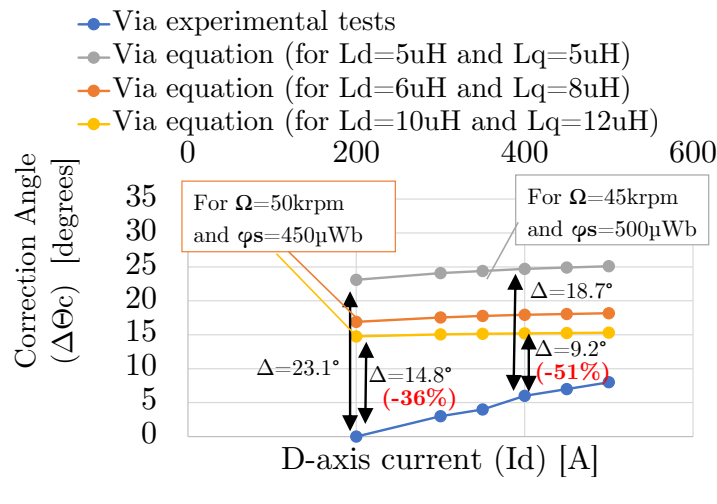


Figure 3.44: Comparison between correction angles for magnetizing the VFMM via simulation and experimental tests for multiple I_{mag} .

3.11 Conclusion of the Chapter 3

This chapter investigated the behavior of the Fe-Cr-Co-based Variable Flux Memory Machine when exposed to an external field created while $\Omega \neq 0rpm$. A focus is given to two controlled operating modes: magnetization (for adjusting the magnet flux) and torque control. Being both dependent on the rotor position, attention is also given in this chapter to the development of a sensorless algorithm for estimating the mentioned rotor position as well as the rotor speed.

Although little explored for VFMMs, sensorless strategies are a requirement for high-speed machines. Among the multiple methods available, a model-based Proportional-Integral Phase Locked-Loop (PI-PLL) has been chosen and developed for estimating the rotor speed and position based on the measurements of the three-phase voltages of the machine. The relative simplicity of implementation and low consumption of computation time justifies the preference for this system over the classically used observers. An external airflow drive is used to impose a regime through a turbocharger. In this PLL-based sensorless system, an offset angle compensation stage is proposed for correcting in the position estimated, the phase shifts generated by: (1) the angle between the real direct-quadrature referential frame (related to the rotor) and the estimated (PLL) referential frame, due to extraction of the position information using the output voltages; (2) the filtering chain used for reconstituting the voltage measurements in the inverter; and (3) the calculus time, a consequence of the interruption sequences defined in the control software to schedule the different steps between the signal acquisition and processing. These angles are corrected according to the equations described in the present chapter. Validation of the system comprising the global correction angle stage is proposed via simulations using

MATLAB/Simulink. The control system response to variations in speed and the dq-axis currents is also investigated.

From a machine model considered well-known in terms of the dq-axis inductances ($L_d=L_q$, non-salient model) and stator resistance, the global offset angles for different operating conditions (in terms of regime and current) are estimated. However, experimental tests indicated a loss of control when these respective calculated correction angles were manually adjusted in the sensorless algorithm. For this reason, it is proposed an experimental identification of the global correction angle required for ensuring the convergence of the control system during (1) magnetization from different d-axis current amplitudes, using as reference the magnetization state results achieved at standstill in Chapter 2 and (2) torque control, using as reference the maximization of the DC and AC power. These experimentally adjusted global offset angles are compared with the ones initially estimated from the non-salient machine model for the same operating condition. From parametric sensitivity investigations, the dq-axis inductances are identified as the most important parameter affecting the correction angle, especially during torque control. Due to these results and aiming to obtain a reliable machine model for estimating the correction angles, it is proposed an in-depth study via FEA simulations of the VFMM with a focus on the dq-inductances. This investigation takes into account the magnet anisotropy described in Chapter 2, which describes the magnetic behavior of the FeCrCo36/5 in the easy and hard magnetization directions, and also the saturation effects on the material composing the stator (reduced stator saturation culminates in increased dq-axis inductances). Salient poles are identified as a result of this study ($L_d \neq L_q$). In addition, the torque angle defining the dq-axis current components required to be adjusted in the control for obtaining the maximal torque in the machine can be determined. With this new machine model, the correction angles can be recalculated. From the analysis of the estimated AC and DC power obtained from simulations considering the model proposed and a comparison of these results with the ones experimentally measured, it can be observed that the correction angles estimated have a good order of magnitude. In addition, it is noticed that considering the torque angles identified from these studies, the amplitude of currents that can be regulated in the machine increases, and the system can run for longer periods without a divergence.

General Conclusion

The studies developed in this present thesis explored the magnetic behavior and control of a Fe-Cr-Co-based Variable Flux Memory Machine (VFMM). Designed from an initially proposed Permanent Magnet Synchronous Machine by replacing a Nd-Fe-B-based rotor with a cylindrical massif Fe-Cr-Co-based one, this machine is classified as a single-type AC-magnetized geometry having a single pole pair.

It should be remembered that VFMMs have been attracting attention for transportation electrification applications, especially because these machines are characterized by an additional degree of freedom for control: the adjustment of the magnetic flux. Although this characteristic could also be achieved in some other machine geometries through flux-weakening strategies, the Joule losses related to their application are usually mentioned as inconvenient. For VFMMs, the use of short-time current pulses for creating an external field in the magnetization axis (usually the d-axis) allows the variation of the magnetization state of the magnet used with reduced losses. At the same time, environmental concerns related to the extraction, recycling, and refinement of rare-earth magnets (such as Nd-Fe-B) can also be addressed by VFMMs, as their designs are proposed to avoid partially or totally the use of these mentioned permanent magnets. Instead, low coercive force magnets (such as the Fe-Cr-Co ones) are preferred, as their highly non-linear hysteresis profile favors the adjustment of the working point under dynamically changing load conditions. Within this framework, three major axes were discussed in this thesis research:

- Chapter 1 introduced the positioning of VFMMs in the electrical machines scenario and their classification according to the different magnets (e.g., hybrid or single-type) and geometries (e.g., AC or DC-magnetized magnetized) arrangements. The alloys used for producing the flux in these machines are differentiated according to the magnetic characteristics. The Fe-Cr-Co is presented as an advantageous low coercive force magnetic material, especially in terms of mechanical/corrosion resistance, which allows the low-cost shaping of several magnet geometries, and a lower content of Cobalt, which is expected to positively impact the price as Cobalt is considered a critical material in terms of supply and environmental exploitation. Within this framework, the present thesis research responds to a lack of information in the current literature regarding the use of Fe-Cr-Co alloys in VFMMs. Finding technical information about these last-mentioned alloys is observed to be more difficult than for other materials commonly used by authors (e.g., Al-Ni-Co magnets). This scenario indicates a possible challenge for the large-scale use of Fe-Cr-Co-based VFMMs and can eventually be a blocking factor in the evolution of studies and the development of these machine designs.
- Chapter 2 explored the magnetic behavior of the FeCrCo36/5, the anisotropic magnet used for composing the rotor in the VFMM studied in this thesis. Differently from the existing State-of-the-Art, which focuses on presenting the low coercive force as similar materials to the rare-earth ones in terms of remanence and shape of the hysteresis curve, this present research proposes the analysis in the case of a magnetic response to the external field

characterized by the absence of a well-defined knee in the second quadrant. The importance of this complementary study lies in the fact that some magnets adapted for VFMMs (e.g., the FeCrCo12/4, characterized by a remanence level equivalent to that of a permanent magnet and a low coercivity) present this last-mentioned hysteresis characteristic. In this context, the VFMM proposed is studied by a distinction between two FeCrCo36/5 magnets, manufactured for being respectively crossed by the external field in the hard and easy magnetization directions. In these directions, the absence or presence of a well-defined knee in the second quadrant of the hysteresis curve is, respectively, identified. In light of this distinction, a methodology of magnetization at standstill is developed for describing the hysteresis model of each of these mentioned magnetic axes in the case of partial magnetization states achieved during the flux adjustment phases. The magnetic profile defined from these results in the easy magnetization direction is the main focus of this study, due to the considerably higher levels of magnetization achieved (evaluated from the back-EMF measured). However, they and also the ones obtained in the hard magnetization direction lead to the same conclusions: the proposal of designing a VFMM from a geometry initially conceived for a PMSM can compromise the performance of this new machine. For the VFMM studied in this thesis, not only the initial magnetization capacity of the d-axis current pulses supplying the armature windings is affected, but also the level of back-EMF that could be induced from a pre-defined magnetization state. Mostly as a consequence of the stator material saturation and the presence of closed slot wedges in the stator geometry, the results presented in this chapter indicate that the sensitivity of the operating point in a VFMM requires a geometry adapted to the magnet characteristics used for producing the flux. Otherwise, the description of the internal hysteresis curves from the working point experimentally measured does not directly represent the intrinsic magnet behavior as expected. In this case, as it was for the Fe-Cr-Co-based VFMM studied in this present research, it is necessary to propose a strategy for correcting these effects in the stator before validating the behavior of the working points according to the reference provided by an ideal measuring equipment (HysteresisGraph).

- Chapter 3 studied the running magnetization of the Fe-Cr-Co-based Variable Flux Memory Machine, using as reference the standstill magnetization results introduced in the previous chapter. Because the machine is designed for high-speed applications and because the regime is established via external axial airflow, a sensorless algorithm is proposed. Although largely studied for PMSMs, the use of these sensorless techniques for estimating the rotor speed and position of VFMMs was only very recently introduced in the literature. More than the dependence of the Field Oriented Control on knowledge of rotor position for magnetization and torque control, as is widely known for PMSMs, VFMMs depend on this information to avoid an unintentional demagnetization of the magnet. A model-based strategy using a Proportional Integral Phase Locked Loop is developed for estimating the rotor speed and position from the measured output phase voltages in this present thesis research. In this system, a supplementary state is developed for analytically correcting the phase shifts that impact the rotor position initially evaluated due to the estimation model (PLL), the acquisition system (filters), and the calculus time (often neglected by authors). Because these angles are calculated from the machine (dq-axis inductances, L_d and L_q , and stator resistance, R_s) and system (speed, ω , and flux linkage, φ_s) quantities, a parametric sensitivity study is introduced. A hypothesis of well-known non-salience in the rotor ($L_d = L_q$) is defined as a massif cylinder. This study identified a dependency of the correction angles to be adjusted during the torque control on the q-axis inductance. From this conclusion, the focus of this chapter is on better modeling the dq-axis inductances of the machine since the non-salience initially assumed to be known is not sufficient to describe

the real machine behavior observed in the experimental tests. Studies via simulations are proposed taking into account the anisotropic hysteresis profile of the FeCrCo36/5 in the easy and hard magnetization directions and the saturation effects on the material composing the stator. The evolution of dq-inductances according to the dq-axis currents supplying the armature windings is investigated, as is their impact on the global correction angle. It is observed that the model obtained allows one to estimate the global correction angle with a good order of magnitude, sufficient to keep the system stable for fine-tuning during the experimental tests.

From the conclusions above presented regarding Chapters [1](#), [2](#) and [3](#), five points can be mentioned as advancements provided by this thesis research to the currently available State-of-the-Art in Variable Flux Memory Machines:

1. The machine geometry: A cylindrical Fe-Cr-Co-based rotor is used, whereas the majority of VFMMs currently explore the use of rectangular magnet bars for composing the rotor. This cylindrical rotor, easily adapted to different stator geometries, is particularly interesting for high-speed applications. However, it makes more complex the calculation of the working points due to the variation of the magnet length. Additionally, this present research proposes an evaluation of the consequences of designing a PMSM from a VFMM only by replacing the magnetic rotor, discussing the feasibility and challenges involved in this proposition.
2. The magnetic material: As previously discussed, a Fe-Cr-Co magnet is preferred in this present research rather than the Al-Ni-Co ones usually chosen for these applications. Moreover, the use of rare-earth magnets is totally avoided by a machine geometry only composed of low coercive force magnets, while most parts of the currently presented studies are focused on the use of hybrid-type machines (for which the magnetic flux is generated by a combination of low and high coercive force magnets).
3. The power electronics system: An inverter that incorporates a DC/DC mode without supplementary components or neutral access is proposed for supplying the machine with the current pulses required for adjusting the magnetization state of Fe-Cr-Co-based VFMM.
4. The magnet characteristics and its magnetic behavior when inserted in the machine: the distinction and study of the hysteresis model, characterized by the absence and presence of a well-defined knee in the second quadrant.
5. The sensorless and angle compensation strategies: The use of a sensorless is required for high-speed applications, such as those discussed in this thesis research but is rarely explored in the current literature for VFMMs.

Given these conclusions, some axes of study can be potentially interesting for the evolution and follow-up of the works carried out. These tracks are set out below:

- The direct replacement of a rare-earth magnet by a low coercive force one in a machine whose stator was originally designed for a PMSM was demonstrated to be challenging. According to the results discussed in this present study, stator saturation and design can have a strong influence on the achieved results. For this reason, one of the most important requirements for future works is the design of a stator geometry optimized and adapted to the properties of the low coercive force magnet used. Also, flux barriers can be developed to reduce the armature reaction.
- The hypothesis that by maximizing the DC power, the torque in the machine is maximized was proposed for the studies developed in this present thesis. However, this assumption

does not take into account the increase in iron losses that can be particularly important for high-speed operations (this parameter is expected to increase approximately to the square of the speed) as the authors in [44] explored. Within this context, future studies require attention to an investigation of the losses in the machine and especially their effect on the global offset correction angle.

- For the moment, the magnetization state of the magnet is only modified when the q-axis current component is null. According to studies developed in [12], [46], and [145], a torque ripple can be observed when the flux adjustment is realized at loaded conditions. To avoid it, methods for controlling the current vector are required. Future work focused on the adaptation of these methods to the control of the Fe-Cr-Co-based VFMM is necessary. The complexity involved in this procedure is especially related to the sensorless strategy response to this injection d-axis current that will modify instantaneously the global correction angle.
- Finally, future works also foresee the study and proof of the stability of the control system proposed. For this, the mathematical model describing this system around a linear operating point has to be developed for defining the state vector and the state equations. The eigenvalues can therefore be evaluated, knowing that a negative real part of all poles indicates an asymptotically stable working point.

Bibliography

- [1] S. Tumanski, *Handbook of Magnetic Measurements*. Series in Sensors, CRC Press, 2016.
- [2] B. W. Williams, *Power Electronics: Devices, Drivers, Applications, and Passive Components*. University of Strathclyde, 2006.
- [3] C. Yu, S. Niu, S. L. Ho, W. Fu, and L. Li, “Hysteresis Modeling in Transient Analysis of Electric Motors With Alnico Magnets,” *IEEE Transactions on Magnetics*, vol. 51, no. 3, pp. 1–4, 2015.
- [4] H. Yang, H. Zheng, S. Lyu, H. Lin, Z.-Q. Zhu, and W. Fu, “Analysis of Flux Regulation Principle in a Novel Hybrid-Magnet-Circuit Variable Flux Memory Machine,” in *2019 22nd International Conference on Electrical Machines and Systems (ICEMS)*, pp. 1–6, 2019.
- [5] G. B. Haxel, J. B. Hedrick, and G. J. Orris, “Rare Earth Elements—Critical Resources for High Technology - U.S. Geology survey - Fact Sheet 087-02.” <https://pubs.usgs.gov/fs/2002/fs087-02/>. Online: accessed 02 April 2022.
- [6] J. Cui, M. Kramer, L. Zhou, F. Liu, A. Gabay, G. Hadjipanayis, B. Balasubramanian, and D. Sellmyer, “Current Progress and Future Challenges in Rare-Earth-Free Permanent Magnets,” *Acta Materialia*, vol. 158, pp. 118–137, 2018.
- [7] European Commission and Joint Research Centre, P. Alves Dias, S. Bobba, S. Carrara, and B. Plazzotta, *The Role of Rare Earth Elements in Wind Energy and Electric Mobility - An Analysis of Future Supply/Demand Balances*. Publications Office, 2020.
- [8] J. Coey, “Perspective and Prospects for Rare Earth Permanent Magnets,” *Engineering*, vol. 6, no. 2, pp. 119–131, 2020.
- [9] A. Elshkaki, “Sustainability of Emerging Energy and Transportation Technologies is Impacted by the Coexistence of Minerals in Nature,” *Communications Earth & Environment*, vol. 2, p. 186, 09 2021.
- [10] J. D. Widmer and R. Martin and M. Kimiabeigi, “Electric vehicle traction motors without rare earth magnets,” *Sustainable Materials and Technologies*, vol. 3, pp. 7 – 13, 2015.
- [11] K. Binnemans, T. P. Jones, B. Blanpain, T. Van Gerven, Y. Yang, A. Walton, and M. Buchert, “Recycling of Rare Earths: a Critical Review,” *Journal of Cleaner Production*, vol. 51, pp. 1–22, 2013.
- [12] R. Jayarajan, N. Fernando, and I. Ullah Nutkani, “A Review on Variable Flux Machine Technology: Topologies, Control Strategies and Magnetic Materials,” *IEEE Access*, vol. 7, pp. 70141–70156, 2019.

- [13] Z. Q. Zhu and D. Howe, "Electrical Machines and Drives for Electric, Hybrid, and Fuel Cell Vehicles," *Proceedings of the IEEE*, vol. 95, no. 4, pp. 746–765, 2007.
- [14] S. Zhang, P. Zheng, Y. Liu, M. Wang, and G. Qiao, "Performance evaluation and design consideration of low coercivity magnets used in variable-flux permanent magnet synchronous machine," in *2018 21st International Conference on Electrical Machines and Systems (ICEMS)*, pp. 449–453, 2018.
- [15] O. Gutfleisch, M. Willard, B. E., C. Chen, S. Sankar, and J. Liu, "Magnetic Materials and Devices for the 21st Century: Stronger, Lighter, and More Energy Efficient," *Advanced Materials*, vol. 20, pp. 1–22, 08 2011.
- [16] K. Sakai, K. Yuki, Y. Hashiba, N. Takahashi, and K. Yasui, "Principle of the Variable-Magnetic-Force Memory Motor," in *2009 International Conference on Electrical Machines and Systems*, pp. 1–6, 2009.
- [17] C. Besson, A. Savary, and M. Jaccard, "Moteur Synchrone avec Contrôle de la Magnétisation des Aimants en Fonctionnement," in *Symposium de Génie Électrique*, (France), 2014.
- [18] A. M. Aljehaimi and P. Pillay, "Torque and Power Improvement for a Variable Flux Permanent Magnet Synchronous Machine," in *2017 IEEE Transportation Electrification Conference and Expo (ITEC)*, pp. 425–429, 2017.
- [19] H. Yang, H. Lin, and Z. Q. Zhu, "Recent Advances in Variable Flux Memory Machines for Traction Applications: a review," *CES Transactions on Electrical Machines and Systems*, vol. 2, no. 1, pp. 34–50, 2018.
- [20] J. Lei, C. Wei, H. Yang, H. Zheng, W. Wang, and S. Feng, "Design Considerations of Switched Flux Memory Machine with Partitioned Stators," *Energies*, vol. 12, no. 20, p. 3868, 2019.
- [21] H. Yang, Z. Q. Zhu, H. Lin, S. Fang, and Y. Huang, "Comparative Study of Novel Variable-Flux Memory Machines Having Stator Permanent Magnet Topologies," *IEEE Transactions on Magnetics*, vol. 51, no. 11, pp. 1–4, 2015.
- [22] V. Ostovic, "Pole-Changing Permanent-Magnet Machines," *IEEE Transactions on Industry Applications*, vol. 38, no. 6, pp. 1493–1499, 2002.
- [23] V. Ostovic, "Memory Motors," *Industry Applications Magazine, IEEE*, pp. 52–61, 2003.
- [24] A. Takbash and P. Pillay, "Magnet Design Consideration of a Variable-Flux PM machine," in *2017 IEEE Energy Conversion Congress and Exposition (ECCE)*, pp. 3935–3941, 2017.
- [25] N. Haje Obeid and A. Battiston, "Model Based Angle Compensation Method for Sensorless Control of a Wide Range High Speed PMSM," in *IECON 2019 - 45th Annual Conference of the IEEE Industrial Electronics Society*, vol. 1, pp. 2701–2706, 2019.
- [26] B. Magnets, "Grades of Ferrite." <https://e-magnetsuk.com/ferrite-magnets/grades-of-ferrite/>. Online: accessed 02 January 2023.
- [27] M. Ibrahim, L. Masisi, and P. Pillay, "Design of Variable-Flux Permanent-Magnet Machines Using Alnico Magnets," *IEEE Transactions on Industry Applications*, vol. 51, no. 6, pp. 4482–4491, 2015.

- [28] A. M. Aljehaimi and P. Pillay, "Operating envelopes of the variable-flux machine with positive reluctance torque," *IEEE Transactions on Transportation Electrification*, vol. 4, no. 3, pp. 707–719, 2018.
- [29] R. Eggert, C. Wadia, C. Anderson, D. Bauer, F. Fields, L. Meinert, and P. Taylor, "Rare Earths: Market Disruption, Innovation, and Global Supply Chains," *Annual Review of Environment and Resources*, vol. 41, no. 1, pp. 199–222, 2016.
- [30] L. Sepulchre, M. Fadel, M. Pietrzak-David, and G. Porte, "MTPV Flux-Weakening Strategy for PMSM High Speed Drive," *IEEE Transactions on Industry Applications*, vol. 54, no. 6, 2018.
- [31] A. Takbash and P. Pillay, "Magnetization and Demagnetization Energy Estimation and Torque Characterization of a Variable-Flux Machine," *IEEE Transactions on Energy Conversion*, vol. 33, no. 4, pp. 1837–1845, 2018.
- [32] X. Zhu, W. Wu, S. Yang, Z. Xiang, and L. Quan, "Comparative Design and Analysis of New Type of Flux-Intensifying Interior Permanent Magnet Motors With Different Q-Axis Rotor Flux Barriers," *IEEE Transactions on Energy Conversion*, vol. 33, no. 4, pp. 2260–2269, 2018.
- [33] H. Hua, Z. Q. Zhu, A. Pride, R. Deodhar, and T. Sasaki, "Comparative Study on Variable Flux Memory Machines With Parallel or Series Hybrid Magnets," *IEEE Transactions on Industry Applications*, vol. 55, no. 2, pp. 1408–1419, 2019.
- [34] L. Masisi, M. Ibrahim, and P. Pillay, "Control Strategy of a Variable Flux Machine Using AlNiCo Permanent Magnets," in *2015 IEEE Energy Conversion Congress and Exposition (ECCE)*, pp. 5249–5255, 2015.
- [35] F. Luborsky and G. Livingston, J.D. and Chin, *Chapter 29 - Magnetic Properties of Metals and Alloys*. Oxford: North-Holland, fourth edition ed., 1996.
- [36] S. Jin, "Deformation-induced anisotropic Cr-Co-Fe permanent magnet alloys," *IEEE Transactions on Magnetics*, vol. 15, no. 6, pp. 1748–1750, 1979.
- [37] N. Limsuwan, T. Kato, K. Akatsu, and R. D. Lorenz, "Design and Evaluation of a Variable-Flux Flux-Intensifying Interior Permanent-Magnet Machine," *IEEE Transactions on Industry Applications*, vol. 50, no. 2, pp. 1015–1024, 2014.
- [38] H. Yang, S. Lyu, H. Lin, Z. qiang Zhu, H. Zheng, and T. Wang, "A Novel Hybrid-Magnetic-Circuit Variable Flux Memory Machine," *IEEE Transactions on Industrial Electronics*, vol. 67, no. 7, pp. 5258–5268, 2020.
- [39] B. Basnet, A. M. Aljehaimi, and P. Pillay, "Back-EMF Analysis of a Variable Flux Machine for Different Magnetization States," *IEEE Transactions on Industrial Electronics*, vol. 68, no. 10, pp. 9125–9135, 2021.
- [40] H. Liu, H. Lin, Z. qiang Zhu, M. Huang, and P. Jin, "Permanent Magnet Remagnetizing Physics of a Variable Flux Memory Motor," *IEEE Transactions on Magnetics*, vol. 46, no. 6, pp. 1679–1682, 2010.
- [41] M. Ibrahim and P. Pillay, "Design of Variable Flux Permanent Magnet Machine for Reduced Inverter Rating," in *2014 International Conference on Electrical Machines (ICEM)*, pp. 1083–1089, 2014.

- [42] E. Tranco, E. Ibarra, A. Arias, C. Salazar, I. Lopez, A. Diaz de Guereñu, and A. Peña, “A novel PMSM Hybrid Sensorless Control Strategy for EV Applications based on PLL and HFI,” in *IECON 2016 - 42nd Annual Conference of the IEEE Industrial Electronics Society*, pp. 6669–6674, 2016.
- [43] Z. Zhang, “Sensorless Back EMF Based Control of Synchronous PM and Reluctance Motor Drives—A Review,” *IEEE Transactions on Power Electronics*, vol. 37, no. 9, pp. 10290–10305, 2022.
- [44] J. Kim, I. Jeong, K. Nam, J. Yang, and T. Hwang, “Sensorless Control of PMSM in a High-Speed Region Considering Iron Loss,” *IEEE Transactions on Industrial Electronics*, vol. 62, no. 10, pp. 6151–6159, 2015.
- [45] S. Bujacz, A. Cichowski, P. Szczepankowski, and J. Nieznanski, “Sensorless Control of High Speed Permanent-Magnet Synchronous Motor,” in *2008 18th International Conference on Electrical Machines*, pp. 1–5, 2008.
- [46] S. Lyu, H. Yang, H. Lin, and Y. Ren, “A Magnetization State Initialization Control Scheme for Variable Flux Memory Machines Without Requiring Position Sensor Information,” *IEEE Transactions on Transportation Electrification*, vol. 6, no. 3, pp. 1157–1166, 2020.
- [47] R. Petrie, “Permanent Magnet Material from Loadstone to Rare Earth Cobalt,” in *Proceedings: Electrical Electronics Insulation Conference and Electrical Manufacturing Coil Winding Conference*, pp. 63–64, 1995.
- [48] J. M. D. Coey, *Magnetism and Magnetic Materials*. Cambridge University Press, 2010.
- [49] L. Bickford, “Magnetism During the IEEE’s First One Hundred Years (1884-1984),” *IEEE Transactions on Magnetics*, vol. 21, no. 1, pp. 2–9, 1985.
- [50] M. Mitolo and R. Araneo, “A Brief History of Electromagnetism,” *IEEE Industry Applications Magazine*, vol. 25, no. 2, pp. 7–11, 2019.
- [51] F. Fiorillo, “Measurements of Magnetic Materials,” *Metrologia*, vol. 47, pp. S114–S142, March 2010.
- [52] “Constitutive Relations: Macroscopic Properties of Matter.” <http://www.eecs.umich.edu/courses/eecs530/lec%203%20-%202011.pdf>. Online: accessed 09 October 2022.
- [53] W. Callister and D. Rethwisch, *Materials Science and Engineering: An Introduction*. Wiley, 8th edition ed., 2009.
- [54] M. Tawalbeh, H. A. Khan, A. A. Hajar, and A. Al-Othman, “Applications of Metamaterials,” in *Encyclopedia of Smart Materials* (A.-G. Olabi, ed.), pp. 11–24, Oxford: Elsevier, 2022.
- [55] P. Darlene Mitchler, *Characterization of Hysteresis in Magnetic Systems: A Preisach Approach*. PhD thesis, University of Manitoba, 2000.
- [56] D. Takahashi and V. C. Oliveira Jr., “Ellipsoids (v1.0): 3-D Magnetic Modelling of Ellipsoidal Bodies,” *Geoscientific Model Development*, vol. 10, no. 9, pp. 3591–3608, 2017.
- [57] R. Skomski and J. Coey, “Magnetic Anisotropy — How Much is Enough for a Permanent Magnet?,” *Scripta Materialia*, vol. 112, pp. 3–8, 2016.

- [58] J. Fliegans, G. Delette, A. N. Dobrynin, N. M. Dempsey, and D. Givord, "Closed-Circuit Versus Open-Circuit Characterization of Hard Magnets," *IEEE Transactions on Magnetics*, vol. 55, no. 2, pp. 1–5, 2019.
- [59] J. B. Thoelke, *Magnetization and Magnetostriction in Highly Magnetostrictive Materials*. PhD thesis, Iowa State University, 5 1993.
- [60] M. P. Paranthaman, I. Nlebedim, F. Johnson, and S. K. McCall, "Additive Manufacturing of Permanent Magnets," *Material Matters*, vol. 11, 11 2016.
- [61] R. Prozorov and V. G. Kogan, "Effective Demagnetizing Factors of Diamagnetic Samples of Various Shapes," *Phys. Rev. Applied*, vol. 10, p. 014030, Jul 2018.
- [62] H. Czichos, T. Saito, and L. Smith, *Springer Handbook of Materials Measurement Methods*, vol. 153-158. Springer Berlin, Heidelberg, 01 2006.
- [63] "The Vocabulary of Magnetism - TechNotes." <https://www.arnoldmagnetics.com/wp-content/uploads/2017/10/Vocabulary-of-Magnetism.pdf/>. Online: accessed 02 April 2022.
- [64] D. Jiles and D. Atherton, "Theory of Ferromagnetic Hysteresis," *Journal of Magnetism and Magnetic Materials*, vol. 61, no. 1, pp. 48–60, 1986.
- [65] F. Preisach, "Über die magnetische Nachwirkung," *Zeitschrift für physik*, vol. 94, no. 5-6, pp. 277–302, 1935.
- [66] D. Sedira, Y. Gabi, A. Kedous-Lebouc, K. Jacob, B. Wolter, and B. Strass, "ABC Method for Hysteresis Model Parameters Identification," *Journal of Magnetism and Magnetic Materials*, vol. 505, 2020.
- [67] S. Hussain, A. Benabou, S. Clénet, and D. A. Lowther, "Temperature Dependence in the Jiles–Atherton Model for Non-Oriented Electrical Steels: An Engineering Approach," *IEEE Transactions on Magnetics*, vol. 54, no. 11, pp. 1–5, 2018.
- [68] J. V. Leite, *Contribuição à Modelagem Vetorial da Histerese Magnética*. PhD thesis, Universidade Federal de Santa Catarina, Centro Tecnológico, 2006.
- [69] A. Bermúdez, D. Gómez, and P. Venegas, "Preisach Hysteresis Model - Some Applications in Electrical Engineering," in *Magnetic Materials - Recent Advances and Applications* (P. D. R. Sahu, ed.), ch. 2, Rijeka: IntechOpen, 2021.
- [70] Y. Gong, K. T. Chau, J. Z. Jiang, C. Yu, and W. Li, "Analysis of Doubly Salient Memory Motors Using Preisach Theory," *IEEE Transactions on Magnetics*, vol. 45, no. 10, pp. 4676–4679, 2009.
- [71] Z. Szabo and J. Füzi, "Preisach Type Hysteresis Models with Everett Function in Closed Form," in *Conference on the Computation of Electromagnetic Fields*, 06 2015.
- [72] M. E. Mathekga, R. A. McMahon, and A. M. Knight, "Application of the Fixed Point Method for Solution in Time Stepping Finite Element Analysis Using the Inverse Vector Jiles-Atherton Model," *IEEE Transactions on Magnetics*, vol. 47, no. 10, pp. 3048–3051, 2011.
- [73] H. Yang, H. Lin, Z. Q. Zhu, S. Lyu, and H. Wang, "A Novel Dual-Layer PM Variable Flux Hybrid Memory Machine," in *2018 IEEE Energy Conversion Congress and Exposition (ECCE)*, pp. 262–268, 2018.

- [74] R. Thike and P. Pillay, "Characterization of a Variable Flux Machine for Transportation Using a Vector-Controlled Drive," *IEEE Transactions on Transportation Electrification*, vol. 4, no. 2, pp. 494–505, 2018.
- [75] "The Rare-Earth Elements — Vital to Modern Technologies and Lifestyles." <https://pubs.usgs.gov/fs/2014/3078/pdf/fs2014-3078.pdf>. Online: accessed 02 April 2022.
- [76] A. Taherizadeh, S. Javadpour, and H. Alikhani, "Investigation of Optimized Process Parameters on Densification of Samarium Cobalt 1:5 Series (SMCO 5) Magnets," *International Journal of Electromagnetic (IJEL)*, 03 2020.
- [77] B. Cui, X. Liu, A. H. King, G. Ouyang, C. I Nlebedim, and J. Cui, "Overcoming mechanical fragility in sm-co permanent magnet materials," *Acta Materialia*, vol. 196, pp. 528–538, 2020.
- [78] Arnold Magnetic Technologies, "Neodymium Iron Boron Magnet Catalog." <https://www.arnoldmagnetics.com/wp-content/uploads/2019/06/Arnold-Neo-Catalog.pdf>. Online: accessed 22 January 2022.
- [79] J. Morgan, "Rare earths, we can touch them everyday." <https://www.asx.com.au/asxpdf/20100927/pdf/31sqqzmv0ng1tb.pdf/>. Online: accessed 22 January 2022.
- [80] Z. Li, A. Kedous-Lebouc, J.-M. Dubus, L. Garbuio, and S. Personnaz, "Direct Reuse Strategies of Rare Earth Permanent Magnets for PM Electrical Machines - An Overview Study," *European Physical Journal: Applied Physics*, vol. 86, no. 2, p. 20901, 2019.
- [81] A. K. Jha, Z. Li, A. Garcia, P. Upadhayay, P. O. Rasmussen, A. Kedous-Lcbouc, and L. Garbuio, "Weighted Index of Recycling and Energy (WIRE) Cost for Motors in Electric Vehicles," in *2018 International Symposium on Power Electronics, Electrical Drives, Automation and Motion (SPEEDAM)*, pp. 407–412, 2018.
- [82] Y. Bian, S. Guo, K. Tang, and W. Ding, "Extraction of Rare Earth Elements from Permanent Magnet Scraps by FeO-B₂O₃ Flux Treatment," *Metallurgical and Materials Transactions B*, 01 2014.
- [83] J. Kitagawa and R. Uemura, "Rare Earth Extraction from NdFeB Magnet Using a Closed-Loop Acid Process," *Scientific Reports*, vol. 7, no. 8039, pp. 2045–2322, 1994.
- [84] Valeo Group, "Renault Group, Valeo And Valeo Siemens eAutomotive Join Forces to Develop and Manufacture a New-Generation Automotive Electric Motor in France." <https://www.valeo.com/en/renault-group-valeo-and-valeo-siemens-eautomotive-join-forces-to-develop-and-manufacture-a-new-generation-automotive-electric-motor-in-france/>. Online: Accessed 05 April 2022.
- [85] J. Banner, "No Magnets, Big Power: BMW's Fifth-Generation Electric Motor." <https://www.motortrend.com/news/bmw-ix-m60-brushed-electric-motor-tech-deep-dive/>. Online: accessed 05 February 2022.
- [86] BMW Group, "The New BMW iX M60." <https://www.press.bmwgroup.com/middle-east/article/detail/T0363105EN/the-new-bmw-ix-m60>. Online: accessed 05 February 2022.
- [87] European Comission, "Rare Earth Free e-Drives Featuring Low Cost Manufacturing." <http://www.refreedrive.eu/>, 2020. Online: Accessed 01 April 2022.

- [88] D. Lu and N. C. Kar, "A Review of Flux-Weakening Control in Permanent Magnet Synchronous Machines," in *2010 IEEE Vehicle Power and Propulsion Conference*, pp. 1–6, 2010.
- [89] A. Sun, J. Li, R. Qu, J. Chen, and H. Lu, "Rotor Design Considerations for a Variable-Flux Flux-Intensifying Interior Permanent Magnet Machine with Improved Torque Quality and Reduced Magnetization Current," in *2015 IEEE Energy Conversion Congress and Exposition (ECCE)*, pp. 784–790, 2015.
- [90] B. Magnet, "Permanent magnets Ferrite, NdFeB, AlNiCo & SmCo magnets." <http://www.blsmagnet.com/images/pdf/permanent-magnets.pdf>. Online: accessed 22 January 2022.
- [91] B. Slusarek and K. Zakrzewski, "Magnetic Properties of Permanent Magnets for Magnetic Sensors Working in Wide Range of Temperature," *Przegląd Elektrotechniczny*, vol. 88, 01 2012.
- [92] Arnold Magnetic Technologies, "Cast AlNiCo Permanent Magnets." <https://www.arnoldmagnetics.com/wp-content/uploads/2017/10/Cast-Alnico-Permanent-Magnet-Brochure-101117.pdf>, 2003. Online: accessed 20 January 2022.
- [93] M. Humphries - Congressional Research Service, "Critical Minerals and U.S. Public Policy." <https://crsreports.congress.gov/product/pdf/R/R45810>. Online: accessed 02 April 2022.
- [94] European Commission, "Critical raw materials." https://ec.europa.eu/growth/sectors/raw-materials/areas-specific-interest/critical-raw-materials_en. Online: accessed 17 Mai 2022.
- [95] T. Kubota, G. Wakui, and M. Itagaki, "Hysteresis Motor Using Magnetically Anisotropic Fe-Cr-Co Magnet," *IEEE Transactions on Magnetics*, vol. 34, no. 6, pp. 3888–3896, 1998.
- [96] National Aeronautics and Space Administration, "Study and Review of Permanent Magnets for Electric Vehicle Propulsion Motors." <https://ntrs.nasa.gov/api/citations/19840006003/downloads/19840006003.pdf>, 1983.
- [97] M. Altafi, E. Mohammad Sharifi, and A. Ghasemi, "The Effect of Various Heat Treatments on the Magnetic Behavior of the Fe-Cr-Co Magnetically Hard Alloy," *Journal of Magnetism and Magnetic Materials*, vol. 507, p. 166837, 2020.
- [98] L. Zhang, Z. Xiang, X. Li, and E. WANG, "Spinodal Decomposition in Fe-25Cr-12Co Alloys under the Influence of High Magnetic Field and the Effect of Grain Boundary," *Nanomaterials*, vol. 8, p. 578, 07 2018.
- [99] Q. Gao, M. Gong, Y. Wang, F. Qu, and J. Huang, "Phase Transformation and Properties of Fe-Cr-Co Alloys with Low Cobalt Content," *MATERIALS TRANSACTIONS*, vol. 56, 09 2015.
- [100] I. M. Milyaev, M. I. Alymov, I. N. Bouryakov, V. S. Yusupov, and D. M. Abashev, "Magnetic properties of powder hard magnetic Fe-27Cr-10Co-0.5Mo and Fe-27Cr-10Co-2Mo alloys," *IOP Conference Series: Materials Science and Engineering*, vol. 347, p. 012053, apr 2018.
- [101] Stanford Magnetics, *FeCrCo Magnet Introduction*.

- [102] Magnetic Materials Producers Association, *MMPA Standard 0010-Standard Specifications for Permanent Magnet Materials*, 1990.
- [103] Kyle Magnetics Co. LTD, “FeCrCo magnet.” <http://www.kylemagnet.info/projects/fecrco-magnet/>. Online: accessed 02 April 2022.
- [104] Hangzhou KEDE Magnetics Components Co. LTD, “Typical Magnetic Properties of FeCrCo Magnets.” <http://www.kedemagnetics.com/download/fecrco.pdf>. Online: accessed 02 April 2022.
- [105] Eclipse Magnetics, *Ferrite Magnets/Ceramic Magnets Datasheet*.
- [106] C. Granados-Miralles and P. Jenuš, “On the potential of hard ferrite ceramics for permanent magnet technology: A review on sintering strategies,” *Journal of Physics D: Applied Physics*, vol. 54, p. 303001, may 2021.
- [107] H. Tahanian, M. Aliahmadi, and J. Faiz, “Ferrite permanent magnets in electrical machines: Opportunities and challenges of a non-rare-earth alternative,” *IEEE Transactions on Magnetics*, vol. 56, no. 3, pp. 1–20, 2020.
- [108] B. Nahid Mobarakeh, *Commande Vectorielle Sans Capteur Mécanique des Machines Synchrones à Aimants : Méthodes, Convergence, Robustesse, Identification "En ligne" des Paramètres*. PhD thesis, Université de Lorraine, 2001.
- [109] Y. Hu, J. Chen, R. Qu, B. Chen, Y. Xiao, and X. Li, “Closed-Loop Magnetization State Control for a Variable-Flux Memory Machine,” *IEEE Access*, vol. 8, pp. 146983–146993, 2020.
- [110] H. Yang, S. Lyu, H. Lin, Z. Q. Zhu, F. Peng, E. Zhuang, S. Fang, and Y. Huang, “Stepwise Magnetization Control Strategy for DC-Magnetized Memory Machine,” *IEEE Transactions on Industrial Electronics*, vol. 66, no. 6, pp. 4273–4285, 2019.
- [111] H. J. Jia, W. Xinjian, and S. Zechang, “Variable Flux Memory Motors: A Review,” in *IEEE Conference and Expo Transportation Electrification Asia-Pacific (ITEC Asia-Pacific)*, pp. 1–6, 2014.
- [112] M. M. et al., “Towards High Speed and High Efficiency Compact Electric Systems for Future 48V Automotive on Board Electricity Generation,” May 2018.
- [113] A. Battiston, *Modélisation, Commande, Stabilité et Mise en Oeuvre des Onduleurs à Source Impédante: Application aux Systèmes Embarqués*. PhD thesis, Université de Lorraine, 2014.
- [114] R. Groessinger, “Characterisation of Hard Magnetic Materials,” *Journal of ELECTRICAL ENGINEERING*, vol. 59, pp. 15–20, 01 2008.
- [115] N. Mehboob, *Hysteresis Properties of Soft Magnetic Materials*. PhD thesis, Universität Wien, 2012.
- [116] E. Dennison, “The Hysteresisgraph as a Quality Control Tool,” in *Proceedings of Electrical/Electronics Insulation Conference*, pp. 221–227, 1993.
- [117] Laboratorio Elettrofisico, *AMH-500 - Hysteresisgraph Hard Magnetic Materials*.
- [118] H. Czichos, T. Saito, and L. Smith, *Springer Handbook of Metrology and Testing*, vol. 2. Springer Berlin, Heidelberg, 01 2011.

- [119] J. Coey and R. Skomski, *Permanent Magnetism*. Routledge, 01 1999.
- [120] Brockhaus Measurement, *Measuring Technology for Hard Magnetic Materials - Hystograph HG 200*.
- [121] J. Fidler, T. Schrefl, S. Hoefinger, and M. Hajduga, “Recent Developments in Hard Magnetic Bulk Materials,” *Journal of Physics: Condensed Matter*, vol. 16, pp. S455–S470, jan 2004.
- [122] B. K. Pugh, D. P. Kramer, and C. H. Chen, “Demagnetizing Factors for Various Geometries Precisely Determined Using 3-D Electromagnetic Field Simulation,” *IEEE Transactions on Magnetism*, vol. 47, no. 10, pp. 4100–4103, 2011.
- [123] J. Fujisaki, A. Furuya, H. Shitara, Y. Uehara, K. Kobayashi, Y. Hayashi, and K. Ozaki, “Demagnetization Correction Method by Using Inverse Analysis Considering Demagnetizing Field Distribution,” *IEEE Transactions on Magnetism*, vol. 56, no. 4, pp. 1–4, 2020.
- [124] D.-X. Chen, E. Pardo, Y.-H. Zhu, L.-X. Xiang, and J.-Q. Ding, “Demagnetizing Correction in Fluxmetric Measurements of Magnetization Curves and Hysteresis Loops of Ferromagnetic Cylinders,” *Journal of Magnetism and Magnetic Materials*, vol. 449, pp. 447–454, 2018.
- [125] W. S. Levine, *The Control Handbook*. CRC Press, 2011.
- [126] “Sensored Field Oriented Control of 3-Phase Permanent Magnet Synchronous Motors.” https://www.ti.com/lit/an/sprabq2/sprabq2.pdf?ts=1662361521715&ref_url=https%253A%252F%252Fwww.google.com%252F. Online: accessed 05 September 2022.
- [127] Microsemi, *Field Oriented Control of Permanent Magnet Synchronous Motors User’s Guide*.
- [128] J. Yoo, J. Lee, and S.-K. Sul, “Analysis of Instability in Torque Control of Sensorless PMSM Drives in Flux Weakening Region,” *IEEE Transactions on Power Electronics*, vol. 36, no. 9, pp. 10815–10826, 2021.
- [129] S. Wu, C. Hu, Z. Zhao, R. Zhou, and Y. Zhu, “A Novel Flux Estimator Using α - β Orthogonality Drift Elimination for High Performance Full-Speed-Range Sensorless Control,” in *2022 IEEE/ASME International Conference on Advanced Intelligent Mechatronics (AIM)*, pp. 1315–1320, 2022.
- [130] J. Hu and B. Wu, “New integration algorithms for estimating motor flux over a wide speed range,” *IEEE Transactions on Power Electronics*, vol. 13, no. 5, pp. 969–977, 1998.
- [131] P. Bernard and L. Praly, “Estimation of Position and Resistance of a Sensorless PMSM: A Nonlinear Luenberger Approach for a Nonobservable System,” *IEEE Transactions on Automatic Control*, vol. 66, no. 2, pp. 481–496, 2021.
- [132] N. Henwood, J. Malaizé, and L. Praly, “A Robust Nonlinear Luenberger Observer For The Sensorless Control Of SM-PMSM: Rotor Position And Magnets Flux Estimation,” in *IECON 2012 - 38th Annual Conference on IEEE Industrial Electronics Society*, pp. 1625–1630, 2012.

- [133] S. Chi, Z. Zhang, and L. Xu, "Sliding-Mode Sensorless Control of Direct-Drive PM Synchronous Motors for Washing Machine Applications," *IEEE Transactions on Industry Applications*, vol. 45, no. 2, pp. 582–590, 2009.
- [134] S. Jin, J. Gu, W. Jin, Z. Zhang, and F. Zhang, "Sensorless Control of Low Speed PMSM Based on Novel Sliding Mode Observer," in *2021 IEEE 4th International Electrical and Energy Conference (CIEEC)*, pp. 1–5, 2021.
- [135] B. Mobarakeh, F. Meibody-Tabar, and F. Sargos, "A Globally Converging Observer of Mechanical Variables for Sensorless PMSM," in *2000 IEEE 31st Annual Power Electronics Specialists Conference. Conference Proceedings (Cat. No.00CH37018)*, vol. 2, pp. 885–890 vol.2, 2000.
- [136] B. Nahid-Mobarakeh, F. Meibody-Tabar, and F.-M. Sargos, "Back-EMF Estimation based Sensorless Control of PMSM: Robustness with Respect to Measurement Errors and Inverter Irregularities," in *Conference Record of the 2004 IEEE Industry Applications Conference, 2004. 39th IAS Annual Meeting.*, vol. 3, pp. 1858–1865 vol.3, 2004.
- [137] G. Wang, M. Valla, and J. Solsona, "Position Sensorless Permanent Magnet Synchronous Machine Drives—A Review," *IEEE Transactions on Industrial Electronics*, vol. 67, no. 7, pp. 5830–5842, 2020.
- [138] G. Foo and M. F. Rahman, "Evaluation of Velocity Servo Performance of IMPSM Drive Under High-Performance Sensorless Operation," in *8th International Conference on Power Electronics - ECCE Asia*, pp. 1–10, 2011.
- [139] Y.-D. Yoon, S.-K. Sul, S. Morimoto, and K. Ide, "High-Bandwidth Sensorless Algorithm for AC Machines Based on Square-Wave-Type Voltage Injection," *IEEE Transactions on Industry Applications*, vol. 47, no. 3, pp. 1361–1370, 2011.
- [140] Y.-C. Kwon, J. Lee, and S.-K. Sul, "Extending Operational Limit of IPMSM in Signal-Injection Sensorless Control by Manipulation of Convergence Point," *IEEE Transactions on Industry Applications*, vol. 55, no. 2, pp. 1574–1586, 2019.
- [141] S. Kim, J.-I. Ha, and S.-K. Sul, "PWM Switching Frequency Signal Injection Sensorless Method in IPMSM," in *2011 IEEE Energy Conversion Congress and Exposition*, pp. 3021–3028, 2011.
- [142] B. Basnet, A. M. Aljehaimi, and P. Pillay, "Effect of Magnetization Pulse Width on the Back EMF of a Variable Flux Machine and on Inverter Sizing," in *IECON 2019 - 45th Annual Conference of the IEEE Industrial Electronics Society*, vol. 1, pp. 1028–1033, 2019.
- [143] A. Payman, *Contribution à la Gestion d'Énergie dans les Systèmes Hybrides Multi-Sources Multi-Charges*. PhD thesis, Institut National Polytechnique de Lorraine, 2009.
- [144] S. Zaim, *Contribution à la Commande sans Capteur Mécanique d'Actionneurs Électriques Motorisés par des Machines Synchrones à Aimants Permanents*. PhD thesis, Université de Lorraine, 2013.
- [145] B. S. Gagas, K. Sasaki, T. Fukushige, A. Athavale, T. Kato, and R. D. Lorenz, "Analysis of Magnetizing Trajectories for Variable Flux PM Synchronous Machines Considering Voltage, High-Speed Capability, Torque Ripple, and Time Duration," *IEEE Transactions on Industry Applications*, vol. 52, no. 5, pp. 4029–4038, 2016.

- [146] G. Yang, M. Lin, N. Li, G. Tan, and B. Zhang, “Comparative Study of Flux-Regulation Method for Stator Permanent Magnet Memory Machine,” in *2017 20th International Conference on Electrical Machines and Systems (ICEMS)*, pp. 1–5, 2017.

Appendix

Appendix A

State of the Art

A.1 Soft and hard magnetic materials

Figure [A.1](#) illustrates the hysteresis loop of a soft and hard magnetic material. This first is characterized by a low coercivity, which narrows their BH loop when compared with the one of hard magnets.

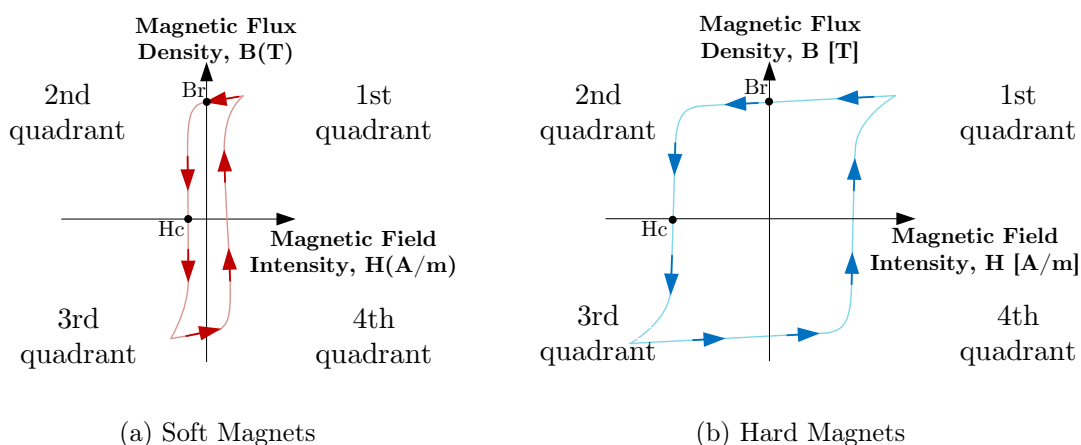


Figure A.1: Typical hysteresis loops of soft (left) and hard(right) hysteresis loops, being $H_{csoft} \gg H_{chard}$.

A.2 The anisotropy of magnetic materials

According to [\[60\]](#), [\[61\]](#), and [\[48\]](#), Three major factors, as described below, are presented in the literature as sources of this mentioned anisotropy: intrinsic factors, as the crystal structure and atomic or micro-scale texture, and an extrinsic factor, related to the shape of the magnet:

1. Magnetocrystalline anisotropy depends on the crystalline structure of each magnetic material, being defined as the difference in the magnetization achieved by a material when the external field is applied along different crystallographic directions.
2. Induced anisotropy depends on the creation of atomic-scale structure in the magnetic material, via an applied stress or by depositing or annealing a disordered alloy

3. The shape anisotropy is a consequence of the different effective fields achieved in different directions of a magnet sample due to the effects of demagnetizing field \vec{H}_d previously introduced.

A.3 Rare-earth magnets: insights about the reuse of these magnetic materials

Authors in this paper summarize the reusing methods discussed in [81] of magnets present in these machines, exhibited here in the Table below:

Table A.1: Methods of reusing magnets used in Interior Permanent Magnet Synchronous Machines and Surface Mounted Permanent Magnet Synchronous Machine [80][81].

Summary of magnet reusing strategies			
Reuse strategy	Application scope	Advantages	Disadvantages
Complete magnet reuse	Small	Easy to extract magnet	Magnet shape is unchangeable.
Magnet powder reusing	Medium	Can form to any shape or different applications	Complex magnetization and need of special tools for assembly and disassembly.
Modular design	High	Modular design can apply to most of the machine types	Using special materials, complex mechanical structure, and degraded machine performances.

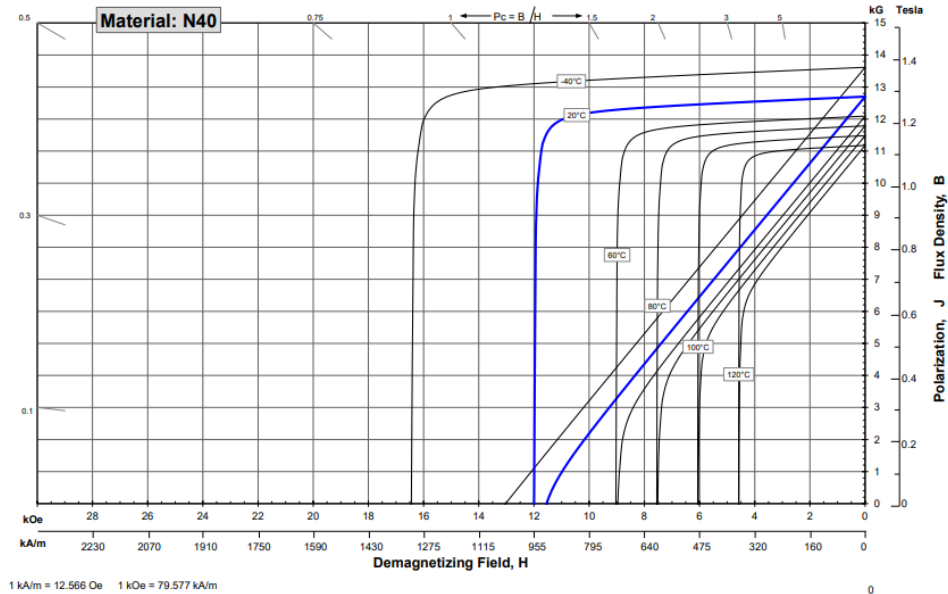
Also in [80], authors introduce an overview of methodologies for quantifying magnet recyclability considering different types of machines. According to them, two indexes can be used for this purpose: the first one focuses on the recyclability from the point of view of assembly and disassembly of motors, and the second one, is regarding the impact of motor performances when using recycled or reused magnets. In this first index, known as the "Weighted index of recycling and disassembly", the motor components composing the stator and rotor are evaluated according to their standardization¹ and cost². A scoring pattern of 0 to 5 (where 0 is the lowest score - worst evaluation - and 5 is the highest one - better evaluation) is used for this evaluation. Finally, each item is also evaluated from 0 to 5 to define the importance (or criticality) of the recyclability of the material or the process used. The second mentioned index, called the "Weighted index of energy" evaluates the relationship between saved cost from the use of recycled magnets and increased one, as a consequence of the efficiency degradation when these recycled materials are applied. For this index, simulations and experimental tests can be used.

¹Standard, in this case, means commonly used. More standardized components are related to simplified recycling processes, which are represented by higher scores.

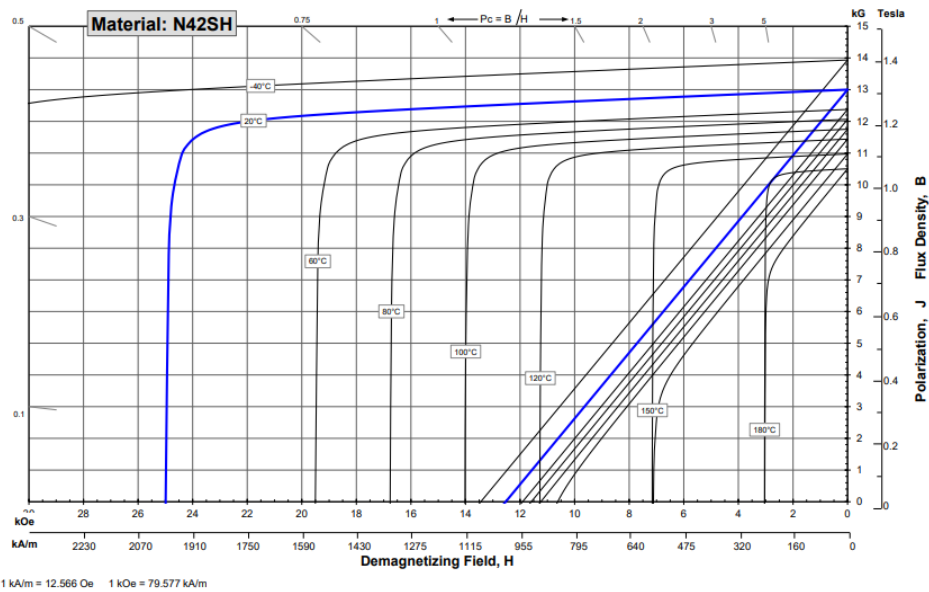
²Cost can be analyzed from the material or process cost. The score is defined according to the comparison between the machines analyzed, which means that

A.4 Hysteresis loop of commercial available magnets

A.4.1 Neodymium Iron Bor magnets



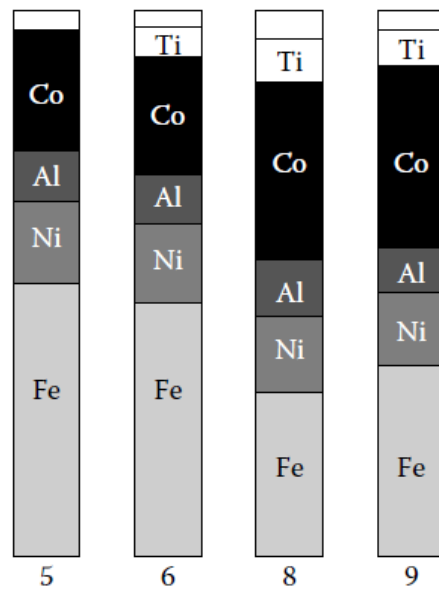
(a) Grade N40



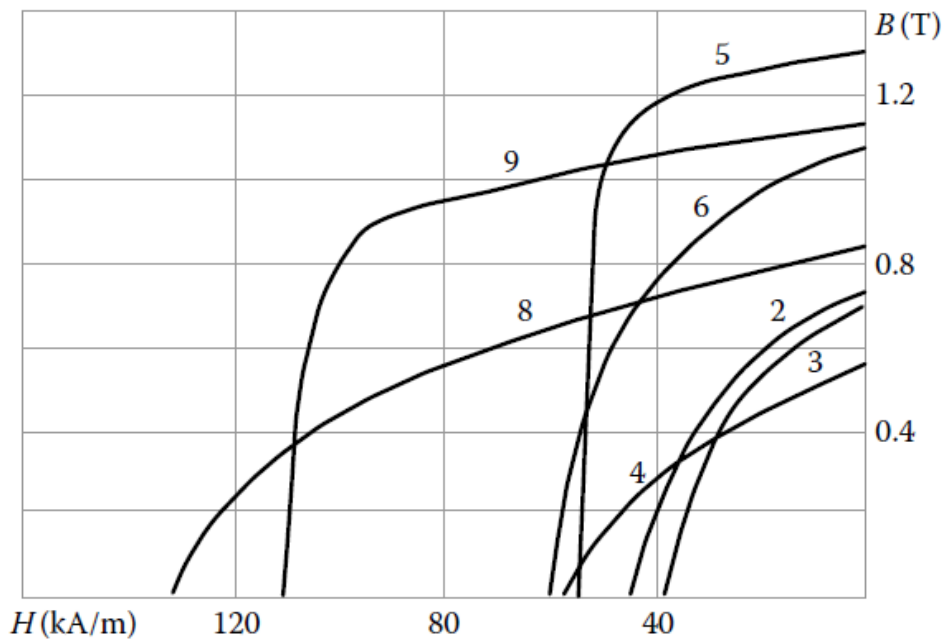
(b) Grade N42H

Figure A.2: Demagnetization curves of commercially available Nd-Fe-B magnets [8].

A.4.2 Aluminium Nickel Cobalt magnets



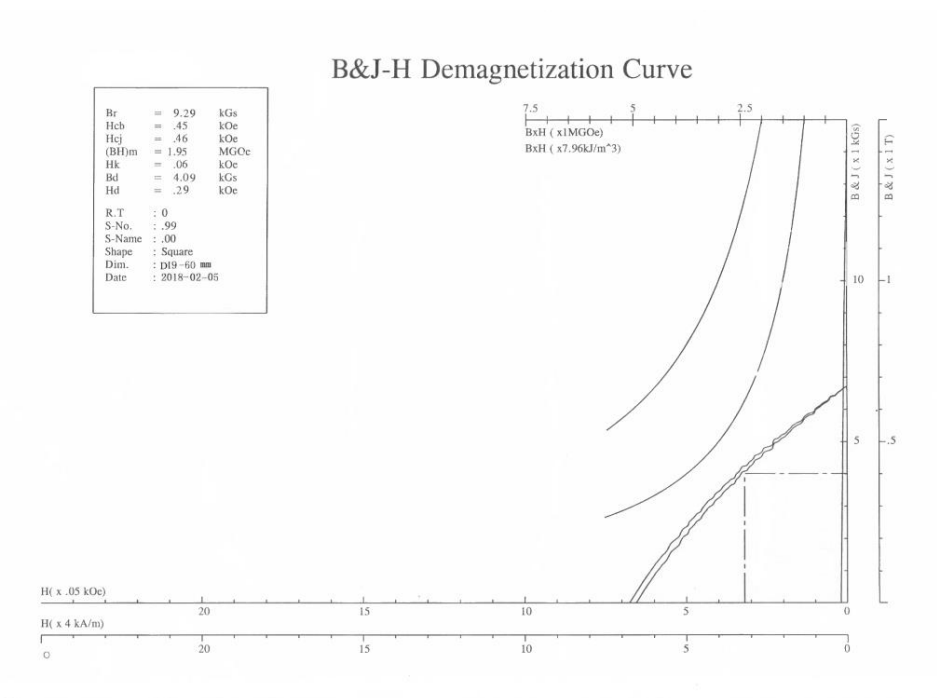
(a) Composition



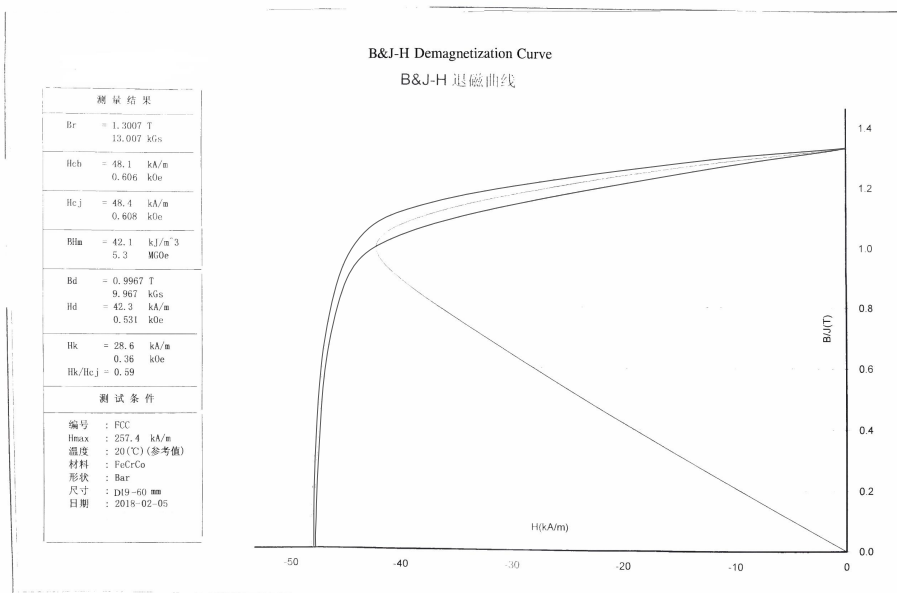
(b) Demagnetization curves

Figure A.3: Magnetic properties of commercially available Al-Ni-Co magnets [1].

A.4.3 Iron Chrome Cobalt magnets



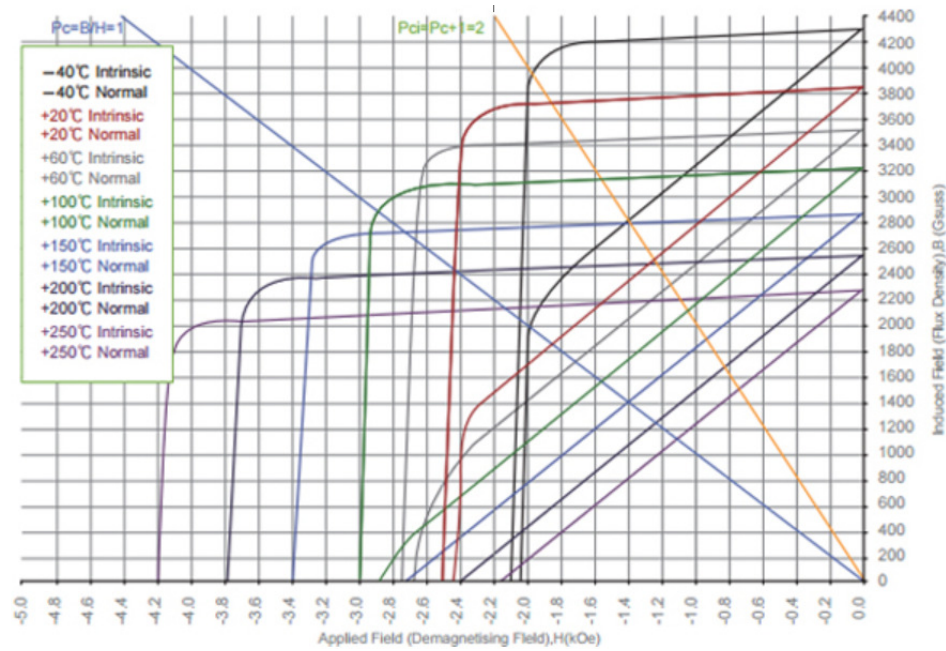
(a) Grade 12-4



(b) Grade 36-5

Figure A.4: Demagnetization curves of commercially available Fe-Cr-Co magnets - Provided by the supplier XFMagnets.

A.4.4 Ferrites



(a) Ferrite Y30

Figure A.5: Demagnetization curves of commercially available Ferrite magnets [26].

A.5 Critical Minerals for the United States and Europe

Table A.2: Critical Minerals for the United States (data in metric tons (mt) or million metric tons (m mt) unless otherwise noted) - Adapted from [93].

Global Production and Leading Producers, Selected Years					
Mineral	Global Production			Leading	Comments
	2000	2010	2017	Producers in 2017	
Aluminum (bauxite)	135.0 m mt	209.0 m mt	309 m mt	Australia (28.5%), China (22.6%), Brazil (12.5%), Guinea (15%), Others (21.4%)	No bauxite produced in the United States
Chromium	14.4 m mt	23.7 m mt	30.2 m mt	South Africa (46.2%)	
Cobalt	33,300 mt	89,500 mt	120 m mt	DRC (61%), Others (39%)	Some U.S. production as byproduct of copper
Rare Earth Elements	83,500 mt	133,000 mt	132,000 mt	China (80%), Australia (14%), Others (6%)	No production in 2017. The USGS estimates U.S. production to be around 15,000 mt in 2018.

LEGEND:

DRC: Democratic Republic of the Congo; USGS: U.S. Geological Survey

Table A.3: Critical Minerals for the Europe - Adapted from [94].

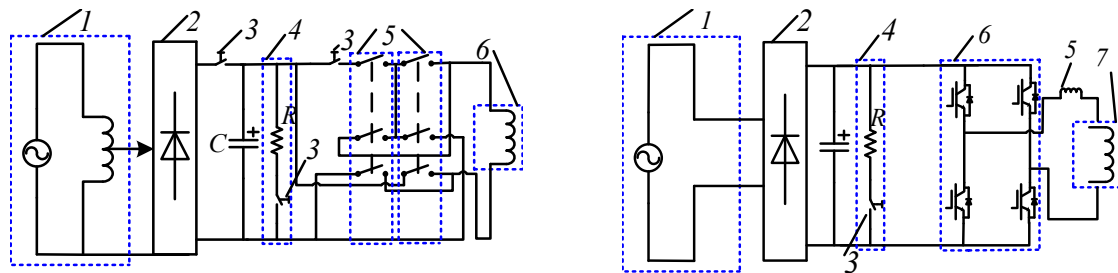
Antimony	Gallium	Magnesium	Scandium
Baryte	Germanium	Natural Graphite	Silicon metal
Beryllium	Hafnium	Natural Rubber	Tantalum
Bismuth	Helium	Niobium	Tungsten
Borate	HREEs	PGMs	Vanadium
Cobalt	Indium	Phosphate rock	
Fluorspar	LREEs	Phosphorus	

LEGEND:

HREEs: Heavy rare earth elements; PGMs: Platinum Group Metals, LREEs: Light rare earth elements

A.6 Power electronics architectures for generating the current pulses: first insights

Regarding the generation of these pulses, [146] investigate possible power electronics topologies to be used in the variation of the MS. The stored capacitor discharge pulse (SCDP, in the Figure A.6a), the constant current source pulse (CCSP), and quantitative flux regulation pulse (QFRP, in the Figure A.6b) are introduced and compared in by this mentioned study. A classic system composed of an adjustable AC voltage source and a rectifier is considered fas for each topology.



(a) SCDP, where can be identified: (1) adjustable AC voltage source, (2) rectifier, (3) switch, (4) discharge protect circuit, (5) polarity reversible switches, and (6) magnetization winding

(b) QFRP, where can be identified: (1) AC voltage source, (2) rectifier, (3) switch, (4) discharge protect circuit, (5) filter inductance, (6) power switches, and (7) magnetization winding

Figure A.6: Circuit topologies proposed for generating the current pulses.

In a SCDP method, a capacitor, polarity-reversal switches, and a discharge protect circuit are connected to the rectifier. The capacitor is charged by the AC source and will discharge its energy to the magnetization winding through the polarity-reversible switches. The sense of magnetization is dependent on the switches closed at each moment. The CCSP represents a bi-directional strategy composed of similar circuit to those of SCDP. The main differences are the connection of the capacitor permanently to the rectifier and the use of a power switch to control the pulse duration. As a consequence, a flat pulse can be achieved by this last-mentioned strategy due to the continuous power supply. Unlike the previously mentioned methods, QFRP is designed by substituting the polarity-reversal switches used in SCDP and CCSP by IGBTs. The advantage is the easy definition of the pulse direction according to the switches in the on-state. Conclusions presented by the authors indicate the simplicity of these two first-mentioned

methodologies in terms of construction and operation, but the limitations regarding their use for generating pulses of different amplitudes and directions. This problem can be solved by using the QFRP, which under the same conditions provides better results related to the variation of the MS in the VFMM studied.

Appendix B

Chapter 1

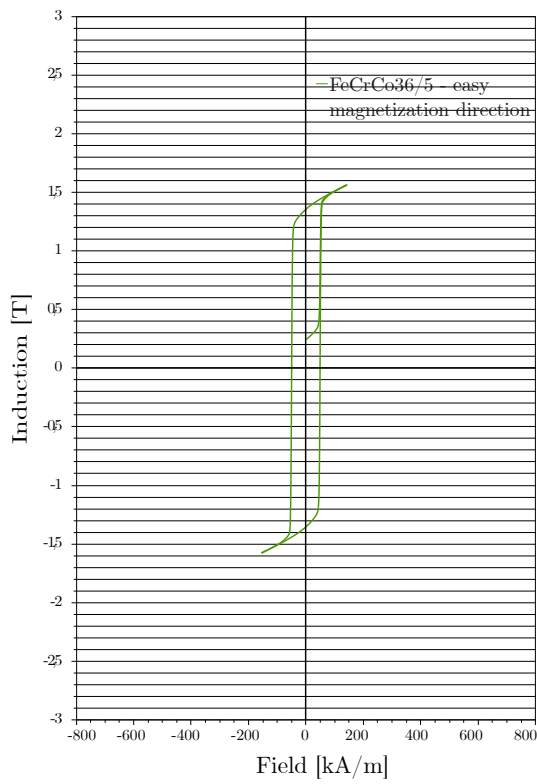
B.1 Specifications of the HysteresisGraph

Table B.1: Technical specifications of the Hystograph HG 200 (Brockhaus) [120].

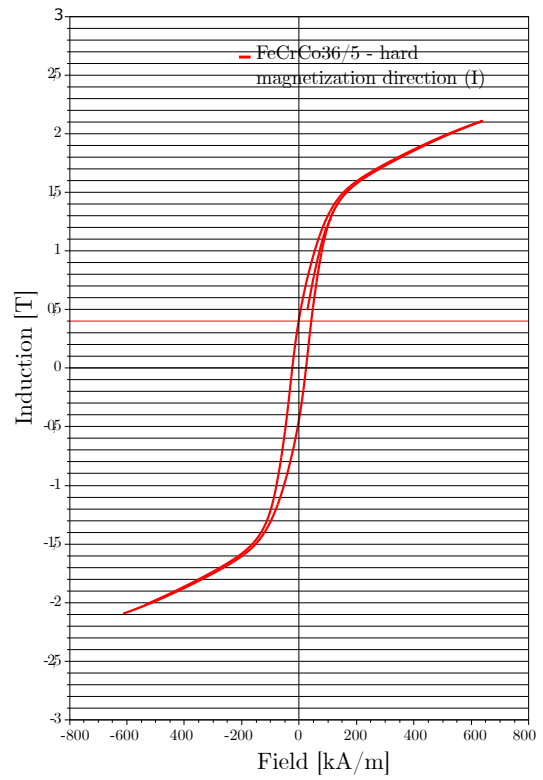
Technical Specifications	
Technical data:	Hystograph HG 200
Measuring fixture:	2 free of drift Fluxmeters F 10
Measuring ranges:	1, 10, 100 mV s and ± 1 Vs
Drift:	$< \pm 1 \mu\text{V s} / \text{min}$
Measuring coils:	surrounding coils, pole coils, field coils
Power supply:	0 to $\pm 125\text{V}$, 0 to $\pm 25\text{A}$, optionally to ± 50 A
Electromagnet:	with interchangeable poles and coil fixture
Maximum field strength:	1.500–1.800 kA/m (dependent on air gap), optionally 2.500 kA/m
Air gap:	0–80mm
Measuring poles:	interchangeable with a maximum diameter of 92mm
Computer:	PC, monitor, printer
Software:	MAG Expert under Windows
Cabinet:	measuring table with container
Dimensions:	760 x 1760 x 800mm (height x width x depth)
Mains supply:	3x200–3x400V, 16A 50/60Hz

B.2 Magnetic characterization of the FeCrCo36/5 studied in the three magnetization directions

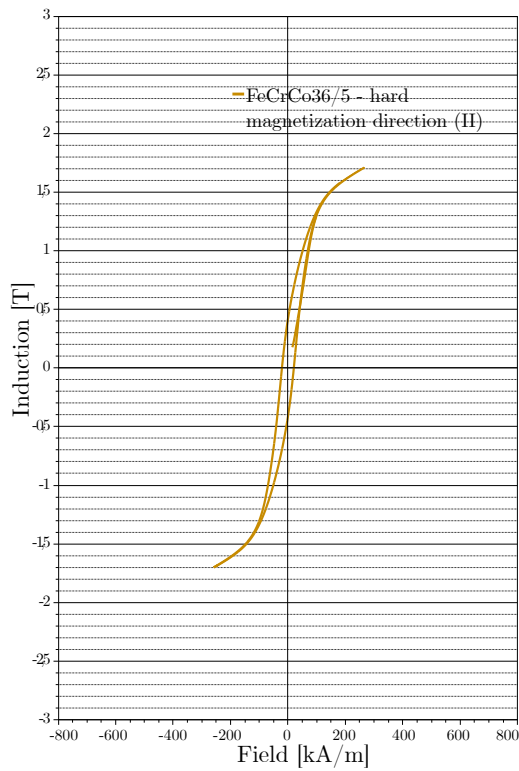
As discussed in the section 2.3, the FeCrCo36/5 composing of the rotor is anisotropic and presents a directional-dependent set of magnetic proprieties. Using the HysteresisGraph presented in Figure 2.6 and the magnet specimen showed in 2.7, the below hysteresis curves characterizing the magnet in its three magnetization directions can be exposed. A comparison between the hysteresis loops obtained in these three magnetization directions can be observed in Figure B.1d. It can be concluded that the magnetic behavior of this magnet is similar in its two hard magnetization directions. For these, no knees are noticed in the second quadrant. However, this is not the case for the easy magnetization direction, in which the BH loop has a similar profile as the one usually described in the literature for the AlNiCo9 or AlNiCo5.



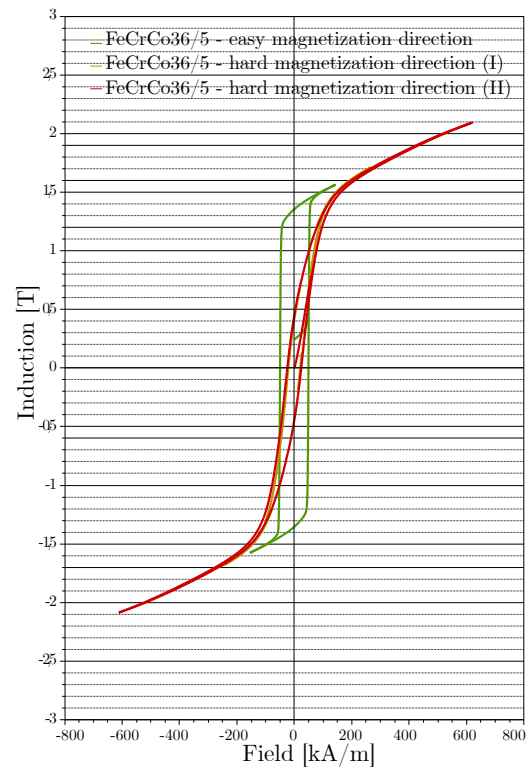
(a) Easy magnetization direction



(b) Hard magnetization direction (I)



(c) Hard magnetization direction (II)

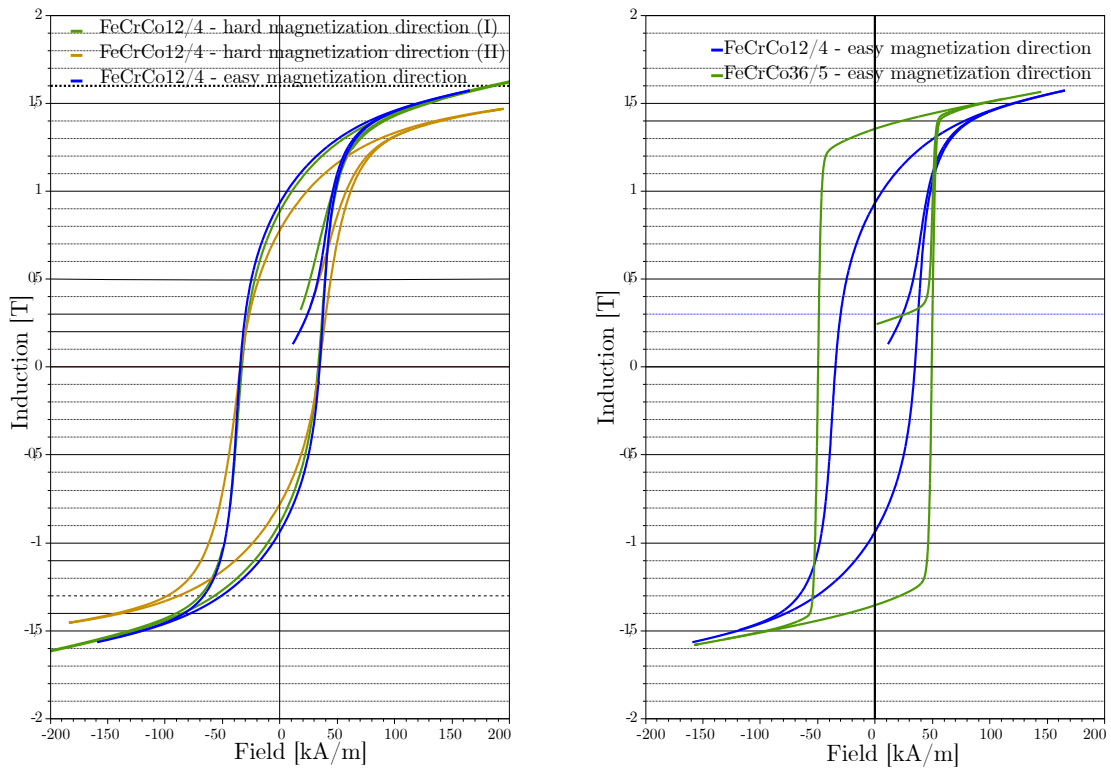


(d) Comparison between the (a), (b) and (c)

Figure B.1: Characterization of the magnet FeCrCo36/5 - HysteresisGraph.

B.3 Magnetic characterization of the FeCrCo12/4 studied in the three directions

The objective of this appendix is to present a grade of magnet for which the hysteresis loop presents no knee on the second quadrant to justify the interest in modeling the FeCrCo36/5 in its hard magnetization direction. As mentioned in the section 2.3 the FeCrCo12/4 is an isotropic magnet for which magnetic the behavior is similar in the three magnetization axes (as exhibited in the Figure B.2a). The levels of remanent induction (B_r around 0.8T) could make them interesting for applications in VFMMs. However, as can be seen in the comparison proposed in Figure B.2b, different of the magnet FeCrCo36/5 or even of the AlNiCo5/AlNiCo9, no well-defined knee is observed in the second quadrant of the hysteresis loop of the FeCrCo12/4. This BH-loop has a profile that hinders the direct use of the models described in the literature because these use this knee as a reference.



(a) Three magnetization directions

(b) Comparison with the FeCrCo36/4

Figure B.2: Magnetic characterization of the magnet FeCrCo12/4.

B.4 Simulations of magnet behavior - analysis of the magnet flux crossing the rotor

This appendix presents the magnetic behavior of each one of the six regions defined in the magnet and presented in Figure 2.10b. Figure B.3 exhibits the flux lines through the machine when e.g., $I_{mag} = 200A$ using Finite Element Analysis simulations. The vector plot for both cases is used to investigate the path taken for these mentioned flux lines. It can be observed that six major regions are in the rotor for the flux lines that cross each pair of stator teeth. These results justify

the six portions of the magnet used as a reference for defining the working points mathematically.

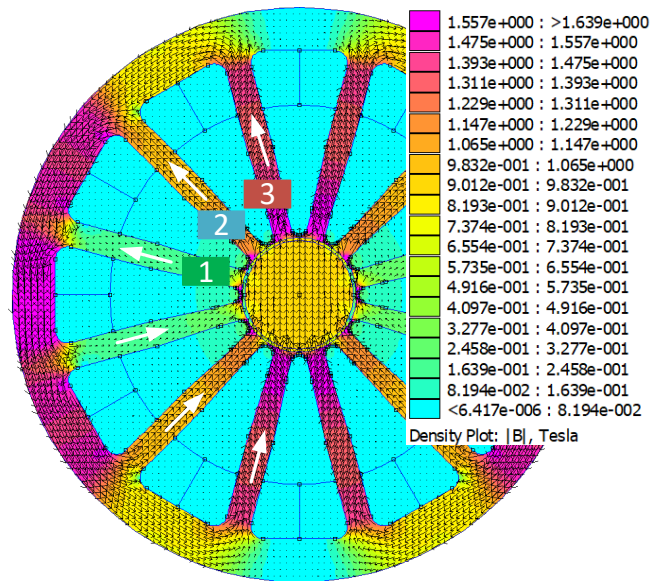


Figure B.3: Cross-section view of the machine for investigating via simulations the flux lines through the rotor for a current pattern $I_A = 0$, $I_B = I_{mag}$ and $I_C = -I_{mag}$.

In Figure B.4 above, a zoom on the rotor simulated above is presented to demonstrate the uniformity of the induction achieved. The portions of the magnet closer to the teeth are non-uniform regions. Because the magnetic flux density is calculated by the volume integral of each limited region, this behavior is taken into account for results achieved via FEA. Even though, this represents a source of uncertainties for defining the working points via equations.

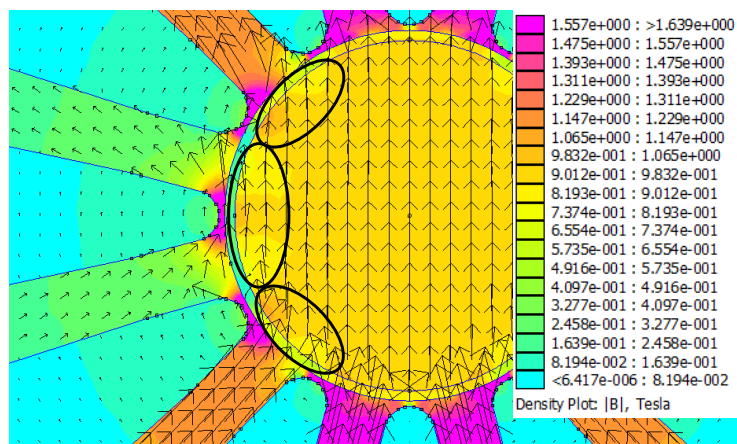


Figure B.4: Cross-section view of the machine for investigating via simulations the magnetic flux density uniformity in the rotor for a current pattern $I_A = 0$, $I_B = I_{mag}$ and $I_C = -I_{mag}$.

B.5 Modeling of working points in the hysteresis loop of the Fe-Cr-Co magnetized in the hard magnetization direction (via simulations by FEA)

The working points defined via FEA by characterizing the magnet with the hysteresis loop obtained using the HysteresisGraph are presented in this section.

The placement of the recoil lines according to the different amplitude of magnetization current defines the working points on the demagnetization curves presented in Table B.5a. For $I_{mag} > 0$, the load lines are placed in the first quadrant of the BH-loop whereas for $I_{mag} < 0$, load lines are placed in the first quadrant. Working points on the initial magnetization curve are strictly obtained for $I_{mag} > 0$ (positive excitation field). This is justified because for $I_{mag} < 0$, working points are not presented (N/A = not applicable). The intersection of these curves with the B-axis (point Y, where $H=0$) and the H-axis (point X, where $B=0$) can be mathematically obtained for modeling the linear functions describing each load line, which slope is equal to the one calculated for the load line $I_{mag} = 0A$, which is given by:

$$slope = \frac{B_0}{H_0} \quad (B.1)$$

where B_0 and H_0 are the magnetic flux density (in [T]) and the field strength (in [kA/m]) of the load line $I_{mag} = 0A$.

Therefore:

$$X(B = 0, H = X) = -\frac{H_m}{\frac{B_0}{H_0}} \quad (B.2)$$

$$Y(B = Y, H = 0) = -H_m \left(\frac{B_0}{H_0} \right) + B_m \quad (B.3)$$

Table B.5b presents the values X and Y for each amplitude of magnetization current. These points, with the ones in Table B.5a define the load lines.

B.6 Modeling of working points in the hysteresis loop of the Fe-Cr-Co magnetized in the easy magnetization direction (via simulations by FEA)

This section is focused on the definition of the working points obtained via FEA by characterizing the magnet with the hysteresis loop obtained using the HysteresisGraph.

As described in the Appendix B.5 for a condition in which the magnetization was realized in the hard magnetization direction, the placement of the recoil lines in this new magnet varies also according to the amplitude of magnetization current, by the same logic as before. The equations B.2 and B.3 are applied again to calculate the intersection of each load line with the BH-axes. The Table B.6b presents the values X and Y for each amplitude of magnetization current. These points, with the ones in Table B.6a, define the load lines.

Figure B.5: Definition of the working points characterizing the load lines for several magnetization current amplitude - FeCrCo36/5 magnetized in the hard magnetization direction ($B_r = 0.45T$, $H_c = -24.4kA/m$) - N/A = Not applicable.

(a) Working points					(b) Parameters of the load lines		
Magnetization current	Points in the demagnetization curve		Points in the initial magnetization curve		Magnetization current	Point X (for B=0,H=X)	Point Y (for B=Y,H=0)
I_{mag} [A _{pk}]	H_m [kA/m]	B_m [T]	H_{exc} [kA/m]	B_{exc} [T]	I_{mag} [A _{pk}]	H_m [kA/m]	B_m [T]
-60	-26.83	-0.05	N/A	N/A	-60	-28.98	-0.64
-50	-24.16	0.004	N/A	N/A	-50	-23.96	-0.53
-45	-22.82	0.03	N/A	N/A	-42	-20.07	-0.44
-40	-21.48	0.06	N/A	N/A	-40	-18.92	-0.42
-30	-19.14	0.11	N/A	N/A	-30	-14.19	-0.31
0	-11.74	0.25	0.00	0.00	0	0.00	0.00
100	16.23	0.66	29.98	0.37	100	46.34	1.02
200	41.97	0.92	56.86	0.76	200	83.82	1.84
300	54.81	1.03	71.04	0.94	300	101.77	2.24
400	63.78	1.10	77.72	1.03	400	113.78	2.50
500	68.94	1.14	82.69	1.09	500	120.84	2.66
600	73.76	1.17	87.46	1.12	600	126.91	2.79
700	76.86	1.19	89.18	1.15	700	130.93	2.88
800	81.26	1.21	90.90	1.17	800	136.07	2.99
900	82.30	1.22	92.71	1.18	900	137.76	3.03
1000	83.37	1.23	94.53	1.20	1000	139.39	3.07
1500	94.82	1.29	103.70	1.26	1500	153.33	3.37

Figure B.6: Definition of the working points characterizing the load lines for several magnetization current amplitude - FeCrCo36/5 magnetized in the easy magnetization direction ($B_r = 1.36T$, $H_c = -49.6kA/m$)- N/A = Not applicable.

(a) Working points					(b) Parameters of the load lines		
Magnetization current	Points on the demagnetization curve		Points on the initial magnetization curve		Magnetization current	Point X (for B=0,H=X)	Point Y (for B=Y,H=0)
I_{mag} [A _{pk}]	H_m [kA/m]	B_m [T]	H_{exc} [kA/m]	B_{exc} [T]	I_{mag} [A _{pk}]	H_m [kA/m]	B_m [T]
-100	-49.60	0.03	N/A	N/A	-100	-48.19	-1.00
-60	-48.79	0.42	N/A	N/A	-60	-28.50	-0.59
-40	-48.17	0.62	N/A	N/A	-40	-18.28	-0.38
0	-46.64	0.96	0.00	0.00	0	0.00	0.00
100	-37.10	1.24	36.38	0.32	100	22.23	0.46
200	-22.21	1.30	49.61	0.85	200	40.46	0.84
300	-10.46	1.33	50.66	1.05	300	53.29	1.10
400	-1.68	1.35	51.23	1.14	400	63.03	1.30
500	2.51	1.36	51.52	1.19	500	69.30	1.43
600	7.28	1.37	51.66	1.23	600	78.77	1.63
700	12.68	1.39	52.05	1.25	700	79.84	1.65
800	18.17	1.39	52.15	1.27	800	84.02	1.74
900	21.13	1.40	52.42	1.29	900	88.31	1.83
1000	25.04	1.40	52.76	1.31	1000	91.91	1.90
1500	41.37	1.43	53.91	1.38	1500	110.53	2.28

B.7 Evaluation of the magnetic behavior of the FeCrCo36/5 considering a standstill magnetization - Hard magnetization direction

When the flux crosses the magnet in its hard magnetization direction, due to the absence of a well-defined knee in the second quadrant, the model proposed in the literature for the Al-Ni-Co magnets cannot be directly applied for estimating the recoil lines or in other words, the behavior of the magnet inserted in the machine environment. Within this context, the main objective of this appendix is to define, using the results provided by the experimental tests, the working point placement at the load line $I_{mag} = 0A$, when magnetization currents of different amplitudes are used to supply the machine. Subsequently, by using these working points as well as the ones at the initial magnetization curve obtained via simulation, the recoil lines can be estimated.

B.7.1 Description of the methodology proposed

A flowchart summarizing the steps of the model proposed for validating the experimental tests is presented in Figure B.7

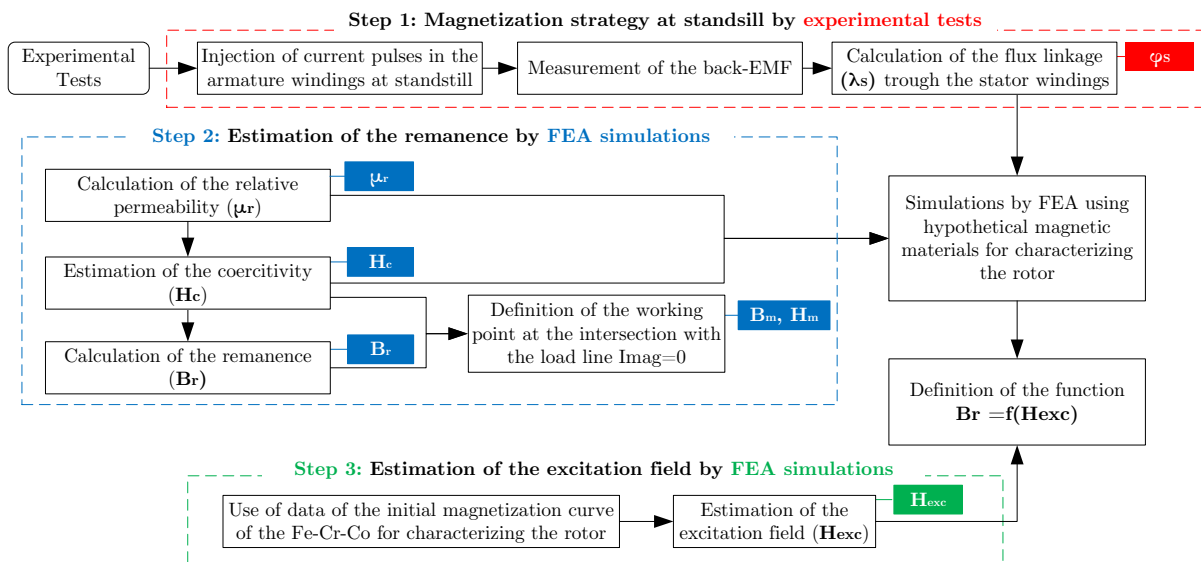


Figure B.7: Overview of the methodology proposed for validating the working point placement of the Fe-Cr-Co magnetized in the hard magnetization direction.

Three steps can be identified in this methodology:

1. The back-EMFs measured during the experimental tests are used for calculating the flux linkage through the stator windings.
2. Second, for describing the behavior of the load lines in the second quadrant of the BH loop, an assumption of parallelism between the recoil lines and the major demagnetization curve is proposed. As a consequence, these internal curves will be characterized by the same relative permeability (μ_r) as the one of the external loop, having each a different coercivity. Considering linear the behavior of the major BH loop in the second quadrant, this mentioned μ_r can be obtained by:

$$\mu_r = \frac{\Delta B}{\mu_0 \Delta H} = \frac{-B_r}{\mu_0 H_c} \quad (\text{B.4})$$

which defines $\mu_r = 14.65$ using the values of the remanence (B_r) and the coercivity (H_c) fixed respectively at $0.45T$ and at $-24.4kA/m$ (see Figure 2.8b). For modeling the behavior of each recoil line, hypothetical materials characterized by the previously calculated $\mu_r = 14.65$ are embedded on the rotor in simulations by FEA, replacing the FeCrCo36/5 that composes the rotor of the VFMM studied. The coercivities of these hypothetical materials representing the recoil lines are estimated to ensure a flux through the stator windings equal to the ones calculated from the back-EMF measured during the experimental tests at no load, which results are shown in the section 2.5.2. From these values of H_c , the remanence defining each recoil line can be calculated using the again the equation B.4, for a constant $\mu_r = 14.65$. The results obtained (pairs of H_c , B_r) are used for describing the behavior of the recoil lines of the FeCrCo36/5 in the second quadrant of the hysteresis loop and can be analyzed in Table B.2. The ratio between each remanence and the one characterizing the major hysteresis loop can be used to evaluate the magnetization state (MS) of the magnet. It can be concluded that a MS of 39.8% is achieved for $I_{mag} = 900A$.

The recoil lines obtained from this methodology intercept the load line $I_{mag} = 0A$. The slope of this mentioned load line, calculated according to the data exhibited in Table B.5a in the Appendix B.5, is used for calculating the magnetic field intensity at the intersection of this linear curve and each recoil line analyzed. The equation B.5 is used for these calculations:

$$H_m = -\frac{B_r}{(PC) - (\mu_0 \mu_r)} \quad (\text{B.5})$$

where PC is the permeance coefficient calculated according to the magnetic circuit geometry, as exposed in Chapter 1 and rewritten below:

$$B_m = -\mu_0 \left(\frac{l_m}{l_g} \right) \left(\frac{A_g}{A_m} \right) H_m = (PC)H_m \quad (\text{B.6})$$

where the cross-sectional area of the air gap and the magnet, are respectively presented by A_g and A_m (in $[m^2]$), the air gap and the magnet length by l_g and l_m (in $[m]$). From each H_m calculated, B_m can be obtained by applying this result in the equation B.6.

3. In the third step of the methodology proposed, the behavior of the recoil lines in the first quadrant of the hysteresis loop is established. For this, data presented in Figure 2.8a in the section 2.3 for the initial magnetization curve are embedded in the rotor during simulations by FEA. The objective is to estimate the excitation field (H_{exc} , in $[A/m]$) in the magnet when the different amplitudes of magnetization current were injected in the armature windings during the experimental tests. A current pattern of current pattern $I_A = 0A$, $I_B = I_{mag}$, $I_C = -I_{mag}$ is defined for supplying the machine during the same magnetization conditions used during the experimental tests. The achieved results are presented in Table B.2.

Table B.2: Characterization of the recoil lines - FeCrCo36/5 magnetized in the hard magnetization direction ($B_r = 0.45T$, $H_c = -24.4kA/m$).

Experimental Tests		Recoil lines					Initial magnetization curve - by FEA simulations	
Magnetization current	Flux linkage	Coercivity	Remanence	Magnetization state	Points in the load line $I_{mag} = 0A$		Points in the initial magnetization curve	
I_{mag} [A _{pk}]	φ_s [μ Wb]	H_c [kA/m]	B_r [T]	MS [%]	H_m [kA/m]	B_m [T]	H_{exc} [kA/m]	B_{exc} [T]
500	27.95	-3.90	0.07	15.96	-1.78	0.04	84.22	1.09
600	34.33	-4.90	0.09	20.04	-2.23	0.05	87.46	1.13
700	42.45	-6.00	0.11	24.55	-2.73	0.06	89.18	1.15
750	52.32	-7.30	0.13	29.86	-3.32	0.07	90.04	1.16
800	57.10	-8.00	0.15	32.73	-3.64	0.08	90.90	1.17
900	71.44	-9.70	0.18	39.68	-4.42	0.10	93.63	1.18

B.7.2 Evaluation of the results obtained from methodology proposed

The estimation of this flux linkage per phase (φ_s , in [Wb]) crossing the armature windings in case each magnetization condition is realized via simulations. The variation of this flux according to the electrical rotor position of the rotor (θ , in [radians]) can be later applied to Faraday's Law (equation B.7) for estimating the back-EMF, assumed sinusoidal, at a set speed ω

$$e = -N \frac{d\varphi_s}{dt} = -N \frac{d\varphi_s}{d\theta} \frac{d\theta}{dt} = -N \frac{d\varphi_s}{d\theta} \omega \quad (\text{B.7})$$

Considering the recoil line obtained for $I_{mag} = 600A$ ($B_r = 0.09T$, $H_c = -4.9kA/m$ and $\mu_r = 14.65$) and the one for $I_{mag} = 800A$ ($B_r = 0.15T$, $H_c = -8.0kA/m$ and $\mu_r = 14.65$) the flux linkage through the stator windings and the estimated back-EMF can be obtained. Figure B.8 shows the results achieved for the phase back-EMF. Table B.3 compares these results with the ones reached via experimental tests. An error of 1.8% is observed comparing the flux linkage of both simulated and measured results for $I_{mag} = 600A$ and of 2.7% in the case of $I_{mag} = 800A$. As discussed before, the back-EMF is assumed to be sinusoidal for these analyses.

 Table B.3: Validation of the estimated recoil lines - FeCrCo36/5 magnetized in the hard magnetization direction ($B_r = 0.45T$, $H_c = -24.4kA/m$).

Comparison between experimental and simulation results				
Experimental tests			Simulations	
Magnetization current	Line back-EMF	Flux linkage	Line back-EMF	Flux linkage
I_{mag} [A _{pk}]	e [mV _{pp}]	φ_s [μ Wb]	e [mV _{pp}]	φ_s [μ Wb]
600	566	34.33	555.64	34.44
800	956	57.10	929.76	57.97

In Figure B.9c, the recoil lines characterized using the methodology presented in the flowchart B.7 are exhibited. The magnetic behavior described can be compared to the one of recoil lines obtained from a sample of the magnet characterized via HysteresisGraph, as demonstrated in the section 2.6. Figure B.9a presents these last-mentioned results again for comparison. A first investigation demonstrates a similar shape for the recoil lines exhibited in both Figure B.9c and Figure B.9a are similar, but the ones estimated by using the methodology proposed have a higher relative permeability (higher slope). Consequently, from the same level of excitation field achieved in the initial magnetization curve of both mentioned BH loops, lower remanences are seen for the

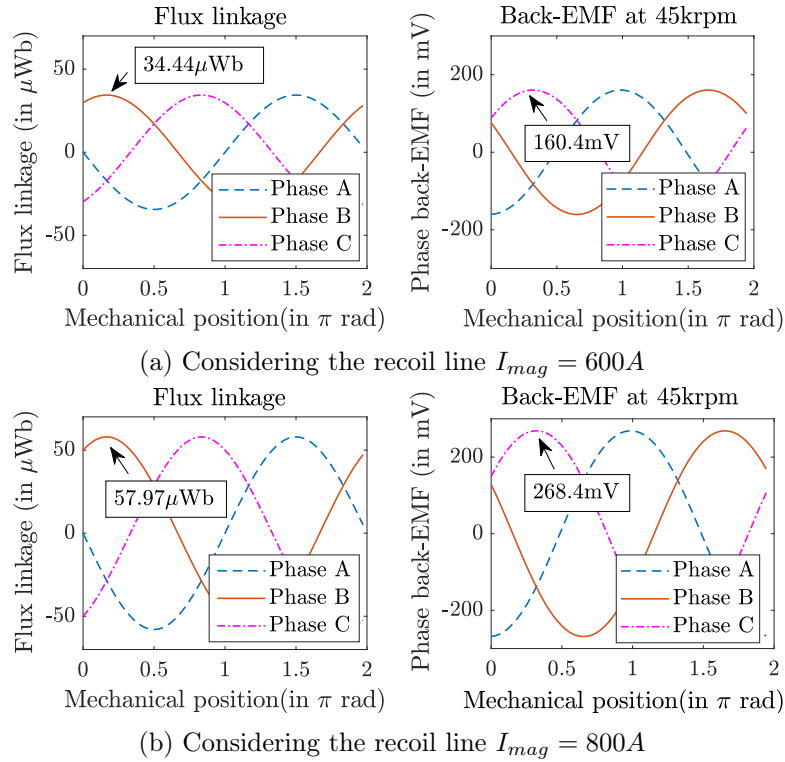


Figure B.8: Validation via simulations of the estimated recoil lines.

recoil lines in Figure [B.9c](#). In both cases, a parallel behavior to the major demagnetization curve in the second quadrant is identified. Additionally, different coercivities characterize each recoil line, which represents the main difference in the magnetic behavior observed when the Al-Ni-Co magnets are used.

For comparing between results presented in Figures [B.9a](#) and [B.9c](#), the remanence in function of the excitation field ($B_r = f(H_{exc})$) is exhibited in the Figure [B.10](#). This curve provides a clear feature for analyzing the differences between these mentioned magnet characterizations.

B.7.2.1 Analysis of the differences observed

Investigations revealed that four major factors justify the differences observed in Figure [B.10](#). These same topics were previously discussed for the FeCrCo36/5 magnetized in its easy magnetization direction in the section [2.7](#). For this reason, this appendix is going to be focused on the adaptation of the conclusions for the magnet studied in this appendix.

The following justifications affect the modeling of recoil lines from the experimental results:

- First, due to the presence of closed slot wedges in the stator in the stator geometry, more ampere-turns are required for magnetizing the LCF magnet inserted in the machine when compared to the one inserted in the measuring equipment. As described in the section [2.7](#), for testing in the machine an analogous condition as the one in which the magnet is inserted in the HysteresisGraph, the slot wedges are opened. This new geometry is used for studying via simulations the behavior of the magnet excitation when the machine is supplied with different amplitudes of magnetization current. The results achieved using these analyses are described in Table [B.4](#). It can be concluded that for achieving the same magnet flux density, lower ampere-turns (in this case, lower I_{mag}) are required for the machine designed by opened slot wedges. These levels of current amplitudes identified

using the new geometry are the ones to be considered for comparing the magnetic behavior of the Fe-Cr-Co inserted in the original machine and one for which the magnet behavior is closer to the one observed in a HysteresisGraph.

Table B.4: Study by FEA of the effects of a stator geometry designed with closed slot wedges.

Working points in the initial magnetization curve			
Both geometries		Closed slot wedges	Opened slot wedges
Magnetic flux strength	Magnetic flux density	Magnetization current	
H_{exc} [kA/m]	B_{exc} [T]	I_{mag} [A _{pk}]	
1.09	84.22	500	420
1.13	87.46	600	470
1.15	89.18	700	520
1.16	90.04	750	540
1.17	90.90	800	570
1.18	93.62	900	620

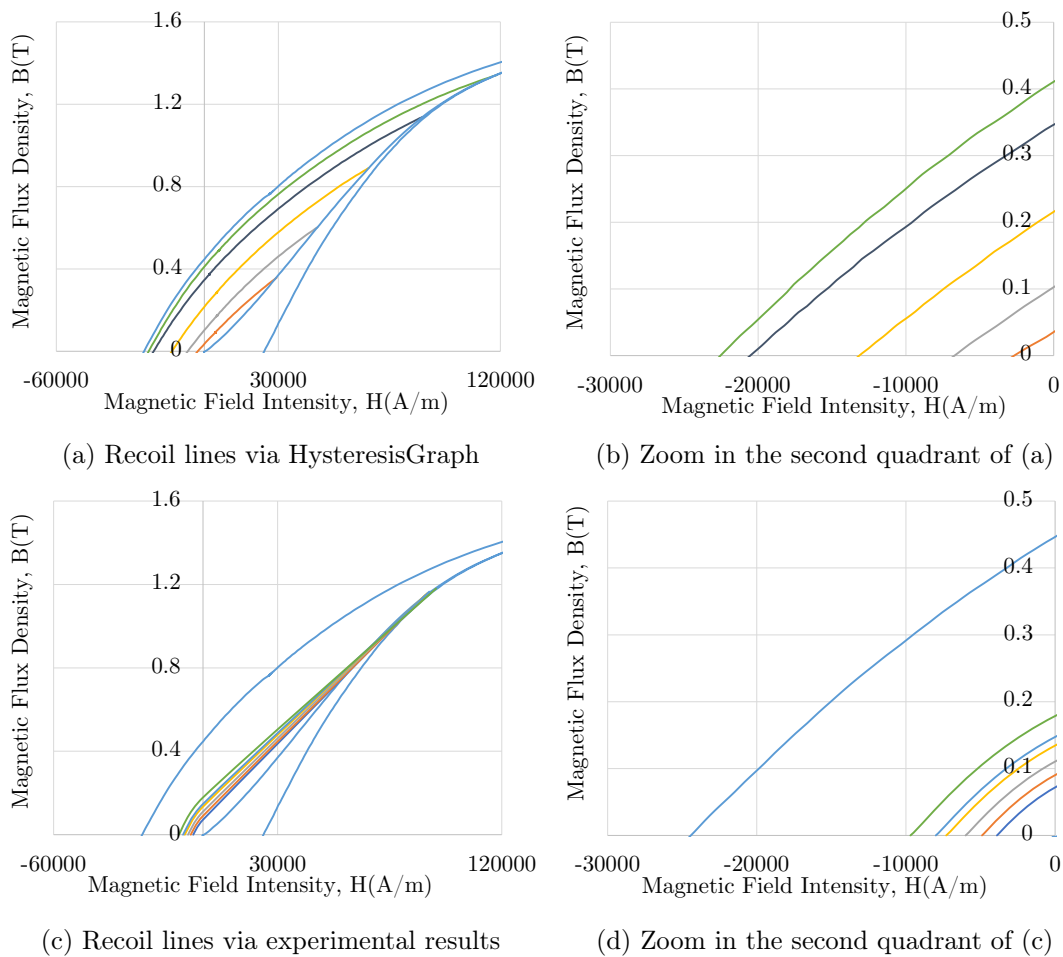
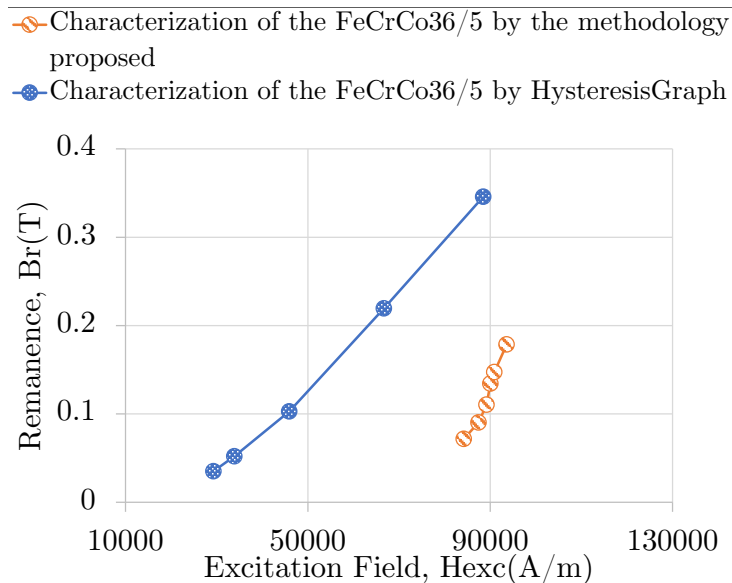


Figure B.9: Recoil lines obtained via HysteresisGraph and simulations using the proposed methodology.

Figure B.10: Remanence in terms of the excitation field in the Fe-Cr-Co magnet ($B_r=f(H_{exc})$).

- Also for an equivalence between the studies realized in the HysteresisGraph with the original machine environment, the saturation of the steel composing of the stator is investigated. These effects, as exposed in the section 2.7 are a consequence of the direct adaptation of a PMSM into a VFMM only by the replacement of the magnetic rotor. Because no saturation effect exists in the measuring equipment, approximating the behavior of the original machine to the one of the HysteresisGraph requires a modification of the stator magnetic material. Therefore, simulations were carried out considering an opened slot wedges stator geometry characterized by a hypothetical ferromagnetic material ($\mu_r \gg 1$). The profile of the curve BH used for these tests is shown in the section 2.7, being the same as the one used for the studies regarding the magnet manufactured for being magnetized in the easy magnetization direction. Table B.5 exhibits the achieved results and the levels of current to be considered in each magnetization case for observing in the machine a magnetic behavior analogous to the one on the HysteresisGraph.

Table B.5: Study by FEA of the effects of the steel saturation.

Working points in the initial magnetization curve			
Both geometries		Closed slot wedges and saturable steel	Opened slot wedges and non-saturable steel
Magnetic flux strength H_{exc} [kA/m]	Magnetic flux density B_{exc} [T]	Magnetization current I_{mag} [A _{pk}]	
1.09	84.22	500	304
1.13	87.46	600	315
1.15	89.18	700	325
1.16	90.04	750	328
1.17	90.90	800	332
1.18	93.62	900	340

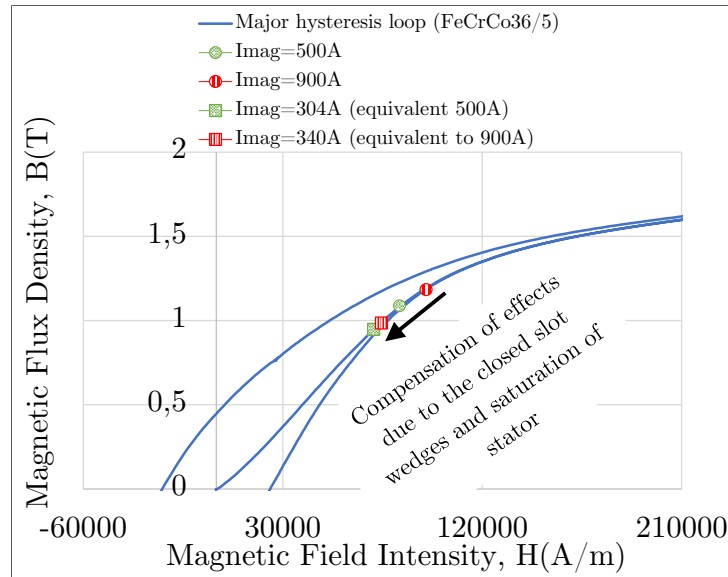
Figure B.11a shows the working point in the initial magnetization curve obtained via FEA considering the machine supplied with the current amplitudes (1) considered for the experimental tests and (2) the ones that allow the equivalence with the results achieved using the HysteresisGraph.

- Analyzing now, as proposed in the section 2.7, the machine performance during the induction of back-EMF in the stator windings, it is observed that flux leakage exists as a consequence of a short-circuit of the magnet flux lines by the path provided by the slot wedges. Table B.6 shows the % flux leakage observed for different recoil lines characterizing the rotor. It should be noticed that for recoil lines of higher remanence (i.e., for the ones obtained for higher levels of magnetization current), this flux leakage is reduced because this higher induction implies more saturation of the closed slot wedges. A compensation of these losses is proposed for calculating the working point on the load line $I_{mag} = 0A$ using the methodology described in Figure B.7. By this strategy, the magnetic behavior of the machine is consequently approximated from the one of the measuring equipment. Figure B.11b presents the new placement of the recoil lines in the second quadrant of the hysteresis loop. Differently from what was proposed for studying the magnet manufactured for being crossed by the easy magnetization direction, the relative permeability is unchanged for maintaining parallel the behavior of the recoil lines in the second quadrant. As a consequence, the coercivity and remanence are going to be changed.

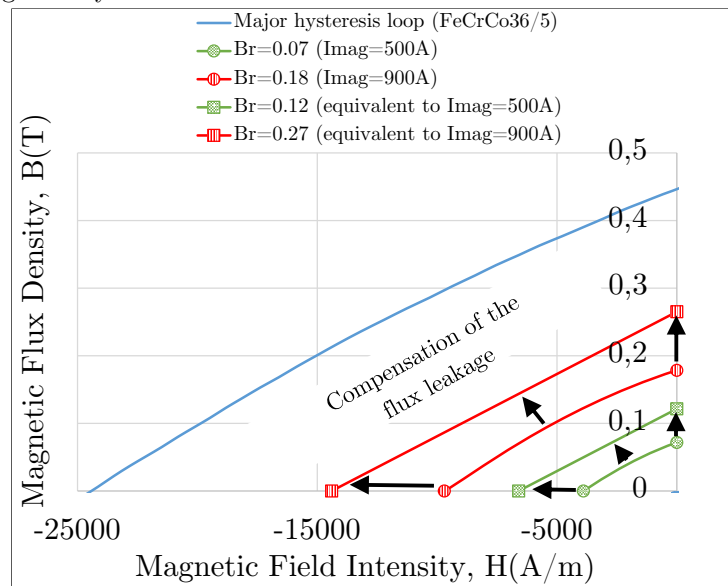
Table B.6: Study by FEA of the effects of the short-circuit of magnetic flux lines.

Working points in the load line $I_{mag} = 0A$							
		Before corrections of short-circuit effect s(experimental tests)			After corrections of short-circuit effects (simulations)		
Magnetization current	% of losses due to short-circuit of the magnetic flux	Flux linkage	Coercivity	Remanence	Flux linkage	Coercivity	Remanence
I_{mag} [A _{pk}]	[%]	φ_s [μWb]	H_c [kA/m]	B_r [T]	φ_s [μWb]	H_c [kA/m]	B_r [T]
500	40	27.95	-3.90	0.07	46.58	-6.6	0.12
600	39	34.33	- 4.90	0.09	56.28	-7.9	0.14
700	38	42.45	-6.00	0.11	68.47	-9.4	0.17
750	38	52.32	-7.30	0.13	84.39	-10.9	0.20
800	37	57.1	-8.00	0.15	90.63	-12.1	0.22
900	36	71.44	-9.70	0.18	111.63	-14.4	0.27

- Finally, as exposed in the section 2.7, two other factors can be mentioned as supplementary sources of differences between the working points obtained via measures realized in the HysteresisGraph and the ones achieved using the methodology proposed. First, the shape anisotropy is observed in the machine due to the non-uniformity of the magnet flux. Second, the analysis of the whole magnet by a single load line represents a simplification because, in practice, the magnet has different lengths crossed by each flux line due to its cylindrical shape.



(a) Working points in the initial magnetization considering the compensation of effects due the closed slot wedges in the stator geometry and due to the steel saturation



(b) Recoil lines in the second quadrant considering the compensation of effects flux leakage during the back-EMF induction because of the closed slot wedges in the stator geometry

Figure B.11: Studies for achieving equivalence between the results obtained via experimental tests and the methodology proposed.

Figure B.12 shows the function $B_r = f(H_{exc})$ before and after the proposed corrections described in each one of these topics above. In step (1), results presented in Table B.4 are presented. In step (2), the ones of Table B.5. Finally, step (3) represents the results discussed in Table B.6. It can be observed that after these corrections, the behavior of the magnet inserted in the machine is closer to the one observed in the ideal circuit of measurement, the HysteresiGraph.

Figure B.13a presents the new recoil lines that can be used for describing the magnet behavior.

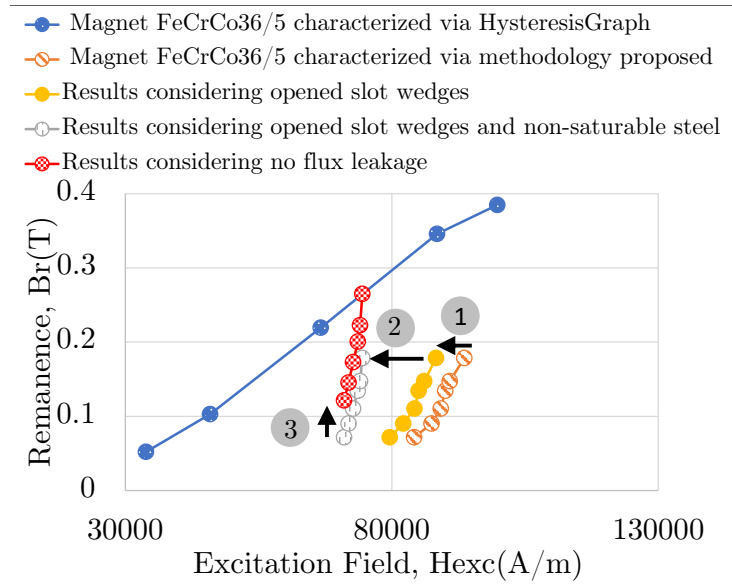


Figure B.12: Remanence in terms of the excitation field in the Fe-Cr-Co magnet ($B_r = f(H_{exc})$) considering the corrections proposed for the model, being (1) compensation due to the closed slot wedges in the stator geometry, (2) compensation of the saturation effects in the stator and (3) compensation of the short-circuit effects observed during the back-EMF induction.

They can be compared to the ones introduced in Figure [B.9a](#) and Figure [B.9c](#).

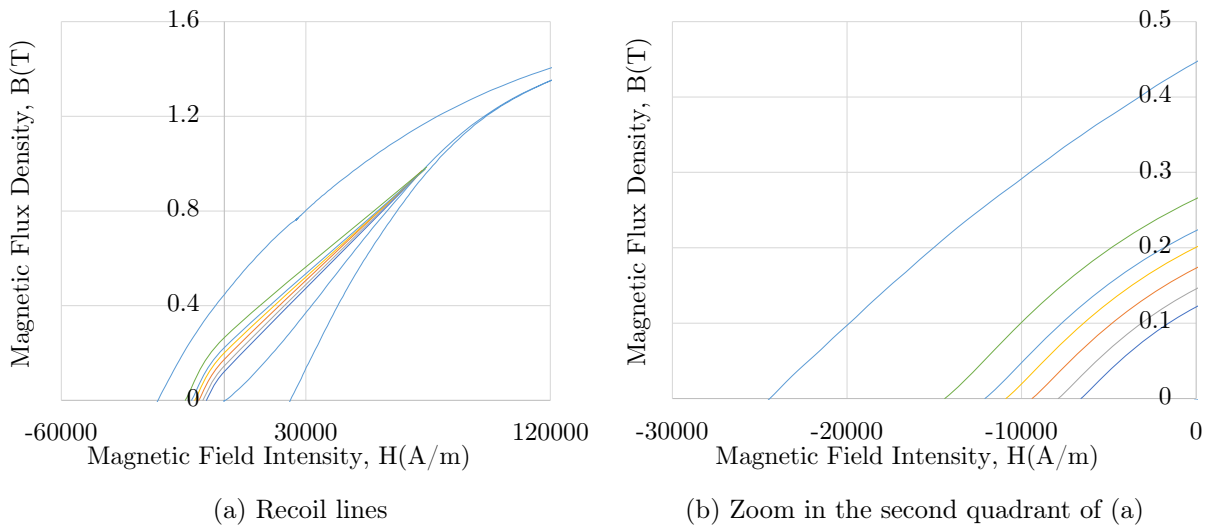


Figure B.13: Recoil lines obtained by correcting the methodology proposed for approximating the magnetic behavior of the machine to the one of the HysteresisGraph.

Remark: The slope of the curve $B_r = f(H_{exc})$ obtained using the experimental results is not the same as the one traced using the results obtained via HysteresisGraph, as can be noticed by analyzing the curves exhibited in the Figure [B.10](#). Investigations demonstrated that the saturation of the steel composing of the stator is the main reason for this difference. It should be remembered that a HysteresisGraph is a measuring equipment. Hence, it should not influence

the magnet characterization while measurements are done. However, as already known, for a magnet inserted in an environment in which saturation is present, the results are affected. For verifying the effects of inaccuracies regarding the magnetic behavior of the steel composing of the stator on the results obtained, the material composing of this portion of the rotor is replaced during simulations by (1) a hypothetical ferromagnetic material having a constant $\mu_r = 10000$ in regions of non-saturation and a level of saturation two times higher than the one of the COGENT NO20 currently used and (2) a hypothetical ferromagnetic material having a constant a constant $\mu_r = 10000$ in regions of non-saturation and a level of saturation three times higher than the one of the COGENT NO20 currently used. Figure B.14 shows the BH curve for these materials.

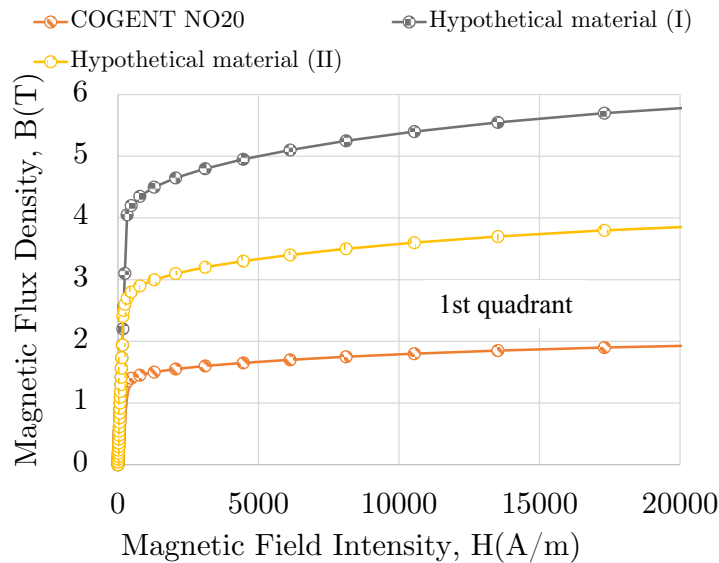


Figure B.14: Magnetic characteristic of the materials composing of the stator during simulations.

In Table B.7, the results obtained when the working points in the initial magnetization curve and in the intersection with the load line $I_{mag} = 0A$ are identified considering these two cases are presented. The methodology applied for these simulations is the same as already described.

Table B.7: Study by FEA of the effects on the rotor magnetization for different stator materials.

Parameters estimated applying the proposed methodology						
Magnetization current	For the stator composed of the COGENT NO20		For the stator composed of the hypothetical material (I)		For the stator composed of the hypothetical material (II)	
	Excitation field	Remanence	Excitation field	Remanence	Excitation field	Remanence
I_{mag} [A _{pk}]	H_{exc} [kA/m]	B_r [T]	H_{exc} [kA/m]	B_r [T]	H_{exc} [kA/m]	B_r [T]
500	84.22	0.07	159.27	0.08	159.27	0.08
600	87.46	0.09	193.26	0.09	208.06	0.09
700	89.18	0.11	224.48	0.12	249.79	0.12
750	90.04	0.13	238.33	0.15	273.27	0.15
800	90.90	0.15	252.17	0.16	296.09	0.16
900	93.62	0.18	281.29	0.20	338.11	0.20

Figure B.15 demonstrates the difference observed in the parameters estimated (B_r and H_{exc})

when the stator is composed by these three described materials (COGENT NO20 or the two hypothetical ferromagnetic materials). It can be seen that the magnetic profile used for the stator material has an impact on the slope of the curve $B_r = f(H_{exc})$. A steep slope is observed for the machine in which the stator material saturates first. This is because higher saturation levels imply in high excitation field required for saturating the closed slot wedges before magnetizing the rotor.

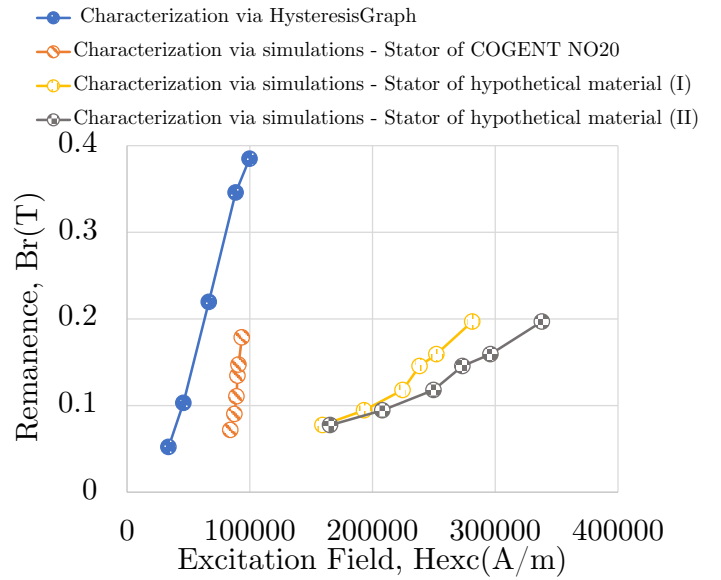


Figure B.15: Remanence in terms of the excitation field ($B_r = f(H_{exc})$) of the magnet FeCrCo36/5 via HysteresisGraph and simulations, considering the stator composed of COGENT NO20 and two different hypothetical materials presented in the Figure [B.14](#).

Appendix C

Chapter 2

C.1 Machine Parameters

The section is dedicated to the presentation of the machine parameters. The values indicated for characterizing the stator resistance (R_s) and the dq-axis inductances (L_d and L_q) are the ones considered well-known for the first simulations realized. Later discussions will demonstrate that this initial assumption requires adjustments for better representing the real machine model.

Table C.1: Presentation of parameters for evaluation of the machine control.

Control system parameters		
Parameter	Symbol	Amplitude
Cutoff frequency	f	35000
Stator resistance	R_s	$5m\Omega$
d-axis inductance	L_d	$5\mu H$
Bus DC voltage	V_{DC}	48V
q-axis inductance	L_q	$5\mu H$
Friction	f_r	$0.5\mu N.m.s$
Moment of inertia	J	$5n.kg.m^2$

C.2 Parametric sensitivity according to the angle between the voltage and current vectors

This section is dedicated to the presentation of parametric sensitivity of angle θ_{PLL} according to the two operation conditions described in the section 3.2.5: (1) $I_q = 50A$ and $I_{mag} = 0A$, or torque control, for $\theta_{PLL} = atan((-ωL_q i_q)/(R_s i_q + ωφ_s))$ and (2) $I_{mag} = 50A$ and $I_q = 0A$, which represents a magnetization control, for which $\theta_{PLL} = atan((R_s i_d)/(ω(L_d i_d + φ_s)))$. The behavior of θ_{filter} is not explored in this section, as θ_{PLL} is the angle the most affected by the parametric errors.

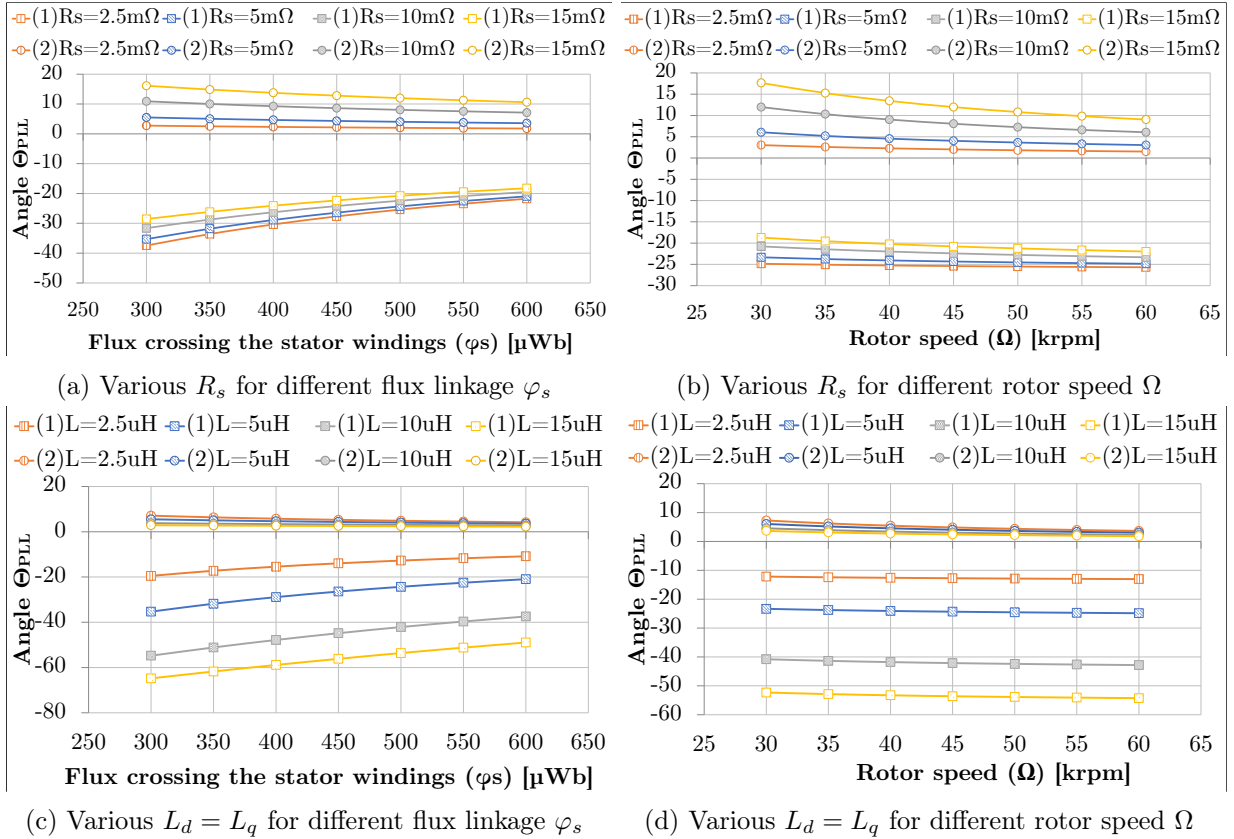


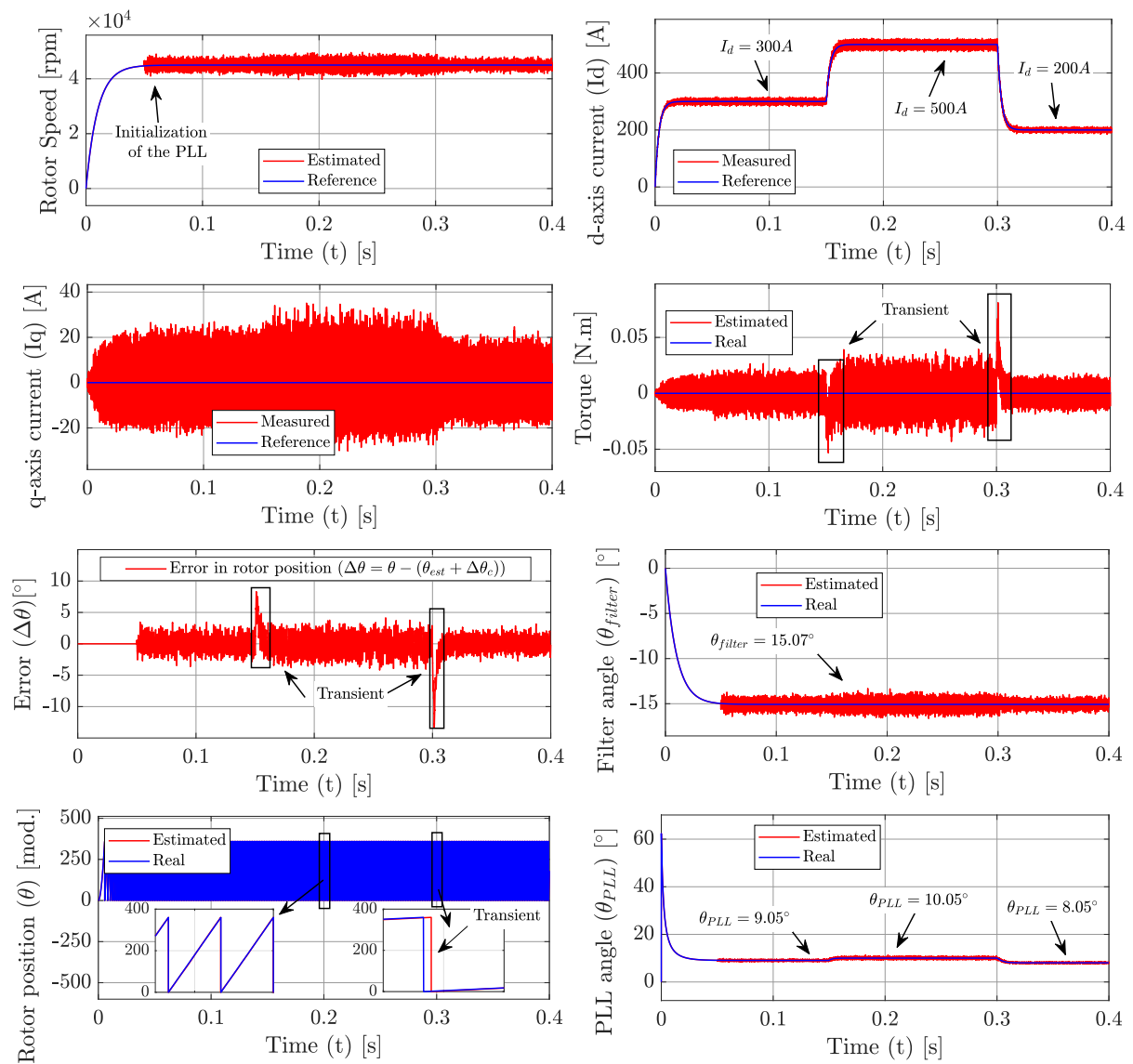
Figure C.1: Study by simulation of sensitivity of the angle θ_{PLL} for different system parameters considering: (a) and (c) different flux linkage conditions and (b) and (d) different regimes. Case (1) represents the $I_{mag} = 0A$ and $I_q = 50A$ and (2) $I_{mag} = 50A$ and $I_q = 0A$.

C.3 Validation of the PLL-based sensorless strategy

The study of validation of the PLL-based sensorless strategy regarding variations on the speed (Ω) and the magnetization current (I_d) are respectively exhibited in Figures C.2 and C.3. As discussed in the section 3.5.1, the PLL is initialized at $t=0.05s$ aiming for the estimation of the rotor position and speed. The angles θ_{PLL} and θ_{filter} are calculated for each working condition. For evaluating the errors obtained by the use of the system proposed, the difference between the rotor position (θ) and the estimated one ($\theta_{est} + \Delta\theta_c$) is also presented. Table C.2 summarizes the results achieved for these two case studies.

Table C.2: Study of the displacement angles.

Case	Magnetization current	Torque current	Rotor speed	Angle between voltage and current vectors	Filtering angle	Correction angle
	I_{mag} [A]	I_q [A]	Ω [krpm]	θ_{PLL} [°]	θ_{filter} [°]	$\Delta\theta_c$ [°]
Rotor speed variation	0	50	20	-21.98	-6.72	-15.26
d-axis current variation	0	50	30	-23.33	-10.07	-13.26
d-axis current variation	0	50	45	-24.32	-15.07	-9.25
d-axis current variation	200	0	45	8.05	-15.07	23.1
d-axis current variation	300	0	45	9.04	-15.07	24.1
d-axis current variation	500	0	45	10.02	-15.07	25.1


 Figure C.2: Validation of the sensorless strategy - Study at $I_d = 300A$, $I_d = 500A$ and $I_q = 200A$.

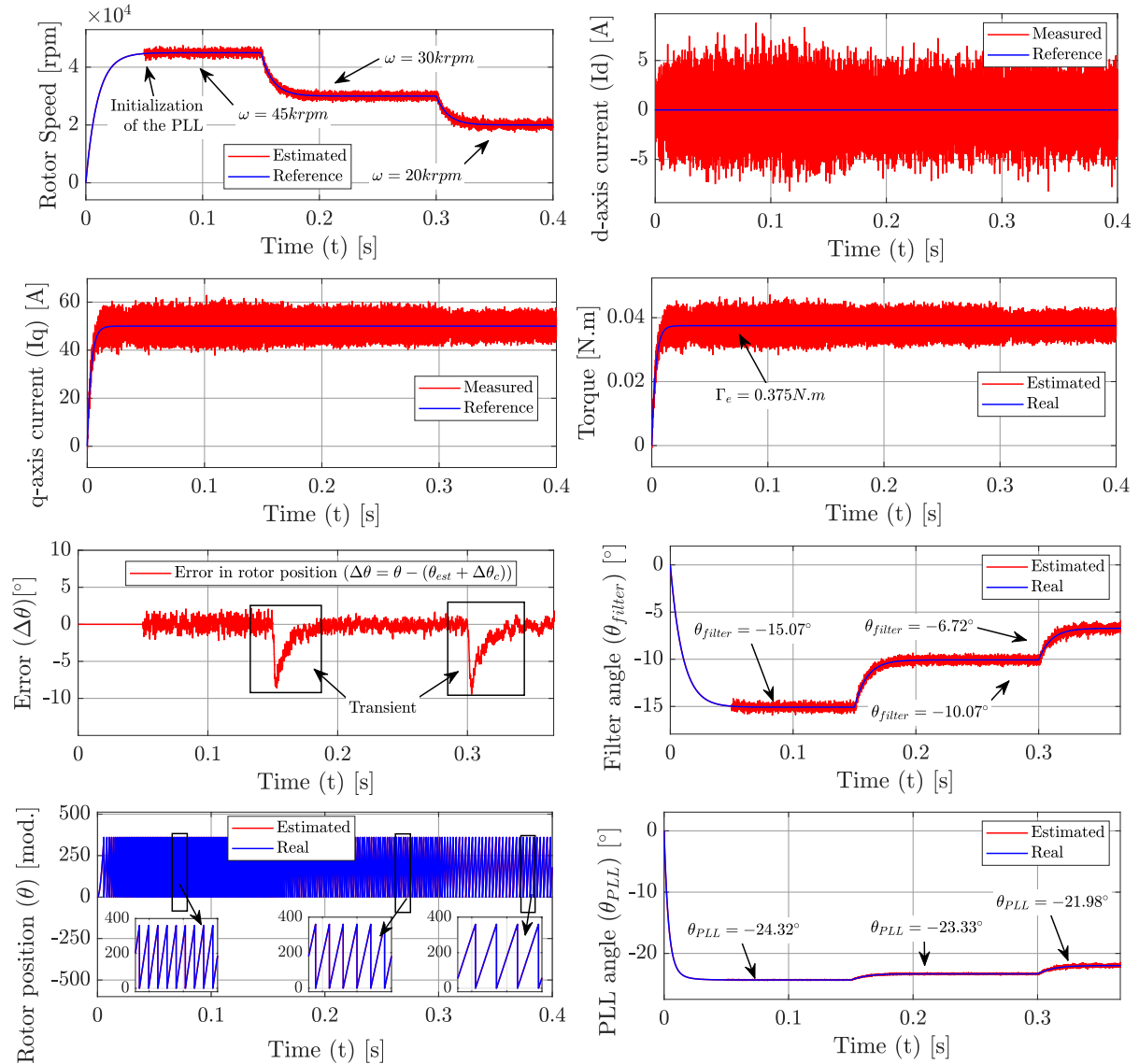


Figure C.3: Validation of the sensorless strategy - Study at $\Omega = 45krpm$, $\Omega = 30krpm$ and $\Omega = 20krpm$.

C.4 Parametric sensitivity

This exhibits the results obtained in case of parametric errors in the stator resistance and the d-axis inductance (L_d), both studies developed considering $I_q = 50A$ and $I_d = 0A$ in a regime $\Omega = 45krpm$. The first case, presented in Figure C.4, investigates a variation on R_s of $R_s = 5m\Omega$, $R_s = 10m\Omega$ and $R_s = 2.5m\Omega$. Because the correction angles are calculated from the reference currents (control currents), both θ_{PLL} and θ_{filter} are constant and respectively equal to $\theta_{PLL} = -24.3^\circ$ and $\theta_{filter} = 15.07^\circ$. Errors in R_s , however, generate a divergence between these mentioned reference currents and the machine ones. As a consequence, the correcting angles are badly calculated, which leads to errors in the rotor position estimated ($\theta_{est} + \Delta\theta_c$) with regard to the real one (θ). The results in Figure C.5 investigate a variation on L_d , that assumes values of $L_d = 5\mu H$, $L_d = 2.5\mu H$ and $L_d = 10\mu H$. Angles $\theta_{PLL} = -24.3^\circ$ and $\theta_{filter} = 15.07^\circ$ are also obtained in this case, as the current references (or control currents) are not modified. Because I_d does not affect the correction angle in the case studied, $\Delta\theta = 0^\circ$.

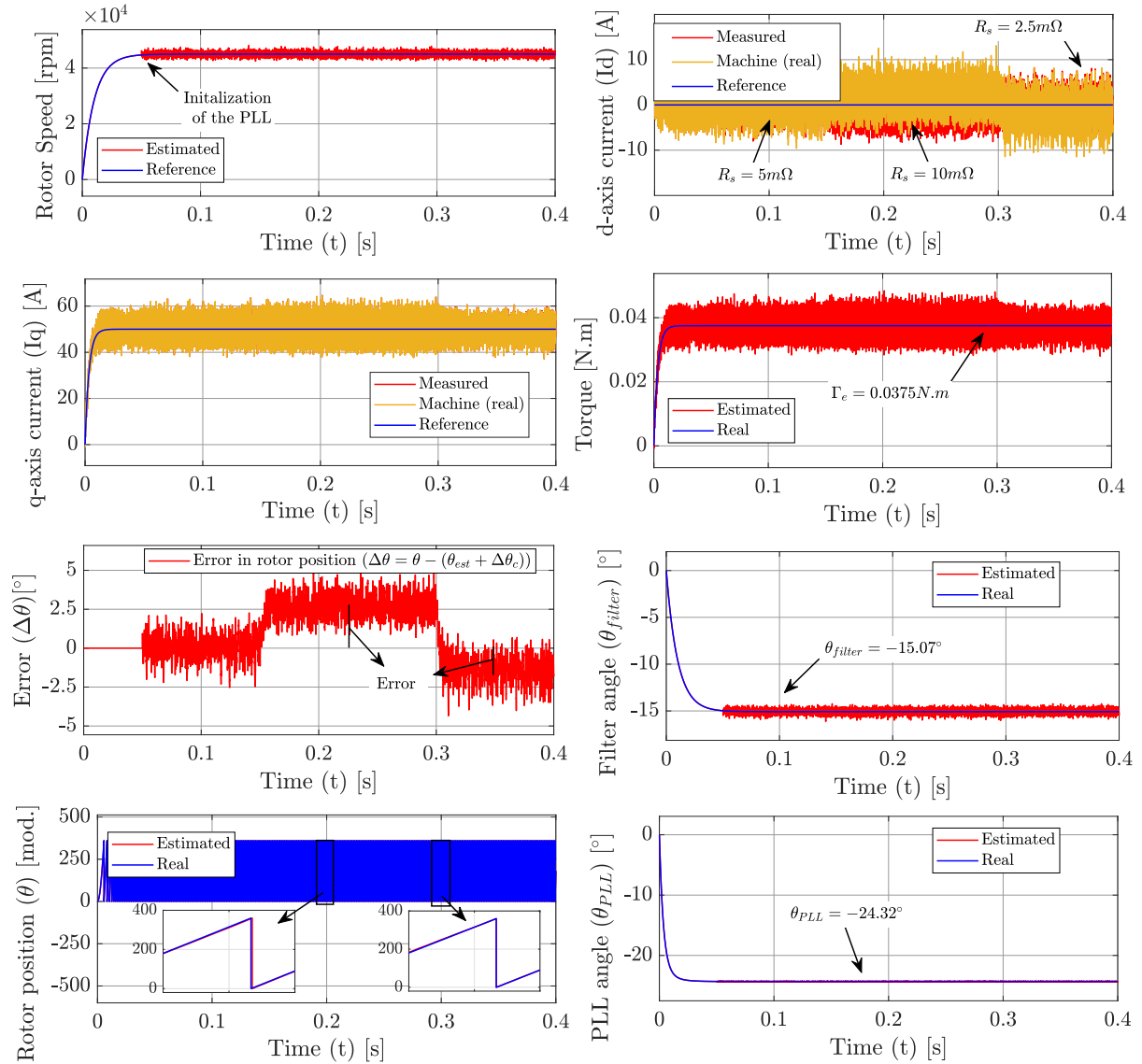


Figure C.4: Investigation of the parametric sensitivity via simulation - Study considering the variation of the machine parameter $R_s = 5m\Omega$, $R_s = 10m\Omega$ and $R_s = 2.5m\Omega$, for a control stator resistance $R_s = 5m\Omega$.

C.5 Study of the Global Offset angle considering the reluctance effects

The study of the system for $I_{ref} = 50A$ is going to be discussed in this section to demonstrate the effects of the reluctance in the definition of $\Delta\theta_c$. The Figure [C.6](#) exposes the investigation developed. Considering $\delta = 0^\circ$ (as established during the experimental tests), a $\Delta\theta_{c_{ref}}$ is calculated from the simulations carried out taking into account the mean inductance values $L_d = 6\mu H$ and $L_q = 8\mu H$ obtained using the inductance model proposed via FEA (Case (1) in the Figure [C.6](#)). Because $I_d = 0A$ at this working condition, this angle does not represent the one for a maximal torque and both DC and AC power. For angles $\Delta\theta_c < \Delta\theta_{c_{ref}}$ manually adjusted as correction angle in this control system it is noticed that a positive d-axis current component passes through the machine (Case (2)). The DC and AC power and torque are reduced in this

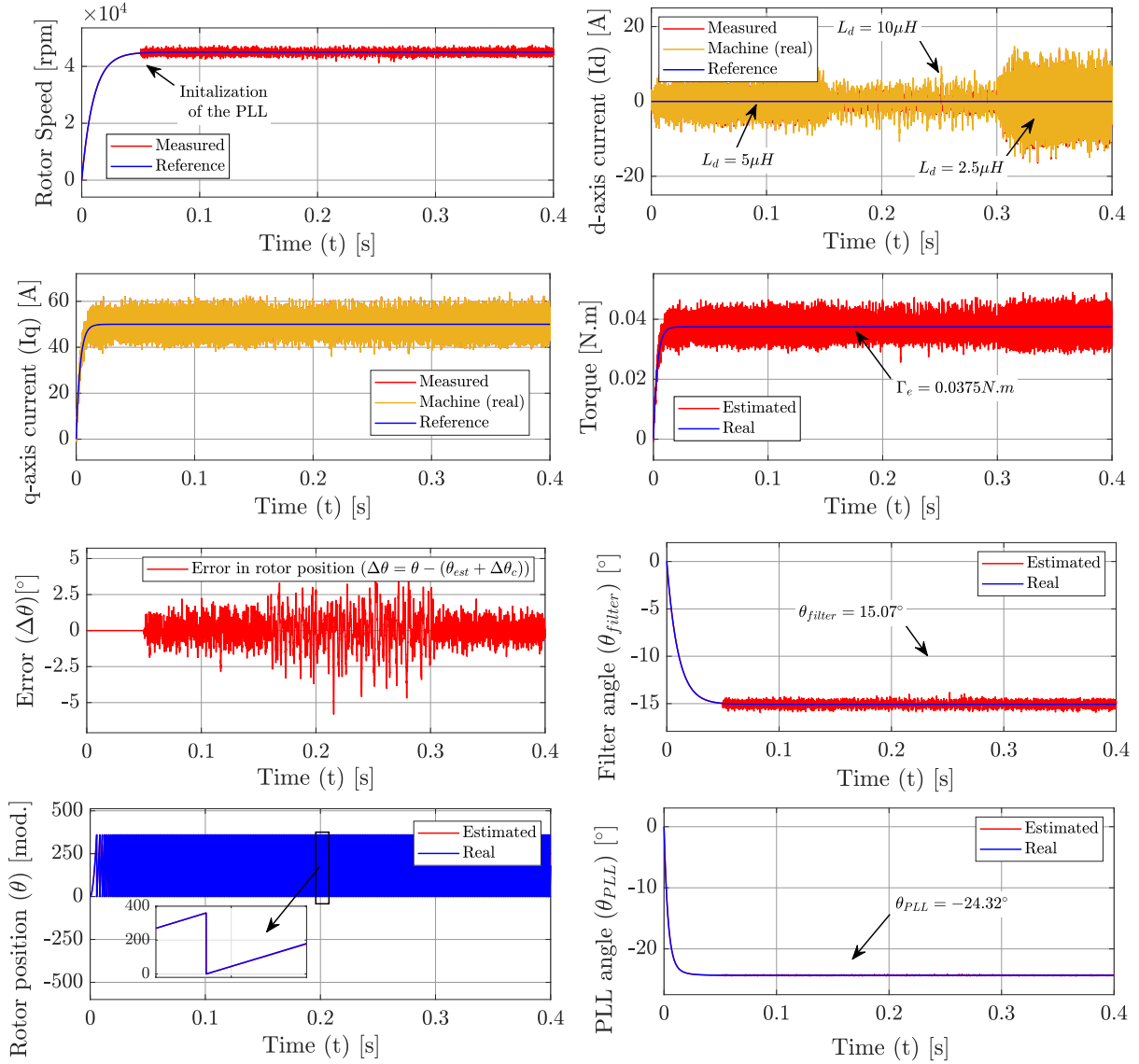


Figure C.5: Investigation of the parametric sensitivity via simulation - Study considering the variation of the machine parameter $L_d = 5\mu H$, $L_d = 2.5\mu H$ and $L_d = 10\mu H$, for control dq-axis inductances $L_d = L_q = 5\mu H$.

case. By the same logic, For angles $\Delta\theta_c > \Delta\theta_{c_{ref}}$, it is observed a negative d-axis current in the machine and an increase in the DC and AC power and torque due to the reluctance, as can be observed in the Case (3). Enhancing this adjusted compensation angle (Case (4)), it is noticed that these DC and AC power and torque can be also increased. For higher $\Delta\theta_c$, as exhibited in Case (5), the torque produced is not more maximal. Reducing it again to the same values as proposed in Case (4), the maximization can be again observed (Case (6)). Finally, Case (7) exhibits the results achieved when the current set points are defined by using this mentioned $\delta = \delta_{max} = 15.5^\circ$. The control currents are again observed converging to the machine and reference currents and the maximal torque and DC and AC power are achieved.

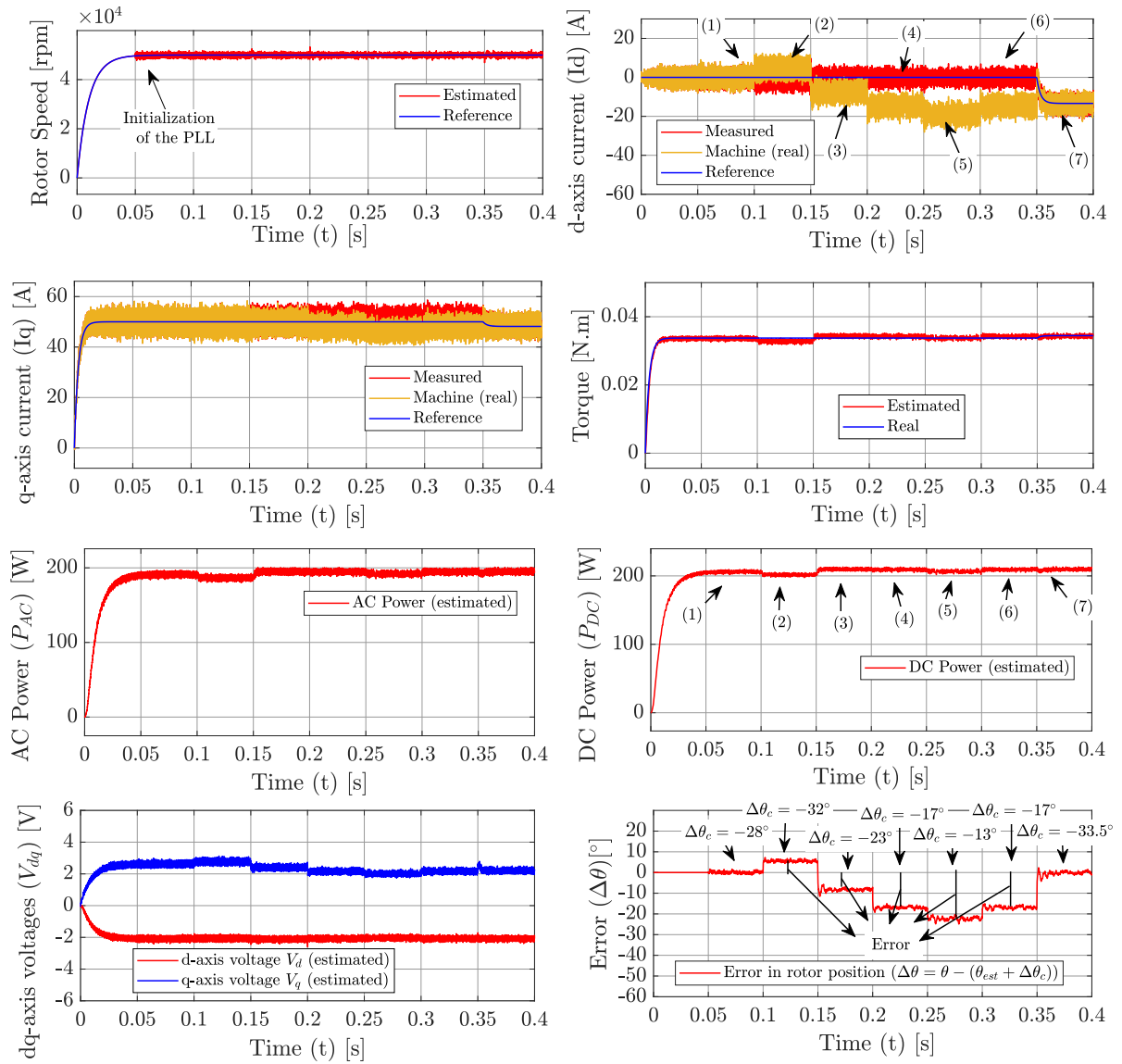


Figure C.6: Effect of the variation of the compensation angle ($\Delta\theta_c$) considering the hypothesis of a salient machine ($L_d = 6\mu H$ and $L_q = 8\mu H$) - Study for $I_{ref} = 50A$.

List of publications

- **International journal with peer review:**

1. **F. D. de Sousa**, A. Battiston, F. Meibody-Tabar and S. Pierfederici, "Evaluation of the Magnetic Behavior of a Single Pole Pair Fe-Cr-Co-based Memory Motor Considering a Standstill Magnetization", in *IEEE Transactions on Magnetics*.

- **International conferences with proceedings:**

1. **F. D. de Sousa**, A. Battiston, S. Sarabi, S. Pierfederici and F. Meibody-Tabar, "Magnetization strategy for a FeCrCo-based variable flux machine", *2020 23rd International Conference on Electrical Machines and Systems (ICEMS)*, Hamamatsu, Japan, 2020, pp. 1604-1609.
2. **F. D. de Sousa**, A. Battiston, S. Pierfederici and F. Meibody-Tabar, "Validation of the standstill magnetization strategy of a FeCrCo-based Variable Flux Memory Machine", *2021 24th International Conference on Electrical Machines and Systems (ICEMS)*, pp. 536-541.

Extended abstract (French version)

Introduction générale

Les machines synchrones à aimant permanent (MSAPs) ont été utilisées dans de nombreux domaines industriels, et sont particulièrement intéressantes pour les entraînements de traction utilisés dans les véhicules électriques (VE) [12, 27, 28]. Dans des conditions de fonctionnement normales, ces machines sont conçues pour maintenir une magnétisation constante grâce aux aimants de terres rares (aimants permanents) utilisés comme source de champ magnétique. Néanmoins, les risques d'approvisionnement, la variabilité des prix et les défis environnementaux liés à l'extraction et au recyclage de ces matériaux ont été présentés dans la littérature actuelle [10, 7, 8, 29] comme des préoccupations majeures pour l'utilisation de ces machines à long terme. En outre, pour étendre la plage couple-vitesse caractérisant ces machines au-delà de la vitesse de base, des stratégies d'affaiblissement du flux (défluxage) à partir de l'injection dans les enroulements d'induit d'un courant négatif pour générer un champ dans l'axe de magnétisation (axe d) sont généralement proposées pour contrer l'augmentation de la force contre-électromotrice (FEM) [12, 27, 30]. Néanmoins, des pertes de cuivre supplémentaires pour les machines à pôles non saillants [17, 28] et des risques de démagnétisation permanente de l'aimant de terre rare utilisé [31, 32] sont associés à l'utilisation de ces stratégies de défluxage, qui limitent également les MSAPs en termes de production de couple car une partie de la capacité des courants statoriques est compromise [33].

Dans ce scénario de transition énergétique pour des systèmes électromoteurs plus durables, cette thèse est dédiée à l'étude des machines à mémoire à flux variable (MMFVs). Basées sur l'utilisation d'aimants à faible force coercitive (FCC) caractérisés par une boucle d'hystérésis hautement non linéaire, ces machines présentent comme caractéristique principale la possibilité de voir leur densité de flux magnétique régulée par un champ d'aimantation externe créé par l'injection de courants d'axe d de courte durée dans les enroulements du stator. Lorsque ces courants d'axe d sont supprimés, une partie de l'état d'aimantation initial de l'aimant FCC est conservée, ce qui représente la "mémoire" de ces aimants. De nombreux auteurs ont étudié l'utilisation d'alliages Al-Ni-Co (Aluminium-Nickel-Cobalt) comme aimants FCC dans les MMFV (citecite58, cite192, cite204. Toutefois, des matériaux magnétiques similaires comme le Fe-Cr-Co (Fer-Chrome-Cobalt) sont encore peu explorés, bien qu'ils présentent des caractéristiques avantageuses comme la faible teneur en Cobalt et les propriétés mécaniques [6, 35, 36].

Selon la méthode d'excitation utilisée [19, 37, 34], les MMFVs peuvent être classés comme étant magnétisés à partir d'un enroulement dédié (dans la littérature, "DC-magnetized"), pour lesquels une bobine spécifique est disposée dans le stator pour l'injection des courants de magnétisation, ou comme étant magnétisés sans enroulement dédié (dans la littérature, "AC-magnetized"), si ces courants sont directement injectés dans les enroulements du stator. Cette dernière catégorie prend en compte les topologies de type simple [23, 34], dans lesquelles seuls les aimants FCC sont utilisés pour produire le flux magnétique, ou dans des topologies de type hybride ([33, 38]), qui utilisent des aimants à force coercitive élevée pour produire un flux lié en série ou en parallèle à celui généré par l'aimant à faible force coercitive. La plupart des géométries de machines étudiées dans la littérature actuelle sont de type hybride, mais la présente thèse se concentre sur

les aspects une machine à mémoire à flux variable du type simple. Sans enroulement dédié à la magnétisation et avec une paire de pôles, cette machine a été conçue à partir d'une MSAP dans laquelle le rotor à base de Nd-Fe-B (Néodyme-Fer-Bore) est remplacé par un rotor solide à base de Fe-Cr-Co. La géométrie du stator est conservée et une forme cylindrique est définie pour le rotor en vue d'une adaptation facile à multiples géométries de stator mentionné et d'une réduction de la fragilité dans les opérations à haute vitesse.

La variation du niveau de magnétisation de l'aimant est proposée via deux stratégies: la magnétisation à l'arrêt, qui considère l'injection de courants dans les enroulements du stator à une vitesse nulle du rotor ($\Omega = 0rpm$) et qui est utilisée pour initialiser l'état de magnétisation dans le cas d'une machine complètement démagnétisée, et la magnétisation en dynamique, caractérisée par un ajustement de cet état de magnétisation en cours de fonctionnement ($\Omega \neq 0rpm$). Pour les opérations à $\Omega \neq 0rpm$, l'utilisation d'un contrôle vectoriel visant le découplage du contrôle du couple et du flux nécessite l'identification de l'axe direct (pour le contrôle de la magnétisation) et de l'axe en quadrature (pour le contrôle du couple). Des erreurs dans la position du rotor peuvent avoir des conséquences comme une mauvaise magnétisation ou une démagnétisation involontaire du rotor magnétique. En outre, le couple mentionné doit être théoriquement contrôlé sans modifier l'état de magnétisation de la machine. En fonction de la géométrie de la machine et des propriétés de l'aimant (faible champ coercitif), cependant, une interaction entre ce champ extérieur créé dans l'axe q pendant le contrôle et celui de la magnétisation peut entraîner l'établissement de régions de renforcement et d'affaiblissement du flux dans l'aimant. En fonction de l'amplitude du courant utilisé pour créer ce champ de l'axe q, ce phénomène connu sous le nom de réaction de l'induit [27, 31] peut conduire aussi à la démagnétisation de l'aimant.

Habituellement, la position du rotor est obtenue par l'utilisation de codeurs incrémentaux ou absolus ou de résolveurs. Néanmoins, ces capteurs présentent certains inconvénients tels que des coûts supplémentaires, des exigences de maintenance, une augmentation de la sensibilité et des limites de vitesse. La machine à base de Fe-Cr-Co proposée dans le cadre de cette recherche est spécialement destinée aux applications à haute vitesse, pour lesquelles le moindre déséquilibre sur l'arbre du rotor est très préjudiciable, et l'utilisation de stratégies sans capteurs est nécessaire [25, 44, 45]. Bien que largement explorée pour les MSAPs, l'utilisation de stratégies sans capteur pour les MMFVs n'a été présentée que très récemment dans [46], qui propose une commande sans capteur basée sur la saillance pour un MMFV hybride à double-couche, sans enroulement dédiée à la magnétisation. Étant donné que pour le MMFV à base de Fe-Cr-Co étudié, un régime prédéfini est entraîné par un flux d'air axial (pas d'opérations à vitesse nulle), un algorithme basé sur un modèle est proposé pour estimer la position et la vitesse du rotor.

Dans ce contexte, les études proposées dans cette thèse sont divisées en trois chapitres détaillés ci-dessous :

- Chapitre I présente la revue de la littérature pour contextualiser l'utilisation des machines à mémoire à flux variable. Les concepts de base de la théorie magnétique sont présentés en mettant l'accent sur les paramètres définissant la boucle d'hystérésis qui caractérise les matériaux magnétiques. L'utilisation d'aimants de terres rares pour générer le flux dans les MSAP est abordée, ainsi que les défis économiques et environnementaux liés à la continuité leur utilisation à long terme. Des matériaux magnétiques à faible force coercitive possibles pour remplacer les aimants permanents pour des applications liées à l'électrification des véhicules sont présentés. Parmi eux, les propriétés du Fe-Cr-Co sont décrites et comparées à celles des alliages Al-Ni-Co, majoritairement utilisés dans les MMFVs. Le grade d'aimant FeCrCo36/5 est présenté comme celui choisi pour composer le rotor cylindrique de la machine étudiée dans cette recherche. Ensuite, la théorie derrière le comportement magnétique des machines à mémoire à flux variable est discutée ainsi que

leur place parmi les machines électrique et ses différents catégories. Finalement, un modèle mathématique décrivant le principe de fonctionnement des MMFV est également introduit et discuté.

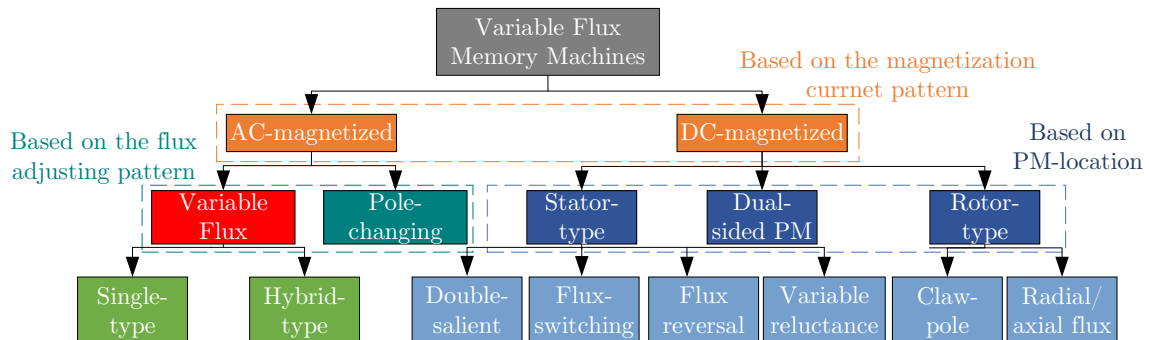


Figure C.7: Catégories de machines à mémoire à flux variable - Adapté à partir de [19].

- Chapitre 2 est consacré au développement et à l'évaluation d'une stratégie de magnétisation à l'arrêt de la MMFV à base de Fe-Cr-Co (grade FeCrCo36/5). La géométrie de la machine considérée pour cette étude est présentée ainsi que l'architecture de l'électronique de puissance, composée d'un onduleur à deux niveaux utilisé pour générer les impulsions de courant nécessaires à la variation de l'état de magnétisation de l'aimant FeCrCo36/5. En raison du profil anisotrope présenté par ce matériau magnétique, deux études sont distinguées dans ce chapitre: une première étude, à partir de la rotor initialement usiné de manière à être traversé par le flux magnétique dans la direction de magnétisation difficile, et une deuxième étude, considérant un nouveau rotor, proposé pour assurer un flux passant par la direction de magnétisation facile. Des tests expérimentaux ainsi que des simulations via l'analyse par éléments finis sont proposés pour caractériser le comportement magnétique de ces deux rotors magnétiques mentionnés dans des différents états de magnétisation partielle. Ces résultats sont ensuite comparés aux résultats intrinsèques obtenus via un équipement de mesure idéal, le HysteresisGraph. Les différences observées sont évaluées et des stratégies pour les compenser sont discutées.

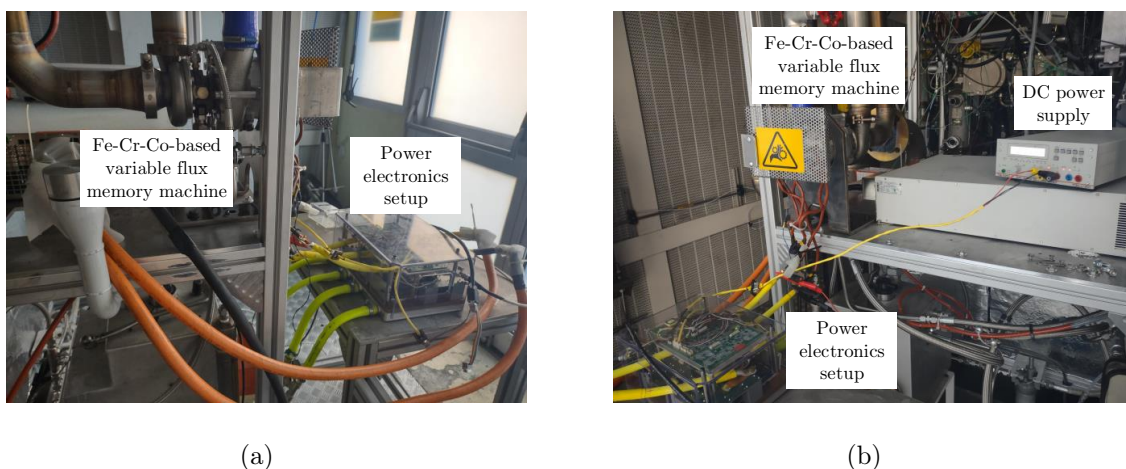


Figure C.8: Banc d'essais.

- Chapitre 3 introduit une stratégie sans capteur basée sur une Boucle à Verrouillage de Phase du type Proportionnel Intégral (BVP) basée sur la mesure de la tension de phase de sortie pour estimer la position et la vitesse du rotor. Une attention particulière est accordée à la compensation des retards de phase qui composent cet angle initialement estimé en raison de la chaîne de filtrage, de la méthode d'estimation (BVP) et du temps de calcul. Les équations décrivant les angles mentionnés sont définies et les résultats sont comparés à ceux obtenus expérimentalement. Les différences observées entre eux sont discutées sur la base d'une étude de sensibilité paramétrique. Déterminant l'impact sur les angles calculés des erreurs dans les paramètres de la machine (inductances de l'axe dq et résistance du stator) et du système (régime et liaison de flux), cette étude est utilisée pour justifier la dépendance de l'angle de compensation global par rapport aux inductances de l'axe dq mentionnées. Dans ce contexte, une analyse approfondie de la modélisation de paramètres machine est proposée en tenant compte du profil d'hystérésis anisotrope du Fe-Cr-Co composant le rotor et de la saturation du matériau du stator.

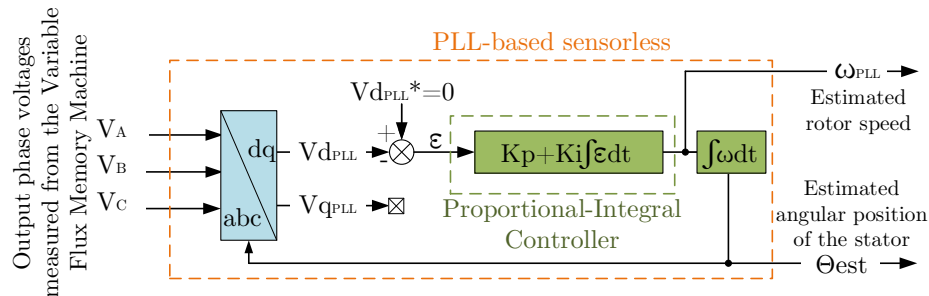


Figure C.9: Schéma fonctionnel de l'algorithme à Boucle de Verrouillage de Phase.

A la suite de ces chapitres, les conclusions générales sont exposées ainsi que quelques pistes qui peuvent potentiellement être utilisées comme axes d'étude pour des travaux futurs.

Ce projet de thèse s'inscrit dans un scénario de transition énergétique pour des systèmes électromoteurs plus durables et présente comme objectifs majeurs :

- Proposer une machine à mémoire à flux variable à base de Fe-Cr-Co à un paire de pôles conçue à partir d'une MSAP dans laquelle l'aimant permanent initialement utilisé (Nd-Fe-B) sera remplacé par un aimant à faible force coercitive (Fe-Cr-Co).
- Valider expérimentalement les concepts en utilisant un modèle de preuve de concept.
- Évaluer le comportement magnétique de la machine à mémoire à flux variable proposée à base de Fe-Cr-Co à partir du développement de stratégies de magnétisation à l'arrêt et en dynamique;
- Proposer une stratégie de contrôle robuste pour produire un couple dans cette machine.

Conclusion Générale

Les études développées dans cette thèse ont exploré le comportement magnétique et le contrôle d'une machine à mémoire de flux variable (MMFV) à base des aimants Fe-Cr-Co. Conçue à partir d'une machine synchrone à aimant permanent (MSAP) en remplaçant un rotor à base de Nd-Fe-B par un rotor cylindrique massif à base de Fe-Cr-Co, cette machine du type unique est caractérisée par une géométrie à une paire de pôles, sans enroulements supplémentaires pour dédiés à la magnétisation.

Il convient de rappeler que les MMFV ont attiré l'attention dans les domaines d'application de l'électrification des transports, notamment en raison de leur degré de liberté supplémentaire pour le contrôle, défini par l'ajustement du flux magnétique. Bien que cette caractéristique puisse également être obtenue dans d'autres géométries de machines grâce à des stratégies d'affaiblissement du flux (défluxage), les pertes Joule qui y sont liées représentent généralement un inconvénient. Pour les MMFV, l'utilisation d'impulsions de courant de courte durée pour créer un champ externe dans l'axe de magnétisation (généralement, l'axe d) permet la variation de l'état de magnétisation de l'aimant avec des pertes réduites. Dans le même temps, les préoccupations environnementales liées à l'extraction, au recyclage et au raffinage des aimants de terres rares (comme le Nd-Fe-B) peuvent également être prises en compte par ces machines, car leurs conceptions sont proposées en évitant partiellement ou totalement l'utilisation de ces alliages. Les aimants à faible force coercitive (comme ceux de Fe-Cr-Co) sont préférés, car leur profil d'hystérésis hautement non linéaire permet d'ajuster le point de travail dans des conditions de changement dynamique de charge.

Dans ce cadre, trois axes majeurs ont été discutés dans cette recherche de thèse :

- Chapitre [I](#) a présenté le positionnement des MMFV dans le scénario des machines électriques et leur classification selon les différents arrangements d'aimants (par exemple, hybrides ou à type unique) et de géométries (par exemple, sans ou avec des enroulements dédiés à la magnétisation). Les aimants utilisés pour produire le flux dans ces machines sont différenciés en fonction de leurs caractéristiques magnétiques. Le Fe-Cr-Co est présenté comme un matériau magnétique à faible force coercitive, notamment avantageux en termes de résistance mécanique/corrosion, ce qui permet sa usinage en plusieurs géométries à faible coût, et une teneur réduite en Cobalt, ce qui devrait avoir un impact positif sur le prix, car il se consiste en un matériau critique en termes d'approvisionnement.

Dans ce contexte, cette recherche de thèse répond à un manque d'information dans la littérature actuelle concernant l'utilisation d'alliages Fe-Cr-Co dans les MMFV. Il est plus difficile de trouver des informations techniques sur ces derniers alliages que sur d'autres matériaux couramment utilisés par les auteurs (par exemple, les aimants Al-Ni-Co). Ce scénario indique un défi possible pour l'utilisation à grande échelle des MMFV à base de Fe-Cr-Co et peut éventuellement être un facteur bloquant pour l'évolution des études et le développement de ces conceptions de machines.

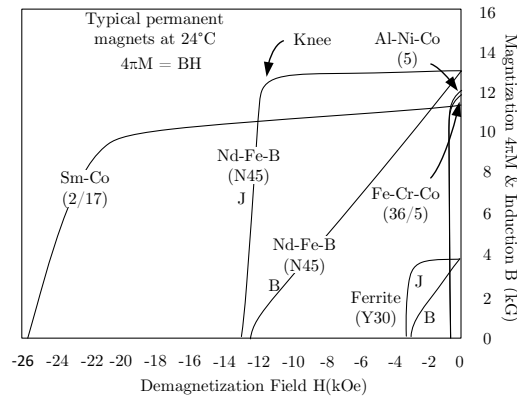


Figure C.10: Courbes de démagnétisation des aimants typiquement utilisés pour produire le flux magnétique dans des machines électriques - Adapté à partir de [15].

- Chapitre 2 a exploré le comportement magnétique du FeCrCo36/5, l'aimant anisotrope utilisé pour composer le rotor du VFMM étudié dans cette thèse. L'état de l'art existant se concentre uniquement sur la présentation des matériaux à faible force coercitive comme des matériaux similaires à ceux de terres rares en termes de rémanence et de forme de la courbe d'hystérésis. Cette recherche propose également l'analyse dans le cas d'une réponse magnétique au champ externe caractérisée par l'absence d'un coude bien défini dans le deuxième quadrant. L'importance de cette étude complémentaire réside dans le fait que certains aimants adaptés aux MMFV (par exemple, le FeCrCo12/4, caractérisé par un niveau de rémanence équivalent à celui d'un aimant permanent et une faible coercivité) présentent cette dernière caractéristique d'hystérésis mentionnée. Dans ce contexte, la MMFV proposée est étudié par une distinction entre deux aimants FeCrCo36/5, fabriqués pour être respectivement traversés par le champ externe dans les directions d'aimantation difficile et facile. Ces directions sont respectivement identifiées l'absence ou la présence d'un coude bien défini dans le deuxième quadrant de la courbe d'hystérésis.

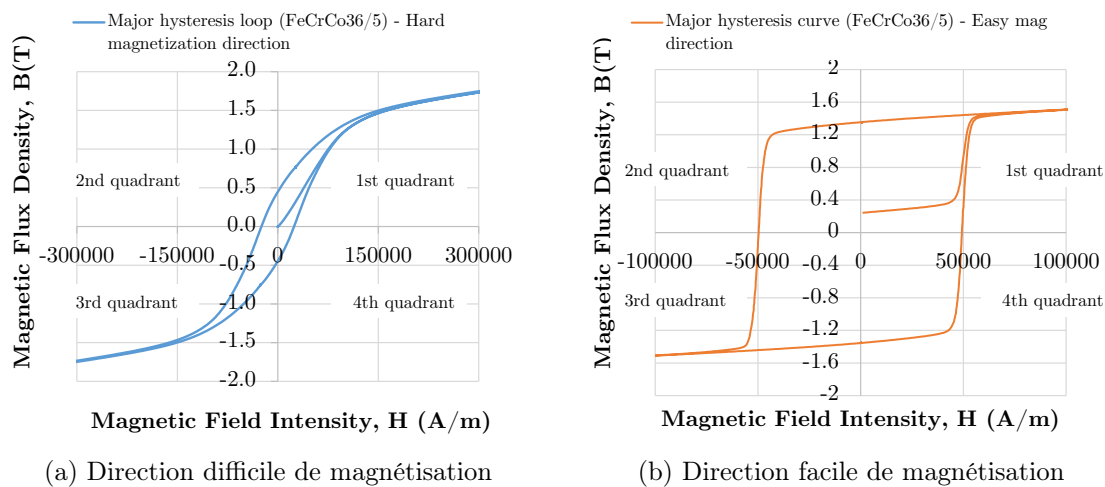


Figure C.11: Boucle d'hystérésis externe du FeCrCo36/5 obtenue à l'aide du HysteresisGraph.

À cause de cette distinction, une méthodologie d'aimantation à l'arrêt est développée pour décrire le modèle d'hystérésis de chacun des axes magnétiques mentionnés dans le cas d'états d'aimantation partiels, atteints pendant les phases d'ajustement du flux. Le profil magnétique défini à partir de ces résultats dans la direction de magnétisation facile est l'objet principal de cette étude en raison des niveaux d'aimantation considérablement plus élevés atteints. Cependant, ces résultats et ceux obtenus dans la direction de magnétisation difficile conduisent aux mêmes conclusions: la proposition de concevoir une MMFV à partir d'une géométrie initialement conçue pour une MSAP peut compromettre les performances de cette nouvelle machine. Pour la MMFV étudié dans cette thèse, non seulement la capacité de magnétisation initiale des impulsions de courant de l'axe d alimentant les enroulements de l'induit est affectée, mais aussi le niveau de la FEM qui pourrait être induite à partir d'un état de magnétisation prédéfini. Principalement en raison de la saturation du matériau du stator et de la présence des isthmes d'encoches fermées dans la géométrie du stator, les résultats présentés dans ce chapitre indiquent que la sensibilité du point de fonctionnement dans une MMFV nécessite une géométrie adaptée aux caractéristiques de l'aimant utilisé pour produire le flux. Sinon, la description des courbes d'hystérésis internes à partir du point de fonctionnement mesuré expérimentalement ne représente pas directement le comportement intrinsèque de l'aimant comme prévu. Dans ce cas, comme pour la MMFV à base de Fe-Cr-Co, il est nécessaire de proposer une stratégie pour corriger ces effets dans le stator avant de valider le comportement des points de travail selon la référence fournie par un équipement de mesure idéal (HysteresisGraph).

- Chapitre 3 a étudié l'aimantation en cours de fonctionnement de la machine à mémoire à flux variable à base de Fe-Cr-Co, en utilisant comme référence les résultats de l'aimantation à l'arrêt présentés dans le chapitre précédent. La machine étant conçue pour des applications à haute vitesse, un algorithme sans capteur est proposé. Bien que largement étudiée pour les MSAPs, l'utilisation de ces techniques sans capteur pour estimer la vitesse et de la position rotorique des MMFV n'a été introduite que très récemment dans la littérature. En effet, plus que la dépendance de la commande vectorielle à la connaissance de la position du rotor pour le contrôle de la magnétisation et du couple, comme largement

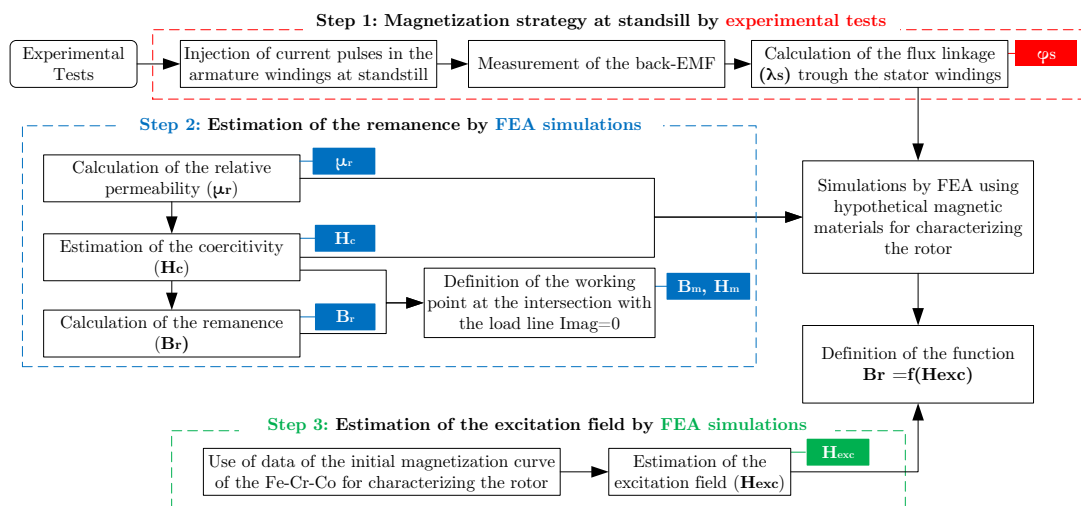


Figure C.12: Synthèse de la méthodologie proposée pour la validation du placement du point de travail du Fe-Cr-Co magnétisé dans la direction de la magnétisation difficile.

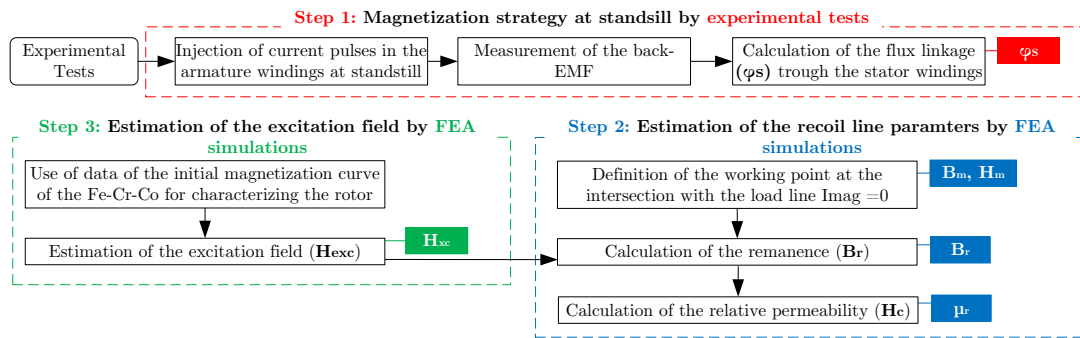


Figure C.13: Synthèse de la méthodologie proposée pour la validation du placement du point de travail du Fe-Cr-Co magnétisé dans la direction de la magnétisation facile.

connu pour les MSAPs, les MMFVs dépendent également de cette information pour éviter une démagnétisation involontaire de l'aimant. Une stratégie basée une Boucle à Verrouillage de Phase du type Proportionnel Intégral est développée pour estimer la vitesse et la position du rotor à partir de la mesure des tensions de phase de sortie. Composant ce système, un étage de correction d'angle global est aussi développé analytiquement et validé par des simulations. L'objectif est de prendre en compte dans la position du rotor obtenue les déphasages d'angle générés par le modèle d'estimation (BVP), en prenant également en compte ceux causés par le système d'acquisition (filtres) et le temps de calcul, souvent négligés par les auteurs.

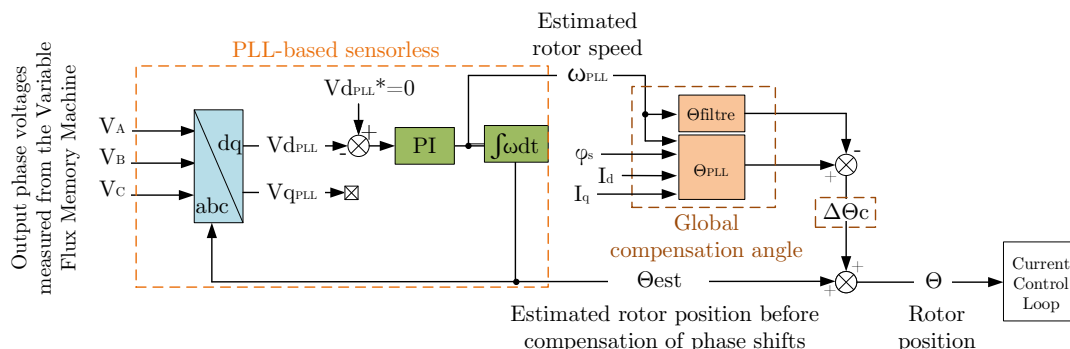


Figure C.14: Schéma fonctionnel de l'algorithme sans capteur basé sur PLL et de l'angle de décalage global à compenser.

Comme ces angles sont calculés à partir des grandeurs de la machine (inductances de l'axe dq, L_d et L_q , et résistance du stator, R_s) et du système (vitesse, ω , et liaison de flux, φ_s), une étude de sensibilité paramétrique est introduite. Une hypothèse de non-salience bien connue dans le rotor ($L_d = L_q$) est définie à cause du cylindre massif utilisé. Cette étude démontre une dépendance à l'inductance de l'axe q des angles de correction à ajuster pendant le contrôle du couple. Cela représente une conclusion qui oriente le présent chapitre vers une meilleure modélisation des inductances de l'axe dq de la machine, étant donné que la non-salience initialement supposée connue n'est pas suffisante pour décrire le comportement réel de la machine observé dans les essais expérimentaux. Des études par simulations sont proposées en tenant compte du profil d'hystérésis anisotrope du FeCrCo36/5 dans les directions d'aimantation facile et difficile et des effets de saturation sur

le matériau composant le stator. L'évolution des inductances dq en fonction des courants d'axe dq alimentant les enroulements de l'induit est étudiée ainsi que leur impact sur l'angle de correction global. Il est observé que le modèle obtenu permet d'estimer cet angle mentionné avec un bon ordre de grandeur, suffisant pour maintenir le système stable afin de permettre un réglage pendant les essais expérimentaux.

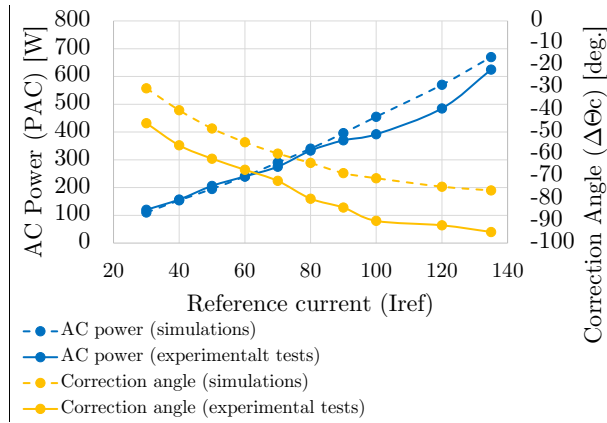


Figure C.15: Comparaison entre les angles de correction et la puissance AC maximale obtenue via la simulation et les tests expérimentaux pour de multiples amplitudes de courant I_{ref}

A partir conclusions présentées ci-dessus concernant les chapitres [1](#), [2](#) et [3](#), cinq points peuvent être mentionnés comme des avancées apportées par cette thèse à l'état de l'art actuellement disponible dans la littérature concernant des Machines à Mémoire de Flux Variable:

1. La géométrie de la machine : un rotor cylindrique à base de Fe-Cr-Co est utilisé, alors que la plupart des MMFVs explorent actuellement l'utilisation de barres d'aimants rectangulaires pour composer le rotor. Ce rotor cylindrique, facilement adaptable à différentes géométries de stator, est particulièrement intéressante pour les applications à haute vitesse, mais rend plus complexe le calcul des points de fonctionnement en raison de la variation de la longueur de l'aimant. En outre, cette recherche propose une évaluation des conséquences de la transformation d'une MSAP en un MMFV par le remplacement du rotor magnétique, en discutant de la faisabilité et des défis liés à cette proposition.

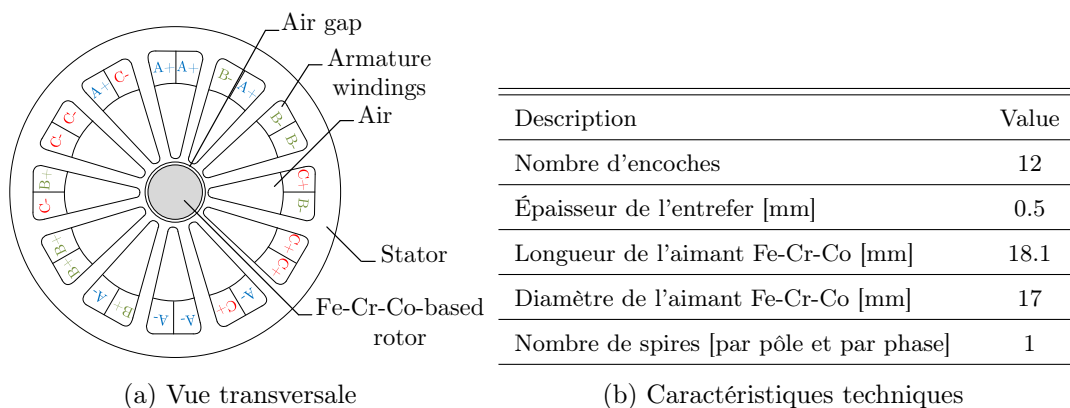


Figure C.16: Géométrie de la Machine à Mémoire à Flux Variable étudiée

2. Le matériau magnétique : comme indiqué précédemment, un aimant Fe-Cr-Co est préféré dans cette recherche aux aimants Al-Ni-Co habituellement choisis pour ces applications. En outre, l'utilisation d'aimants à basse des terres rares est totalement évitée grâce à une géométrie de machine composée uniquement d'aimants à faible force coercitive, alors que la plupart des études actuelles présentées se concentrent sur l'utilisation de types hybrides (donc une combinaison d'aimants à faible et à forte force coercitive).
3. Le système d'électronique de puissance : un onduleur qui intègre un mode DC/DC sans composants supplémentaires ni accès au neutre est proposé pour alimenter la machine avec les impulsions de courant nécessaires à l'ajustement de l'état de magnétisation des VFMM à base de Fe-Cr-Co. Il comprend les fonctions d'arrêt et de magnétisation en cours.

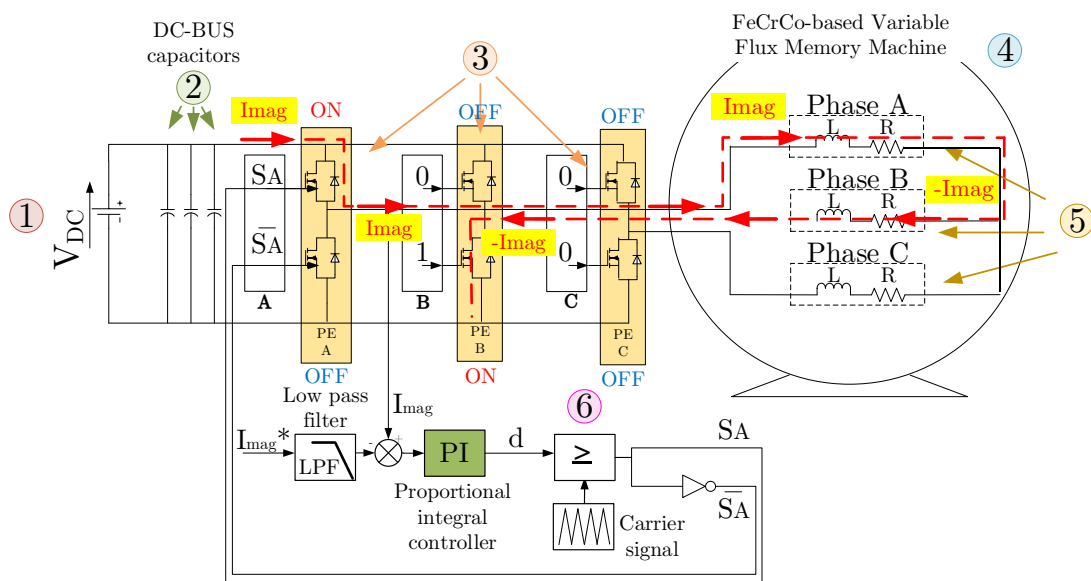


Figure C.17: Présentation de l'architecture d'électronique de puissance proposée pour l'alimentation des enroulements de l'induit lors des essais expérimentaux

4. Les caractéristiques de l'aimant et son comportement magnétique lors de son insertion dans l'environnement machine: la distinction et l'étude du modèle d'hystérésis caractérisé par l'absence et la présence d'une coude bien défini dans le deuxième quadrant.
5. Les stratégies sans capteur et de compensation d'angle : l'utilisation d'une stratégie sans capteur est nécessaire pour les applications à haute vitesse comme celles discutées dans cette thèse, mais son application pour des MMFV est rarement discutée dans la littérature scientifique.

Compte tenu de ces conclusions, quelques axes d'étude peuvent être potentiellement intéressants pour l'évolution et la suite des travaux réalisés. Quelques pistes sont présentées ci-dessous:

- Le remplacement direct d'un aimant de terres rares par un aimant à faible force coercitive dans une machine dont le stator a été conçu à l'origine pour une MSAP s'est avéré difficile. Selon les résultats discutés dans cette étude, certains aspects tels que la saturation et la

conception du stator peuvent avoir une forte influence sur le champ d'excitation nécessaire pour atteindre un certain niveau de densité de flux magnétique et également sur le chemin emprunté par les lignes de flux magnétique induisant la force contre-électromagnétique à l'arrêt. Pour cette raison, l'une des exigences les plus importantes pour les travaux futurs est la conception d'une géométrie de stator adaptée et optimisée aux propriétés de l'aimant utilisé. En outre, parce que cette géométrie massive favorise la réaction de l'induit, la géométrie du rotor en tenant compte des barrières de flux doit également être considérée.

- Comme indiqué dans les chapitres précédents, les performances magnétiques des aimants Al-Ni-Co insérés dans les machines à mémoire à flux variable devraient être similaires à celles obtenues avec les aimants Fe-Cr-Co. Pour les travaux futurs, il est proposé que cette comparaison soit réalisée en se concentrant sur lequel de ces aimants est le plus adapté pour optimiser la machine en termes d'efficacité et de performance.
- L'hypothèse selon laquelle en maximisant la puissance DC, le couple dans la machine est maximisé a été proposée pour les études développées dans ce thèse. Cependant, cette hypothèse ne tient pas compte de l'augmentation des pertes dans le fer qui peut être particulièrement importante pour les opérations à haute vitesse (ce paramètre est censé augmenter approximativement au carré de la vitesse) comme étudié par [44]. Dans ce contexte, les études futures nécessitent une attention particulière sur les pertes dans la machine et spécialement sur leur effet sur l'angle de correction global.
- Pour l'instant, l'état de magnétisation de l'aimant n'est modifié que lorsque la composante de courant de l'axe q est nulle. Selon les études développées dans [12], [46] et [145], une ondulation du couple est observée lorsque l'ajustement du flux est réalisé en charge. Pour l'éviter, des méthodes de contrôle du vecteur courant sont nécessaires. Des travaux futurs axés sur l'adaptation de ces méthodes à la commande du VFMM à base de Fe-Cr-Co sont nécessaires. La complexité impliquée dans cette procédure est spécialement liée à la réponse de la stratégie sans capteur à ce courant d'injection de l'axe d qui modifiera instantanément l'angle de correction global.
- Enfin, les travaux futurs prévoient également l'étude et la preuve de la stabilité du système de contrôle proposé. Pour ce faire, le modèle mathématique décrivant ce système autour d'un point de fonctionnement doit être développé pour définir le vecteur d'état et les équations d'état. Les valeurs propres peuvent donc être évaluées, sachant qu'une partie réelle négative de tous les pôles indique un point de fonctionnement asymptotiquement stable.